The Interplay of Magnetism and Topology in Topological Insulators

Niall Brendan Devlin

Department of Physics
University of Cambridge

This dissertation is submitted for the degree of
Doctor of Philosophy

Jesus College

June 2023

Declaration

This thesis is the result of my own work and includes nothing which is the outcome of work done in collaboration except as declared in the preface and specified in the text. It is not substantially the same as any work that has already been submitted, or, is being concurrently submitted, for any degree, diploma or other qualification at the University of Cambridge or any other University or similar institution except as declared in the preface and specified in the text. It does not exceed the prescribed word limit for the relevant Degree Committee.

Niall Brendan Devlin
June 2023

The Interplay of Magnetism and Topology in Topological Insulators

Niall Brendan Devlin

The conductive helical edge states in topological insulators (TIs) have been lauded over the last decade as a means towards the development of low-energy electronic and spintronic devices. Unfortunately, development of TI devices have been hampered by issues such as impurities and difficulty in fabrication, meaning that they are no closer to replacing traditional semiconductor platforms than when they were discovered over a decade ago. However, while the low carrier mobility of edge states in TI devices may always preclude their use in the electronics industry, the non-trivial topological nature of these edge states mean they are also a novel playground for the development and observation of exotic physics and emergent phenomena. Indeed, in recent years focus has transitioned from finding utility in bare TI devices to investigating combination of topological protection with other effects, such as magnetism and superconductivity. In particular, the introduction of magnetism into TIs leads to a variety of unique phenomena and exotic quasiparticles not observed in conventional material systems, such as the quantum anomalous Hall effect (QAHE) and Majorana fermions. The study and development of devices based on such phenomena are not only interesting from the perspective of fundamental physics, but also propose practical applications in spintronics and quantum computing. This thesis presents work on the interplay between magnetism and topology and discusses the technological significance of such an interaction.

Early stage research into the introduction of magnetism into TIs focused on doping TIs with magnetic adatoms, or engineering magnetic insulator/TI interfaces to induce magnetism into the TI edge states through a proximity effect. However, as was the case with bare TI devices, fabricating devices based on such platforms is not without difficulty. Inhomogeneities in the concentration of magnetic adatoms in doped samples, and the very weak interaction between the TI and magnetic insulator in proximity based devices mean that interesting effects and phenomena are only observable at temperatures on the range of 10's of millikelvins. In recent years, the discovery of intrinsic magnetic TIs has attracted an intense amount of research activity, as they provide a novel platform to investigate both topology and magnetism in van der Waals materials without suffering from many of the shortcomings of magnetically doped TIs or TI/magnetic insulator heterostructures. Furthermore, the antiferromagnetic coupling between layers gives rise to interesting layer dependent phenomena, where the electronic structure of samples is dependent on the parity of the number of layers, i.e. whether there are an even or odd number of layers. Literature has mainly focused on $MnBi_2Te_4$, whose order along the $\hat{z}$ axis means that it can host the QAHE and axionic insulator state.

However, the family of intrinsic magnetic TIs is extensive and can host different magnetic configurations.

In particular, in this thesis we have investigated in-plane magnetisation as a means to engineer flat-bands in the energy dispersion relation of topologically non-trivial materials. When considering antiferromagnetic interlayer coupling, we uncover an interesting dependence of the electronic dispersion and the local density of states on the parity of the number of layers. Furthermore, we demonstrate that magnetic textures at the surface of magnetic topological materials lead to spin-polarised flat-bands. In addition, the infinite mass quasiparticles occupying these flat-band states are strongly localised around magnetic domain walls.

The means of engineering flat-bands developed in this thesis may have great technological significance in electronic and spintronic applications. For instance, we propose that the system discussed in chapter 4 could be used in re-configurable magnetic memory, however they may also prove useful in the investigation of exotic physics and emergent phenomena. It is well known that the high density of electronic states in flat-bands leads to many-body interactions gaining greater importance in the overall dynamics of a system. As a result, flat-band systems can exhibit strong electronic correlations, which can result in the emergence of interesting phenomena such as non-BCS superconductivity, and other non-Fermi liquid phases, and charge or spin fractionalization. While the investigation of strongly correlated physics is beyond the scope of this thesis, the results presented here nevertheless demonstrate that magnetic TI systems are novel playgrounds for the investigation of emergent phenomena that could advance our understanding of fundamental physics in condensed matter systems.

Acknowledgements

There have been a number of individuals who have provided me with support and guidance throughout my PhD (and beyond) whom I wish to thank here. Any body of work as long as a PhD is challenging, but a series of lockdowns and lab closures during the pandemic made these four years some of the most difficult of my life, and without these people I'm sure I would not have managed to complete this undertaking.

I must start by thanking my supervisor, Professor Crispin Barnes. Professor Barnes was integral to the process of securing my funding and provided me with a great deal of support over the four years of my studies. I am also indebted to Dr Thierry Ferrus of the Hitachi Laboratory for his work as my second supervisor, providing guidance on the experimental aspects of my research. I am grateful to him, for not only all the academic support he provided, but for the life lessons taught over lunch and coffee in the Cavendish. My knowledge of topological insulators and the wider field of condensed matter physics was also greatly enriched by Professor Christopher Ford, who created an intellectually stimulating atmosphere in our weekly TI meetings.

I acknowledge funding from the European Physical Sciences Research Council and the Hitachi Cambridge Laboratory via an iCASE studentship.

I am grateful to the members of the *Thin Film Magnetism* and *Semiconductor Physics* groups at the Cavendish Laboratory for providing a great deal of support during my studies. Dr Peter Newton provided me with advice on and help with molecular beam epitaxy, device fabrication, beamline experimentation, low temperature electronic transport and real ale to name only a few of vast number of topics he has expert knowledge in. He, along with Dr James Aldous, made the TIMBE project a great deal more bearable than it would have otherwise been and I am fortunate to call both of them friends. I would also like to thank Dr Adrien Ionescu for always taking the time to help me with any questions I had, regarding subjects as diverse as physics, history geopolitics and lab politics. Again, I am very lucky to count this talented individual as a friend.

To Dr Hugo Lepage and Dr David Arvidsson-Shukur, thank you for your guidance and for ensuring that Friday group meetings (and the pub trips that sometimes replaced them) were always a joy to attend. To Dr Ankita Anirban, without your advice and the work you produced during your thesis I am sure that I would still be none the wiser as to what a topological insulator actually is. A notable mention should also go to the cryptic crosswords that myself, Hugo and Ankita spent far too much time in the canteen attempting to finish.

I spent a total of 8 years in Cambridge, and so it feels remiss to write acknowledgements without expressing my gratitude to the friends I made during my undergraduate studies. It fills me with incredible happiness that I still see all of you so regularly. In particular, I'd like to thank Ailidh, Amelia, Amy, Emma, Holly, Rachel and Sam without whom I wouldn't be the person that I am today.

I'd also like to pay thanks to my family and friends beyond Cambridge. Robbie, thank you for the last 15 years of friendship. I know I can rely on you for anything. For encouraging me in my education, for driving me to endless athletics events, and for their unending support I would like to thank my parents. I am incredibly grateful for their continuous belief in me throughout my life. I'd also like to thank my sisters, Nicola and Roisin, for being so supportive of me over the years. I can't thank Rosh, my brother-in-law Michael and their daughter Aoibhí enough for putting me up during the pandemic and letting me work on (/providing extremely welcome distraction from) my PhD during that time. To the youngest members of the family, Aoibhí, Theo and Osh, your input into the physics content on this PhD might be limited (even with Aoibhí's best efforts on the taptop), but you all deserve a mention anyway. I'm so excited to see the people you'll grow up to be.

Finally, to Maddi - if it weren't for you I'd have probably quit the PhD six or seven times. Your love and support mean more to me than any degree or title. Thank you for filling every one of my days with joy. We're very lucky.

Table of contents

Nomenclature

Mathematical notation

$\mathbb{C}$	Complex numbers
$\mathbb{H}$	Quaternions
$\mathbb{R}$	Real numbers

Acronyms / Abbreviations

UHV	Ultra-High Vacuum
2DEG	Two-Dimensional Electron Gas
AFMTI	Antiferromagnetic Topological Insulator
ARPES	Angle Resolved Photoemission Spectroscopy
AZ	Altland Zirnbauer
BHZ	Bernevig, Zhang, Hughes
BSTS	$(\mathrm{Bi, Sb})_2(\mathrm{Te, Se})_3$
BZ	Brillouin Zone
DP	Dirac Point
DW	Domain Wall
FET	Field Effect Transistor
FM	Ferromagnetic
HOTI	Higher Order Topological Insulator

IP	In-Plane
LDOS	Local Density of States
MBE	Molecular Beam Epitaxy
MBT	$Mn_2Bi_2Te_4$
MPE	Magnetic Proximity Effect
MTI	Magnetic Topological Insulator
NN	Nearest Neighbour
NN	Next Nearest Neighbour
OOP	Out-of-Plane
PHS	Particle Hole Symmetry
QAHE	Quantum Anomalous Hall Effect
QHE	Quantum Hall Effect
QL	Quintuple Layer
QSHI	Quantum Spin Hall Insulator
SdH	Shubnikov de-Haas
SOT	Spin Orbit Torque
SPTP	Symmetry Protected Topological Phase
STI	Strong Topological Insualator
STT	Spin Transfer Torque
TCI	Topological Crystalline Insulator
TI	Topological Insulator
TKNN	Thouless, Kohmoto, Nightingale, den Nijs
TRIM	Time Reversal Invariant Momenta
TRS	Time Reversal Symmetry

TSS	Topological Surface States
WAL	Weak Antilocalization
WL	Weak Localization
WTI	Weak Topological Insulator

List of figures

Chapter 1

Introduction

1.1 Topology in Condensed Matter

The concept of topology in condensed matter physics was introduced as early as the 1970s through the discovery of a superfluid phase of helium-3 [102]. However, in the 1980s the concept of *topological order* was introduced 1980's following von Klitzing, Dorda and Pepper's discovery of the integer quantum Hall effect (QHE) [175]. Since then it has transformed from a purely theoretical topic on the fringes of condensed matter physics into being one of the most widely researched areas of modern physics, with applications in low-power electronics, spintronics and quantum information processing, to name only a few [28, 176, 103, 183, 190, 49, 108].

A topological phase, more correctly referred to as a symmetry protected topological (SPT) phase, is a band insulator that falls outside the Landau-Ginzburg paradigm used in the traditional description of phase-transitions. Rather than being characterised by a local order parameter that can change through the process of spontaneous symmetry breaking, a topological phase's properties are related to the underlying global symmetries of its Hamiltonian and are robust to perturbations in material parameters. The ground state electronic properties of the system can only change through a *topological phase-transition* which occurs when the underlying symmetries are broken, e.g. by an externally applied field, or through the addition of a potential term that does respect the underlying symmetries of the system, but is large enough such that the energy gap is closed. It is for this reason that the ground state electronic properties of topological phases are referred to as *topologically protected*.

This thesis will focus primarily on the family of topological insulators (TIs) protected by time-reversal symmetry (TRS) and a charge conservation symmetry (generally, we will not refer to the presence of charge conservation symmetry as it is only broken in topological superconductors which fall outside of the remit of this thesis). The strong spin-orbit coupling in TIs leads to an inversion between the valence and conduction bands at an odd number of points in the Brillouin zone (BZ), leading to linearly dispersing conductive surface states [48, 50]. As such, these materials are insulators within their bulk, but also have a metallic boundary when interfaced with a *trivial* insulator (we will clarify the notions of trivial and non-trivial in the following sections when we introduce the concept of topological invariants). A conductive boundary/interface is not a unique feature of TIs and can appear in band insulators/semiconductors due to sharp changes in the crystal potential, but what makes TI surface states remarkable is that are robust to small perturbations that do not break TRS or uninvert the electronic bands, i.e. they are symmetry protected. These small perturbations may be non-magnetic impurities and disorder, surface roughness or other interfacial imperfections. It is this proposed immunity to the usual imperfections that hamper electronic devices that has led many to suggest that TIs may be a platform upon which future microelectronics are built, moving beyond traditional semiconductor based transistors. However, while there has been some promising work in this regard, TI devices have been hampered by a range of issues that have kept their carrier mobility well below theoretical predictions. As yet, there is a long way to go before a TI based field effect transistor FET can compete with current technologies and becomes commercially viable.

However, TIs possess many remarkable and unique properties that offer numerous applications beyond FETs. In particular, another consequence of TRS is that electrons at the surface of a TI are spin-momentum locked meaning that the spin of an electron is always orientated perpendicularly to its momentum. TI surface states are usually composed of counterpropagating spin-up and spin-down electrons (known as a helical mode) which may be exploited to realise extremely large spin-orbit torques (SOT), a method of switching the magnetisation of a ferromagnet (FM) through a spin-polarised current in an adjacent layer. The helical nature of TI surface states means that an unpolarised current injected into a TI generates a pure spin current perpendicularly to the applied current (this is also known as the spin Hall effect). The resulting spin accumulation can be harnessed to switch the magnetisation in a proximate FM layer with a much higher efficiency than current methods, such as spin-transfer torque (STT). This offers the possibility of future SOT-MRAM technologies operating at much lower current densities and much higher efficiency than current STT-MRAM. So far, topological materials have shown plenty of promise in SOT-based devices and appear to be the material platform of choice over other materials with charge-spin conversion capabilities, such as heavy metals.

In the above examples of the potential uses in TIs in low-power electronics, TRS played an important role. Breaking TRS, however, offers the possibility of realising novel states of matter and exotic quantum phenomena. In particular, breaking TRS through the introduction of magnetic exchange terms can provide a platform for the topological magnetoelectric effect, the Weyl semimetal phase and the quantum anomalous Hall effect (QAHE). Of all of these effects, it is perhaps the QAHE with the greatest technological promise. The QAHE is a zero magnetic field version of the QHE and was predicted by Haldane in 1988 [55], well before the discovery of TIs. Similarly to non-magnetic TIs the QAHE has a plethora of proposed uses in low-power electronics and spintronics, but it is also one of the key building blocks in realising Majorana fermions which provide the basis for topological quantum computing architectures [49, 108]. We will discuss magnetic TIs, particularly with regard to the QAHE, in greater detail below, but we briefly mention that considerable progress has been made in realising a high temperature QAHE through the discovery and subsequent development of intrinsic magnetic TIs over the last 4 years.

In the remainder of this introductory chapter, we will give a brief history of SPT phases in condensed matter physics and early models of TIs. After developing this theoretical framework, we will discuss the relevant aspects of quantum electron transport in TIs. Following from this we will briefly review the interplay of magnetism with topology and offer a discussion on current trends within the research field of magnetic TIs. We will then conclude this section with an outline of the remainder of this thesis.

1.1.1 A Pedagogical Review of Topological Insulators

In this section we will expand upon the details mentioned in the previous. Readers already familiar with the fundamentals of topological band theory of insulators may skip this section.

The integer quantum Hall effect

The history of TIs begins in 1980 with the experimental discovery of the QHE by von Klitzing *et al.* In the classical Hall effect [56], first observed in 1879, applying an external magnetic field perpendicularly to a metal leads to a Lorentz force that deflects charge perpendicularly to the current direction leading to a finite transverse voltage, known as the Hall voltage given by

$$\begin{aligned} V_{xy} &= -\frac{I_x B_z}{t} R_H \\ \text{where} \quad R_H &= \frac{1}{ne}, \end{aligned} \tag{1.1}$$

where I_x is the current, B_z is the magnetic field and t is the thickness of the metal. The quantity R_H is known as the Hall coefficient and can be calculated using the elementary charge, e, and the carrier density n. In terms of the conductance

$$\sigma_{xy}^{\text{Hall}} = \frac{j_x}{E_y} = -\frac{ne}{B_z} = -\frac{1}{R_H B_z}. \tag{1.2}$$

where j_x is the current density along the x axis and E_y the electric field along the y axis.

However, work in the 1970's hinted that this may not be the whole story and that quantum effects may play an important role in the Hall effect in 2D electron gases (2DEGs). This culminated in 1980 with von Klitzing's seminal experiment on a silicon based MOSFET in a high magnetic field [175]. He discovered that the longitudinal conductance vanished whilst the transverse conductance was exactly quantized:

$$\sigma_{xy}^{QHE} = -\frac{\nu e^2}{h}, \quad \nu \in \mathbb{N} \tag{1.3}$$

according to some integer $\nu = nh/eB_z$, referred to as the filling factor. This quantization persists over a range of values of B_z, giving rise to the famous quantized plateaus of the QHE experiment. Undergraduate courses in physics usually explain the QHE in terms of Landau levels and filled bands, however this simple description fails to account for the universality of the quantization i.e. why the quantization is independent of the device geometry or impurities within it. In 1981, Laughlin proposed an elegant thought experiment based on charge pumping to explain the observed quantization [100]. First consider a 2D metallic ribbon subject to a strong perpendicular magnetic field, B. In the Landau gauge, $\boldsymbol{A} = -By\hat{\boldsymbol{x}}$, the system Hamiltonian is given by

$$H = \frac{1}{2m}\left((\hbar k_x - eBy)^2 + p_y^2\right) \tag{1.4}$$

with solutions given by

$$\psi_{n,k_x}(x,y) \propto e^{ik_x x} e^{(y-y_0)^2/2l_B^2} \frac{\partial^n}{\partial y^n} e^{-(y-y_0)^2/l_B^2} \tag{1.5}$$

where $l_B = \sqrt{\hbar/eB}$ is the magnetic length and $y_0 = k_x l_B^2$ shifts the centre of the wavefunction to y_0 for the n^{th} Landau level at energy $E_n = (n + 1/2)\hbar\omega_c$ where $\omega_c = eB/m$ is the cyclotron frequency. We assume that the Fermi level is located in the gap between Landau levels meaning that the system is in an insulating phase.

The next step of Laughlin's argument is to first attach the edges of the ribbon at $y = 0, L_y$ to two electron reservoirs and then wrap the ribbon into a cylinder by tapping together the ends at $x = 0, L_x$. A magnetic flux, ϕ, is threaded through the cylinder

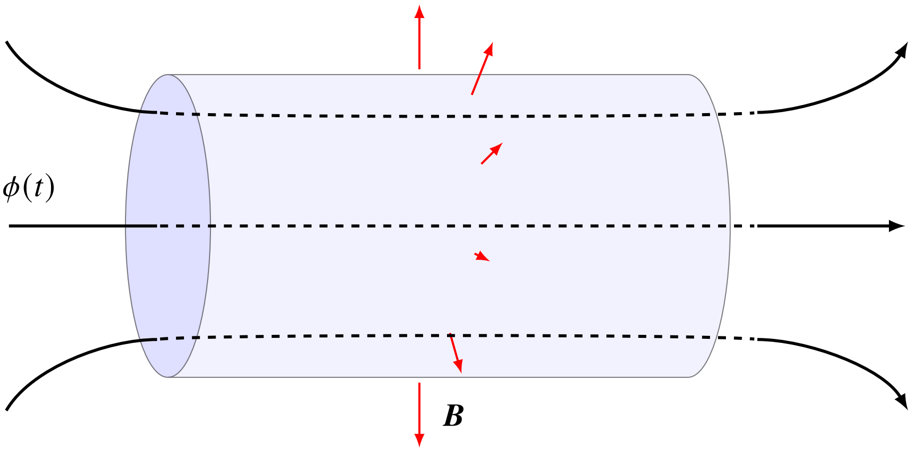

Fig. 1.1 Schematic of a Laughlin cylinder. A radial magnetic field $\boldsymbol{B}$ penetrates the cylinder at a normal angle, while an additional, tunable magnetic flux ϕ threads the cylinder. The edges of the cylinder are a $y = 0, L_y$.

while maintaining the perpendicular (now radial) magnetic field, as shown in figure 1.1. From the definition of magnetic flux and Stokes' theorem $\phi = \int \boldsymbol{B} \cdot d\boldsymbol{S} = \oint \boldsymbol{A} \cdot d\boldsymbol{l}$. Therefore, it is possible to incorporate an additional flux through the gauge transformation $\boldsymbol{A} \longrightarrow \boldsymbol{A} + \delta\boldsymbol{A} = \boldsymbol{A} + \nabla\lambda = \boldsymbol{A} + \phi/L_x\hat{\boldsymbol{y}}$. As a result, the wavefunction is transformed according to $\psi \longrightarrow e^{i\lambda}\psi$. Normally, this redefinition would have no physical meaning since the addition of a constant to the vector potential can be gauged away. We also note that wrapping the ribbon into a cylinder quantizes k_x such that $k_x = 2\pi m/L_x$ due to the periodic boundary conditions, for integer $m = 0, 1, ..., L_x$. As such, the system Hamiltonian is modified to

$$H = \frac{1}{2m}\left(\left(\frac{2\pi m\hbar}{L_x} - eBy - \frac{e\phi}{L_x}\right)^2 + p_y^2\right) \tag{1.6}$$

with the same solutions as we had previously but now shifted such that

$$\begin{aligned} y_0 \longrightarrow y_m &= \left(\frac{\hbar k_x}{eB} - \frac{\Phi}{BL_x}\right) \\ &= \left(\frac{2\pi m\hbar}{eBL_x} - \frac{\phi}{BL_x}\right) \\ &= \left(m - \frac{\phi}{\phi_0}\right)\frac{h}{eBL_x} \\ &= k_m(\phi) l_B^2 \end{aligned} \tag{1.7}$$

where $\phi_0 = h/e$ is a single flux quantum. The final step is to make ϕ time dependent, i.e. $\phi \longrightarrow \phi(t)$. If we adiabatically increase ϕ from 0 to ϕ_0 in time Δt, then the wavefunctions centred around y_m will have shifted to y_{m-1}, meaning that all the electrons along the cylinder axis will have simply shifted one step along.

The net result is that if n Landau levels are filled, a total charge of

$$\Delta Q = ne \tag{1.8}$$

has been transferred from one edge of the cylinder to the other. Furthermore, by Faraday's law the change in flux will induce a potential difference around the cylinder, in turn generating a current between the edges of the cylinder

$$\begin{aligned} I &= \sigma_{xy}\frac{\partial\phi}{\partial t} \\ &= \sigma_{xy}\frac{h}{e\Delta t}, \end{aligned} \tag{1.9}$$

and the conductance is therefore

$$\sigma_{xy} = -\frac{eI\Delta t}{h} = -\frac{e\Delta Q}{h} = -\frac{ne^2}{h}, \tag{1.10}$$

where we identify n, the number of filled Landau levels, with von Klitzing's filling factor, ν! Recall that we have placed the Fermi level between Landau levels and the system is an insulator, i.e. $\sigma_{xx} = 0$ - this is why a voltage around the cylinder does not induce a current which is also directed around the cylinder, but rather is directed across it between the edges. Examining the Hamiltonian (1.6), we find that the periodic boundary conditions (in reality, we consider the the large L limit of system size) ensure that increasing the flux by a single quantum, $\Delta\phi = \phi_0 = h/e$, maps the Hamiltonian back onto itself

$$H(\phi = 0) = H(\phi = \phi_0). \tag{1.11}$$

In other words, periodic boundary conditions and gauge invariance have ensured that the system is back in its original state, but $Q = ne$ worth of charge has been pumped from one side to the other. The actual geometry of the setup is unimportant and the above argument is still applicable for periodic ribbons.

There does, however, seem to be a blatant paradox in the above argument. Namely, if the Fermi level is deliberately placed between Landau levels such that the QHE is in an insulating state, what is carrying the Hall current? The answer lies at the edges of our geometry and

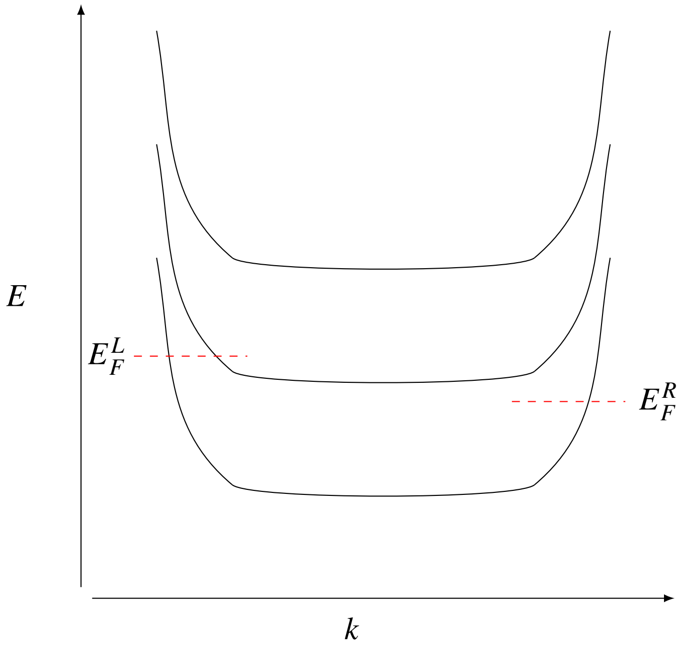

Fig. 1.2 Energy-dispersion relation of a 2DEG in a ribbon geometry with an externally applied perpendicular magnetic field. At the edges of the sample a strong confining potential causes the otherwise flat Landau levels to gain a non-zero group velocity. Applying a non-zero transverse voltage between the two edges in a sufficiently clean system leads to differing chemical potentials on either edge, E_F^L, E_F^R, and a resulting current along the length of the ribbon.

can actually be clearly understood from the classical Hall effect. In the classical Hall effect, electrons are forced to move in cyclotron orbits due to the Lorentz force. However, the edges interrupt these cyclotron orbits and cause skipping along the edge of the sample, with electrons on one edge moving in one direction and electrons on the other edge moving in the opposite (so called *chiral* edge states). It is therefore only the 2D bulk of our 2DEG that is insulating, the edges are 1D conductors [57]. However, it is a well known result that are disorder can localise 1D conducting channels and yet the QHE has been shown to exist in systems with a high concentration of impurities. The resolution to this is that these edge states are immune to backscattering because of their chiral nature. Currents on one edge can only travel in a single direction and, provided the two edges are far enough away from each other and electron-electron interactions are neglected, cannot backscatter and become localised by impurities.

Examining the energy dispersion of a 2DEG in the ribbon geometry in an externally applied perpendicular magnetic field is perhaps the simplest way to understand this edge transport. Figure 1.2 shows the band structure of this geometry, where the dispersionless (non-conductive) regions correspond to the bulk Landau levels. Near the edge of the sample, however, there is a strong confining potential which results in linearly dispersing edge states with a positive drift velocity on one edge of the ribbon and a negative velocity on the other. Since the bulk of the 2DEG ribbon is insulating when the Fermi energy is between Landau levels, we may separately consider the chemical potentials on the left and right edge, where the difference is given by $\Delta\mu = \mu_L - \mu_R$. Physically, of course, this difference can be induced by the application of a transverse electric field/voltage, $eV_{xy} = \Delta\mu$. If $\Delta\mu = 0$ then no current flows along the ribbon since there are the same number of forward moving edge modes as there are backward moving. However, if we apply a transverse voltage such that $\mu \neq 0$ then we can ensure that there are different populations of electrons on either edge. An elementary result in quantum mechanics tells us that a single transport channel has a quantum of conductance $G_0 = e^2/h$, and therefore for n edge channels in the presence of an applied voltage

$$\begin{aligned} I_x = \frac{ne^2}{h} V_{xy} &\implies \\ \sigma_{xy} = \frac{-ne^2}{h}&. \end{aligned} \tag{1.12}$$

Changing the magnetic field or the Fermi energy changes the number of edge states available, allowing us to access different QHE plateaus. From this argument, it is clear that the edge states are pumping the electrons across the bulk in Laughlin's QHE cylinder. This treatment of the QHE with respect to edge states was first made by Halperin in 1982 [57], where he showed that the QHE and its associated edge states were robust to weak disorder in the 2D bulk.

An interesting question develops from the edge state argument we just made above: what happens when two QHE ribbons are glued together? Separately, each ribbon has a certain number of chiral modes on either edge. If there are the same number of edge states in either ribbon, then gluing them together just makes a fatter ribbon, as in figure 1.3, since the oppositely moving modes on the glued edges cancel each other out. However, if there are different number of edge modes in either ribbon, say n_1 and n_2 then we will still have a net number, $n = n_1 - n_2$ of edge modes at the point they were glued together, i.e. conductive channels appear at the domain wall between the two different QHE states. This is our first introduction to the concept of *topological invariants*.

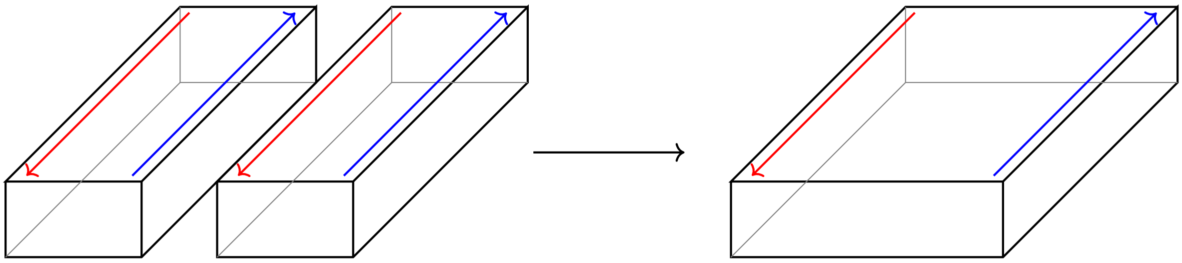

Fig. 1.3 Gluing two QHE ribbons together creates a thicker ribbon with the same number of edge states, since the forward and backward propagating states along the two edges that are joined cancel out.

The TKNN invariant and Chern numbers

While the above arguments provided by Laughlin and Halperin are elegant and motivated by simple thought experiments, the Hall conductivity can be calculated in a more rigorous fashion through the use of linear response theory. In 1982, Thouloss, Kohmoto, Nightingale and den Nijs (TKNN) did exactly this in order to demonstrate a deep connection between the transverse (Hall) conductivity, the Bloch wavefunctions and the topology of the Brillouin zone [174, 11].

First, it is helpful to define the Bloch wavefunctions. In a periodic potential, Schrodinger's equation can be written as

$$H(\boldsymbol{k})\left|\psi_{n,\boldsymbol{k}}(\boldsymbol{r})\right\rangle = E_n(\boldsymbol{k})\left|\psi_{n,\boldsymbol{k}}(\boldsymbol{r})\right\rangle \tag{1.13}$$

where n is the band index and $\left|\psi_{n,\boldsymbol{k}}(\boldsymbol{r})\right\rangle$ the single-electron wavefunction. Using Bloch's theorem, this wavefunction can be written as the product of a plane-wave and a periodic function

$$\left|\psi_{n,\boldsymbol{k}}(\boldsymbol{r})\right\rangle = e^{i\boldsymbol{k}\cdot\boldsymbol{r}}\left|u_{n,\boldsymbol{k}}(\boldsymbol{r})\right\rangle \tag{1.14}$$

where $\left|u_{n,\boldsymbol{k}}(\boldsymbol{r})\right\rangle$ has the same periodicity as the crystal potential. The periodicity of the BZ means that it is topologically equivalent to a torus. In the DC regime at absolute zero temperature, the Hall conductivity can be calculated using the Kubo formula as

$$\sigma_{xy} = \frac{ie^2}{\hbar A_0}\sum_{\boldsymbol{k}\in BZ}\sum_{E_\alpha<\mu<E_\beta}\frac{\langle u_\alpha|\,\partial_{k_x}H\left|u_\beta\right\rangle\left\langle u_\beta\right|\partial_{k_y}H\left|u_\alpha\right\rangle - \langle u_\alpha|\,\partial_{k_y}H\left|u_\beta\right\rangle\left\langle u_\beta\right|\partial_{k_x}H\left|u_\alpha\right\rangle}{(E_\alpha - E_\beta)^2} \tag{1.15}$$

where $\partial_{k_i} H = \frac{\partial H}{\partial k_i}$ where H is the Hamiltonian, similar to that given in (1.4), and A_0 is the are of the system. We have dropped the $\boldsymbol{k}$ dependence of the Bloch wavefunctions for notational clarity, but it is implied. We rewrite

$$\begin{aligned} \langle u_\alpha | \partial_{k_i} H \left| u_\beta \right\rangle &= \langle u_\alpha | \partial_{k_i} \left(H \left| u_\beta \right\rangle \right) - \langle u_\alpha | H \left| \partial_{k_i} u_\beta \right\rangle \\ &= (E_\beta - E_\alpha) \left\langle u_\alpha \middle| \partial_{k_i} u_\beta \right\rangle \\ &= -(E_\beta - E_\alpha) \left\langle \partial_{k_i} u_\alpha \middle| u_\beta \right\rangle \end{aligned} \tag{1.16}$$

using $\partial_{k_i} \left\langle u_\alpha \middle| u_\beta \right\rangle = 0 \implies \left\langle \partial_{k_i} u_\alpha \middle| u_\beta \right\rangle = -\left\langle u_\alpha \middle| \partial_{k_i} u_\beta \right\rangle$ in the final two lines. We therefore rewrite our expression for σ_{xy} as

$$\sigma_{xy} = \frac{ie^2}{\hbar A_0} \sum_{\boldsymbol{k} \in BZ} \sum_{E_\alpha < \mu < E_\beta} \left\langle \partial_{k_y} u_\alpha \middle| u_\beta \right\rangle \left\langle u_\beta \middle| \partial_{k_x} u_\alpha \right\rangle - \left\langle \partial_{k_x} u_\alpha \middle| u_\beta \right\rangle \left\langle u_\beta \middle| \partial_{k_y} u_\alpha \right\rangle . \tag{1.17}$$

The next step is to utilise the completeness relation to eliminate the unoccupied states, i.e.

$$\sum_{\mu < E_\beta} \left| u_\beta \right\rangle \left\langle u_\beta \right| = 1 - \sum_{E_\beta < \mu} \left| u_\beta \right\rangle \left\langle u_\beta \right| \tag{1.18}$$

to give

$$\begin{aligned} \sigma_{xy} &= \frac{ie^2}{\hbar A_0} \sum_{\boldsymbol{k} \in BZ} \sum_{E_\alpha < \mu} \left\langle \partial_{k_y} u_\alpha \middle| \partial_{k_x} u_\alpha \right\rangle - \left\langle \partial_{k_x} u_\alpha \middle| \partial_{k_y} u_\alpha \right\rangle \\ &\rightarrow \frac{ie^2}{\hbar} \sum_{E_\alpha < \mu} \int_{BZ} \frac{d^2 \boldsymbol{k}}{(2\pi)^2} \left\langle \partial_{k_y} u_\alpha \middle| \partial_{k_x} u_\alpha \right\rangle - \left\langle \partial_{k_x} u_\alpha \middle| \partial_{k_y} u_\alpha \right\rangle \\ &= -\frac{ie^2}{h} \sum_{E_\alpha < \mu} \int_{BZ} \frac{d^2 \boldsymbol{k}}{2\pi} \langle \nabla_{\boldsymbol{k}} u_\alpha | \times | \nabla_{\boldsymbol{k}} u_\alpha \rangle_{\hat{z}} \end{aligned} \tag{1.19}$$

where we have taken the sum over k-space to an integral in the first two lines. Defining

$$\mathcal{A}_i = -i \sum_{E_\alpha < \mu} \langle u_\alpha | \partial_{k_i} | u_\alpha \rangle \tag{1.20}$$

we find a final expression for the transverse conductivity

$$\sigma_{xy} = \frac{e^2}{h} \int_{BZ} \frac{d^2 \boldsymbol{k}}{2\pi} (\nabla_k \times \boldsymbol{\mathcal{A}})_{\hat{z}}. \tag{1.21}$$

We notice that the quantity defined in (1.20) is none other than the Berry connection, a geometric vector potential first introduced by Michael Berry in 1984 when he considered the cyclic adiabatic evolution of an eigenstate in parameter space [17]. Rather than cyclically evolving a parameter, the Berry connection in (1.20) describes the evolution of eigenstates in k-space and, in addition, is summed over all the occupied bands. Furthermore, the integrand in (1.21) is often referred to as the Berry curvature $\Omega_{ij} = \partial_{k_i}\mathcal{A}_j - \partial_{k_j}\mathcal{A}_i$ which is analogous to a k-space magnetic field. The integral of the curvature, analogous to the flux, is known as the first Chern number

$$\begin{aligned} C &= \sum_{E_\alpha<\mu} C_\alpha \\ \text{where} \quad C_\alpha &= \frac{1}{2\pi}\int_{BZ} d^2\boldsymbol{k}\,\Omega^\alpha_{xy} \end{aligned} \tag{1.22}$$

where C_α is the Chern number associatted with a particular band. In order to demonstrate that the Chern number is an integer, it is quite tempting to use the usual gauge transformation argument to show that the integral of $\boldsymbol{\mathcal{A}}$ around a closed path (known as the Berry phase) must be an integer. However, since the BZ (we are actually dealing with the magnetic BZ, but that won't make any difference to our arguments) is topologically equivalent to a torus, it is unclear how to take the surface integral in (1.21) to a path integral using Stokes' theorem. However, as shown by Kohmoto in 1985 [92], we are free to chose a loop in the BZ, γ to divide the torus into closed interior and exterior regions such that

$$\begin{aligned} \int_{BZ} d^2\boldsymbol{k}\,\Omega_{xy} &= \int_{\text{int}} d^2\boldsymbol{k}\,\Omega_{xy} + \int_{\text{ext}} d^2\boldsymbol{k}\,\Omega_{xy} \\ &= \oint_\gamma d\boldsymbol{k}\cdot\boldsymbol{\mathcal{A}}_{\text{int}} + \oint_{-\gamma} d\boldsymbol{k}\cdot\boldsymbol{\mathcal{A}}_{\text{ext}} \\ &= \oint_\gamma d\boldsymbol{k}\cdot\boldsymbol{\mathcal{A}}_{\text{int}} - \oint_\gamma d\boldsymbol{k}\cdot\boldsymbol{\mathcal{A}}_{\text{ext}} \end{aligned} \tag{1.23}$$

where we have used the fact that if the boundary of the interior is γ then the boundary of the exterior is $-\gamma$. The Berry connection is not a gauge invariant quantity (the curvature is) and therefore at the boundary between the interior and exterior regions, can be related by a gauge transformation

$$\boldsymbol{\mathcal{A}}_{\text{ext}} = \boldsymbol{\mathcal{A}}_{\text{int}} + \nabla\chi(\boldsymbol{k}) \tag{1.24}$$

for some scalar function $\chi(\boldsymbol{k})$. Therefore

$$\int_{BZ} d^2\boldsymbol{k}\Omega_{xy} = \oint_{\gamma} d\boldsymbol{k} \cdot \nabla\chi \tag{1.25}$$

In terms of the Bloch wavefunction, this gauge transformation amounts to $|u_{\alpha,\boldsymbol{k}}\rangle \to e^{i\chi(\boldsymbol{k})}|u_{\alpha,\boldsymbol{k}}\rangle$ and therefore

$$\int_{BZ} d^2\boldsymbol{k}\Omega_{xy} = 2\pi n, \quad n \in \mathbb{Z}, \tag{1.26}$$

since the wavefunctions must match exactly after completing a full loop around γ. Finally, we arrive at the TKNN invariant

$$\sigma_{xy} = \frac{e^2}{2\pi h}\sum_{\alpha} C_\alpha = \frac{ne^2}{h}, \quad n \in \mathbb{Z}. \tag{1.27}$$

which describes the relationship between the first Chern number, an integer topological invariant, and the Hall conductivity. Of course, there is no guarantee that the Chern number will be non-zero. Again using the analogy of the Berry connection and curvature to the vector potential and magnetic field of classical electrodynamics, we see that $n \neq 0$ when there is a singularity in $\mathcal{A}(\boldsymbol{k})$ in the BZ corresponding to a monopole source of Berry curvature. Mathematically, this occurs if we cannot define a smooth and continuous gauge for the phases, $\chi(\boldsymbol{k})$ of $|u_{\alpha,\boldsymbol{k}}\rangle$ everywhere in the BZ, i.e. $\mathcal{A}(\boldsymbol{k})$ is not globally well-defined across the entire BZ. In this case, we divide the BZ into various patches, each with their own local gauge - this corresponds to the loop we described in the previous paragraph to separate the BZ into and interior and an exterior (we can generalise this to taking many loops and breaking the BZ into many patches if there are multiple singularities). Generally, this tells us something about the topology of the manifold of Bloch states $|u_{\alpha,\boldsymbol{k}}\rangle$ defined over the toroidal BZ.

From the above discussion, it is clear that there are topologically distinct QHE states characterised by different Chern numbers, since different insulating phases are characterised by a different number of filled Landau levels/topological invariants. Moving between distinct topological phases is only possible through closing the bulk energy gap, that is moving the Fermi level through the next Landau level.

We can now revisit our discussion from the previous section and rephrase our argument of gluing distinct QHE states together in terms of topological invariants. At the boundary between two inequivalent topological phases, characterised by the invariants n_1 and n_2, the bulk band gap must close such that there is a topological transition at the interface between the two materials, resulting in $n_1 - n_2$ chiral modes. This is known as the *bulk-boundary correspondence* so-called as we have calculated the topological invariants using only the bulk spectrum, but these uniquely define the behaviour at the boundary between topologically inequivalent phases.

Are there any other topological phases apart from the quantum Hall state? That is, are there other means of inducing non-trivial topology that do not involve the application of an external magnetic field? In 1988, Haldane showed that this was indeed possible by constructing a toy-model based on graphene [55]. Before going into the detail of Haldane's model, we will discuss why a magnetic field can induce non-trivial topology in the first place.

Time-reversal and Inversion symmetry

The concept of time-reversal symmetry (TRS) is relatively easy to understand - it is a transformation, T which reverses the direction of time $T : t \longrightarrow -t$. As an example of TRS in classical mechanics, consider the case of a simple harmonic oscillator with the equation of motion given as

$$m\ddot{x} + kx = 0 \tag{1.28}$$

where x gives the position of the mass m and k is a constant paramterising the restoring force acting on the mass. The position of the mass, x is unchanged under $t \longrightarrow -t$ as is the acceleration and, therefore, this system respects TRS. If we now consider a realistic oscillator with some damping then we must modify our equation of motion to

$$m\ddot{x} + b\dot{x} + kx = 0 \tag{1.29}$$

where b parameterises the damping force. Since $\dot{x} = dx/dt \longrightarrow dx/d(-t) = -\dot{x}$, the inclusion of a dissipative force ensures that our system no longer respects TRS.

A more relevant example for our circumstances is the situation of a charged particle moving in a perpendicular magnetic field. It is well known that the Lorentz force is given by

$$\boldsymbol{F} = q\boldsymbol{v} \times \boldsymbol{B}. \tag{1.30}$$

If a proton is fired into a region where $B_z \neq 0$, it will be deflected perpendicular to its path and generally undergo circular motion. Applying the time-reversal operator to this equation, i.e. reversing the direction of motion/the sign of $\boldsymbol{v}$, we find the equation of motion is now given by

$$\boldsymbol{F} = -q\boldsymbol{v} \times \boldsymbol{B}. \tag{1.31}$$

With this equation of motion the particle will not travel backwards along its original path, since the direction of the centripetal force is also reversed. A magnetic field, therefore, breaks TRS.

Of course, the concept of TRS is well-defined in quantum mechanics as well. We will discuss this in greater detail in the next section, but for now we will simply state that the action of time-reversal, T on the Bloch Hamiltonian and associated eigenstates in systems respecting TRS is

$$\begin{aligned} TH(\boldsymbol{k})T^{-1} &= H(-\boldsymbol{k}) \\ T\left|u_{n,\boldsymbol{k}}\right\rangle = \left|u^*_{n,\boldsymbol{k}}\right\rangle &= e^{i\phi(\boldsymbol{k})}\left|u_{n,-\boldsymbol{k}}\right\rangle \end{aligned} \tag{1.32}$$

where the definition of a time-reversal eigenstate includes an arbitrary phase since quantum states are only defined up to an arbitrary phase.

As a brief aside, we note that spin (a type of angular momentum) must be odd under time-reversal. For spin 1/2 particles this requires $T\boldsymbol{S}T^{-1} = -\boldsymbol{S}$ where $\boldsymbol{S} = \frac{\hbar}{2}\boldsymbol{\sigma}$ and $\boldsymbol{\sigma}$ is the vector of Pauli matrices. If T is a unitary operator then it can be chosen, without loss of generalisation, to be

$$T = e^{i\hat{\boldsymbol{n}}\cdot\boldsymbol{\sigma}\theta/2} \tag{1.33}$$

where $\hat{\boldsymbol{n}}$ is a unit vector. It is clear to see that applying T is akin to a rotation about the axis along $\hat{\boldsymbol{n}}$ and, therefore, we cannot recover the behaviour that spin 1/2 systems are odd under time-reversal with this definition. In order to do so we must define

$$T = U_T K \tag{1.34}$$

where U_T is a unitary matrix and K is the operation of complex conjugation. Given that $K\sigma_y K = -\sigma_y$, the only possible choice for T is

$$\begin{aligned} T &= e^{i\sigma_y\pi/4}K \\ &= i\sigma_y K \end{aligned} \tag{1.35}$$

T is therefore an anti-unitary operator (this is true for all systems, not just spin 1/2) and $T^2 = -1$ for spin 1/2 systems (generally, $T^2 = -1$ for half integer spin and $T^2 = 1$ for integer spin).

As well as TRS, we introduce the concept of inversion symmetry. Again, more details will follow in the next section, but for now we define the action of inversion symmetry to be

$$\begin{gathered} PH(\boldsymbol{k})P^{-1} = H(-\boldsymbol{k}) \\ P\left|u_{n,\boldsymbol{k}}\right\rangle = \left|u_{n,-\boldsymbol{k}}\right\rangle = e^{i\phi(\boldsymbol{k})}\left|u_{n,\boldsymbol{k}}\right\rangle \end{gathered} \tag{1.36}$$

similar to the action of time-reversal, but without the complex conjugation. Inversion is, therefore, a unitary symmetry.

Armed with our definitions of time-reversal and inversion symmetry, we will now re-examine the (quantum) Hall effect. The Hall conductivity, $\sigma_{xy} = j_x/E_y$, is odd under time-reversal, $T : \sigma_{xy} \rightarrow -\sigma_{xy}$ since the current is odd under time-reversal. Therefore, the only way to get a non-zero Hall conductivity is to break TRS. This is also reflected in the Berry curvature

$$\begin{aligned} T\Omega(\boldsymbol{k}) &= -i\left\langle\nabla_{\boldsymbol{k}}Tu_{n,\boldsymbol{k}}\right| \times \left|\nabla_{\boldsymbol{k}}Tu_{n,\boldsymbol{k}}\right\rangle \\ &= -i\epsilon_{ij}\int \mathrm{d}\boldsymbol{r}\partial_{k_i}Tu^*_{n,\boldsymbol{k}}\partial_{k_j}Tu_{n,\boldsymbol{k}} \\ &= -i\epsilon_{ij}\int \mathrm{d}\boldsymbol{r}\partial_{k_i}u_{n,-\boldsymbol{k}}\partial_{k_j}u^*_{n,-\boldsymbol{k}} \\ &= -i\epsilon_{ij}\int \mathrm{d}\boldsymbol{r}\partial_{k_j}u^*_{n,\boldsymbol{k}}\partial_{k_i}u_{n,\boldsymbol{k}} \\ &= -i\epsilon_{ji}\int \mathrm{d}\boldsymbol{r}\partial_{k_i}u^*_{n,\boldsymbol{k}}\partial_{k_j}u_{n,\boldsymbol{k}} \\ &= i\epsilon_{ij}\int \mathrm{d}\boldsymbol{r}\partial_{k_i}u^*_{n,\boldsymbol{k}}\partial_{k_j}u_{n,\boldsymbol{k}} \\ &= -\Omega(\boldsymbol{k}) \end{aligned} \tag{1.37}$$

where we have used the definitions given in (1.32) and the antisymmetry of the Levi-Civita tensor, $\epsilon_{ij} = -\epsilon_{ji}$. Therefore, in systems where TRS is respected the Berry curvature is odd under time-reversal , $\Omega(-\boldsymbol{k}) = -\Omega(\boldsymbol{k})$. Similarly, in systems with TRS the Chern number obeys $C_\alpha = -C_\alpha$ for all filled bands, the only solution of which is $C_\alpha = 0$.

We note that TRS does not demand that the Berry curvature must vanish, only that the Chern number/Hall conductivity does. However, investigating the action of inversion on the Berry curvature

$$\begin{aligned} I\Omega(\boldsymbol{k}) &= -i \left\langle \nabla_{\boldsymbol{k}} I u_{n,\boldsymbol{k}} \right| \times \left| \nabla_{\boldsymbol{k}} I u_{n,\boldsymbol{k}} \right\rangle \\ &= -i\epsilon_{ij} \int \mathrm{d}\boldsymbol{r} \partial_{k_i} I u^*_{n,\boldsymbol{k}} \partial_{k_j} I u_{n,\boldsymbol{k}} \\ &= -i\epsilon_{ij} \int \mathrm{d}\boldsymbol{r} \partial_{k_i} u^*_{n,-\boldsymbol{k}} \partial_{k_j} u_{n,-\boldsymbol{k}} \\ &= -i\epsilon_{ij} \int \mathrm{d}\boldsymbol{r} \partial_{k_i} u^*_{n,\boldsymbol{k}} \partial_{k_j} u_{n,\boldsymbol{k}} \\ &= \Omega(\boldsymbol{k}) \end{aligned} \tag{1.38}$$

implying $\Omega(-\boldsymbol{k}) = \Omega(\boldsymbol{k})$ in systems with inversion symmetry, i.e. the Berry curvature is even. To force the Berry curvature to vanish, it is therefore sufficient to demand that system respects both time-reversal and inversion symmetry (since the only solution for a function that is both even and odd is that it vanishes everywhere).

The Haldane model

Given our symmetry considerations, it is now clear that magnetic fields induce a non-trivial topology because they break TRS. Haldane's aim in constructing his model was to realise the QHE, i.e. a non-trivial topological phase, without the application of a magnetic field. He began by considering a spinless toy-model of graphene, constructed using a triangular lattice and two sites per unit cell, A and B, see Figure 1.4. Considering only nearest-neighbour (NN) hopping terms, the Bloch Hamiltonian is given as

$$H(\boldsymbol{k}) = t_1 \sum_{i=1}^{3} (\cos(\boldsymbol{k} \cdot \boldsymbol{a}_i)\sigma_x - \sin(\boldsymbol{k} \cdot \boldsymbol{a}_i)\sigma_y) \tag{1.39}$$

where $\boldsymbol{a}_1 = (1, 0)$, $\boldsymbol{a}_2 = \frac{1}{2}(-\sqrt{3}, 1)$ and $\boldsymbol{a}_2 = \frac{1}{2}(-\sqrt{3}, -1)$ are the NN lattice vectors and $\sigma_{x,y,z}$ are the Pauli matrices acting on the sublattice degrees of freedom. The energy dispersion of this toy model is shown in figure 1.5.

At the six corners of the hexagonal BZ, the energy gap closes and the dispersion relation is approximately linear. Due to the threefold rotational symmetry of the Hamiltonian only two of the six corners are distinct, referred to as K and K'. Since the dispersion relation around these points is linear, they are also known as Dirac points (DPs) due to the similar dispersion relation found in Dirac Hamiltonian. This system respects both time-reversal and inversion symmetry according to the operators

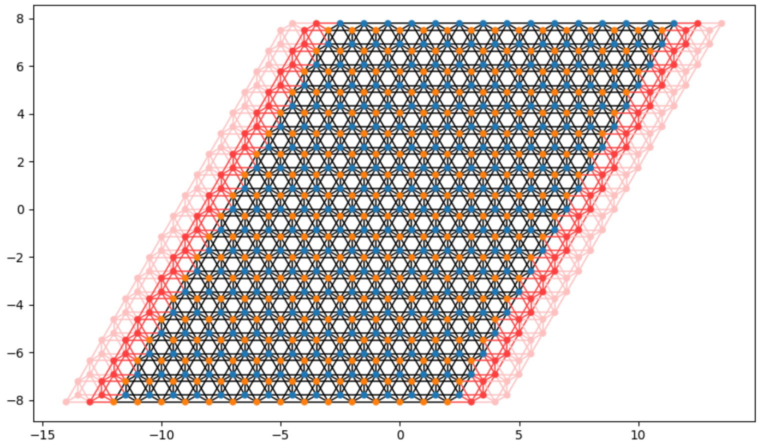

Fig. 1.4 Hexagonal lattice for graphene with NN and NNN hoppings. The two lattice points per unit cell are shown by the orange and blue points. Note that the model given in 1.39 considers only the NN hoppings between blue and orange sites (AB hoppings) while the model QAHE model given in equation 1.41 considers NNN hoppings, i.e. AA and BB hoppings between sites of the same colour.

$$\begin{aligned} T &= K \\ I &= \sigma_x \end{aligned} \tag{1.40}$$

Haldane's brilliance, which eventually saw him share the 2016 Nobel prize in physics, was to introduce a next-nearest-neighbour (NNN) hopping and a local magnetic field, $\boldsymbol{B}(\boldsymbol{r})$, perpendicular to the 2D plane and with the periodicity of the underlying lattice, but with *zero total flux* through the unit cell. In addition, Haldane included an energy offset between the A and B sublattices, controlled by a parameter M. The modified Hamiltonian is given as

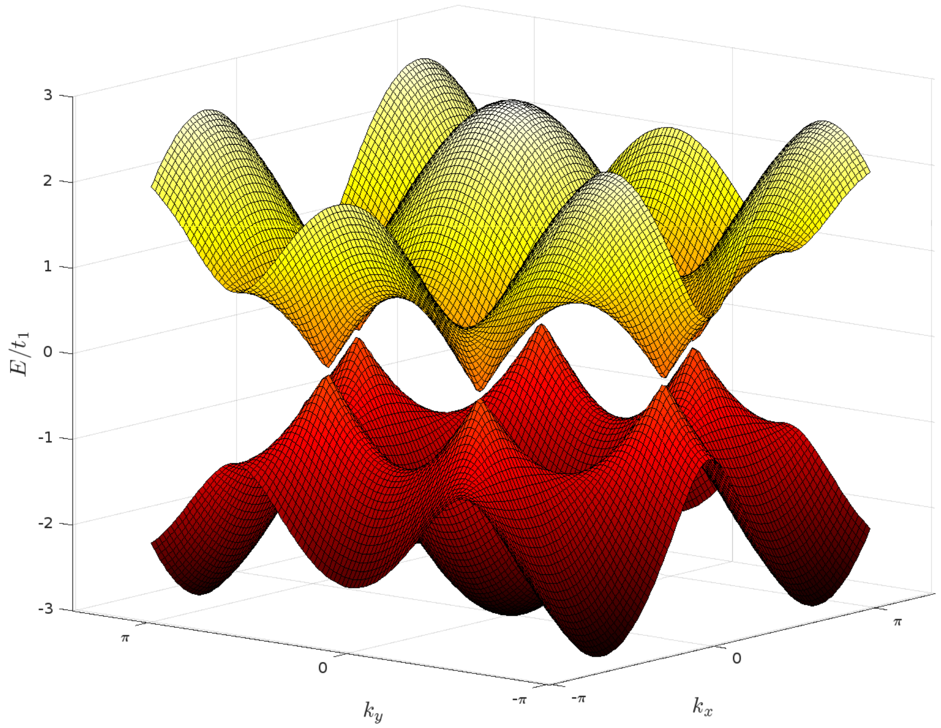

Fig. 1.5 Energy dispersion of the Haldane model with only a nearest-neighbour hopping term as described by 1.39. In the dispersion relation shown there are 6 points where the conduction and valence band touch, however the threefold rotational symmetry means only two of these points are inequivalent.

$$\begin{aligned}H(\boldsymbol{k}) &= t_2 \cos\phi \sum_i \cos\left(\boldsymbol{k}\cdot\boldsymbol{b}_i\right) + t_1 \sum_i \left(\cos(\boldsymbol{k}\cdot\boldsymbol{a}_i)\sigma_x - \sin(\boldsymbol{k}\cdot\boldsymbol{a}_i)\sigma_y\right)\\ &+ \left(M - 2t_2 \sin\phi \sum_i \sin\left(\boldsymbol{k}\cdot\boldsymbol{b}_i\right)\right)\sigma_z\\ &= \epsilon(\boldsymbol{k}) + \boldsymbol{d}(\boldsymbol{k})\cdot\boldsymbol{\sigma}\end{aligned} \tag{1.41}$$

where ϕ is a tunable parameter related to the periodic magnetic field and $\boldsymbol{b}_i$ are the NNN lattice vectors, see Figure 1.4. The effect of the NNN hoppings is to break TRS when $\sin\phi \neq 0$, while the $M\sigma_z$ term breaks inversion symmetry. The low-energy effective Hamiltonian near the $\boldsymbol{K}$ and $\boldsymbol{K}'$ points is given as

$$H_\pm = \hbar v_f(\delta k_x\sigma_x - \delta k_y\sigma_y) + m_\pm\sigma_z \tag{1.42}$$

where $\hbar v_f = 3t_1/2a$ and $m_\pm = M \mp 3\sqrt{3}t_2 \sin\phi$. The spectrum of this Hamiltonian looks like a massive Dirac spectrum, with an energy gap proportional to $2m_\pm$ at the K/K' points. Tuning the flux ϕ can, therefore, result in the energy gap closing and eventually inverting, i.e. a band inversion. As previously discussed, closing the energy gap is sufficient for a change in the value of the Chern number and the topological phase. In fact, the Chern number of the full system can be calculated as

$$C = \frac{1}{2}(\mathrm{sign}(m_-) - \mathrm{sign}(m_+)). \tag{1.43}$$

i.e. the difference of the Chern numbers (given by the sign of the mass term) for the Hamiltonians at the two distinct corners of the hexagonal BZ. A final point to mention is that since the band gaps at the K and K^{prime} points switch at different values of ϕ, there will be points where the value of the sum of their signs is non-zero, i.e. the Haldane model is in a topologically non-trivial phase.

Figure 1.6 shows the phase diagram Haldane derived. The regions labelled $C = \pm 1$ show a zero-field QHE, i.e. the QHE without a magnetic field, and occur when $|M/t_2| < 3\sqrt{3}\sin\phi$ for $t_2/t_1 < 1/3$ where the latter condition always us to safely assume that the conduction and valence band never overlap (that is, there is always a gap between them or they touch).

It is for this reason that this topological phase is often referred to as the quantum *anomalous* Hall effect (QAHE). Furthermore, comparing the equations (1.15) and (1.21) we find an alternative expression for the Berry curvature

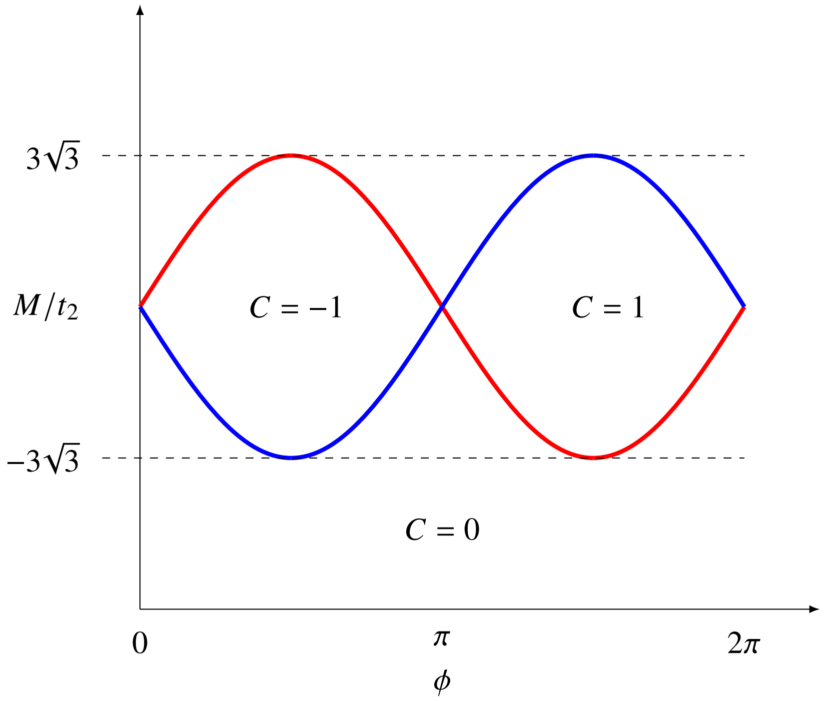

Fig. 1.6 Schematic of the phase diagram for the Haldane model with a net nearest neighbour hopping and a mass term, given in equation 1.41. The red line and blue lines plot the curves $M/t_2 \mp 3\sqrt{3}\sin\phi$, respectively. Below the red line, the mass term in the effective Hamiltonian at the K point is positive, while below the blue the line the mass term at the K' point is positive. Between the two curves the mass terms have different signs resulting in a non-trivial phase.

$$\Omega(\boldsymbol{k}) = i\sum_{\alpha\neq\beta}\frac{\langle u_\alpha|\,\partial_{k_x}H\,|u_\beta\rangle\,\langle u_\beta|\,\partial_{k_y}H\,|u_\alpha\rangle - \langle u_\alpha|\,\partial_{k_y}H\,|u_\beta\rangle\,\langle u_\beta|\,\partial_{k_x}H\,|u_\alpha\rangle}{(E_\alpha - E_\beta)^2}, \tag{1.44}$$

i.e., near band degeneracies where the denominator becomes small the Berry curvature should take on large values. We conclude that band degeneracies (in this context, Dirac points) are sources/sinks of Berry curvature. The Berry curvature is very strongly localised around the DPs.

The quantum spin Hall effect and Kramers degeneracy

In the QHE and the QAHE TRS is explicitly broken, resulting in a non-trivial topological phase characterised by a $\mathbb{Z}$ invariant which reflects how many 1D chiral modes are present at the edge. It is fair to ask if this is the only 'flavour' of topology we can get in condensed matter, or are there other types of topological invariant that can exist in Hamiltonians with different symmetries?

In 2005, Kane and Mele published two groundbreaking papers demonstrating the existence of non-trivial topology in systems respecting TRS [78, 79]. Their work generalised Haldane's spinless model of graphene at $\phi = \pi/2$ to spin 1/2 electrons and included an inversion symmetry breaking Rashba spin-orbit coupling term. Essentially, this is just two time-reversed copies of the Haldane model with a time-reversal invariant coupling between the $H_\uparrow$ and $H_\downarrow$ blocks. In the tight-binding formalism, the Kane-Mele Hamiltonian is given as

$$\hat{H} = \sum_i \epsilon_i \hat{c}_i^\dagger \hat{c}_i + t_1 \sum_{\langle i,j \rangle} \hat{c}_i^\dagger \hat{c}_j + i\lambda_{SO} \sum_{\langle\langle i,j \rangle\rangle} \nu_{ij} \hat{c}_i^\dagger \sigma_z \hat{c}_j + i\lambda_R \sum_{\langle i,j \rangle} \hat{c}_i^\dagger (\boldsymbol{\sigma} \times \boldsymbol{d}_{ij})_{\hat{z}} \hat{c}_j \tag{1.45}$$

where $\hat{c}_i^\dagger \hat{c}_i$ are the two component fermionic creation/annihilation operators, $\hat{c}_i = \hat{c}_{i,\uparrow}, \hat{c}_{i,\downarrow})$, obeying the usual anticommutation relations, $\{c_i, c_j\} = 0$ and $\{c_i, c_j^\dagger\} = \delta_{ij}$, $\sigma_{x,y,z}$ are the Pauli matrices acting in spin space and $\boldsymbol{d}_{ij} = \boldsymbol{d}_j - \boldsymbol{d}_i$ is the lattice vector from site i to j. The first term is a staggered sublattice potential, where $\epsilon_i = \pm\epsilon$ depending on whether i corresponds to an A or B site, and the second term is the NN hopping. The third term is a NNN, where $\nu_{ij} = 2(\boldsymbol{d}_i \times \boldsymbol{d}_j)/\sqrt{3} = \pm 1$ depending on whether the bond is directed clockwise/anticlockwise. This is essentially identical to the NNN hopping at $\phi = \pi/2$ in the Haldane model, however arises from a spin-orbit interaction rather than a periodic magnetic field and the sign is reversed depending on the electron spin. The final term is a Rashba coupling between NNs which breaks inversion symmetry.

In the case $\lambda_R = 0$, the Kane-Mele model is exactly equal to two time-reversed copies of the Haldane model. Since the Chern number is odd under time-reversal, the topological invariant for the two spin layers are opposite one another, $n_\uparrow = -n_\downarrow$, and the total Chern number for the full Hamiltonian vanishes $n = n_\uparrow + n_\downarrow = 0$. Clearly there are edge states present in the model, however they will not be the usual chiral edge states present in the QHE/QAHE. Due to the presence of TRS edge states will come in spin-up and spin-down pairs which will be counter-propagating, i.e. opposite spins will move in opposite directions. This is known as a *helical* edge mode. Rather than carrying a charge current, this edge mode carries a pure spin current. When $\lambda_R = 0$ we can use the Laughlin argument to show that each copy of the Haldane model will pump $\hbar/2$ worth of spin between the edges of a 1D Kane-Mele model, resulting in a pure spin current between the edges characterised by the spin conductivity

$$\sigma_{xy}^{QSH} = \frac{e}{2\pi}. \tag{1.46}$$

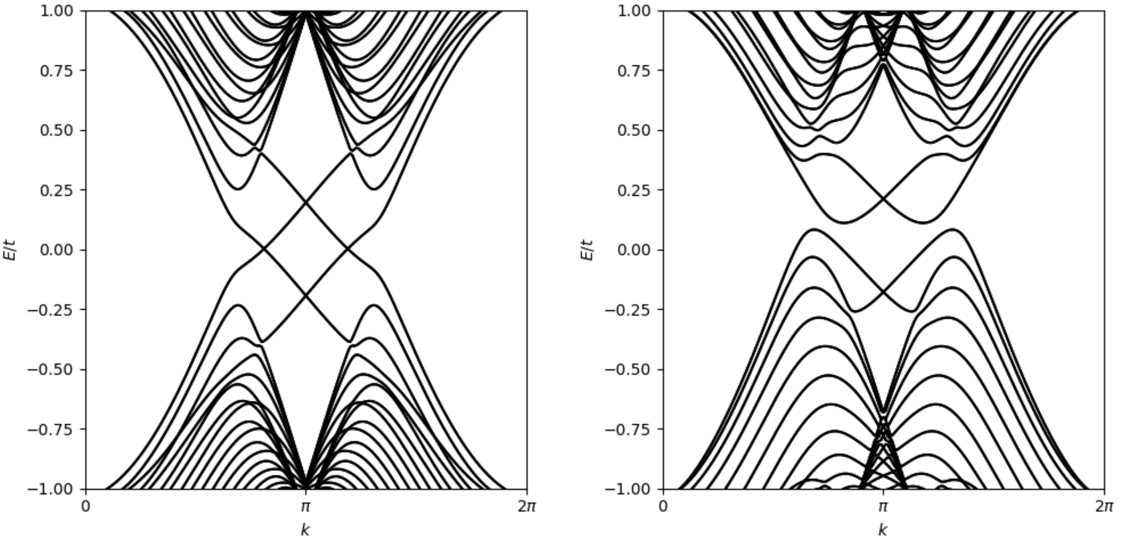

Fig. 1.7 The energy dispersion relations for the Kane-Mele model in a 1D nanoribbon geometry with a zigzag edge. On the left is the topological quantum spin-Hall state, while on the right is the trivial gapped state. These dispersion relations were numerically calculated on a 21 site wide ribbon using KWANT. In both cases, the dispersion relations were calculated using the parameters $t = 1$, $\epsilon = 0.2$ and $\lambda_{SO} = 0.06$. However, in the topological phase $\lambda_R = 0.05$, while in the trivial phase a value of $\lambda_R = 0.35$ has opened a gap.

For this reason, the Kane-Mele model is a realisation of the quantum *spin* Hall insulator (QSHI). The dispersion relations of the Kane-Mele system in the gapless QSH phase and the trivial insulating phase for a 1D zigzag strip geometry are shown in Figure 1.7.

Clearly, since it is always zero, the Chern number is not a useful topological invariant to use when characterising this system. We could use the difference between the Chern numbers between the two spin sectors, $n_\uparrow - n_\downarrow$, however this will only work for $\lambda_R = 0$. When $\lambda_R \neq 0$ and $|\lambda_R/\lambda_{SO}| < 3\sqrt{3}$ the energy gap does not close and the edge states persist. However, since $[H, \sigma_z] \neq 0$ spin is no longer a good quantum number and we cannot separate the system into two spin sectors with independent Chern numbers, n_σ. A further consequence of this is that σ_{xy}^{QSH} is generally not quantized when $\lambda_R \neq 0$.

Kane and Mele proposed that the answer to this problem could be found by considering the concept of Kramers theorem. Kramers theorem, sometimes also referred to as Kramers degeneracy, states that in a half-integer spin system respecting TRS every energy level is at least doubly degenerate. Put another way, for every eigenstate with energy E there is at least one more eigenstate with energy E. To prove this, assume $|\psi\rangle$ is an eigenstate of the Hamiltonian with energy E

$$H\left|\psi\right\rangle = E\left|\psi\right\rangle . \tag{1.47}$$

Recall that in a system with TRS $[H, T] = 0$. Therefore $T\left|\psi\right\rangle$ must also be an eigenstate of H with energy E since

$$\begin{aligned} HT\left|\psi\right\rangle &= TH\left|\psi\right\rangle \\ &= ET\left|\psi\right\rangle . \end{aligned} \tag{1.48}$$

Kramers theorem then essentially amounts to showing $\left|\psi\right\rangle$ and $T\left|\psi\right\rangle$ are different states, i.e. that they are orthogonal. To show this recall that $T^2 = -1$ for spin 1/2 systems and therefore

$$\begin{aligned} T^2 &= U_T K U_T K \\ &= U_T U_T^* = -1 \implies \\ T^2 &= U_T^T U_T^\dagger \implies \\ T^2 U_T &= U_T^T \implies \\ U_T^T &= -U_T . \end{aligned} \tag{1.49}$$

Using this identity

$$\begin{aligned} \left\langle\psi|T\psi\right\rangle &= \sum_{i,j} \psi_i^* (U_T)_{ij} K \psi_j \\ &= \sum_{i,j} \psi_i^* (U_T)_{ij} \psi_j^* \\ &= -\sum_{i,j} \psi_j^* (U_T)_{ji} K \psi_i \\ &= -\left\langle\psi|T\psi\right\rangle \end{aligned} \tag{1.50}$$

where we have used $U_T^T = -U_T$ between the second and third lines. The only solution to this is that $\left\langle\psi|T\psi\right\rangle = 0$ and time-reversed partners, also known as a Kramers pair, are orthogonal in spin 1/2 systems. Therefore, spin 1/2 systems with TRS are at least doubly degenerate. Extending this to translationally invariant systems, for a Bloch state $\left|u_{n,\boldsymbol{k},\sigma}\right\rangle$ its Kramers partner is $T\left|u_{n,\boldsymbol{k},\sigma}\right\rangle = e^{i\phi(\boldsymbol{k})}\left|u_{n,-\boldsymbol{k},-\sigma}\right\rangle$ which is generally at a different momentum. Note that we have included the spin index in the Bloch states and that it has been reversed by the action of T. Moreover, TRS precludes any mixing of Kramers pairs, since $\langle\psi| H |T\psi\rangle = 0$, and ensures they cannot backscatter into one another.

Points in the BZ where $\boldsymbol{k} = -\boldsymbol{k} + \boldsymbol{G}$, where $\boldsymbol{G}$ is a reciprocal lattice vector, play a special role in the QSHI. Clearly $\boldsymbol{k} = \boldsymbol{0}$ satisfies this condition, but the periodicity of the BZ ensures that the points at the corners of the BZ will also obey this condition. For example, in 1D these points are $k = 0, \pi/a$ while in 2D these points are $k = (0,0), (\pi/a, 0), (0, \pi/a)\ (\pi/a, \pi/a)$ where a is the lattice constant (there will generally by 2^n TRIM in n dimensions). These points are known as time-reversal invariant momenta (TRIM). Kramers theorem guarantees that at TRIM points the Kramers pairs are degenerate, and protected from mixing with one another by any time-reversal invariant perturbations. Considering gapless modes located in the energy gap of a 1D BZ, bands are necessarily degenerate with one another at $k = 0, \pi/a$, but the degeneracy is generally lifted between these points in the absence of any other symmetries. The distinction between trivial and non-trivial states lies in how the bands traverse the energy gap between these two TRIM. Figure 1.8 shows the situations of a topologically trivial phase and a non-trivial phase, with robust mid-gap states. In the trivial case, bands forming Kramers pairs at $k = 0$ form another Kramers pair at $k = \pi/a$. However, in the non-trivial phase two bands will touch to form a Kramers pair at one TRIM, but they will not form a Kramers pair at the other. The result of this is that the Fermi level will always intersect a mid-gap states in the non-trivial case but can be placed between mid-gap states in the trivial insulating phase.

The consequence of this can be understood by analysing the scattering matrix of the system [15]. The scattering matrix is defined as the unitary matrix relating the states incoming to a transmission region to those which are outgoing

$$S = \begin{pmatrix} r & t \\ t' & r', \end{pmatrix} \tag{1.51}$$

where r/r' and t/t' are square matrix blocks describing reflection and transmission, respectively. In a system with TRS, we can always write a general scattering state in the input lead as

$$|\psi\rangle = \sum_n c^n_{\text{in},L} |n\rangle + c^n_{\text{out},L} |Tn\rangle \tag{1.52}$$

where in and out refer to whether the states are travelling in or out of the scattering region. A similar expression can be written for states in the output lead. The scattering matrix then relates the scattering states in either lead through

$$\begin{pmatrix} c_{\text{out},L} \\ c_{\text{out},R} \end{pmatrix} = S \begin{pmatrix} c_{\text{in},L} \\ c_{\text{in},R} \end{pmatrix} \tag{1.53}$$

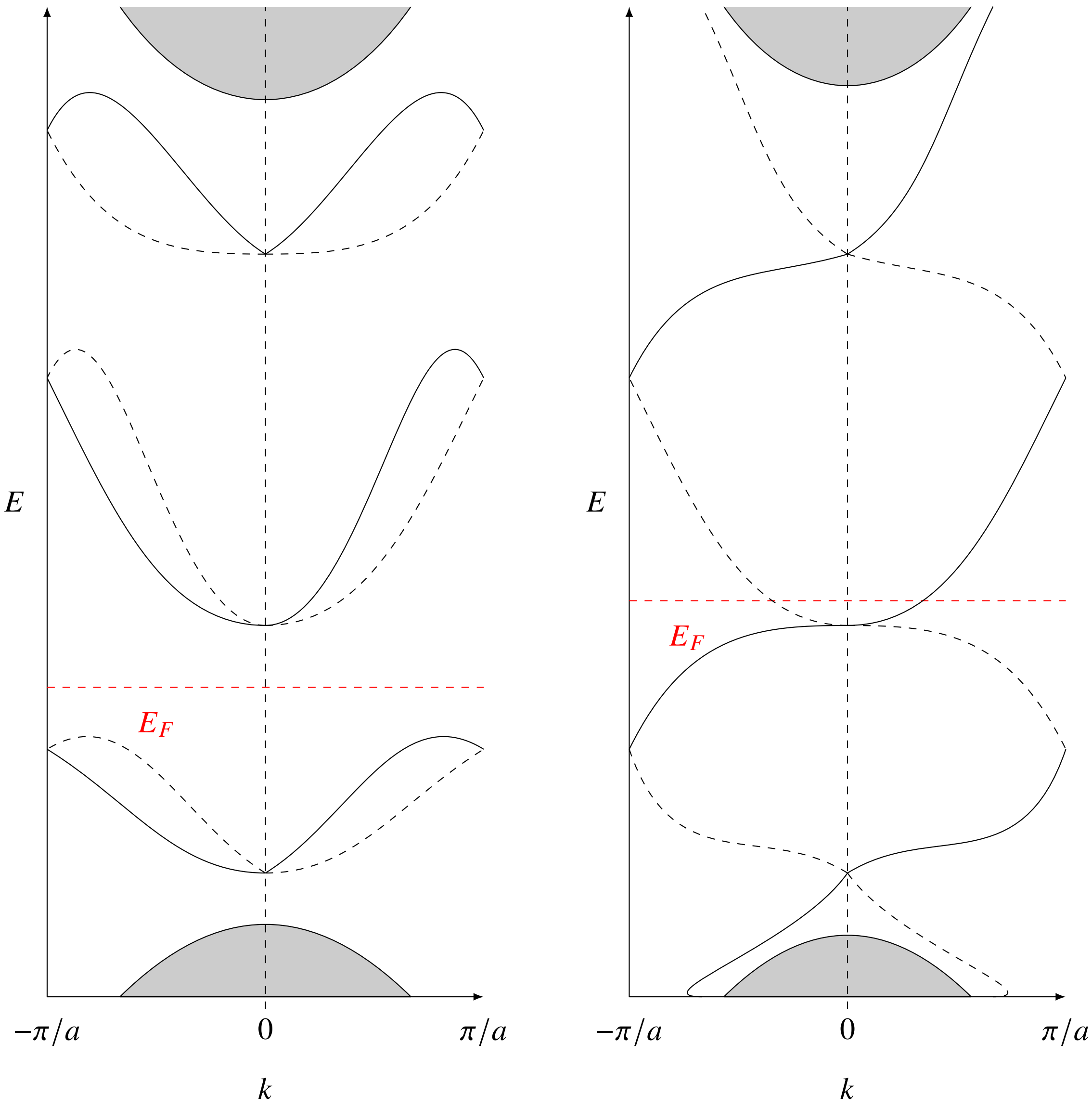

Fig. 1.8 Schematic of mid-gap states for topologically trivial (left) and non-trivial (right) band structures with time-reversal symmetry. In both schematics, bulk states are filled with grey. Midgap states are shown as (dashed) lines, where dashed lines are the time-reversal partners of un-dashed lines. As demonstrated, non-trivial topological states form when a midgap state switches its Kramer's partner between 0 and π/a. The result is that, for a non-trivial state, the Fermi energy will always intersect a midgap band while the Fermi energy can be placed between mid-gap bands in the trivial insulating state.

where we have dropped the band index for clarity. Due to TRS, we can also consider the time reversal partner at the same energy

$$\begin{aligned}
T\left|\psi\right\rangle &= \sum_n (c^n_{\text{in},L})^* \left|Tn\right\rangle + (c^n_{\text{out},L})^* \left|T^2 n\right\rangle \\
&= \sum_n (c^n_{\text{in},L})^* \left|Tn\right\rangle - (c^n_{\text{out},L})^* \left|n\right\rangle \\
&= \sum_n -(c^n_{\text{out},L})^* \left|n\right\rangle + (c^n_{\text{in},L})^* \left|Tn\right\rangle .
\end{aligned} \tag{1.54}$$

giving an equivalent expression for scattering states

$$\begin{pmatrix} c^*_{\text{in},L} \\ c^*_{\text{in},R} \end{pmatrix} = S \begin{pmatrix} -c^*_{\text{out},L} \\ -c^*_{\text{out},R}. \end{pmatrix} \tag{1.55}$$

Left multiplying by $s^\dagger$ and complex conjugating both sides we find

$$\begin{pmatrix} c_{\text{out},L} \\ c_{\text{out},R} \end{pmatrix} = -S^T \begin{pmatrix} c_{\text{in},L} \\ c_{\text{in},R} \end{pmatrix} \tag{1.56}$$

resulting in the identity

$$S = -S^T. \tag{1.57}$$

As a result of this identity, the on-diagonal elements of S must also obey an antisymmetry condition $r = -r^T$. However, it is known that antisymmetric matrices of odd rank (i.e. an $N \times N$ matrix where N is odd) have at least one eigenvalue equal to zero. Therefore, systems with TRS and an odd number of Kramers pairs will always have at least one reflection eigenvalue equal to zero and, by conservation of probability, perfect transmission. Kramers theorem is, therefore, the origin of dissipationless edge states in time-reversal topological insulators. Put more simply, if there are an even number of edge states then states can scatter into backpropagating modes that are not their time-reversal pair. If there are an odd number of modes then there is always an extra edge state that cannot be gapped out. This should be compared with Figure 1.8 where there are always an even number of forward (backward) propagating modes at the Fermi level in the trivial phase, but an odd number in the non-trivial phase.

When discussing the topological nature of chiral edge states, it made sense to consider a $\mathbb{Z}$ topological invariant since states on either edge couldn't backscatter into one another due to their spatial separation. In the case of helical edge states however, it is clear that it is the parity of the number of pairs of edge modes that dictates whether the system is topological. In this case, we can describe the system by a $\mathbb{Z}_2$ topological invariant, i.e. the cyclic group of order two. In the limit of decoupled spin blocks ($\lambda_R \to 0$) we can calculate the $\mathbb{Z}_2$ as

$$\begin{aligned} \nu &= \frac{1}{2}(n_\uparrow - n_\downarrow) \mod 2 \\ &= n_\sigma \mod 2. \end{aligned} \tag{1.58}$$

More generally, however, it is convenient to formulate the $\mathbb{Z}_2$ invariant in terms of Bloch functions as this will provide a more general method for calculating the topological invariant in systems where spin is not conserved.

Re-examining the Berry connection and calculating the $\mathbb{Z}_2$ invariant

Before discussing the calculation of the $\mathbb{Z}_2$ topological invariant in systems where spin is not conserved, let us first revisit the formulation of the $\mathbb{Z}$ topological invariant in terms of the Berry connection.

Under the modern theory of polarisation proposed by King-Smith and Vanderbilt [88], the spontaneous polarisation of a crystal can be rewritten in terms of the Berry connection as

$$\boldsymbol{P} = \frac{1}{2\pi}\int_{BZ} \mathrm{d}\boldsymbol{k}\,\boldsymbol{\mathcal{A}}(\boldsymbol{k}) \tag{1.59}$$

where $\boldsymbol{\mathcal{A}}(\boldsymbol{k})$ is the Berry connection previously defined in (1.20). For now, we will only consider the 1D case for simplicity. Since the Berry connection is not a gauge invariant quantity, neither is the polarisation under this definition, i.e. if we perform the gauge transformation $u_{\alpha,\boldsymbol{k}} \to e^{i\phi_\alpha(\boldsymbol{k})}u_{\alpha,\boldsymbol{k}}$ then the Berry connection of each band transforms as $\mathcal{A}_\alpha \to \mathcal{A}_\alpha + \partial_k\phi_\alpha(k)$. As a result the polarisation is also changed

$$P_\alpha \to P_\alpha + \frac{e}{2\pi}(\phi_\alpha(k=\pi) - \phi_\alpha(k=-\pi)), \tag{1.60}$$

where $P = \sum_\alpha P_\alpha$. Since the phase is defined up to modulo 2π, we conclude $\phi_\alpha(k = \pi) - \phi_\alpha(k = -\pi) = 2m\pi$ and the polarisation is only defined up to modulo an integer, i.e. only the fractional part of the polarisation is gauge invariant. This is, initially, quite a surprising result. After all, in the classical picture we are used to thinking of the polarisation as a macroscopic quantity where the net polarisation of a crystal is the sum of the contributions from each localized electron dipole. At first glance, the description of the polarisation in terms of a Berry phase appears counterinutive. However, rather than focusing on the polarization of a crystal as an equilibrium property, the modern theory postulates that one should speak about differences in the polarization between two different states, as this does remain a gauge invariant quantity. Indeed, this view on the theory of polarisation actually matches experiments where only differences in polarisation can be measured (switches in polarisation upon the application of an external electric field are measured, rather than absolute values). The interested reader is referred to [145] for a detailed discussion on the matter, however this is intimately linked to the inability to specify the locations of the Wannier charge centres (Fourier transforms of the Bloch wavefunctions) beyond modulo a lattice vector. Coming back to the matter at hand, imagine we adiabatically tune some parameter, λ, that changes the polarisation of a Bloch band. The change in polarisation of the α^{th} band can be calculated as

$$\begin{aligned}\Delta P_\alpha &= \int_{\lambda_i}^{\lambda_f} \mathrm{d}\lambda \frac{\partial P_\alpha}{\partial \lambda} \\ &= P_\alpha(\lambda_f) - P_\alpha(\lambda_i) \\ &= \frac{1}{2\pi}\left(\int_{c_f} \mathrm{d}k \mathcal{A}_\alpha - \int_{c_i} \mathrm{d}k \mathcal{A}_\alpha \right).\end{aligned} \tag{1.61}$$

provided the wavefunctions are continuously defined between λ_i and λ_f and where c_f and c_i are the loops $k_x = -\pi \longrightarrow \pi$ for λ_f and λ_i. Note that λ is simply a parameter of the quantum system that we are at liberty to tune. Therefore, we may interpret it as a flux, as in the case of the charge pump in the Laughlin argument, or as another momentum component. At this point we will force the path in λ space to be a loop. As such, the change in polarisation by adibatically varying λ in a closed loop is

$$\Delta P_\alpha = \frac{1}{2\pi} \oint \mathrm{d}\boldsymbol{k} \cdot \mathcal{A}_\alpha(\boldsymbol{k}) \tag{1.62}$$

where $\boldsymbol{k} = (k, \lambda)$. Comparing this to our expression for the Hall conductance (1.22), we realise that this integral is exactly the Chern number. This equation should be compared to (1.21) to observe the link between the change in electric polarisation through a cyclic evolution of some Hamiltonian parameter and the Hall conductance.

The genius of Fu and Kane was to realise that the key quantity in describing the topology of the QSH insulator in the presence of spin coupling, was not the charge conductance, nor the spin conductance, but rather the change in the *time-reversal polarisation* [47]. To explain what the time-reversal polarisation is, we will once again revisit the Laughlin argument for the QHE. Laughlin's argument was that by threading a single magnetic flux quantum, $\phi_0 = h/e$, through a cylinder with a radial magnetic field, one could pump $\Delta Q = ne$ worth of charge between the edges of the cylinder, where n is the number of filled Landau levels. Because of the periodic boundary conditions, changing the flux in this manner mapped the system back to itself. Moreover, if for simplicity we consider the cylinder to have circumference of a single unit cell then we may reinterpret threading a single flux quantum through the cylinder as traversing the 1D BZ $k_x = 0 \to 2\pi$.

If we naively try and copy the Laughlin argument for the QSH state, we will immediately encounter an issue. Namely, the QSH state in a cylindrical geometry is two, time-reversed copies of the Laughlin cylinder. We will refer to the two time-reversed copies of the Laughlin cylinder as I and II. Then, if ϕ_0 worth of flux is threaded through the full QSH cylinder charge in I will be pumped in the opposite direction to charge in II, such that the change in polarisation is zero

$$\begin{aligned}\Delta P &= \int_0^{\phi_0} \mathrm{d}\phi \left(\partial_\phi P^I + \partial_\phi P^{II}\right) \\ &= 0.\end{aligned} \tag{1.63}$$

Rather, Fu and Kane's desire was to modify the Laughlin argument in order to observe Kramers pairs at the edge switching partners between TRIM points, as discussed in the previous subsection and shown in Figure 1.8. Therefore, we wish to measure the difference in the charge polarisation pumped by the two time-reversed cylinders as *half* a flux quantum is threaded

$$\begin{aligned}\Delta P_T &= P_T(\phi_0/2) - P_T(0) \\ &= \int_0^{\phi_0/2} \mathrm{d}\phi \left(\partial_\phi P^I - \partial_\phi P^{II}\right)\end{aligned} \tag{1.64}$$

where $P_T = P^I - P^{II}$ is the time-reversed polarisation.

In order to define this quantity, we consider the case of a system with N occupied Kramers pairs (i.e. $2N$ occupied bands), with no additional symmetry beyond TRS such that the only band degeneracies are between Kramers pairs at TRIM points. Once again, we limit our discussion to the 1D BZ for simplicity. Following on from the discussion above, we split the set of occupied states into two time-reversed sets and label the α^{th} Kramers pair eigenstates as $\left|u^I_{\alpha,k}\right\rangle$ and $\left|u^{II}_{\alpha,k}\right\rangle$ such that the combined index (α, S) labels the band where $S = I, II$. From our earlier definitions of TRS and Kramers pairs we have

$$\begin{aligned} T\left|u^{I}_{\alpha,k}\right\rangle &= -e^{-i\phi_\alpha(-k)}\left|u^{II}_{\alpha,-k}\right\rangle \\ T\left|u^{II}_{\alpha,k}\right\rangle &= e^{-i\phi_\alpha(k)}\left|u^{I}_{\alpha,-k}\right\rangle \end{aligned} \tag{1.65}$$

since the Bloch functions are only defined up to a phase. In a more succinct form

$$T\left|u^{S}_{\alpha,k}\right\rangle = (-1)^S e^{-i\phi_\alpha((-1)^S k)}\left|u^{\bar{S}}_{\alpha,-k}\right\rangle \tag{1.66}$$

where $S = I, II$ and $\bar{S}$ is the complement of S. We then define the partial polarisation due to the S state in a Kramers pair as

$$\begin{aligned} P^S &= \frac{1}{2\pi}\int_{-\pi}^{\pi} \mathrm{d}k \mathcal{A}^S(k) \\ &= \frac{1}{2\pi}\int_{-\pi}^{\pi} \mathrm{d}k \sum_\alpha i\left\langle u^{S}_{\alpha,k}\right| \partial_k \left|u^{S}_{\alpha,k}\right\rangle \end{aligned} \tag{1.67}$$

Of course, the labels I, II were an arbitrary choice and, as such, we should be able to write P^S in a more symmetric fashion. We do so by considering the positive and negative parts of the integral separately

$$P^S = \frac{1}{2\pi}\int_{0}^{\pi} \mathrm{d}k \left(\mathcal{A}^S(k) + \mathcal{A}^S(-k)\right), \tag{1.68}$$

and then rewriting the second term in terms of $A^{\bar{S}}(k)$

$$\begin{aligned} \mathcal{A}^S_\alpha(-k) &= i\left\langle u^{S}_{n,-k}\right| \partial_{-k} \left|u^{S}_{\alpha,-k}\right\rangle \\ &= -i\left\langle Tu^{\bar{S}}_{\alpha,k}\right| e^{-i\phi_\alpha((-1)^{\bar{S}}k)}\partial_k e^{i\phi_\alpha((-1)^{\bar{S}}k)} \left|Tu^{\bar{S}}_{\alpha,k}\right\rangle \\ &= \partial_k\phi_\alpha((-1)^{\bar{S}}k)\left\langle Tu^{\bar{S}}_{\alpha,k}\middle|Tu^{\bar{S}}_{\alpha,k}\right\rangle - i\left\langle Tu^{\bar{S}}_{\alpha,k}\right| \partial_k \left|Tu^{\bar{S}}_{\alpha,k}\right\rangle \\ &= \partial_k\phi_\alpha((-1)^{\bar{S}}k) + i\left\langle u^{\bar{S}}_{\alpha,k}\right| \partial_k \left|u^{\bar{S}}_{\alpha,k}\right\rangle \\ &= \partial_k\phi_\alpha((-1)^{\bar{S}}k) + \mathcal{A}^{\bar{S}}_\alpha(k). \end{aligned} \tag{1.69}$$

where we have used the definitions in equation (1.65) between the first two lines and $T^2 = -1$ between the third and fourth. The result is a more symmetric expression for the partial polarisation, invariant under any unitary transformation of the form $\left|u_{\alpha,k}\right\rangle \longrightarrow \sum_\beta U_{\alpha\beta}\left|u_{\beta,k}\right\rangle$

$$\begin{aligned} P^S &= \frac{1}{2\pi}\int_0^\pi \mathrm{d}k\mathcal{A}(k) + \frac{1}{2\pi}\sum_n \left(\phi_\alpha((-1)^{\bar{S}}\pi) - \phi_\alpha(0)\right) \\ &= \frac{1}{2\pi}\int_0^\pi \mathrm{d}k\mathcal{A}(k) + \frac{1}{2\pi}\sum_\alpha \left(\phi_\alpha(\pi) - \phi_\alpha(0)\right) \end{aligned} \tag{1.70}$$

where $\mathcal{A}(k) = \mathcal{A}^I(k) + \mathcal{A}^{II}(k)$ and we have used $\phi_\alpha(k_{\text{TRIM}}) = \phi_\alpha(-k_{\text{TRIM}})$ since the BZ is periodic.

Perhaps naively, we might assume that $P_T = 0$ since equation (1.70) appears identical for $S = I, II$. However, we must take care since $\mathcal{A}$ is not a gauge invariant quantity. In fact $P^I = P^{II}$ modulo an integer, reflecting the ambiguity of the charge polarisation in (1.60). Indeed, by rewriting the partial polarisation as

$$\begin{aligned} P^S &= \frac{1}{2\pi}\int_{-\pi}^0 \mathrm{d}k\mathcal{A}^S(k) + \mathcal{A}^S(-k) \\ &= \frac{1}{2\pi}\int_{-\pi}^0 \mathrm{d}k\mathcal{A}(k) + \frac{1}{2\pi}\sum_\alpha(\phi_\alpha(0) - \phi_\alpha(\pi)) \\ &= \frac{1}{2\pi}\int_0^\pi \mathrm{d}k\mathcal{A}(-k) - \frac{1}{2\pi}\sum_\alpha(\phi_\alpha(\pi) - \phi_\alpha(0)) \end{aligned} \tag{1.71}$$

we now find

$$\begin{aligned} P_T &= \frac{1}{2\pi}\int_0^\pi \mathrm{d}k\,\left(\mathcal{A}(k) - \mathcal{A}(-k)\right) + \frac{1}{\pi}\sum_\alpha \left(\phi_\alpha(\pi) - \phi_\alpha(0)\right) \\ &= -\frac{1}{2\pi}\int_0^\pi \mathrm{d}k \sum_\alpha \partial_k(\phi_\alpha(k) + \phi_\alpha(-k)) + \frac{1}{\pi}\sum_\alpha \left(\phi_\alpha(\pi) - \phi_\alpha(0)\right) \end{aligned} \tag{1.72}$$

Noting (1.65) and the orthogonality of the Bloch functions

$$\left\langle u^S_{\alpha,-k}\middle| T \middle| u^{\bar{S}}_{\beta,k}\right\rangle = \delta_{\alpha\beta}(-1)^{\bar{S}} e^{-i\phi((-1)^{\bar{S}}k)}, \tag{1.73}$$

Fu and Kane were motivated to define the sewing matrix

$$w^{II,I}_{\alpha\beta}(k) = \left\langle u^{II}_{\alpha,-k} \middle| T \middle| u^{I}_{\beta,k} \right\rangle = -w^{I,II}_{\alpha\beta}(-k) \implies$$
$$w_\alpha(k) = \begin{pmatrix} 0 & -e^{-i\phi_\alpha(-k)} \\ e^{-i\phi_\alpha(k)} & 0 \end{pmatrix} \tag{1.74}$$

in order to relate time-reversed wavefunctions. Using $\phi_\alpha(k_{\text{TRIM}}) = \phi_\alpha(-k_{\text{TRIM}})$, we note that $w_\alpha(k_{\text{TRIM}}) = -(w_\alpha(k_{\text{TRIM}}))^T$, i.e. the sewing matrix is skew-symmetric at TRIM points. The full sewing matrix, w is a tridiagonal block matrix with each block along the diagonal of the form given in (1.74) for each Kramers pair, i.e.

$$w(k) = \bigoplus_{\alpha}^{N} w_\alpha(k) \tag{1.75}$$

and is also skew-symmetric at TRIM points, by the skew-symmetry of each block. We will now introduce a useful concept for skew-symmetric matrices known as the Pfaffian. The determinant of a skew-symmetric matrix is the Pfaffian squared,

$$\text{Pf}(A)^2 = \det(A). \tag{1.76}$$

We will use the Pfaffian here as it has the convenient property that for a tridiagonal $2N \times 2N$ skew-symmetric matrix, such as $w(k_{\text{TRIM}})$ the Pffaffian is [48],

$$\begin{aligned}\text{Pf}\left(w(k_{\text{TRIM}})\right) &= \text{Pf}\begin{pmatrix} 0 & -e^{-i\phi_1(k_{\text{TRIM}})} & \cdots & 0 & 0 \\ e^{-i\phi_1(k_{\text{TRIM}})} & 0 & \cdots & 0 & 0 \\ \vdots & & \ddots & & \vdots \\ 0 & 0 & \cdots & 0 & -e^{-i\phi_N(k_{\text{TRIM}})} \\ 0 & 0 & \cdots & e^{-i\phi_N(k_{\text{TRIM}})} & 0 \end{pmatrix} \\ &= (-1)^N \exp\left(-i\sum_\alpha \phi_\alpha(k_{\text{TRIM}})\right).\end{aligned} \tag{1.77}$$

This allows us to rewrite the second term in (1.72) as

$$\sum_\alpha \left(\phi_\alpha(\pi) - \phi_\alpha(0)\right) = i \log \frac{\text{Pf}(w(\pi))}{\text{Pf}(w(0))} \mod 2\pi \tag{1.78}$$

where we are required to take the modulo of both sides by 2π in order to remove the ambiguity of the logarithm function.

On the other hand, the determinant of the sewing matrix is defined throughout the full 1D BZ and is given as

$$\begin{aligned}\det(w(k)) &= \prod_{\alpha} \det(w_n(k)) \\ &= \exp\left(-i\sum_{\alpha}(\phi_\alpha(k)+\phi_\alpha(-k))\right),\end{aligned} \tag{1.79}$$

and so we can write the first term in (1.72) as

$$\sum_{\alpha} \partial_k\left(\phi_\alpha(k)+\phi_\alpha(-k)\right) = i\partial_k \log(\det(w(k))) \mod 2\pi \tag{1.80}$$

Putting this all together, in terms of the sewing matrix the time-reversal polarisation is

$$\begin{aligned}P_T &= \frac{1}{2\pi i}\left(\log\frac{\det(w(\pi))}{\det(w(0))} - 2\log\frac{\mathrm{Pf}(w(\pi))}{\mathrm{Pf}(w(0))}\right) \\ &= \frac{1}{i\pi}\left(\log\frac{\sqrt{\det(w(\pi))}}{\mathrm{Pf}(w(\pi))}\frac{\mathrm{Pf}(w(0))}{\sqrt{\det(w(0))}}\right) \mod 2\end{aligned} \tag{1.81}$$

where, once again, the time-reversal polarisation is only defined up to $\mod 2$ due to the logarithm. Note that each term in the logarithm amounts to sgn $(\mathrm{Pf}(w(\Gamma_i)))$, where Γ_i is a TRIM point.

In order to complete our definition of the $\mathbb{Z}_2$ topological invariant, we recall that we should calculate the change in P_T after threading $\phi_0/2$ flux through our cylinder

$$\begin{aligned}\Delta P_T &= P_T(\phi_0/2) - P_T(0) \\ &= P_T(k_x=\pi) - P_T(k_x=0)\end{aligned} \tag{1.82}$$

where we have made an equivalence between the flux through the cylinder and the momentum. Furthermore, to remove the log in our expression, it is typical to exponentiate ΔP_T such that

$$\begin{aligned} e^{i\pi\Delta P_T} &= (-1)^{\nu} \\ &= \prod_{\boldsymbol{\Gamma}_i \in \mathrm{TRIM}} \frac{\sqrt{\det(w(\boldsymbol{\Gamma}_i))}}{\mathrm{Pf}(w(\boldsymbol{\Gamma}_i))} \\ &= \prod_{i=1}^{4} \delta_i = \pm 1 \end{aligned} \tag{1.83}$$

where the TRIM points are at $(0,0)$, $(\pi,0)$, $(0,\pi)$, (π,π) in the 2D BZ and we have relabelled the $\mathbb{Z}_2$ invariant as ν. If there is no change in the time-reversal polarisation across a pumping cycle, i.e. no switching of Kramers pairs and therefore topologically trivial, $\prod_i \delta_i = 1$, while if there is a change in time-reversal polarisation $\prod_i \delta_i = -1$.

In fact an enormous simplification of this invariant is possible in systems with TRS and inversion symmetry. Extending their previous work, Fu and Kane demonstrated that the $\mathbb{Z}_2$ invariant could be written in terms of the inversion eigenvalues of each occupied Kramers pair at the TRIM points

$$\delta_i = \prod_{m=1}^{N} \xi_{2m}(\Gamma_i), \tag{1.84}$$

where $\xi_m(\boldsymbol{k}) = \pm 1$ is the inversion eigenvalue of the m^{th} band, also known as the parity eigenvalue, and the index is $2m$ since degenerate Kramers pairs have the same inversion eigenvalue [48].

The reformulation of the $\mathbb{Z}_2$ invariant is a remarkable discovery, and its importance to the development of topological band theory cannot be understated. Band structures have the potential to be enormously complicated and time-consuming to fully characterise, however this simple reformulation of the $\mathbb{Z}_2$ invariant offers a means to classify the topology of any system by considering the eigenvalues of occupied states at a handful of points in the BZ. Furthermore, it offers a simple technique for engineering TI phases - *band inversion*. It is known that the parity eigenvalues of s-orbitals are even, while the parity of p-orbitals are odd. If we have a semiconductor respecting TRS and possessing a band structure with s-orbitals and p-orbitals either side of the Fermi level, then inverting the order in the orbitals in the band structure will induce a topological phase transition. This is complementary to our previous discussions regarding the fact that topological phase transitions may only occur through the closure of the bulk band gap.

Topological Insulators in 2D and 3D

Graphene was initially proposed as a candidate material to realise the QSH/2D TI phase, but it became clear that the spin-orbit coupling in carbon was far too low to induce a topological transition. However, soon after Kane and Mele's original paper, Konig *et al.* announced the first experimental discovery of a 2D TI in HgTe/(Hg,Cd)Te quantum wells (QWs) [94]. The ability of this set-up to produce a non-trivial QSH phase can be attributed to the large spin-orbit coupling in Te (which is also present in other heavy chalcogenides). Concurrent to the experimental work, Bernevig, Zhang and Hughes derived a low-energy $\boldsymbol{k} \cdot \boldsymbol{p}$ Hamiltonian for HgTe/(Hg,Cd)Te QWs now known as the BHZ model

$$H_{BHZ} = \begin{pmatrix} h(\boldsymbol{k}) & 0 \\ 0 & h^*(-\boldsymbol{k}) \end{pmatrix}$$

$$\begin{aligned} \text{where} \quad h(\boldsymbol{k}) =& \epsilon(\boldsymbol{k}) + (M - B(k_x^2 + k_y^2))\tau_z + A(k_x\tau_x - k_y\tau_y) \implies \\ H_{BHZ}(\boldsymbol{k}) =& \epsilon(\boldsymbol{k}) + M(\boldsymbol{k})\tau_z + A(k_x\tau_x\sigma_z - k_y\tau_y) \end{aligned} \tag{1.85}$$

in the basis $|E, \uparrow\rangle, |H, \uparrow\rangle, |E, \downarrow\rangle, |H, \downarrow\rangle$ where E, H label the QW subband and are of opposite parity eigenvalue and $\tau_{x,y,z}$ are the Pauli matrices acting in orbital space [16]. Note the similarity of this model to the low-energy Hamiltonian about the $\boldsymbol{K}/\boldsymbol{K}'$ points in the Haldane model. In this case, the spectra will once again include massive Dirac cones centred around $(k_x, k_y) = (0, 0)$ with an energy gap controlled by the mass term $M(\boldsymbol{k}) = M - Bk^2$. The motivation for introducing this model was to describe a topological transition through a band inversion procedure, as discussed in the previous subsection. In order to demonstrate the band inversion, let us regularise the continuum BHZ Hamiltonian on the lattice according to the transformations

$$\begin{aligned} k_i \rightarrow& \sin(k_i) \\ k_i^2 \rightarrow& 2\,(1 - \cos(k_i)) \end{aligned} \tag{1.86}$$

giving the tight-binding form of (half of) the BHZ Hamiltonian

$$h(\boldsymbol{k}) = \epsilon(\boldsymbol{k}) + (M - 4B + 2B(\cos k_x + \cos k_y))\tau_z + A(\sin k_x\tau_x + \sin k_y\tau_y). \tag{1.87}$$

By calculating the Chern number of either block (examining the full BHZ model should convince readers that each block is a time-reversed copy of the other and, therefore, the Chern numbers should be equal and opposite when non-zero), BHZ showed that the model enters a topologically non-trivial phase in the regime $0 < M/B < 4$ where the band gap inverts at either end of this inequality.

By tuning the thickness of the HgTe/(Hg,Cd)Te QW, Konig *et al.* were able to observe a topological transition in the form of a quantized spin conductivity (recall that the spin conductivity is generally not quantised, but is here due to the lack of coupling between the two blocks of the BHZ model). As an interesting aside, HgTe wells were proposed as early as the 1980s as a means to engineer a band inversion by Volkov and Pankratov [134]. The massive surface states arising from a band inversion due to a smooth, spatially varying mass term are referred to as Volkov-Pankratov states in the modern literature [172].

Concurrent to the experimental realisations of the 2D TI phase, the theoretical groundwork for 3D TIs was being laid by Fu and Kane [50]. In 3D there are now eight TRIM points however, we can reduce the problem of calculating the $\mathbb{Z}_2$ invariant in 3D to the same problem in two dimensions by considering the six faces of the parallelepiped with the the eight TRIM points forming the vertices at $\mathbf{\Gamma}_i = (n_1\pi, n_2\pi, n_3\pi)$ where $n_i = 0, 1$. Each face of the parallelepiped can be considered as its own 2D BZ with an associated time-reversal polarisation/$\mathbb{Z}_2$ index. The full $\mathbb{Z}_2$ index can be expressed as

$$(-1)^{\nu_0} = \prod_{i=1}^{8} \delta_i \tag{1.88}$$

however, because of the redundancy $\nu_0 = \nu_{n_1=0}\nu_{n_1=1} = \nu_{n_2=0}\nu_{n_2=1} = \nu_{n_3=0}\nu_{n_3=1}$, there are only 3 other independent $\mathbb{Z}_2$ indices, which are generally chosen as $\nu_1 = \nu_{n_1=1}$, $\nu_2 = \nu_{n_2=1}$ $\nu_3 = \nu_{n_3=1}$. Each index in the full set $\nu_0; (\nu_1\nu_2\nu_3)$ can be $0, 1$ meaning that there are a total of 16 possible 3D TIs. In the case where all of the indices are 0 the topological phase is trivial. If $\nu_0 = 1$ the phase is known as a *strong topological insulator* (STI), however if $\nu_0 = 0$ and any of the other indices are non-zero then the phase is known as a *weak topological insulator* (WTI). STIs have an odd number of Dirac cones on all crystal surfaces, while WTIs possess an even number of Dirac cones on surfaces with normal $\boldsymbol{G}_\nu = \nu_1\boldsymbol{b}_1 + \nu_2\boldsymbol{b}_2 + \nu_3\boldsymbol{b}_3$ for reciprocal lattice vectors $\boldsymbol{b}_i$. The inherent anisotropy of WTI phases is interesting from a device engineering perspective, however candidate materials are in short supply and platforms based on STIs have tended to dominate the literature. In addition, since the weak topological indices rely on the translational invariance of the lattice they are not robust to disorder [48]. In any case, the work in this thesis will focus mainly on STI based platforms and we will therefore neglect further discussion of WTI properties.

In 2008, nearly four decades on from the original discovery of topological condensed matter, the 3D TI phase was experimentally observed by Hsieh *et al.* in $\mathrm{Bi}_{1-x}\mathrm{Sb}_x$ crystals, for small x [67]. Angle resolved photoemission spectroscopy (ARPES) was used to confirm that the $\mathrm{Bi}_x\mathrm{Sb}_{1-x}$ alloy had a complicated surface dispersion with five Dirac cones. Following this momentous discovery, predictions were made that the $(\mathrm{Bi, Sb})_2(\mathrm{Te, Se})_3$ (BSTS) family (previously used for their thermoelectric properties) hosted a single Dirac cone, resulting in a far simpler energy dispersion relationship than $\mathrm{Bi}_{1-x}\mathrm{Sb}_x$ [203]. Furthermore, the bulk band-gap was predicted and later confirmed to be around 0.3 meV, a large value which offered the possibility of reducing the effect of bulk carriers to zero by effectively tuning the Fermi level. Therefore, despite being the second generation of 3D TIs, the BSTS family became (and remains) the archetypal 3D TI material due to their wide band-gap permitting observation of their topological surface states (TSSs) at higher temperatures, greatly increasing their potential technological applications.

BSTS and model Hamiltonians for 3D TI phases

To complete our pedagogical review of TRS protected TIs, we will discuss the BSTS TI family and also introduce a number of Hamiltonians that will make several appearances throughout the course of this thesis. We will not discuss the detailed quantum transport behaviour of BSTS and instead leave that for section 1.2.

The crystal structure of the BSTS family is rhombohedral with space group $R\bar{3}m$. The crystal has a layered structure with each layer of $\mathrm{X}_2\mathrm{T}_3$, stacked in the order T-X-T-X-T, referred to as a quintuple layer and weakly bound to the adjacent layers with van der Waals forces. The crystal possesses inversion symmetry as well as a threefold rotational symmetry around the z axis. Furthermore, the lack of magnetic materials in this structure ensures that TRS is also respected, at least in the single-particle regime where electron-electron interactions may be neglected. *Ab initio* calculations of $\mathrm{Bi}_2\mathrm{Se}_3$ performed by Zhang *et al.* demonstrated that the large spin-orbit coupling led to an inversion of the energy levels at the Fermi level, inducing a topological transition analogous to the mechanism of a 2D TI in HgTe/(Hg,Cd)Te QWs [203]. The relevant orbitals around the Fermi level are $|P1^{+}, \uparrow/\downarrow\rangle$, $|P2^{-}, \uparrow/\downarrow\rangle$ which are hybrid orbitals formed of the original p_z orbitals of the Bi and Se atoms respectively, where ± labels the parity eigenvalue and $\uparrow/\downarrow$ the spin.

Rather than go through the full derivation of the BSTS Hamiltonian, we will sketch out the symmetry argument utilised by Liu *et al.* to restrict the possible form of the Hamiltonian terms [112]. A general four-band Hamiltonian can be written in terms of the Dirac matrices as

$$H(\boldsymbol{k}) = \epsilon(\boldsymbol{k}) + \sum_{i=1}^{5} d_i(\boldsymbol{k})\gamma_i + \sum_{i,j} d_{ij}(\boldsymbol{k})\gamma_{ij}, \tag{1.89}$$

where the Dirac matrices satisfy the commutation relations $\{\gamma_i, \gamma_j\} = 2\delta_{ij}$ and their commutators are given by $[\gamma_i, \gamma_j] = \gamma_{ij}/2i$. In the basis $|P1^+, \uparrow\rangle, |P1^+, \downarrow\rangle, |P2^-, \uparrow\rangle, |P2^-, \downarrow\rangle$ we may choose a representation of the Dirac matrices as

$$\begin{aligned} \gamma_i &= \sigma_i \tau_x \quad \text{for} \quad i = 1, 2, 3 \\ \gamma_4 &= \tau_y \\ \gamma_5 &= \tau_z \end{aligned} \tag{1.90}$$

where $\sigma_{x,y,z}$ and $\tau_{x,y,z}$ act on the spin and orbital degrees of freedom respectively. In spin 1/2 systems we have already shown that the time-reversal operator takes the form $T = i\sigma_y K$, while consideration of the crystal structure allows us to choose

$$\begin{aligned} P &= \tau_z \\ C_3 &= e^{i\sigma_z \pi/3} \end{aligned} \tag{1.91}$$

for the unitary matrices representation inversion and threefold rotation, respectively. The constraints placed on the Hamiltonian by TRS and inversion have already been discussed, while for a Hamiltonian obeying n-fold rotational symmetry about the z-axis

$$C_{n,z} H(k_\pm, k_z) C_{n,z}^{-1} = H(e^{\pm 2\pi i/n} k_\pm, k_z) \tag{1.92}$$

where $k_\pm = k_x \pm i k_y$. Imposing each of these symmetries restricts the forms of $d_i(\boldsymbol{k})$ and $d_{ij}(\boldsymbol{k})$. For example, under inversion

$$T\gamma_i T^{-1} = \begin{cases} -\gamma_i & \text{for} \quad i = 1, 2, 3, 4 \\ \gamma_i & \text{for} \quad i = 5 \end{cases} \tag{1.93}$$

imposing the restriction

$$d_i(\boldsymbol{k}) = \begin{cases} -d_i(-\boldsymbol{k}) & \text{for} \quad i = 1, 2, 3 \\ d_i(-\boldsymbol{k}) & \text{for} \quad i = 4, 5 \end{cases} \tag{1.94}$$

Examining the restrictions imposed by the other symmetries, the full Hamiltonian can be written up to order $O(k^3)$ as

$$\begin{aligned} H(\boldsymbol{k}) &= H_1(\boldsymbol{k}) + H_3(\boldsymbol{k}) \quad \text{where} \\ H_1(\boldsymbol{k}) &= \epsilon(\boldsymbol{k}) + M(\boldsymbol{k})\tau_z + A(k_y\sigma_x - k_x\sigma_y)\tau_x + Bk_z\sigma_z\tau_x \\ H_3(\boldsymbol{k}) &= R_1(k_x^3 - 3k_y^2k_x)\tau_y + R_2(k_y^3 - 3k_x^2k_y)\sigma_z\tau_x \end{aligned} \tag{1.95}$$

and the orbital splitting is given by $M(\boldsymbol{k}) = M_0 + M_1k_z^2 + M_2(k_x^2 + k_y^2)$. Note the similarly of H_1 to the 2D BHZ model at $k_z = 0$ - in fact, H_1 can be considered as a 3D BHZ model. Also note the appearance of third order terms in H_3. These terms are known as the hexagonal warping terms and will generally deform the Dirac cone at larger energies such that the Fermi surface has hexagonal symmetry.

Often, we are more interested in studying thin film of 3D TIs, for example in order to further suppress bulk conduction or in order to tune the interaction between TSSs on opposite surfaces. In this case, it is more appropriate to use the thin film TI Hamiltonian, first derived by Shan *et al* [155]

$$H(\boldsymbol{k}) = \hbar v_f(k_y\sigma_x - k_x\sigma_y)\tau_z + (m + Bk^2)\tau_x \tag{1.96}$$

in the basis $(|t,\uparrow\rangle, |t,\downarrow\rangle, |b,\uparrow\rangle, |b,\downarrow\rangle)^T$ where t/b label the top/bottom surface and $\sigma_{x,y,z}$, $\tau_{x,y,z}$ are the Pauli matrices acting in spin and surface space respectively [155]. Restricting the geometry of the 3D TI even further, we are often only interested in the TI surface itself. In that case, for a surface with normal parallel to the z-axis, we adopt the Dirac-Rashba Hamiltonian [58] given by

$$H_{\text{surf}} = \hbar v_f(k_y\sigma_x - k_x\sigma_y) \tag{1.97}$$

1.2 Quantum Electron Transport

Having set the scene with a discussion of the history of TIs, we will now address their transport properties. Not only is the study of the transport properties in TIs interesting from the perspective of the development of electronic device technologies, but probing the transport properties also provides a means for material characterisation. We should, however, note that there are a plethora of alternative characterisation methods available, each with their own benefits and drawbacks.

1.2.1 Growth and Device Fabrication

Before introducing the transport experiments that may be used to characterise TI devices, we will discuss the means by which one can grow high quality TI films, as well as the issues and shortcomings of current device fabrication techniques with a particular emphasis on their effect on transport experiments.

Molecular beam epitaxy

Molecular beam epitaxy (MBE) has been established as one of the main growth methods used in the production of high quality TI films since their experimental realisation [52]. Initial studies used the self-flux method where stoichiometric mixtures of Bi/Sb and Se/Te are melted in a quartz tube before being very slowly cooled [171, 144]. However, since no nucleation site is provided at the start of the crystal growth there is quite a high chance that the resultant material is polycrystalline, making this quite an inefficient method of crystal growth. On the other hand, MBE has been the chosen as a preferred growth method due to the higher level of reproducibility in crystal structure (compared to other techniques). While other techniques can lead to very high local fluctuations in material composition, MBE growth is slow enough to allow for atomic reorganisation and diffusion. The ability to reliably control the temperature of the cells independently is also a major advantage over other growth techniques. Once optimisation of the flux rates of the molecules used in growth has been achieved, a growth campaign can be carried out using this recipe to produce many high quality samples. MBE also allows for the production of complex heterostructures and offers a high degree of control over crystal doping. Early efforts to grow the BST family focused on tuning the relative concentrations of Bi and Sb in order to move the Fermi level into the bulk band gap [91, 3, 52] (naturally occurring defects lead to Bi_2Te_3 being n-type, while Sb_2Te_3 is p-type [65, 193]).

MBE growth is performed in Ultra-High Vacuum (UHV) conditions ($P < 10^{-9}$mbar). In these UHV conditions, the mean free path of a molecule can be many orders of magnitude larger than the chamber size, so the molecules are considered non-interacting. During growth, molecules are effused from high temperature cells and deposited on a substrate. Control of the temperature of the substrate is essential in controlling the stoichiometry of the compound formed. While the choice of substrate for any material growth is usually extremely important, TI growth is (in theory) less restrictive and the condition for lattice matching between the TI and substrate is significantly relaxed [179]. This is due to the van der Waals forces between TI QLs which mean that the TI is only weakly bonded to the substrate and grows with lower levels of strain, even on substrates with a relatively large lattice mismatch. This reduction in film strain means that TI growth can be quite different from standard epitaxial growth [124]. There are some reports that the reduction in strain ensures that there are no defects, even within the first QL of Bi_2Te_3 film grown on Si [18], however it is more realistic that the defects due to lattice mismatch with the substrate are contained within the first few QLs [87, 13]. Optimisation of TI thin film growth requires the control of many variables including substrate type, substrate temperature during growth, atomic flux ratio of the constituent elements and atomic growth rate among other factors. As the composition of the TI becomes more complex (for example BST is a ternary compound and more difficult to grow than Bi_2Te_3), the optimisation period grows longer.

In the limit of thin films, the presence of strain in the first few QLs of MBE grown TI thin films becomes more obvious. Defects and disorder at the interface can promote bulk defects (e.g. vacancies, antisites, etc.) causing an increase in bulk carrier concentration and a shift of the Fermi level into the bulk conduction/valence bands, leading to bulk dominated transport [178, 182, 77, 139]. Furthermore, the presence of parallel bulk conduction channels overwhelms the transport contribution from TSSs severely hinders the observation of quantum phenomena. Therefore, in order to promote purely TSS mediated transport in all film thicknesses, it is desirable to control and eliminate defects present within films due to interfacial strain. One such method of achieving this is through the use of an insulating buffer layer between the TI and bare substrate. Promising buffer layers include the family of triel chalcogenides (e.g. In_2Se_3, Al_2Te_3, etc.) due to their wide bulk band gap and close structural and chemical match to BST. Indeed, in 2015 Koirala *et al.* showed that $(Bi_xIn_{1-x})_2Se_3/Bi_2Se_3$ bilayers [93], where the concentration of In and Bi was slowly tuned across the interface between the two materials, led to a then record surface state mobility of $16\,000\,\mathrm{cm^2V^{-1}s^{-1}}$. Recent MBE studies have provided encouraging results with regards to the production of high mobility bilayers [182].

In addition to improving surface state mobility, graded buffer layers offer a means to investigate other novel quantum phenomena. For example, the presence of a graded TI interface raises the interesting question of where exactly the TSS would be located [188]. Additionally, massive Volkov-Pankratov (VP) states (precursors to linearly dispersing TSSs) would exist within the graded region [172]. It is known that these states are massive and lack topological protection, but there is a lack of experimental study on them. While they have been observed in strained HgTe heterostructures [71] they have not been observed in 3D TIs. VP states therefore represent new, exciting physics and understanding their role in electronic transport, as well as their interplay with TSSs, is of paramount importance to the operation of TI devices.

Just as there is the ability to grow higher quality with TI films using a buffer layer, one can also cap the TI *in situ* to prevent unwanted ageing effects through the exposure to ambient gases after it leaves the vacuum chamber [148] (although the exact nature of the contamination remains controversial). Elemental Te remains the most common capping layer for BST, since BST is usually grown in a Te overpressure anyway and can be thermally desorbed prior to return the TSSs to their pristine condition for *ex situ* characterisation [64, 109]. Te, therefore, is a good capping layer for the transfer of BST samples in air before further experiments [127, 95]. However, more work needs to be completed regarding the suitability of capping layers for use in TI devices. As well as providing protection against ambient gases, a long term capping layer is required to not affect the stoichiometry of the TI and not affect the transport properties of the device through band bending or offering alternative conduction pathways. In addition, it would be favourable to develop a capping layer with a large dielectric constant in order to facilitate a top gate that could be used to tune the Fermi level within the TI.

Device fabrication

Following the growth of a TI sample using a suitable method, small pieces can be cleaved from films/exfoliated from crystals to be processed into useful devices. Numerous processing methods exist, the most primitive of which being to simply scratch a pattern into the TI film to create a suitable device architecture. Because of the imprecise nature of this method, scratched devices tend to be limited to Hall bar geometries. Despite this, high quality devices are often achievable because of the lack of harsh chemicals and reduced opportunity for contamination of the TI film.

On the other hand, if more complex device geometries are desired then more advanced etching methods are available. Furthermore, scratching devices is hardly a scaleable means of fabrication and is not commercially viable. Photolithography followed by either dry or wet etching can produce complex device geomtries in bulk. However wet etching of BSTS, in particular, is quite challenging due to the chemicals involved and the relative chemical and structural instability of BSTS. As liquids generally work their way between the van der Waals layers, this can cause long term degradation to the TI and prevent the observation of quantum phenomena. Even something as chemically inert as water can be an issue, due to its polar nature inducing band bending [109] (this also occurs at a much lower rate in atmospheric conditions, leading to the aforementioned degradation of TI surface states). In addition, common developers used during the photolithography process actually etch away at the TI (for example, those based on tetramethylammonium hydroxide, such as MF-319, or polyamides, such as PA401D [24]). To reduce the use of wet chemistry dry etching techniques are generally safer for TSSs, however there is still an element of wet chemistry involved in the development stage of the process.

Therefore, it is desirable to develop a processing method that eliminates the use of wet chemistry as far as possible. However, there has been extremely limited research on this matter with regards to TI devices. One means forward could be to preferentially etch away the native oxide layer on Si (111) substrates prior to loading in an MBE chamber. It is known that BST will preferentially grow on the crystalline Si (111) surface over the amorphous native oxide, due to BST and Si (111) sharing hexagonal symmetry [14]. Therefore, it may be possible to pre-pattern substrates in order to grow TI films in particular device geometries and limit the post-growth patterning stage of device fabrication. While such a method would certainly limit the exposure of the TI to aqueous chemicals, it would severely limit the scale of the features and complexity of the device geometries. Further research is required in order to develop a processing method that is scaleable and limits the degradation of the TSSs.

1.2.2 Magnetotransport

In the previous section, the ballistic nature of helical edge modes was already discussed and explained in terms of TRS and Kramer's degeneracy. Here, we shall discuss in greater detail the transport properties of topologically protected surface states with specific emphasis on the BSTS family. In particular, magnetotransport measurements will offer a means to probe the non-trivial band dispersion and Berry phase of topological materials. In order to understand these measurements in context we will briefly introduce the relevant length scales over which such transport occurs.

- Mean free path l_e: the average distance travelled by an electron before significantly changing its direction of motion due to collisions and interactions with other bodies. l_e is, therefore, the average distance between scattering events. Associated with this length is a characteristic time scale, τ_e given by $l_e = v_f \tau_e$ where v_f is the Fermi velocity.

- Phase coherence length l_ϕ: in the quantum regime, we associate the electron with a wavefunction $\psi = \psi_0 e^{i\phi}$ where ϕ is the phase. l_ϕ is the length after which an electron's phase has significantly changed. After a distance l_ϕ, information related to interference phenomena is lost. In this case, the characteristic time scale is given by $l_\phi = \sqrt{D\tau_\phi}$ where $D = v_f^2 \tau_e / d$ is the diffusion constant where $d = 1, 2, 3$ is the dimensionality of the system.

- Spin-orbit length l_{SO}: approximately the distance an electron has to travel before the spin-orbit interaction induces a π rotation of its spin state (i.e. a spin-flip).

These definitions are also relevant for hole carriers. Generally, however, different charge carrier types will have different length/time scales. Generally the regimes of interest will be:

- Weak localization/quantum diffusive regime, $l_\phi >> l_e$ where electrons maintain their phase coherence even after multiple scattering events and interference phenomena play an important role.
- Mesoscopic regime, $l_\phi > L$ where L is one of the dimensions (length or width) and transport in that dimension can be neglected
- Ballistic regime, $l_e > L$ where the flow of carriers is unimpeded.

Hall effects

The QHE has already been discussed in the previous section as an early ancestor of the TI state, however the use of its classical counterpart remains an effective method of measuring carrier concentrations and mobilities. The classical Hall effect is observed up to moderate magnetic fields ($\sim$ 8 T) in TIs. In the presence of hole and electron carriers the Hall coefficient is given as

$$R_H = \frac{p\mu_h^2 - n\mu_e^2}{e(p\mu_h + n\mu_e)^2} \tag{1.98}$$

where n/p are the electron and hole concentrations, respectively and μ_e/μ_h are the electron/hole mobilities. In the case of a single carrier type, this equation simplifies to (1.1) with the sign of R_H indicating the carrier type. In the more general case where both carrier types are present, one can utilise additional experimental methods to constrain the values of parameters in R_H before fitting using transport data. For example, by measuring the scattering rate/mean free time of the carriers using, e.g. terahertz (THz) spectroscopy, one can calculate the mobility using $\mu = q\tau_e/m^*$ where m^* is the effective mass of the carrier which can be determined through band structure calculations.

At high fields, the observation of a QHE is possible. However, in contrast to the usual linear dependence of the energy spacing of Landau levels on the magnetic field, the Landau level spacing in TIs follow a $\sqrt{nB_z}$ relationship due to the massless nature of the Dirac fermions in the linear surface state dispersion. Another implication of $E_n \propto \sqrt{nB_z}$ is that Dirac fermions in a magnetic field will always exhibit a zero mode, i.e. $E_{n=0} = 0$, and, therefore, the Hall conductance of a single Dirac cone will have *half integer* values:

$$\sigma_{xy} = (n + \frac{1}{2})\frac{e^2}{h}. \tag{1.99}$$

As yet, this half integer quantization has not been observed in any TI QHE experiment as the Dirac cones on the top and bottom surface both contribute to the transport, giving a total conductance is given as

$$\sigma_{xy}^{Total} = (n_{\text{top}} + n_{\text{bottom}} + 1)\frac{e^2}{h}. \tag{1.100}$$

However, evidence of half integer quantization is provided through fabricating a gated device and tuning the carrier densities on either surface to be equal, $n_{\text{top}} = n_{\text{bottom}} = n$ leading to odd integer conductance plateaus $\sigma_{xy} = (2n+1)\frac{e^2}{h}$ [192].

Separate to the Hall effect and QHE is the planar Hall effect (PHE) realised in the case of an in-plane magnetic field. Examining the surface Hamiltonian given in (1.97), applying an in-plane magnetic field (and ignoring the orbital effect)

$$\begin{aligned} H_{surf} &= \hbar v_f (k_y \sigma_x - k_x \sigma_y) + \mu_B \boldsymbol{B} \cdot \boldsymbol{\sigma} \\ &= \hbar v_f \Big((k_y + B'_x)\sigma_x - (k_x - B'_y)\sigma_y \Big) \\ &= \hbar v_f (k'_y \sigma_x - k'_x \sigma_y) \end{aligned} \tag{1.101}$$

it appears as though the only effect of an in-plane field is to trivially shift the position of the Dirac cone in momentum space. However, Taskin *et al.* [170] demonstrated the surprising appearance of a longitudinal anisotropic magnetoresistance (AMR) and a PHE given by

$$\begin{aligned} \sigma_{xx} &= \sigma_{\perp} + (\sigma_{\parallel} - \sigma_{\perp}) \cos^2 \phi \\ \sigma_{xy} &= (\sigma_{\parallel} - \sigma_{\perp}) \cos \phi \sin \phi \end{aligned} \tag{1.102}$$

where the angle ϕ parameterises the magnetic field $\boldsymbol{B} = B(\cos\phi, \sin\phi)$ and $\sigma_{\parallel} = \sigma_{xx}(\theta = 0), \sigma_{\perp} = \sigma_{xx}(\theta = \pi/2)$. As yet, the cause of the PHE and longitudinal AMR are not fully understood, however proposed mechanisms include scattering of electrons due to the in-plane field breaking TRS, or the inclusion of higher order quadratic terms in (1.97) leading to a tilt of the Dirac cone in momentum space and anisotropic backscattering [210, 142].

Weak antilocalization

At low temperatures, the wave-like nature of carriers becomes more apparent and interference effects begin to become visible in the transport data. Localization effects, in particular, offer a useful means of quantifying the length scales over which interference phenomena are visible.

We note that we are discussing localization in the weak localization regime, rather than the Anderson regime of strong disorder.

In trivial semiconductors and metals, the weak localization (WL) effect manifests as a positive correction to the resistivity (negative correction to the conductance) that is destroyed with increasing magnetic field (i.e. negative magnetoresistance). This can be understood in terms of the Aharanov-Bohm effect, where two time-reversed scattering loops, starting at a point A, propagate clockwise and anticlockwise around a defect. The probability of the electron returning to A is given by

$$P_A \propto 1 + \cos 4\pi\phi/\phi_0 \tag{1.103}$$

where ϕ is the magnetic flux through the loop traced out by the electron, $\phi \sim Bl_\phi^2$. At $\phi = 0$, the partial waves constructively interfere leading to an enhanced probability the electron returns to the point A, i.e. the electron is weakly localized and the conductivity is slightly suppressed. Increasing the flux destroys this constructive interference leading to the observation of a positive magnetoconductance/negative magnetoresistance.

Weak antilocalization (WAL), on the other hand, manifests as a negative correction to the resistance (positive correction to the conductivity) that is suppressed in increasing magnetic field. WAL occurs in topologically non-trivial systems due to the presence of a non-zero Berry phase. It can be shown that non-trivial Dirac electrons obtain a π Berry phase after circulating the Fermi surface and, therefore, there will be a π phase difference between the two time-reversed loops. As a result the localization behaviour present in trivial semiconductor and metals is suppressed since the time-reversed trajectory now destructively interfere around the scattering loop. Viewed from another perspective, the presence of time-reversal symmetry in a TI ensures the absence of elastic backscattering around time-reversal invariant defects and, therefore, a positive correction to the conductivity. When a magnetic field is applied, TRS is broken leading to a suppression in the conductivity in the form of a cusp in the resistance data around 0 T.

In any case, the change in the conductivity can be modelled with the Hikami-Larkin-Nagoaka (HLN) formula for 2D transport as

$$\Delta\sigma_{xx}(B) = \alpha \frac{e^2}{2\pi h}\left(\psi\left(\frac{B_\phi}{B} + \frac{1}{2}\right) - \ln\frac{B_\phi}{B}\right) \tag{1.104}$$

where ψ is the digamma function, $B_\phi = \hbar/4|e|l_\phi^2$ is the characteristic field and α is a phenomenological term which is positive for WL and negative for WAL [63]. The log term is due to modelling the scattering as a 2D random walk and solving the resulting diffusion equation, while the digamma function averages over all impurity configurations.

$|\alpha| = \frac{1}{2}$ for each surface state, that is $2|\alpha|$ should give the number of surface states present, however experimentally fitted values of α vary over a wide range due to non-idealities and the non-negligible contribution of bulk carriers. In the limit where the spin orbit length is non-negligible, we must include an additional correction to the model [126]

$$\begin{aligned}\Delta\sigma_{xx}(B) = \alpha\frac{e^2}{2\pi h}\Bigg(&\psi\left(\frac{B_\phi}{B}+\frac{1}{2}\right) - \ln\frac{B_\phi}{B} \\ &-2\psi\left(\frac{B_\phi + B_{SO}}{B}+\frac{1}{2}\right) + 2\ln\frac{B_\phi + B_{SO}}{B} \\ &-\psi\left(\frac{B_\phi + 2B_{SO}}{B}+\frac{1}{2}\right) + 2\ln\frac{B_\phi + 2B_{SO}}{B}\Bigg)\end{aligned} \tag{1.105}$$

In fact, the situation may become more complex still as we consider the crossover between WL and WAL. Such a situation may occur when both topological surface states and trivial bulk states contribute to the transport, or when a gap opens in the Dirac surface states due to magnetic impurities, hybridisation of opposite surface states etc. In this case, the correction to the conductivity is given as a sum of WAL and WL contributions

$$\Delta\sigma_{xx} = \sum_i \alpha_i \frac{e^2}{2\pi h}\left(\psi\left(\frac{B_{\phi_i}}{B}+\frac{1}{2}\right) - \ln\frac{B_{\phi_i}}{B}\right) \tag{1.106}$$

where the index i runs over the WAL and WL contributions [115].

Despite the often variable quality of TI devices, WAL features are often extremely prominent in longitudinal transport data due to $l_\phi >> l_e$. As a result, WAL cusps tend to be quite sharp and extend over quite a narrow range of magnetic field ($B \sim 1$ T).

Shubnikov-de Haas oscillations

As well as the half-integer QHE, the Landau level quantization of TIs, namely $E_n \propto \sqrt{nB_z}$, also modifies the oscillations of longitudinal resistance with magnetic field, known as Shubnikov-de Haas (SdH) oscillations, compared to trivial band structures.

In trivial materials, SdH oscillations occur as the energy of the Landau levels increase with increasing magnetic field. As each Landau level intersects the Fermi surface, it contributes to the density of states and the resistance drops. This leads to periodic oscillations in the longitudinal resistance

$$\Delta\rho_{xx}(B) \sim \cos\left(2\pi\frac{f_{1/B}}{B} - \Gamma\right) \tag{1.107}$$

where $f_{1/B}$ is the characteristic frequency of oscillation given as $f_{1/B} = \frac{E_F^2}{2e\hbar v_f^2}$ for Dirac fermions [159, 6]. Assuming a linear dispersion relation $E_F = \hbar v_f k_F$ where $k_F = \sqrt{4\pi n/g}$ is the Fermi wavevector, n is the 2D carrier concentration and g is the spin degeneracy factor then

$$f_{1/B} = \frac{2\pi\hbar}{eg}n. \tag{1.108}$$

The frequency of SdH oscillations therefore offers a means of measuring the carrier concentration of the TI. The phase shift in (1.107) is given as $\Gamma = \pi - \gamma$ where γ is the Berry phase for the case of small spin-orbit interactions and inversion symmetry [119]. In the more general case of a TI lacking inversion symmetry and with (necessarily) strong spin-orbit interactions, the formula for the phase shift is modified but is generally still dependent on a non-trivial Berry phase. Nevertheless, comparing the phase of the SdH oscillations to those measured from a trivial material offers a means to probe the Berry phase of a TI.

1.3 Magnetism and Topology

Since the experimental discovery of 3D TIs, researchers have been fervently investigating the interplay between magnetism and topology. The introduction of magnetism in a TI breaks TRS leading to a magnetic TI (MTI) ~~in class A of the Altland-Zirnbauer classification (more on this in the next chapter)~~. If the magnetic exchange vector is orientated along the growth ($\hat{z}$) axis and the MTI is taken to the thin film (2D) limit, this offers a means to induce a finite Berry curvature and realise the QAHE, as predicted in the Haldane model. As discussed in section 2.1, rather than the helical edge states protected by a non-trivial $\mathbb{Z}_2$ topological invariant, the QAHE possesses chiral edge states with a $\mathbb{Z}$ topological invariant.

Examining the Hamiltonian for a thin film TI given in equation (4.23) and adding a magnetic exchange term along the growth axis we find

$$\begin{aligned} H &= \hbar v_f(k_y\sigma_x - k_x\sigma_y)\tau_z + t_s\tau_x + \boldsymbol{M}\cdot\boldsymbol{\sigma} \\ &= \hbar v_f(k_y\sigma_x - k_x\sigma_y)\tau_z + t_s\tau_x + M_z\sigma_z \implies \\ UHU^\dagger &= H' = \hbar v_f(k_y\sigma_x - k_x\sigma_y) + t_s\sigma_z\tau_z + M_z\sigma_z \\ &\text{where} \quad U = e^{i\tau_y\frac{\pi}{4}}\begin{pmatrix}\mathbb{1} & 0 \\ 0 & \sigma_z\end{pmatrix} \end{aligned} \tag{1.109}$$

where $t_s = m + Bk^2$ and $\boldsymbol{M} = (M_x, M_y, M_z)$ is the magnetic exchange vector. In the new basis $(|+,\uparrow\rangle, |-,\downarrow\rangle, -|-,\uparrow\rangle, -|+,\downarrow\rangle)^T$, where $|\pm,\uparrow\rangle = \frac{1}{\sqrt{2}}(|t,\uparrow\rangle \pm |b,\uparrow\rangle)$ and $|\pm,\downarrow\rangle = \frac{1}{\sqrt{2}}(|t,\downarrow\rangle \pm |b,\downarrow\rangle)$, H' is given in matrix form as

$$H' = \begin{pmatrix} h_+ + M_z\sigma_z & 0 \\ 0 & h_- + M_z\sigma_z \end{pmatrix} \tag{1.110}$$

where $h_\pm = \hbar v_f(k_y\sigma_x - k_x\sigma_y) \pm t_s\sigma_z$ with eigenvalues

$$E_{\sigma,\eta} = \sigma\sqrt{\hbar^2 v_f^2 k^2 + (t_s + \eta M_z)^2} \tag{1.111}$$

where $\sigma, \eta = \pm 1$ and refer to the spin ($\uparrow$ /$\downarrow$) and parity (+/−) degrees of freedom. In the limit $B \longrightarrow 0$, this is exactly the low energy limit of the Haldane model of graphene. Similarly to Haldane's model, one can calculate the Chern number of (1.110) as $n = \frac{1}{2}(\text{sgn}(m + M) - \text{sgn}(m - M))$, i.e. the difference in the Chern number between the two blocks. For $M = 0$, $n = 0$ and the system is in the QSH state. For sufficiently large M, the Chern number changes sign for one of the blocks and the system enters a QAHE phase [201]. In terms of the band structure, this corresponds to one pair of bands inverting while the other pair of bands are pushed apart even further in energy. In other words, a magnetic exchange gap opens in the TSSs leading to the formation of dissipationless chiral edge states from the original QSH phase helical edge states.

Electronic transport measurements have provided evidence for the presence of the QAHE in thin film MTIs. Provided the Fermi level lies in the exchange gap $\rho_{xy} = h/e^2$ and $\rho_{xx} \longrightarrow 0$. The first experimental observation of the QAHE was in thin film (5 QLs) Chromium doped BST, $Cr_{0.15}(Bi_{0.1}Sb_{0.9})_{1.85}Te_3$ which was noted to be "nearly charge neutral" allowing the Fermi level to be fine tuned using a back gate electrode [28]. Confirmation that this was the QAHE was provided by applying a finite magnetic field, localising all dissipating states, at 30 mK. The effect of the magnetic field is to switch the direction of magnetisation in the sample, only leading to a change in the polarity of ρ_{xy} and a non-zero value of ρ_{xx} at the coercive field, $H_c = \pm M$.

Accessing the QAHE state brings with it an enormous breadth of technological applications in areas such as spintronics and quantum information processing (QIP). The dissipationless nature of the chiral edge modes has applications in low-power electronics and topological transistors [197]. The QAHE state is also a prerequisite for the realisation of chiral Majorana edge modes, via the coupling of a QAHE insulator to a proximate superconductor [108]. The search for Majorana modes is a key issue within the condensed matter community due to their non-Abelian statistics which form the basis for fault tolerant topological quantum computation (particles with non-Abelian statistics are also known as anyons). However, even after millions of dollars of investment into their research and the involvement of global behemoths such as Microsoft, there has been no unambiguous demonstration that Majorana modes have been realised.

A distinct magnetic phase is realised when the net magnetism of an MTI is zero, i.e. an antiferromagnetic MTI where the magnetisation vector on the top and bottom surfaces are anti-aligned. A coercive field can be used to align the magnetisation along the $\hat{z}$ axis, however at intermediate values opposite surfaces have an opposite QAHE response leading to zero Hall conductance plateau (ZHCP), i.e. persistent values of zero transverse conductance across a range of applied fields. In addition to ZHCP, the antiferromagnetic coupling of surface magnetisation vectors leads to an additional term in the Lagrangian of the electromagnetic response of the state

$$\delta\mathcal{L} = \frac{\theta e^2}{2\pi h}\boldsymbol{E}\cdot\boldsymbol{B} \tag{1.112}$$

where $\boldsymbol{E}$ and $\boldsymbol{B}$ are the usual electric and magnetic fields in the material and $\theta(\boldsymbol{r})$ is known as the axion field, which has the effect of mixing $\boldsymbol{E}$ and $\boldsymbol{B}$. It can be shown that in a trivial insulator $\theta = 0$, whereas in a topological phase $\theta = \pi$ modulo 2π [43]. This results in what is known as the topological magnetoelectric effect (TME), where an applied electric field induces a spontaneous magnetic field in the same direction and *vice versa*, with a coupling constant defined in units of $e^2/2h$ [180, 153]. The TME is not only interesting from the standpoint of fundamental physics, but also provides a non-invasive method of optically probing the topological characteristics of a material. There are also magnetic memory applications, where an applied electric field can induce a magnetic field to control the magnetisation vector of a proximate magnetic material. Because of the similarity of the Lagrangian (1.112) to the axion field of electrodynamics, this topological phase is referred to as an Axion Insulator.

The main challenges facing the realisation of these topological phases and the future adoption of their descendent technologies is establishing long range magnetic order in MTIs at technologically relevant temperatures. While magnetically doped TIs such as $(\mathrm{Cr}_y\mathrm{Bi}_x\mathrm{Sb}_{1-x-y})_2\mathrm{Te}_3$ (Cr:BST) and $(\mathrm{V}_y\mathrm{Bi}_x\mathrm{Sb}_{1-x-y})_2\mathrm{Te}_3$ (V:BST) order magnetically below $\sim 15\,\mathrm{K}$ and $\sim 70\,\mathrm{K}$, respectively [28, 106], the QAHE is observed at significantly lower temperatures. Early work observed full conductance quantisation at $\sim 50\,\mathrm{mK}$, and even state-of-the-art co-doping techniques have only increased this temperature to 300 mK [132]. This fragility is most likely due to strong disorder of magnetic dopants (e.g. magnetic adatom antisites, clustering of magnetic dopants, etc.) leading to difficulties in establishing long-range ferromagnetic order [181], the presence of parasitic conduction channels in the bulk and difficulty in stabilising the Fermi level inside the (potentially position-dependent) exchange gap of the TSS [191], among other issues. Increasing the critical temperature at which the QAHE appears could have long-term and far-reaching implications. Low-energy electronics and spintronics devices could herald a new age of microprocessors, beyond Moore's law, while the braiding of anyons provides a platform for topological computation. In an era of big data, dwindling energy reserves and a demand for ever faster computation a high temperature QAHE would be a very timely advance.

While our focus in the following section will be on the QAHE and closely related phases, there are numerous other recent developments regarding alternative phases of matter in and future applications of magnetic TIs. These include real space magnetic textures and skyrmions [206, 136], spin orbit torque for the effective switching of magnetisation and an energy efficient writing mechanism for magnetic memory [133, 189], and higher order TIs (HOTIs) [149, 44, 165]. While the wider field of topological spintronics and magnetoelectrics promises the development of disruptive technologies, we will unfortunately have to forego their inclusion in the following review in the interests of brevity. We refer the interested read to these excellent review articles [166, 113, 60].

1.3.1 The Magnetic Proximity Effect

To overcome the disadvantages of inducing magnetic order through doping, that is disorder and magnetic inhomogeneity, one can attempt to induce magnetism externally by placing a magnetic insulator (MI) proximate to a TI. This method is known as the magnetic proximity effect (MPE). MIs have the benefit of having a much higher Curie temperature than magnetically doped TIs, whilst not providing an alternative conduction pathway due to their high electrical resistance. Additionally, there will be no significant hybridisation between the TI and MI states due to the large bulk band gap present in the MI. However, the growth of such heterostructures is a challenging process. In order to overcome the issues facing their development, numerous material properties of the MI must be considered, which include but are not limited to:

- Wide band gap: this is crucial to avoid the MI becoming an alternative conduction pathway, negating the TSSs;

- High Curie/Néel temperature: it is desirable to ensure that the QAHE critical temperature is not limited by the ordering temperature of the adjacent MI. In addition, higher ordering temperatures may indicate the possibility of higher temperature QAHE;

- Matching the lattice constant: just as when discussing appropriate buffer and capping layers, interfacial strain should be minimised at the MI/TI interface to ensure a small concentration of bulk defects and TSS mediated transport. It is therefore important to ensure that any proximate MPE is sufficiently structurally matched to the TI;

- Matching the chemical environments: it is crucial to ensure minimal diffusion of atoms from the MI across the interface into the TI. Firstly, this will reduce the concentration of bulk defects and prevent the formation of parasitic conduction channels in the bulk. Secondly, interlayer diffusion will lead to a local change in the TI thickness. Since the Chern number is dependent on the thickness (inter-surface tunnelling parameter), as demonstrated in the model given in (1.110), this may lead to a locally varying Chern number and topologically distinct domains throughout [117]. This will hamper the detection of fully quantized conductivity as well as device development;

- Enhanced orbital overlap: there remains debate regarding the exact mechanism of the MPE and it is possible that it varies between materials [1, 106]. However, it is apparent from elementary quantum mechanics that the stronger the orbital overlap, the stronger the magnetic exchange mechanism. Recent experimental studies have indicated that the overlap of $3d$ orbitals in the MI with the Te/Se $5p$ orbitals in BSTS give the highest quality MPE [129, 185]. On the other hand, the tightly localised $4f$ orbitals in rare-earth based MIs are less promising [45], perhaps due to their small spatial extent. However, band alignment is also important to ensure the orbitals are close in energy for a large orbital overlap. A further benefit of band alignment, not directly related to orbital overlap, is that band bending at the interface will be limited precluding as far as possible the existence of trivial interface states that would overwhelm the TSSs in electronic transport.

Early studies of the MPE in TIs focussed on the use of EuS as an adjacent ferromagnetic insulator (FMI). However, early DFT studies on EuS/Bi_2Se_3 found that the MPE had a negligible effect on the tiny exchange gap opened at the Dirac point, with the thickness of the material and inter-surface hybridisation being the largest contributors to the mass term [39]. Surprisingly, experimental studies have directly contradicted these conclusions and results show that EuS/BST heterostructures display weak localization behaviour in transport experiments [196] indicating broken TRS (as previously discussed, bare TIs should show WAL behaviour) while there is also evidence of a high-temperature ferromagnetic phase has been observed along with an anomalous Hall voltage [82]. Despite these intriguing results, recent work has claimed that there is no evidence of an MPE at the EuS/Bi_2Se_3 interface [45].

Besides FMIs, it is also possible to use a proximate antiferromagnetic insulator (AFMI) to induce magnetism in the Dirac electrons, due to the uncompensated spins at the AFMI/TI interface. The benefit of this approach is that AFMIs possess a negligible net magnetisation and therefore produce no stray fields. The lack of macroscopic magnetisation makes the AFMI more robust and insensitive to external magnetic fields, protecting the induced ferromagnetic order induced at the surface of the TI, while the absence of stray fields ensures that there is minimal effect on the bulk properties of the interfacial TI layer and reduced crosstalk between adjacent TI/AFMI layers. The first example of antiferromagnetic exchange coupling in a TI heterostructure was by He *et al* in 2017, when it was shown there was an MPE in superlattices of CrSb (a half metal) and Cr:BST [61]. In addition to the MPE there was also an observed enhancement the magnetic ordering temperature of the Cr-BST to 90 K, despite the bare MTI only ordering below 30 K, demonstrated by the presence of the AHE in the TI layer (although, since CrSb is metallic there could be some ambiguity concerning in which layer the AHE originates). In addition, CrSb/BST/CrSb heterostructures were shown to undergo a process of unsynchronised switching of the magnetisation vectors on opposite surfaces, offering the possibility of realising the Axion Insulator phase [62]. There have also been promising results from the other members of the NiAs family of antiferromagnets.

Nearly a decade on from the original MPE proposals, there are dozens of potential material candidates. There are far too many to survey in this short literature review and the interested reader can refer themselves to table I of [53] for a comprehensive list of proximate magnets and their suitability. Despite the explosion of material candidates and research interest, at the time of writing there is still only a single example of a fully quantized QAHE in a $Zn_{1-x}Cr_xTe/BST/Zn_{1-x}Cr_xTe$ (ZCT/BST/ZCT) trilayer [185]. With reference to the list of requirements for a strong MPE that we gave above, ZCT does indeed appear to be an excellent material choice. It has a wide band gap of 2.28 eV while ZnTe (111) is lattice mismatched to Bi_2Te_3 by only $\sim 1.6\%$. Doping with chromium drives the insulator into the ferromagnetic phase and the authors note that the $3d$ levels of Cr are close in energy to the $5p$ orbitals of Te in the adjacent TI. Furthermore, they theorise that the presence of Te on both sides of the FMI/TI interface draws the TSS further into the ZCT and assists in an even stronger orbital overlap. The same effect was observed by this author in an unpublished collaboration with Anirban, appendix B [7]. Nevertheless, even with such a well matched FMI the temperature at which the QAHE was observed was still only 30 mK. Creativity is required in designing MIs for use in a robust MPE mediated QAHE, perhaps devising a method which combines the use of a proximate magnet and doping the TI with a magnetic species.

1.3.2 Intrinsic Magnetic Topological Insulators

It is fair to ask, given the delayed progress and slow advancement, whether there is an alternative to the MPE in the development of MTIs capable of realising a high temperature QAHE. In order to avoid the worst effects of disorder and the complications of interface engineering, it is desirable to search for a stoichiometric TI with intrinsic magnetic order. In 2017, Eremeev *et al* suggested a new type of TI heterostructure that could overcome these issues [40]. By combining ideas from doping of TIs and the MPE, they developed the concept of using a *magnetic insertion layer* to induce long range magnetism in a TI. This method involved identifying a suitable magnetic bilayer that could be inserted *into a quintuple layer* in order to create magnetic septuple layers, bound by weak van der Waals forces. In other words, given a magnetic bilayer MT and a TI B_2T_3, the bilayer is inserted between the second and third layers of B_2T_3 to form a septuple layer T-B-T-M-T-B-T, i.e. MB_2T_4 where M is some magnetic element, B is Bi or Sb and T is Te or Se. In the year following this suggestion Otrokov *et al* identified the first such intrinsic magnetic TI as the antiferromagnetic TI $MnBi_2Te_4$ (MBT) using ab initio calculations and then confirming their theoretical predictions with experiment [131].

MBT is an A-type antiferromagnet meaning that spins couple ferromagnetically in-plane and antiferromagnetic out of plane. In addition, below its Néel temperature of 25K [131], spins order along the $\hat{z}$ direction. While the presence of magnetism does break TRS in a TI, the antiferromagnetic coupling in MBT ensures that the system still respects the symmetry $S = T\tau_{1/2}$ where $\tau_{1/2}$ is an operator which translates the lattice by half a magnetic unit cell. The presence of S-symmetry ensures that MBT, in fact all antiferromagnetic TIs (AFMTIs), possesses a $\mathbb{Z}_2$ topological classification [121]. This A-type antiferromagnetism endows MBT, and the related family of materials, with interesting thickness dependent properties. Depending on the parity of the number of layers (odd or even) of a sample the magnetisation vector is aligned (odd layer) or anti-aligned (even layer) on opposite surfaces. The uncompensated spins in odd layer samples lead to a QAHE phase, while the net zero magnetisation in even layer samples should give rise to ZHCP due to the opposite signs for the half-integer Hall conductance on either surface. Therefore, depending on the thickness of the sample, the topological phase of MBT oscillates between the QAHE and the axion insulator [130]. Of course, while it is desirable to have atomically flat surfaces it is unlikely that steps and terraces can be avoided even using epitaxial growth techniques. In order to fabricate devices with consistent numbers of layers it is probable that techniques such as exfoliation of single crystal will be used, for at least the near future. Furthermore, the similarity of the lattice constant and structure of MBT with Bi_2Te_3 (both are in space group $R\bar{3}m$ while MBT has an in-plane lattice constant of ~ 4.32 Å compared to 4.38 Å for Bi_2Te_3 [195]) facilitates the growth of $\mathrm{MnBi_2Te_4/(Bi_2Te_3)}_n$ superlattices in an effort to tune the RKKY mediated interlayer coupling from antiferromagnetic to ferromagnetic [90]. This offers a route towards engineering stoichiometric ferromagnetic TIs, Weyl semimetals or HOTI phases, see below [25, 205, 75, 41, 209, 54].

Theory predicts that a magnetic exchange gap should open in the Dirac cone at S breaking surfaces, but given that MBT is naturally n-type due to crystal defects alloying with $\mathrm{MnSb_2Te_4}$, the Fermi level must be tuned to reside within the gap. Calculations indicate that this gap can be quite large (up to 80 meV) [105, 131]. Experimental work by Chen *et al* has corroborated this to an extent by demonstrating a reasonably wide range of compositions for which $\mathrm{Mn(Bi_{1-x}Sb_x)_2Te_4}$ has the Fermi level in the exchange gap, namely $0.25 < x < 0.35$ for bulk samples, however the authors note that increasing Sb composition actually alters the band gap and drives the material towards the trivial phase and uninverting the band gap at $x \sim 0.5$ [29]. Other work indicates that the Sb composition required to reach the charge neutral point may vary with sample thickness and is also affected by unintentional doping during the device fabrication process [184]. As a brief aside, while $\mathrm{MnSb_2Te_4}$ is a topologically trivial ferromagnet the closely related $\mathrm{MnSb_4Te_7}$ (i.e. a $\mathrm{MnSb_2Te_4/Sb_2Te_3}$ superlattice) exhibits a number of topological magnetic phases [69].

However, there are numerous conflicting reports on the observation of a magnetic exchange gap in MBT films in the first place [168, 125]. While MBT research is still in its relative infancy the consensus is that it is likely that this sample dependent gap in MBT is due to crystal defects within the crystal lattice. Specifically, this may be due to the presence of the antisite defects $\mathrm{Mn_{Bi}}$ (Mn at a Bi site) and $\mathrm{Bi_{Mn}}$ (Bi at an Mn site) which lead to ferrimagnetic behaviour, disrupting the interlayer ferromagnetism of perfect MBT [194, 97]. Other issues may be surface quality or the charge states of the antisite defects and vacancies leading to uncompensated surface charge which could change the size of the gap at the Dirac point [157]. Given that tuning the Fermi level to sit in the exchange gap is crucial for the elimination of bulk states transport contributions and the realisation of the QAHE this is an important issue that must be overcome. In fact, there has been an apparent lack of positive progress towards a high temperature QAHE phase and there remains only a single instance of a zero-field QAHE in a five septuple layer sample at 1.4 K [33]. Other instances where the presence of quantized conductance and chiral edge states have been observed have been at high magnetic fields, in order to align the Mn spins in a ferromagnetic phase, but promisingly high temperatures [111, 200]. In fact, one report has shown a Hall resistance plateau (although not a quantized value) at 45 K, well above the Néel temperature of 25K [51].

Within the wider XB_2T_4 family, other possible AFMTIs are X = Eu, V and Ni [105]. While MBT orientates its spins along the $\hat{z}$ axis, the remaining AFMTIs all have their magnetic easy axis orientated in-plane. While this makes them unsuitable for a zero-field QAHE phase, they present a versatile playground for the investigation of magnetic topological phases. For example, it has been predicted that alloying VBi_2Te_4 (VBT) with MBT offers a means to induce a ferromagnetic coupling between septuple layers, while preserving the out-of-plane magnetic easy axis and the non-trivial topological nature of the material [212, 107, 66]. As previously mentioned, single layer steps in thickness are unavoidable during MBE growth of MBT materials. Given the thickness dependent properties of the material in its antiferromagnetic phase, it is then necessary to exfoliate the sample in order to fabricate devices with a deterministic number of layers. However, this method of device fabrication has an extremely low yield and it is desirable to avoid this process altogether. Tuning the interlayer coupling such that MBT and its related alloys order ferromagnetically is, therefore, an interesting route towards a high temperature QAHE phase. While we have previously discussed MBT/BST superlattices in the context of ferromagnetic ordering, they also suffer from the issue of controlling the number of BST spacer layers to a high precision, potentially making it a more difficult approach than MBT/VBT alloys. Theoretical investigations have focused on two approaches - doping MBT with vanadium to form $Mn_{1-x}V_xBi_2Te_4$, or alternating septuple layers of MBT and VBT to form an MBT/VBT superlattice. In the case of the doping strategy, ferromagnetic coupling is promoted for doping concentrations in the range $0.333 < x < 0.667$ and is strongest at $x = 0.5$. However, as with doping strategies of bare TIs, disorder and antisite defects can lead to position dependent exchange gaps and parasitic bulk conduction [66]. Despite the fact that VBT has an easy in-plane magnetic axis, DFT studies have found that the exchange interaction of the Mn and V spins leads to the formation energy of a spin configuration where they are all aligned along the $\hat{z}$ axis is lower than some non-colinear configuration [212]. MBE growth of MBT/VBT superlattices is certainly a more challenging route than doping, however it would be an interesting study to find how sensitive the presence of ferromagnetic coupling is to the exact sequence of MBT and VBT layers.

Beyond alloying the wider family of intrinsic magnetic TIs with MBT, these materials are also interesting in their own right as we shall demonstrate in later chapters. As yet however, MBT has dominated research into intrinsic magnetic TIs and no other member of the wider family has been synthesised.

1.4 Thesis Structure

Having concluded the introductory chapter, the remaining structure of the thesis will now be outlined. Chapter 2 will detail the history and development of topological invariants within the field of condensed matter physics, discussing the various anti-unitary symmetries that give rise to the rich mathematical structure underpinning the classification of topological phases of matter. In Chapter 3 we will utilise the ideas presented in Chapter 2 to show how an in-plane magnetisation can result in topological insulators with trivial and non-trivial flat-bands. Chapter 4 will develop on these ideas by introducing the notion of magnetic textures and how these can be used to control the local-density of states around topological flat-bands. Finally, Chapter 5 concludes this thesis by summarising the main findings, as well as musing on their technological significance, and presenting ideas for further development and research.

Chapter 2

An Introduction to Topological Invariants

2.1 The Role of Symmetries in Quantum Mechanics

Following on from our pedagogical discussion of topology in condensed matter in section 2.1, we will now present a modern analysis of the topic. Much of the following discussion of symmetry has been adapted from [147, 31].

Our discussion of topology within condensed matter systems begins, as with nearly all aspects of quantum mechanics, with the topic of symmetry. Indeed, symmetry is integral to quantum mechanics - the symmetry of a Hamiltonian and its corresponding eigenspectrum reflect the physical observables of the system (von Neumann's principle). Mathematically, symmetry is represented by the invariance of the Hamiltonian under the action of a group of unitary transformations. Specifically, in the case of the second quantized Hamiltonian

$$\hat{H} = \sum_{A,B} \hat{c}_A^\dagger H_{AB} \hat{c}_B, \tag{2.1}$$

where H_{AB} is a component of the first quantized Hamiltonian acting in single particle space, the indices A and B are a tuple representing the site labels and other relevant quantum numbers e.g. spin, $\sigma = \uparrow / \downarrow$, and $\hat{c}_A^\dagger / c_B$ are the (potentially multi-component) fermionic creation/annihilation operators obeying the usual anticommutation relations

$$\begin{gathered} \{\hat{c}_A, \hat{c}_B\} = \{\hat{c}_A^\dagger, \hat{c}_B^\dagger\} = 0 \\ \{\hat{c}_A, \hat{c}_B^\dagger\} = \delta_{AB}, \end{gathered} \tag{2.2}$$

a unitary transformation, $\hat{\mathcal{U}}$ is a symmetry of the Hamiltonian if

$$\hat{\mathcal{U}}\hat{H}\hat{\mathcal{U}}^{\dagger} = \hat{H}. \tag{2.3}$$

In terms of the first quantized Hamiltonian, if the unitary transformation admits a matrix representation U, then the symmetry is expressed as

$$\begin{aligned} UHU^{\dagger} = H \quad \text{i.e.} \\ [U, H] = 0, \end{aligned} \tag{2.4}$$

Using an elementary result of linear algebra, namely that two commuting matrices have a shared eigenbasis, we can block diagonalise H according to its unitary symmetries,

$$H = H_1 \oplus H_2 \oplus \cdots \oplus H_n. \tag{2.5}$$

Each block, H_i, will be symmetry-less in the sense that there are no additional unitary operators that commute with it. Now that we have a set of irreducible block Hamiltonians, each acting on their own regions of the full Hilbert space, we may ask: how many different classes of irreducible Hamiltonians are there? At first, it may appear that our desire to classify arbitrary Hamiltonians is futile given that we have already exhausted all our unitary symmetries. However, Wigner's theorem states that symmetries of a quantum system may be unitary or *anti-unitary*, i.e. operators of the form $A = UK$ where U is a unitary operator and K is the operation of complex conjugation. In contrast to unitary symmetries, anti-unitary symmetries cannot be continuous (since the product of any two anti-unitary symmetries is unitary), however they will impose certain reality conditions on the block Hamiltonian which we may use as part of a classification scheme.

2.1.1 Anti-unitary symmetries

We preface this discussion by noting that the anti-unitary symmetries we consider are *non-spatial* in the sense that they do not act on the spatial part of the Hamiltonian (i.e. do not exchange site labels i and j).

Time Reversal Symmetry

We begin our discussion of anti-unitary symmetries with time-reversal symmetry (TRS). As previously discussed this transformation inverts the direction of time under the transformation $t \to -t$. If $\hat{\mathcal{T}}$ is defined as the operator that implements time reversal, then its action on the position and momentum operators is

$$\hat{\mathcal{T}}\hat{x}\hat{\mathcal{T}}^{-1} = \hat{x}, \quad \hat{\mathcal{T}}\hat{p}\hat{\mathcal{T}}^{-1} = -\hat{p}. \tag{2.6}$$

analogously to time reversal in classical mechanics. Using Heisenberg's uncertainty relation, $[\hat{x}, \hat{p}] = i\hbar$, we may then infer that $\mathcal{T}$ is an anti-unitary operator since

$$\begin{aligned} \hat{\mathcal{T}}[\hat{x},\hat{p}]\hat{\mathcal{T}}^{-1} &= \hat{\mathcal{T}}i\hbar\hat{\mathcal{T}}^{-1} \\ -[\hat{x},\hat{p}] &= \hat{\mathcal{T}}i\hbar\hat{\mathcal{T}}^{-1} \implies \\ \hat{\mathcal{T}}i\hat{\mathcal{T}}^{-1} &= -i. \end{aligned} \tag{2.7}$$

Having established the anti-unitary nature of $\hat{\mathcal{T}}$, we now define its action on the fermionic creation and annihilation operators as

$$\begin{aligned} \hat{\mathcal{T}}\hat{c}_{i,\uparrow}\hat{\mathcal{T}}^{-1} &= \hat{c}_{i,\downarrow}, \quad \hat{\mathcal{T}}\hat{c}^{\dagger}_{i,\uparrow}\hat{\mathcal{T}}^{-1} = \hat{c}^{\dagger}_{i,\downarrow} \\ \hat{\mathcal{T}}\hat{c}_{i,\downarrow}\hat{\mathcal{T}}^{-1} &= -\hat{c}_{i,\uparrow}, \quad \hat{\mathcal{T}}\hat{c}^{\dagger}_{i,\downarrow}\hat{\mathcal{T}}^{-1} = -\hat{c}^{\dagger}_{i,\uparrow} \end{aligned} \tag{2.8}$$

where we pick up an extra minus sign since the spin of an electron is a form of angular momentum which must be odd under time reversal, i.e. $\hat{\mathcal{T}}\hat{\sigma}\hat{\mathcal{T}}^{-1} = -\hat{\sigma}$. We also define the spinor $\hat{\psi} = (\hat{c}_{i,\uparrow}, \hat{c}^{\dagger}_{i,\uparrow}, \hat{c}_{i,\downarrow}, \hat{c}^{\dagger}_{i,\downarrow}, \cdots)$, such that the second quantized Hamiltonian can be written in terms of the first as

$$\hat{H} = \sum_{A,B} \hat{\psi}^{\dagger}_{A} H_{A,B} \hat{\psi}_{B} = \hat{\psi}^{\dagger} H \hat{\psi}. \tag{2.9}$$

We may now summarise the action of $\hat{\mathcal{T}}$ as

$$\hat{\mathcal{T}}\hat{\psi}_{A}\hat{\mathcal{T}}^{-1} = \sum_{B} (U_T)_{A,B}\hat{\psi}_{B} \tag{2.10}$$

where U_T is a unitary operator and $\hat{\psi}_A$ is a component of the spinor $\hat{\psi}$.

It should be emphasised that, so far, we have defined the action of $\hat{\mathcal{T}}$ in Fock space in the formalism of second quantization. In order to move to the first quantized picture, we note that if the second quantized Hamiltonian respects TRS $\hat{\mathcal{T}}\hat{H}\hat{\mathcal{T}}^{-1} = \hat{H}$. Then using (2.10) we find

$$\begin{aligned}\hat{\mathcal{T}}\hat{H}\hat{\mathcal{T}}^{-1} &= \sum_{A,B}\hat{\mathcal{T}}\hat{\psi}_A^{\dagger}\hat{\mathcal{T}}^{-1}\hat{\mathcal{T}}H_{A,B}\hat{\mathcal{T}}^{-1}\hat{\mathcal{T}}\hat{\psi}_B\hat{\mathcal{T}}^{-1}\\ &= \sum_{A,B}\sum_{C,D}(U_T)^{\dagger}_{C,A}\hat{\psi}^{\dagger}_C H^*_{A,B}(U_T)_{B,D}\hat{\psi}_D\\ &= \sum_{C,D}\hat{\psi}^{\dagger}_C H_{C,D}\hat{\psi}_D = \hat{H}\end{aligned} \tag{2.11}$$

where $H_{C,D} = (U_T)^{\dagger}_{C,A}H^*_{A,B}(U_T)_{B,D}$ i.e. $U_T^{\dagger}H^*U_T$. Note that the first quantized Hamiltonian, H, has been complex conjugated since the action of $\hat{\mathcal{T}}$ flips the sign of i. We may then define a first quantized version of $\hat{\mathcal{T}}$ which acts on the single particle space, T. The action of T on the first quantized Hamiltonian is

$$THT^{-1} = H \quad \text{where} \quad T = U_T K \tag{2.12}$$

where K is the operation of complex conjugation. We may constrain the form of U_T by noticing that $\hat{\mathcal{T}}^2\hat{H}\hat{\mathcal{T}}^{-2} = \hat{H}$, or rephrased in terms of the first quantized Hamiltonian

$$(U_T^*U_T)^{\dagger}H(U_T^*U_T) = H \tag{2.13}$$

i.e. $U_T^*U_T$ commutes with the Hamiltonian. By Schur's lemma $U_T^*U_T = e^{i\phi}$, i.e. the identity up to some phase. Right multiplying by $U_T^{\dagger}$ and using the unitarity of U_T we find $U_T^* = e^{i\phi}U_T^{\dagger}$. Similarly, taking the complex conjugate of both sides and left multiplying by $U_T^{\dagger}$ implies $U_T^* = U_T^{\dagger}e^{-i\phi}$. Equating these two conditions, $U_T^{\dagger}e^{-i\phi} = e^{i\phi}U_T^{\dagger}$ or equivalently $U_T e^{i\phi} = e^{-i\phi}U_T$ which implies $e^{i\phi} = \pm 1$ and $T^2 = U_T U_T^* = \pm 1$.

We therefore have three possibilities: the system does not respect TRS, the system respects TRS where $T^2 = 1$ or, the system respects TRS where $T^2 = -1$. In fact, this result predates the concept of topological condensed matter in quantum mechanics by several decades and can be attributed to Freeman Dyson's work in foundational quantum mechanics [37]. In his work, Dyson utilised random matrix theory to show that there can only be three possible types of irreducible representations (irrep) of a Hilbert space and, hence, three possible types of Hamiltonian defined on that Hilbert space. He named these representations complex, real and quaternionic due to the isomorphism between each irrep and the respective number algebra. A correspondence also exists between Dyson's threefold way and our own discussion of TRS: the complex representation corresponding to the case of no TRS, real corresponding to $T^2 = 1$ and the quaternionic to $T^2 = -1$.

Particle-Hole Symmetry

Where-as classical physics and quantum physics alike posses the notion of TRS, particle-hole symmetry (PHS) is a purely quantum phenomenon. The notion of particle-hole symmetry (often also known as charge conjugation) is to interchange electrons for holes. In contrast to $\hat{\mathcal{T}}$, the operator $\hat{\mathcal{P}}$ implementing particle-hole exchange is unitary in the second quantized picture, $\hat{\mathcal{P}} i \hat{\mathcal{P}}^{-1} = i$. Its action on the fermionic creation and annhiliation spinors, $\hat{\psi}^\dagger / \hat{\psi}$ we defined in the previous section is

$$\hat{\mathcal{P}} \hat{\psi}_A \hat{\mathcal{P}}^{-1} = \sum_B \hat{\psi}^\dagger_B (U_P)_{B,A} \tag{2.14}$$

where U_P is a unitary operator. Using this definition, we implement the transformation of $\hat{H}$ under $\hat{\mathcal{P}}$ as

$$\begin{aligned}
\hat{\mathcal{P}} \hat{H} \hat{\mathcal{P}}^{-1} &= \sum_{A,B} \hat{\mathcal{P}} \hat{\psi}^\dagger_A \hat{\mathcal{P}}^{-1} \hat{\mathcal{P}} H_{A,B} \hat{\mathcal{P}}^{-1} \hat{\mathcal{P}} \hat{\psi}_B \hat{\mathcal{P}}^{-1} \\
&= \sum_{A,B} \sum_{C,D} (U_P)^\dagger_{A,C} \hat{\psi}_C H_{A,B} \hat{\psi}^\dagger_D (U_P)_{D,B} \\
&= \sum_{A,B} \sum_{C,D} \delta_{C,D} (U_P)^\dagger_{A,C} H_{A,B} (U_P)_{D,B} - \hat{\psi}^\dagger_D (U_P)_{D,B} H_{A,B} (U_P)^\dagger_{A,C} \hat{\psi}_C \\
&= \sum_{A,B} \sum_{C,D} (U_P)^\dagger_{A,C} H_{A,B} (U_P)_{C,B} - \hat{\psi}^\dagger_D (U_P)_{D,B} H^T_{B,A} (U_P)^\dagger_{A,C} \hat{\psi}_C \\
&= \sum_{A,B} \left(\delta_{A,B} H_{A,B} - \sum_{C,D} \hat{\psi}^\dagger_D (U_P)_{D,B} H^T_{B,A} (U_P)^\dagger_{A,C} \hat{\psi}_C \right) \\
&= \mathrm{Tr}(H) - \sum_{C,D} \hat{\psi}^\dagger_D H_{D,C} \hat{\psi}_C,
\end{aligned} \tag{2.15}$$

where we have used the anticommutation relation $\{\hat{\psi}_A, \hat{\psi}^\dagger_B\} = \delta_{A,B}$ between the second and third lines and the unitarity of U_P between the fourth and fifth lines. Note that the action of $\hat{\mathcal{P}}$ on the first quantized Hamiltonian is trivial, i.e. $\hat{\mathcal{P}} H_{A,B} \hat{\mathcal{P}}^{-1} = H_{A,B}$, contrary to the case of TRS. As before, we require $\hat{\mathcal{P}} \hat{H} \hat{\mathcal{P}}^{-1} = \hat{H}$ if our Hamiltonian respects PHS demanding the conditions

$$\begin{aligned}
\mathrm{Tr}(H) &= 0 \\
U_P H^* U_P^\dagger &= -H.
\end{aligned} \tag{2.16}$$

where we have utilised the Hermicity of $H = H^\dagger \implies H^T = H^*$ in the second inequality. These two conditions are actually complementary since the symmetry condition on the single particle Hamiltonian implies that the eigenspectrum is symmetric

$$\begin{aligned} \text{if} \quad H\left|\psi\right\rangle = E\left|\psi\right\rangle &\implies \\ H^*\left|\bar{\psi}\right\rangle = E^*\left|\bar{\psi}\right\rangle &\implies \\ U_P H^* U_P U_P^\dagger\left|\bar{\psi}\right\rangle = E U_P\left|\bar{\psi}\right\rangle &\implies \\ H\left|\bar{\psi}\right\rangle = -E\left|\bar{\psi}\right\rangle&, \end{aligned} \tag{2.17}$$

i.e. if $\left|\psi\right\rangle$ is an eigenstate of H at energy E then there exists an eigenstate $\left|\bar{\psi}\right\rangle = K\left|\psi\right\rangle$ at energy $-E$. If D is then some unitary operator that diagonalises H then $\mathrm{Tr}(DHD^{-1}) = \mathrm{Tr}(HDD^{-1}) = \mathrm{Tr}(H) = 0$.

Following the same procedure that we used for the case of TRS, we now define a first quantized version of the particle-hole operator, P. The action of P on the first quantized Hamiltonian is then

$$PHP^{-1} = -H \quad \text{where} \quad P = U_P K. \tag{2.18}$$

Interestingly, the particle-hole operator in the second quantized picture was linear and unitary, $\hat{\mathcal{P}} i \hat{\mathcal{P}}^{-1} = i$ where-as in the first quantized picture P is anti-linear and anti-unitary since it contains the operation of complex conjugation. Following an identical argument to that which we used to constrain the form of U_T, we find that $P^2 = U_P U_P^* = \pm 1$. once again then, we have three possibilities: the Hamiltonian does not respect PHS, the Hamiltonian respects PHS and $P^2 = 1$ or, the Hamiltonian respects PHS and $P^2 = -1$.

The Altland-Zirnbauer Classification and Tenfold Way

The existence of PHS as well as TRS extends Dyson's original threefold classification to a nine-fold one, however we have yet to investigate what happens under their product. Therefore, we introduce the concept of chiral symmetry, $\hat{\mathcal{S}} = \hat{\mathcal{T}} \cdot \hat{\mathcal{P}}$, or in terms of the first quantized picture $S = T \cdot P = U_T K \cdot U_P K = U_T U_P^* = U_S$, which transforms our fermionic creation/annihilation operators as

$$\hat{\mathcal{S}} \hat{\psi}_A \hat{\mathcal{S}}^{-1} = \sum_B (U_S)_{A,B} \hat{\psi}_B^\dagger. \tag{2.19}$$

We also note that in the picture of second quantization, $\hat{\mathcal{S}}$ is an anti-unitary operator, $\hat{\mathcal{S}}i\hat{\mathcal{S}}^{-1} = -i$ since it is the product of a unitary and an anti-unitary operator, where-as U_S is a unitary operator in the single particle space. As before, we investigate the action of $\hat{\mathcal{S}}$ on $\hat{H}$,

$$\begin{aligned}
\hat{\mathcal{S}}\hat{H}\hat{\mathcal{S}}^{-1} &= \sum_{A,B} \hat{\mathcal{S}}\hat{\psi}^{\dagger}_{A}\hat{\mathcal{S}}^{-1}\hat{\mathcal{S}}H_{A,B}\hat{\mathcal{S}}^{-1}\hat{\mathcal{S}}\hat{\psi}_{B}\hat{\mathcal{S}}^{-1} \\
&= \sum_{A,B}\sum_{C,D}(U_S)^{\dagger}_{A,C}\hat{\psi}_C H^{*}_{A,B}\hat{\psi}^{\dagger}_{D}(U_S)_{D,B} \\
&= \sum_{A,B}\sum_{C,D}\delta_{C,D}(U_S)^{\dagger}_{A,C}H^{*}_{A,B}(U_S)_{D,B} - \hat{\psi}^{\dagger}_{D}(U_S)_{D,B}H^{*}_{A,B}(U_S)^{\dagger}_{A,C}\hat{\psi}_C \\
&= \sum_{A,B}\sum_{C,D}(U_S)^{\dagger}_{A,C}H_{A,B}(U_S)_{C,B} - \hat{\psi}^{\dagger}_{D}(U_S)_{D,B}H^{\dagger}_{B,A}(U_S)^{\dagger}_{A,C}\hat{\psi}_C \\
&= \sum_{A,B}\left(\delta_{A,B}H_{A,B} - \sum_{C,D}\hat{\psi}^{\dagger}_{D}(U_S)_{D,B}H_{B,A}(U_S)^{\dagger}_{A,C}\hat{\psi}_C\right) \\
&= \mathrm{Tr}(H) - \sum_{C,D}\hat{\psi}^{\dagger}_{D}H_{D,C}\hat{\psi}_C,
\end{aligned} \tag{2.20}$$

where we have complex conjugated the fist quantized Hamiltonian between the first and second lines due to the anti-unitarity of $\hat{\mathcal{S}}$, implemented the fermionic anticommutation relation between the second and third lines and between the fourth and fifth lines we have utilised the unitarity of U_S and the Hermicity of H. If the second quantized Hamiltonian respects chiral symmetry $\hat{\mathcal{S}}\hat{H}\hat{\mathcal{S}}^{-1} = \hat{H}$ and therefore

$$\begin{aligned}
\mathrm{Tr}(H) &= 0 \\
U_S H U_S^{\dagger} &= -H.
\end{aligned} \tag{2.21}$$

Similarly to the case of PHS, this conditions are complementary to one another since the second equality will result in an eigenspectrum which is symmetric about 0. We note that, although U_S is a unitary operator, chiral symmetry is not described as a unitary symmetry of the single particle Hamiltonian since $\{S, H\} = 0$, rather than the usual commutation relationship which defines unitary symmetries. As before, we constrain the form of U_S by examining $S^2 = U_S^2 = e^{i\phi}$ by Schur's lemma. We recall that $U_S = U_T U_P^{*}$ and the relationships $U_T U_T^{*} = \pm 1$ and $U_P U_P^{*} = \pm 1$ imply that the phases of U_T and U_P are completely arbitrary. Without loss of generality, we can therefore redefine $U_S \rightarrow U_S e^{i\phi/2}$ and find that $U_S^2 = 1$, meaning that there are only two possibilities: the system does not respect chiral symmetry, or the system does respect chiral symmetry with $U_S^2 = 1$.

It is clear that in eight of the nine classification schemes we have so far discussed, the question of whether the Hamiltonian respects chiral symmetry is pre-determined, i.e. fixing one or both of TRS/PHS uniquely determines whether $\hat{\mathcal{S}}$ is a symmetry. However, in the case where neither $\hat{\mathcal{T}}$ or $\hat{\mathcal{P}}$ is a symmetry of the Hamiltonian we have the interesting situation where their product, $\hat{\mathcal{S}}$ may or may not be a symmetry. In total then, there are actually 10 possible classes of irreducible Hamiltonian which are summarised in the table below:

class	S	P	T
A			
AIII	1		
AI			1
BDI	1	1	1
D		1	
DIII	1	1	-1
AII			-1
CII	1	-1	-1
C		-1	
CI	1	-1	1

The slightly obscure symmetry class labels in the left hand column of the table are known as Cartan symbols after work by the French mathematician Elie Cartan [27]. Cartan's original work gave a complete classification of Riemannian symmetric spaces (defined as a Riemannian manifold where inversion symmetry exists about each point). Although his work was completed some half a century prior to the discovery of topological matter, it is of fundamental importance in the classification of irreducible Hamiltonians. As discussed below, there is a one-to-one correspondance between equivalence classes of Clifford algebras and Cartan's symmetric spaces. The role of Clifford algebras in representing the various classes of irreducible Hamiltonians then provides the link between Cartan's original classification and the tenfold way of condensed matter physics. The right hand columns in the table detail which symmetries are respected in each class and the value of the symmetry operator squared. For example, the AII ("A-two") class respects TRS where $T^2 = -1$. This tenfold way of classifying irreducible Hamiltonians, also known as the Altland-Zirnbauer classification after the two researchers who identified the tenfold classification in the context of condensed matter, can be considered an extension of Dyson's threefold way once PHS is admitted as a possible anti-unitary symmetry of the single-particle Hamiltonian [5].

Before concluding this section, we briefly discuss the situation where the system possesses translational symmetry. In this case, we may use Bloch's theorem to parameterise the single-particle Hamiltonian in terms on the crystal momentum, $\boldsymbol{k}$ and rewrite the second quantized Hamiltonian as

$$\begin{aligned} \hat{H} &= \sum_{k} \hat{\psi}^{\dagger}_{A}(\boldsymbol{k}) H_{A,B}(\boldsymbol{k}) \hat{\psi}_{B}(\boldsymbol{k}) \\ \text{where} \quad \hat{\psi}_{A}(\boldsymbol{k}) &= \frac{1}{\sqrt{V}} \sum_{\boldsymbol{r}} e^{-i\boldsymbol{k}\cdot\boldsymbol{r}_i} \hat{\psi}_{A}(\boldsymbol{r}), \quad H_{A,B}(\boldsymbol{k}) = \sum_{\boldsymbol{r}} e^{-i\boldsymbol{k}\cdot\boldsymbol{r}_i} H_{A,B}(\boldsymbol{r}). \end{aligned} \tag{2.22}$$

where V is the number of sites/crystal volume and we have explicitly parameterised the real space fermionic operators and single particle Hamiltonian in terms of the displacement $\boldsymbol{r}$. The action of TRS, PHS and chiral symmetry on the single particle Bloch Hamiltonian is then

$$\begin{aligned} TH(\boldsymbol{k})T^{-1} &= H(-\boldsymbol{k}) \\ PH(\boldsymbol{k})P^{-1} &= -H(-\boldsymbol{k}) \\ SH(\boldsymbol{k})S^{-1} &= -H(\boldsymbol{k}) \end{aligned} \tag{2.23}$$

where the momentum is inverted in the cases of TRS and PHS due to the action of complex conjugation.

2.2 Topological Classification of Hamiltonians

Having introduced the concept of 10 symmetry classes describing all irreducible Hamiltonians, we will now discuss the possibility of different phases emerging in each of this classes. Of course, these phases and the transitions between them will not be described within the paradigm of Landau's phenomenological model since this necessarily involves spontaneous symmetry breaking (and we are considering the notion of phases *within* the same symmetry class), but instead we will introduce the notion of *topological equivalence* between Hamiltonians in the same symmetry class. In the course of this discussion we will neglect interactions and only consider Hamiltonians with gapped spectra, i.e. insulators.

We follow the usual definition in the literature and define two irreducible, gapped Hamiltonians, $H_1(\boldsymbol{k})$ and $H_2(\boldsymbol{k})$, to be *homotopy* equivalent if they are in the same symmetry class we can continuously deform their spectra into one another without closing the spectral gap at any point. To clarify, we consider an adiabatic spectral flattening transformation which transforms Hamiltonians to a form such that their eigenvalues, $\epsilon(\boldsymbol{k})$ undergo the transformation $\epsilon(\boldsymbol{k}) \longrightarrow \tilde{\epsilon}(\boldsymbol{k}) = \mathrm{sign}(\epsilon(\boldsymbol{k}))$ i.e. positive/negative eigenvalues are replaced by ± 1, respectively. Thus, the Hamiltonian for a system with m filled bands and n unfilled is given by

$$H(\boldsymbol{k}) = W(\boldsymbol{k}) Q_{m,n} W^{-1}(\boldsymbol{k}) \tag{2.24}$$

where $Q_{mn} = -\mathbb{1}_m \oplus \mathbb{1}_n$ and $W(\boldsymbol{k})$ is a $(n+m) \times (n+m)$ unitary matrix. During the course of this spectral flattening, no eigenvalue passed through 0 and hence the spectral gap did not close. Two Hamiltonians are therefore homotopy equivalent if they have the same number of bands and the same number of negative eigenvalues. Conversely, non-equivalent insulating phases can only be connected to one another through a closure of the spectral gap, which we will define as a *topological phase transition*.

In 2009, Kitaev proposed a general classification of topological insulators and superconductors based on the tenfold-classification of condensed matter by adopting Clifford algebras and K-theory [89]. Kitaev's arguments are well beyond the scope of this thesis, however we give a brief outline of his main points below.

2.2.1 Introduction to Clifford algebras

First, we will go over the basic definitions of a Clifford algebra. For greater detail we refer the interested reader to [9, 101, 81]. A Clifford algebra, usually denoted $Cl_{p,q}$, is defined by an identity element and the set of generators $\{e_1, e_2, ..., e_p, ..., e_{p+q}\}$ such that

$$\{e_\mu, e_\nu\} = 2\eta_{\mu\nu} \tag{2.25}$$

where η is a matrix of the quadratic form defining the algebra, which we will specify below. With these definitions, it is then possible to construct a basis $\{1, e_1, ..., e_{p+q}, e_1e_2, ..., e_1e_{p+q}, ..., e_1e_2...e_{p+q}\}$ containing 2^{p+q} possible elements. A general element of a Clifford algebra is a linear combination of elements of the basis. Multiplication of generators of a Clifford algebra is understood as

$$e_1e_2 = e_1 \cdot e_2 + e_1 \wedge e_2 \tag{2.26}$$

where the first term is the dot/interior product and $e_1 \wedge e_2 = -e_2 \wedge e_1$ is the exterior product.

For a real Clifford algebra, $Cl_{p,q}(\mathbb{R})$

$$\eta_{\mu\nu} = \begin{cases} -\delta_{\mu\nu} & \text{for} \quad 0 < \mu, \nu \leq p \\ \delta_{\mu\nu} & \text{for} \quad p < \mu, \nu \leq p+q \end{cases} \tag{2.27}$$

while for a complex Clifford algebra, $Cl_{p+q}(\mathbb{C})$

$$\eta_{\mu\nu} = \delta_{\mu\nu}. \tag{2.28}$$

In a real Clifford algebra the coefficients of a general element must be real while they may take on complex values in a complex Clifford algebra, i.e. $Cl_{p,q}(\mathbb{R}) \otimes \mathbb{C} \simeq Cl_{p+q}(\mathbb{C})$. In the following, we will distinguish between the signatures of the generators (the signature of an element being the value of e_i^2) by writing the set of generators as $\{e_1, e_2, ..., e_p; e_{p+1}, ..., e_{p+q}\}$ for a real algebra where $e_i^2 = -1, i \leq p$ and $e_i^2 = 1, i > p$.

A fair question at this point is, why have introduced Clifford algebras at all? The reason for it, is that Clifford algebras naturally appear in Dirac Hamiltonians because of their use in describing spinor quantities. In addition, Clifford algebras are a concise way of keeping track of the various symmetries in condensed matter systems, as well as describing the objects that generate these symmetries. For example, we have shown in the preceding section that $THT = H$ where $T^2 = \pm 1$, $PHP = -H$ where $P^2 = \pm 1$ and $SHS = -H$ where $S^2 = 1$. Each symmetry operator may be represented as a generator of a Clifford algebra, while the quadratic form $\eta_{\mu,\nu}$ keeps track of the nature of this symmetry operator.

Before moving on, we note that the lower Clifford algebras give us the division algebras

$$Cl_{0,0} \simeq \mathbb{R} \quad Cl_{1,0} \simeq \mathbb{C} \quad Cl_{2,0} \simeq \mathbb{H} \tag{2.29}$$

where $\simeq$ denotes an isomorphism and $\mathbb{H}$ is the set of quaternions. Higher order Clifford algebras are isomorphic to matrix algebras, i.e.

$$\begin{gathered} Cl_{1,1}(\mathbb{R}) \simeq Cl_{0,2}(\mathbb{R}) \simeq \mathbb{R}(2) \\ Cl_{0,1} \simeq \mathbb{R}^2 \end{gathered} \tag{2.30}$$

where $\mathbb{R}(2)$ is the set of 2×2 real matrices and $\mathbb{R}^n$ is the n-dimensional set of real numbers, i.e. n-dimensional Euclidean space. Furthermore the recurrence relations, which we will simply quote,

$$\begin{aligned} Cl_{p,q} \otimes Cl_{2,0} &\simeq Cl_{q+2,p} \\ Cl_{p,q} \otimes Cl_{1,1} &\simeq Cl_{p+1,q+1} \\ Cl_{p,q} \otimes Cl_{0,2} &\simeq Cl_{q,p+2} \end{aligned} \tag{2.31}$$

allow us to construct all higher order Clifford algebras from the lower ones described above. The result of this is that all Clifford algebras are isomorphic to $\mathbb{R}(d)$, $\mathbb{C}(d)$ or $\mathbb{H}(d)$. Clifford algebras are, therefore, a powerful abstraction of the usual matrix algebras we deal with when describing Dirac Hamiltonians. Importantly though, they do not require an explicit representation. To surmise, the Clifford algebras offer a powerful way to represent our Hamiltonian in that they are covers of the relevant classifying spaces.

2.2.2 The periodic table of topological insulators

We recall that our ultimate goal to to determine how many distinct ground states a Hamiltonian with a particular set of symmetries may posses. As described in the previous section, Clifford algebras offer a means to keep track of these symmetries. Our strategy, therefore, will be to construct the relevant Clifford algebras from the symmetries present and then find which generators can be added under the condition they form another Clifford algebra. Kitaev referred to this as the *Clifford extension problem.* In the language of matrices and Hamiltonians, we are simply asking which terms can be added that respect the symmetry of the system but lead to a new ground state. In the following, we will adopt the framework set out by Morimoto and Furasaki to classify single-particle, gapped Hamiltonians by considering possible extensions to the Clifford algebra with generators corresponding to the allowed terms in the spectral flattened Hamiltonian, Q, and the relevant symmetries [122, 123].

First, we consider a minimal, massive Dirac Hamiltonian in d-dimensions of the form

$$H = \sum_{i=1}^{d} k_i \alpha_i + m\beta \tag{2.32}$$

where $\{\alpha_i, \alpha_j\} = 2\delta_{ij}$, $\beta^2 = 1$ and $\{\alpha_i, \beta\} = 0 \forall i$. This choice of α_i, β define a complex Clifford algebra, Cl_{d+1}. The choice of β may not be unique, depending on the dimensionality of the system and the number of bands (matrix rank). For example in a two band system, we can always describe the Hamiltonian in terms of the Pauli matrices, $\{\sigma_x, \sigma_y, \sigma_z\}$ which form another complex Clifford algebra. Therefore, in 1D there are two possible choices for the matrix β. This ambiguity in the choice of β is actually integral to the Clifford extension problem and we will return to it later.

The conditions for TRS, PHS or chiral symmetry in terms of α_i, β are given as

$$\begin{aligned}\text{TRS}: &\quad \{T,\alpha_i\} = [T,\beta] = 0\\ \text{PHS}: &\quad [P,\alpha_i] = \{P,\beta\} = 0\\ \text{Chiral}: &\quad \{S,\alpha_i\} = \{S,\beta\} = 0.\end{aligned} \tag{2.33}$$

Given that Clifford algebras are based on anticommutation relations, the fact that we have commutation relations describing the above symmetry constraints is an issue if we would like to use this symmetries as generators. However, recalling that $T = U_T K$ and $P = U_P K$ we can define an additional element J such that $J^2 = -1$ and $\{T,J\} = \{P,J\} = 0$, i.e. J takes the role of the imaginary unit i. As such, we can rewrite all the above symmetry constraints as anticommutation relations

$$\begin{aligned}\text{TRS}: &\quad \{T,\alpha_i\} = \{T,J\beta\} = 0\\ \text{PHS}: &\quad \{P,J\alpha_i\} = \{P,\beta\} = 0\end{aligned} \tag{2.34}$$

If we do include this imaginary unit, J, then if T is a generator $TJ = -JT$ is also a generator since $[J,\alpha_i] = [J,\beta] = 0$ and

$$\begin{aligned}\{T,J\} = TJ + JT = 0 &\implies\\ TTJ + TJT = 0 &\implies\\ \{T,TJ\} = 0.&\end{aligned} \tag{2.35}$$

There is, of course, a similar argument for P. Finally, in AZ classes with both T and P present we will consider the generator TPJ instead of S (recall that $S = TP$). Since $TPJ = JTP$ we actually only need to consider one of TPJ and TP as generators in our Clifford algebra, but we chose the latter in order to maintain consistency with the treatment of Murimoto and Furasaki.

With all this in mind, we present an extension of table 2.2.2 with the appropriate Clifford algebra and generators below

class	S	P	T	$Cl_{p,q}$
A				$Cl_{d+1} : \{\alpha, \beta\}$
AIII	1			$Cl_{d+2} : \{\alpha, \beta, S\}$
AI			1	$Cl_{1,d+2} : \{\beta J; \alpha, T, TJ\}$
BDI	1	1	1	$Cl_{d+1,3} : \{\alpha J, TPJ; \beta, P, PJ\}$
D		1		$C_{d,3} : \{\alpha J; \beta, P, PJ\}$
DIII	1	1	-1	$Cl_{d,4} : \{\alpha J; \beta, P, PJ, TPJ\}$
AII			-1	$Cl_{3,d} : \{\beta J, T, TJ; \alpha\}$
CII	1	-1	-1	$Cl_{d+3,1} : \{\alpha J, P, PJ, TPJ; \beta\}$
C		-1		$Cl_{d+2,1} : \{\alpha J, P, PJ; \beta\}$
CI	1	-1	1	$Cl_{d+2,2} : \{\alpha J, P, PJ; \beta, TPJ\}$

Note that in the four classes with TRS and PHS (BDI, DIII, CII, CI) we have only included the operators P, PJ and TPJ, while apparently omitting T and TJ as generators. The reason for this is that we can always chose $[T, P] = 0$, without loss of generality. Therefore, T/TJ cannot be in the same Clifford algebra as P/PJ. However, the symmetry of the time-reversal operator is still captured by the TPJ generator. We also note that A and AIII are complex, while the remaining AZ classes have real Clifford algebras.

Returning to the Clifford extension problem, we are essentially asking which mass terms we can add to the above table of generator sets such that we extend the relevant Clifford algebra. The symmetry of these mass terms will reflect the symmetry of the Clifford algebra and, therefore, will form a *classifying space*, $\mathcal{V}$. The notion of extending Clifford algebras may appear ambiguous - after all, if we have a Clifford algebra $Cl_{p,q}$ we can chose $Cl_{p,q} \longrightarrow Cl_{p+1,q}$ or $Cl_{p,q} \longrightarrow Cl_{p,q+1}$ as two valid extensions. However, we can consider the algebras given in the above table *as the extended algebras*. That is, we remove the $\beta/\beta J$ term from each algebra and then add it back in to form the extended Clifford algebra. The third column of the below table summarises this concept of Clifford algebra extension for each AZ class:

class	Clifford extension	$d = 0$ extension
A	$Cl_d \to Cl_{d+1}$	$\mathcal{C}_0 : Cl_0 \to Cl_1 \simeq \mathbb{C} \to \mathbb{C} \oplus \mathbb{C}$
AIII	$Cl_{d+1} \to Cl_{d+2}$	$\mathcal{C}_1 : Cl_1 \to Cl_2 \simeq \mathbb{C} \oplus \mathbb{C} \to \mathbb{C}(2)$
AI	$Cl_{0,d+2} \to Cl_{1,d+2}$	$\mathcal{R}_0 : Cl_{0,2} \to Cl_{1,2} \simeq \mathbb{R}(2) \to \mathbb{R}(2) \oplus \mathbb{R}(2)$
BDI	$Cl_{d+1,2} \to Cl_{d+1,3}$	$\mathcal{R}_1 : Cl_{1,2} \to Cl_{1,3} \simeq \mathbb{R}(2) \oplus \mathbb{R}(2) \to \mathbb{R}(4)$
D	$Cl_{d,2} \to Cl_{d,3}$	$\mathcal{R}_2 : Cl_{0,2} \to Cl_{0,3} \simeq \mathbb{R}(2) \to \mathbb{C}(2)$
DIII	$Cl_{d,3} \to Cl_{d,4}$	$\mathcal{R}_3 : Cl_{0,3} \to Cl_{0,4} \simeq \mathbb{C}(2) \to \mathbb{H}(2)$
AII	$Cl_{2,d} \to Cl_{3,d}$	$\mathcal{R}_4 : Cl_{2,0} \to Cl_{3,0} \simeq \mathbb{H} \to \mathbb{H} \oplus \mathbb{H}$
CII	$Cl_{d+3,0} \to Cl_{d+3,1}$	$\mathcal{R}_5 : Cl_{3,0} \to Cl_{3,1} \simeq \mathbb{H} \oplus \mathbb{H} \to \mathbb{H}(2)$
C	$Cl_{d+2,0} \to Cl_{d+2,1}$	$\mathcal{R}_6 : Cl_{2,0} \to Cl_{2,1} \simeq \mathbb{H} \to \mathbb{C}(2)$
CI	$Cl_{d+2,1} \to Cl_{d+2,2}$	$\mathcal{R}_7 : Cl_{2,1} \to Cl_{2,2} \simeq \mathbb{C}(2) \to \mathbb{R}(4)$

We will briefly pause to examine some features of this table. The third row shows the Clifford extension problem in the case of $d = 0$ where we have also used the isomorphisms given in (2.29) and (2.30) to rephrase the problem in terms of algebra homomorphisms. We have also labelled each entry in the $d = 0$ classification by $\mathcal{C}_n$ or $\mathcal{R}_n$ in the case of the complex and real classes, respectively. Before elucidating the meaning of these labels, we will examine the recurrence relations given in (2.31) used for constructing higher order algebras. First, using the first two isomorphisms in (2.31) we note that

$$\begin{aligned} Cl_{p+8,q} &\simeq Cl_{p,q} \otimes Cl_{8,0} \\ &\simeq Cl_{q,p} \otimes (Cl_{2,0} \otimes Cl_{0,2} \otimes Cl_{2,0} \otimes Cl_{0,2}) \\ &\simeq Cl_{p,q} \otimes (\mathbb{R}(2) \otimes \mathbb{H} \otimes \mathbb{R}(2) \otimes \mathbb{H}) \\ &\simeq Cl_{p,q} \otimes (\mathbb{R}(4) \otimes \mathbb{R}(4)) \\ &\simeq Cl_{p,q} \otimes \mathbb{R}(16) \end{aligned} \tag{2.36}$$

where we have used $\mathbb{H}(m) \otimes \mathbb{H}(n) \simeq \mathbb{R}(4mn)$. Through an identical argument, we also have the isomorphism

$$Cl_{p,q+8} \simeq Cl_{p,q} \otimes \mathbb{R}(16) \tag{2.37}$$

We also recall that

$$\mathbb{K}(m) \otimes \mathbb{R}(n) \simeq \mathbb{K}(mn) \tag{2.38}$$

where $\mathbb{K}$ is one of $\mathbb{K} = \mathbb{R}, \mathbb{C}$ or $\mathbb{H}$. This isomorphism along with those presented in (2.36) and (2.37) are summarised as

$$Cl_{p+8,q} \simeq Cl_{p,q+8} \simeq Cl_{p,q} \otimes \mathbb{R}(16) \tag{2.39}$$

At this point, we will also use the notion of *Morita equivalence*, which states that $\mathbb{K}(n) \approx \mathbb{K}$ where (in more technically language, Morita equivalence means that two rings have the same representation theory) [81]. We conclude that the Clifford algebras $Cl_{p+8,q} \approx Cl_{p,q+8} \approx Cl_{p,q}$ where $\approx$ denotes Morita equivalence.

An analogous set of arguments may be used to establish the periodicity of complex Clifford algebras. Using the definition of the complex Clifford algebra

$$\begin{aligned} Cl_2(\mathbb{C}) \simeq Cl_{1,0} \otimes Cl_{0,2} &\simeq Cl_{0,3} \\ &\simeq \mathbb{C}(2) \end{aligned} \tag{2.40}$$

Using this result, we can establish periodicity of the complex Clifford algebras up to Morita equivalence as

$$\begin{aligned} Cl_{n+2}(\mathbb{C}) &\simeq Cl_{n+2,0} \otimes \mathbb{C} \\ &\simeq Cl_{n,0} \otimes Cl_{0,2} \otimes \mathbb{C} \\ &\simeq Cl_{n,0} \otimes \mathbb{C}(2) \\ &\simeq Cl_n(\mathbb{C}) \otimes Cl_2(\mathbb{C}) \end{aligned} \tag{2.41}$$

i.e. the complex Clifford algebras are Morita equivalent modulo 2, $Cl_n(\mathbb{C}) \approx Cl_{n+2}(\mathbb{C})$, which is also reflected in the classification of the Clifford algebra extension, $C_n = C_{n \bmod 2}$. The periodicity of Clifford algebras is often known as Bott periodicity in the context of K theory, terminology which we will also adopt here [9, 167].

Having established the Bott periodicity of Clifford algebras up to Morita equivalence, we will return to our explanation of the labels for each Clifford extension. For the complex class the extension $Cl_n \to Cl_{n+1}$ is straightforwardly labelled by $C_{n \bmod 2}$. Ironically, the real case is slightly more complex. This is due to the aforementioned ambiguity in the Clifford extension problem (i.e. whether the positive or negative generators are extended). Except for the classes AI and AII, all the extensions are of the form $Cl_{p,q} \to Cl_{p,q+1}$, i.e. positive generator extension. For now, we will label the positive generator extension as $\mathcal{R}_{p,q}$. Analysing the case of the negative generator extension problem, we recall the final isomorphism in (2.31) such that we map the extension $Cl_{p,q} \to Cl_{p+1,q}$ to $Cl_{q,p+2} \to Cl_{q,p+3}$. Therefore, we may label the extension problem of negative generators by $\mathcal{R}_{q,p+2}$. Finally, using the isomorphisms in (2.30) and the middle relation in (2.31) we find

$$
\begin{aligned}
Cl_{p,q} \otimes Cl_{1,1} &\simeq Cl_{p+1,q+1} \\
&\simeq Cl_{p,q} \otimes \mathbb{R}(2)
\end{aligned}
\tag{2.42}
$$

meaning that the extension problem only depends on $q - p$, since the direct product with $\mathbb{R}(2)$ has no effect on the classification of the problem through the isomorphism (2.38). Therefore, for the positive generator extension $\mathcal{R}_{p,q} = \mathcal{R}_{q-p \mod 8}$ and for the negative generator extension $\mathcal{R}_{p,q} = \mathcal{R}_{p-q+2 \mod 8}$.

Given Bott periodicity, we conclude that it is sufficient to solve the Clifford extension problem for $d = 0$ since considering the dimension will simply shift the classifying spaces of each class by d, that is

$$
\begin{aligned}
\mathcal{C}_n &\longrightarrow \mathcal{C}_{n+d \mod 2} \\
\mathcal{R}_n &\longrightarrow \mathcal{R}_{n+d \mod 8}
\end{aligned}
\tag{2.43}
$$

Having constructed a set of algebra extensions/homomorphisms for each topological class, we can now characterise $\mathcal{V}_i$, that is the classifying space of mass terms that lead to the extended algebra. As discussed by Morimoto *et al*, in d dimensions there is a minimum matrix rank required such that there are any possible mass terms [123]. For example, as discussed at the beginning of this section, there is an ambiguity over the choice of β in a two-band system where $d = 1$, however in $d = 3$ there is no possibility of an additional mass term in a two-band system. Therefore, for each dimension d there will be a minimum matrix rank r_{min} below which there would be no possible mass matrices. However, as will become clear later, it is not particularly illuminating to consider the classifying spaces for the minimum matrix rank, r_{min}.

As previously discussed, it is clear that Hamiltonians in the same topological class should be should be homotopy equivalent (i.e. equivalent under continuous deformation). In terms of the flattened Hamiltonian presented in equation 2.24, Q, homotopy equivalence can be understood as Hamiltonians of equal rank sharing the same number of negative eigenvalues. However, this definition of equivalence is quite restrictive and does not permit a particularly robust classification system, as we shall discuss later in the small dimensional exceptions section as the end of this chapter. Rather, Kitaev proposed that Hamiltonians should be classified on the basis of *stable equivalence*, a notion borrowed from the mathematical subject of K-theory that essentially communicates equivalence of Hamiltonians up to augmentation with some number of trivial valence bands, and in the *stable regime* that is, in the limit of a large number of valence and conduction bands.

A brief introduction to K-theory

While the intricacies of K-theory will not be discussed here, it is worth briefly clarifying its relationship to the task at hand, namely the topological classification of Hamiltonians. Much of this discussion is taken from [10, 81, 83]. K-theory is concerned with the classification of vector bundles up to stable isomorphism. Recall a vector bundle as the triplet $\epsilon = (E, M, p)$, where E is known as the total space, M is known as the base space and p is an infinitely differentiable projection, satisfying the relationship $p : E \longrightarrow M$. For each $x \in M$ the fibres are defined as $E_x := p^{-1}(\{x\})$. This triplet is considered a vector bundle if the following are conditions are satisfied:

- E_x carries the structure of a vector space of dimension $n \in \mathbb{N}$, V^n;
- For each $x \in M$ there exists an open neighbourhood U and an integer $n_x \in \mathbb{N}$ such that there exists a diffeomorphism $\phi : U \times \mathbb{C}^{n_x} \longrightarrow p^{-1}(U)$ which is fibrewise linear $\phi_x : \{x\} \times \mathbb{K}^{n_x} \longrightarrow p^{-1}(\{x\}) := E_x$, i.e. ϵ is locally trivial (as the total space can be considered to locally have a product structure). If $n_x = n$ for all U covering M then the rank of the bundle is said to be n. Here $\mathbb{K}$ is either the field of real or complex numbers, therefore giving a real or complex vector bundle, respectively.

In the current setting, we are considering the valence bundle, a sub-bundle of the Hilbert bundle, with the Brillouin Zone as the base space, $M = \mathbb{T}^d$ where $d \in \mathbb{N}$ is the dimension of the crystalline material, and the fibres are Hilbert spaces formed of the eigenstates of the Hamiltonian, $H(\boldsymbol{k})$ where $\boldsymbol{k} \in M$. In addition, the fibres of the valence bundle come with additional structure due to the symmetries discussed in the previous section.

Two vector bundles with the same base space, $\epsilon_1 = (E_1, M, p_1)$ and $\epsilon_2 = (E_2, M, p_2)$, are isomorphic if there exists a smooth, bijection $f : E_1 \longrightarrow E_2$ that satisfies $p_2 \cdot f = p_1$ and $f|_{p_1^{-1}(\{x\})} : p_1^{-1}(\{x\}) \longrightarrow p_2^{-1}(\{x\}$, i.e. f is a linear isomorphism over each fibre. Just as two Hamiltonians cannot be homotopically equivalent unless they have the same size and number of negative eigenvalues, two vector bundles cannot be isomorphic if they do not have the same rank meaning that different vector bundles over the same base space are classified by their rank. The set of isomorphism classes over the base space X is then denoted $\mathrm{vect}(M) = \bigcup_{m \in \mathbb{N}} \mathrm{vect}_m(M)$ where $\mathrm{vect}_m(M)$ is the set of isomorphism classes of vector bundles of rank $m \in \mathbb{N}$. Furthermore, an additive operation, known as the Whitney sum, can be defined and used to combine vector bundles in a similar manner to the direct sum, i.e if

ϵ, ϵ' are bundles with rank m, n respectively $\epsilon \oplus \epsilon'$ is a vector bundle of rank $n+m$.

At this point, we will quote some useful results without proof that will later aid us in the topological classification of vector bundles. Firstly, let us define the complex Grassmanian, $G_m(\mathbb{C}_n)$ and real Grassmanian, $G_m(\mathbb{R}_n)$ as

$$\begin{aligned} G_m(\mathbb{C}_n) &= U(n)/U(n-m) \times U(m) \\ G_m(\mathbb{R}_n) &= O(n)/O(n-m) \times O(m) \end{aligned} \tag{2.44}$$

which can be interpreted as the space of all p-dimensional linear subspaces of $\mathbb{K}^n$. The relevance of Grassmannians to our discussion on topological classification will become clearer in the following section. Classifying spaces for the unitary and orthogonal groups are then defined in the colimit,

$$\begin{aligned} BU(m) &= \lim_{\to n} G_m(\mathbb{C}^n) \\ BO(m) &= \lim_{\to n} G_m(\mathbb{R}^n) \end{aligned} \tag{2.45}$$

that is, the classifying spaces for the unitary and orthogonal groups are constructed as the Grassmannian of n-planes in an infinite-dimensional space, $\mathbb{C}^\infty$ and $\mathbb{R}^\infty$ respectively.

Using the above definitions we now quote without proof the classification theorem for isomorphism classes of vector bundles. Namely, there is a bijection between the set of isomorphism classes of vector bundles over M and homotopy classes of maps from M into Grassmannians,

$$[M, BU(m)] \cong \mathrm{vect}_m(M) \tag{2.46}$$

for complex vector bundles, with an analogous relation for real vector bundles.

Rather than only considering the set $\mathrm{vect}(M)$, K-theory promotes $\mathrm{vect}(M)$ to a group through the use of Grothendieck completion. For a set X, the Grothendieck group is defined as the product $M \times M/\!\sim$ where the equivalence relation in the 'divisor' is given by $(a,b) \sim (a',b') \implies \exists c \in M st.a + b' + c = a' + b + c$. Rephrased, the Grothendieck group considers the difference class $(a,b) \in X \times X$, usually represented in the group as $a - b$.

The zeroth K-group of the manifold X) is then defined as,

$$\begin{aligned} K^0(M) &= \mathcal{G}(\text{vect}(M)) \\ &= \{(\epsilon, \epsilon')|\epsilon = (E, p, M), \epsilon' = (E', p', M)\} \end{aligned} \tag{2.47}$$

i.e. the elements of $K^0(M)$ are the virtual bundles $\epsilon - \epsilon'$, where the subtraction operation is defined by the Grothendieck completion above. Note that for real vector bundles, we often say that the Grothendieck completion leads to the zeroth KO-group.

The final step towards stable equivalence of vector bundles is to define the reduced K-group of the space M, denoted as $\tilde{K}(M)$, as the group of vector bundles over M under the $\sim$ equivalence relation defined above, namely

$$\begin{aligned} &\epsilon \sim \epsilon' \quad \text{if} \\ &\epsilon + \zeta_{s_1} \cong \epsilon' + \zeta_{s_2} \end{aligned} \tag{2.48}$$

for some integers s_1, s_2, where ζ_s is a trivial vector bundle of rank s. The reduced K-group is then the group of stable equivalence classes of vector bundles. In terms of electronic spectra, these equivalence classes are the valence bundles equivalent with one another modulo a trivial bundle. This is an incredibly powerful result. Rather than only consider homotopy equivalence for Hamiltonians of the same rank and flattened spectra, stable equivalance via Grothendieck completion has allowed us to topologically classify Hamiltonians up to the addition of any number of trivial electronic bands. We will revisit this notion in section 2.2.4, where we shall discuss systems with fragile topology which become trivial under the addition of a trivial band.

Before moving back to the main text, we will give a classification for (reduced) K-theory based on that given for vector bundles above. Given the definition of $\tilde{K}^0(M)$ as the stable equivalence classes of vector bundles over M there is an isomorphism

$$\tilde{K}^0(M) \cong [M, BU] \tag{2.49}$$

where $BU = \lim_{\to m} BU(m)$ is the classifying space of the infinite unitary group. An analogous result is obtained for real vector bundles in terms of the reduced $\tilde{KO}$-group,

$$\tilde{KO}^0(M) \cong [M, BO] \tag{2.50}$$

This result will be used below when classifying the 10 Altland-Zirnbauer classes of topological matter.

Classifying spaces

In order to determine the classifying spaces for the real classes, we introduce the following sequence of groups

$$\begin{aligned}...O(16r) \supset U(8r) \supset Sp(4r) \supset Sp(2r) \times Sp(2r) \supset Sp(2r) \\ \supset U(2r) \supset O(2r) \supset O(r) \times O(r) \supset O(r)...\end{aligned} \tag{2.51}$$

where $\supset$ denotes a proper superset and we have introduced the orthogonal, unitary and symplectic lie groups defined as

$$\begin{aligned} O(r) &= \{M \in GL(r, \mathbb{R}) : MM^T = M^T M = \mathbb{1}\} \\ U(r) &= \{M \in GL(r, \mathbb{C}) : MM^\dagger = M^\dagger M = \mathbb{1}\} \\ Sp(r) &= \{M \in GL(r, \mathbb{H}) : M\bar{M} = \bar{M}M = \mathbb{1}\}, \end{aligned} \tag{2.52}$$

where $GL(n, F)$ are the $n \times n$ general linear matrices over the field F and we have defined $\bar{M} = (M^\star)^T$ and * is the conjugation operation for the quaternions, $q^\star = q_0 - q_1 i - q_2 j - q_3 k$. This should be compared to the nested sequence of algebras

$$\begin{aligned}...\mathbb{R}(16) \supset \mathbb{C}(8) \supset \mathbb{H}(4) \supset \mathbb{H}(2) \oplus \mathbb{H}(2) \supset \mathbb{H}(2) \\ \supset \mathbb{C}(2) \supset \mathbb{R}(2) \supset \mathbb{R} \oplus \mathbb{R} \supset \mathbb{R}.\end{aligned} \tag{2.53}$$

There is a slight abuse of notation in the sequence of groups - the direct product $O(n) \times O(m)$ is isomorphic to

$$\begin{pmatrix} A_n & 0 \\ 0 & A_m \end{pmatrix} \tag{2.54}$$

where $A_{n/m} A_{n/m}^T = \mathbb{1}$. Similarly, for the complex spaces we introduce the sequence of groups

$$...U(2r) \supset U(r) \times U(r) \supset U(r) \tag{2.55}$$

and compare it to

$$...\mathbb{C}(2) \supset \mathbb{C} \oplus \mathbb{C} \supset \mathbb{C}. \tag{2.56}$$

There is a one-to-one correspondence between the group/algebra pairs given above in the sense that matrices in each group are norm preserving [167, 42].

Using these results, it is then possible to establish the classifying space of generators to extend the Clifford algebra. For example, class AIII corresponds to the homomorphism taking 2 block diagonal matrices acting on $\mathbb{C}$ to a 2×2 matrix acting on $\mathbb{C}(2)$. As well, recall that Morita equivalence permits us to write this homomorphism as $\mathbb{C}(m) \oplus \mathbb{C}(m) \longrightarrow \mathbb{C}(2m)$. We should bear this in mind as we are generally dealing with $n + m$ band Hamiltonians, as discussed at the beginning of this section. As argued by Abramovici and Kalugin [2], the action of the Dirac mass matrix, β, is a norm preserving mapping of $\mathbb{C}^m \longrightarrow \mathbb{C}^m$, where m is the number of (filled) bands below the Fermi level. Similarly, classes BDI and CII correspond to the homomorphisms $\mathbb{R}(2) \oplus \mathbb{R}(2) \longrightarrow \mathbb{R}(2)$ and $\mathbb{H} \oplus \mathbb{H} \longrightarrow \mathbb{H}(2)$ and β must be a norm preserving mapping of $\mathbb{R}^m \longrightarrow \mathbb{R}^m$ and $\mathbb{H}^m \longrightarrow \mathbb{H}^m$, respectively. Therefore

$$\mathcal{V} = \begin{cases} \text{BDI:} & O(m) \\ \text{AIII:} & U(m) \\ \text{CII:} & Sp(m) \end{cases} \tag{2.57}$$

Conversely, the classes A, AI and AII all take the form $\mathbb{K}(r) \longrightarrow \mathbb{K}(r) \oplus \mathbb{K}(r)$ for the algebras $\mathbb{R}, \mathbb{C}, \mathbb{H}$ for some matrix rank r. In the case of class A, the action of β is, therefore, to split the space $\mathbb{C}^{n+m}$ into $\mathbb{C}^n \oplus \mathbb{C}^m$. Of course, there is ambiguity with regards into how this splitting should occur and, therefore, the correct form of β should be $U(n+m)/(U(n) \times U(m))$ [1]. Furthermore, there is an ambiguity in the partition of $n + m$ bands (for example, we can just as well split $n + m$ bands into $n - 1$ empty and $m + 1$ filled bands). Therefore the classifying space for each class is actually the union of every unique partition of $n + m$ bands, i.e.

$$\mathcal{V} = \begin{cases} \text{AI:} & \bigcup_m O(n+m)/(O(n) \times O(m)) \\ \text{A:} & \bigcup_m U(n+m)/(U(n) \times U(m)) \\ \text{AIII:} & \bigcup_m Sp(n+m)/(Sp(n) \times Sp(m)) \end{cases} \tag{2.58}$$

Finally, we have the classes D, DIII, C and CI where the algebra homomorphisms take one algebra to another, $\mathbb{K}(m) \longrightarrow \mathbb{K}'(m)$ and $\mathbb{K}(m) \longrightarrow \mathbb{K}'(2m)$. In the case of class D, this involves assigning a complex structure to a real vector space, i.e. $\mathbb{R}^{2m}$ into $\mathbb{C}^m$. Since the complex space is invariant under unitary transformations, the mass matrix must be of the form $O(2m)/U(m)$. Repeating this treatment for the remaining classes we have

---

[1] Recall that if $\mathcal{K}$ is a normal subgroup of $\mathcal{G}$ that is, $K = \{k : gkg^{-1} = k, g \in \mathcal{G}\}$ then $\mathcal{G}/\mathcal{K} = \{gK : K, g \in \mathcal{H}\}$ is the set of all left cosets of $\mathcal{K}$ in $\mathcal{G}$.

$$\mathcal{V} = \begin{cases} \text{D:} \quad O(2m)/U(m) \\ \text{DIII:} \quad U(2m)/Sp(m) \\ \text{C:} \quad Sp(m)/U(m) \\ \text{CI:} \quad U(m)/O(m) \end{cases} \tag{2.59}$$

Note the the factor of 2 is present in the classes D and DIII, but not in C or CII.

We surmise the discussion above in the table below, showing the classifying spaces for each AZ class with reference to the corresponding algebra homomorphisms:

class	S	P	T	$d = 0$ extension	$\mathcal{V}$
A				$\mathcal{C}_0 : \mathbb{C} \to \mathbb{C} \oplus \mathbb{C}$	$\bigcup_m U(n+m)/U(n) \times U(m)$
AIII	1			$\mathcal{C}_1 : \mathbb{C} \oplus \mathbb{C} \to \mathbb{C}(2)$	$U(m) \times U(m)/U(m) \simeq U(m)$
AI			1	$\mathcal{R}_0 : \mathbb{R}(2) \to \mathbb{R}(2) \oplus \mathbb{R}(2)$	$\bigcup_m O(n+m)/O(n) \times O(m)$
BDI	1	1	1	$\mathcal{R}_1 : \mathbb{R}(2) \oplus \mathbb{R}(2) \to \mathbb{R}(4)$	$O(m) \times O(m)/O(m) \simeq O(m)$
D		1		$\mathcal{R}_2 : \mathbb{R}(2) \to \mathbb{C}(2)$	$O(2m)/U(m)$
DIII	1	1	-1	$\mathcal{R}_3 : \mathbb{C}(2) \to \mathbb{H}(2)$	$U(2m)/Sp(m)$
AII			-1	$\mathcal{R}_4 : \mathbb{H} \to \mathbb{H} \oplus \mathbb{H}$	$\bigcup_m Sp(n+m)/Sp(n) \times Sp(m)$
CII	1	-1	-1	$\mathcal{R}_5 : \mathbb{H} \oplus \mathbb{H} \to \mathbb{H}(2)$	$Sp(m) \times Sp(m)/Sp(m) \simeq Sp(m)$
C		-1		$\mathcal{R}_6 : \mathbb{H} \to \mathbb{C}(2)$	$Sp(m)/U(m)$
CI	1	-1	1	$\mathcal{R}_7 : \mathbb{C}(2) \to \mathbb{R}(4)$	$U(m)/O(m)$

It is interesting to compare the classifying spaces to the sequence of groups discussed earlier. Indeed, starting at the appropriate point in the sequence, one can be convinced that $\mathcal{V}_i \simeq \mathcal{G}_i/\mathcal{G}_{i+1}$ where $\mathcal{G}_i$ is the appropriate Lie algebra. Remarkably, the classifying spaces, $\mathcal{V}$ correspond *exactly* to the 10 symmetric spaces considered by Cartan, as mentioned in the previous section. Given this correspondence, the classifying space is occasionally referred to as a manifold.

2.2.3 Topological Invariants in the AZ Classification

Of course, of all the Hamiltonians in a given symmetry class many will not be topologically non-trivial. For instance, as discussed in the previous chapter, Bi_2Se_3 and Sb_2Se_3 possess the same Hamiltonian but while the former possess a non-trivial $\mathbb{Z}_2$ invariant the latter is trivial. A final question remains: can we use the AZ classification to predict the topological invariants that will classify Hamiltonians in a given class? Phrased another way, given the classifying space of each AZ class how many topologically distinct ground-states are there?

Once again we will consider a flattened Hamiltonian, but this time we shall explicitly construct it as

$$Q(\boldsymbol{k}) = \mathbb{1} - 2\sum_{\alpha} |\psi_\alpha(\boldsymbol{k})\rangle \langle\psi_\alpha(\boldsymbol{k})| \tag{2.60}$$

where α runs over all filled bands. Recalling the completeness relation, $\mathbb{1} = \sum_\alpha |\psi_\alpha\rangle\langle\psi_\alpha| + \sum_\beta |\psi_\beta\rangle\langle\psi_\beta|$ where β indexes the empty bands, it is clear to see that the eigenvalues of $Q(\boldsymbol{k})$ are ± 1 and $\mathrm{Tr}(Q(\boldsymbol{k})) = n - m$ [151]. The eigenvectors themselves, however, are the same as $H(\boldsymbol{k})$ and we can, therefore, consider $Q(\boldsymbol{k})$ to be a valid implementation of the spectral flattened Hamiltonian. Given a particular AZ class, $Q(\boldsymbol{k})$ must, of course, possess the relevant symmetries. Indeed, with the previous discussion of classifying spaces in mind we can state that $Q(\boldsymbol{k}) \in \mathcal{V}_i$. Alternatively, we can reinterpret Q as a mapping from the BZ, a d-dimensional torus, to the relevant classifying space manifold, i.e.

$$Q : \mathbb{T}^d \to \mathcal{V}_i \tag{2.61}$$

The question of 'how many distinct ground-states are there?' is actually a question of how many such maps there are. Mathematically this is given by the set of *homotopy class* of maps Q such that $Q : \mathbb{T}^d \to \mathcal{V}_i$, denoted $[\mathbb{T}^d, \mathcal{V}_i]$. Note the similarity of this expression to those given in equations 2.49 and 2.50. In general, computing homotopy classes is not an easy task, however the problem is greatly simplified if we can consider a map from a d-dimensional sphere, S^d rather than the torus, $\mathbb{T}^d$. That is, we wish to consider $[S^l, \mathcal{V}_i]$ where $l \leq d$. While this may appear to be quite an alarming substitution to make (after all, every knows you can't deform an orange into a donut) Avron *et al* [11] demonstrated that, under certain conditions, it is indeed acceptable to consider a spherical BZ (there is actually a slight subtlety here that we will not address - taking the BZ as a sphere rather rather than a torus only allows us to consider strong topological phases, but does not allow us to consider the possibility of weak ones. Generally however, homotopy groups of $\mathbb{T}^d$ can be written as the direct sum of homotopy groups over S^d. For a more detailed mathematical account of this issue, the reader is referred to Kennedy and Guggenheim [86]). As such, the problem of characterising the number of distinct ground states in an AZ class can be reduced to considering the homotopy groups

$$\pi_d(\mathcal{V}_i) \tag{2.62}$$

where $\pi_d(X)$ is the homotopy group describing maps from the d-dimensional sphere S^d to X. As shown by Kitaev using K-theory [89], the homotopy groups of the real and complex spaces possess an iterative structure

$$\begin{aligned}\pi_d(\mathcal{R}_q) &= \pi_0(\mathcal{R}_{q-d}) \\ \pi_d(\mathcal{C}_q) &= \pi_0(\mathcal{C}_{q-d}),\end{aligned} \tag{2.63}$$

meaning that calculating the zeroth order homotopy group for each classifying space solves the problem in every dimension, d. Furthermore, Bott periodicity of complex and real classifying spaces (which was described algebraically in the previous section) is given for sufficiently large m as

$$\begin{aligned}\pi_d(O) &\simeq \pi_{d+8}(O) \\ \pi_d(U) &\simeq \pi_{d+2}(U)\end{aligned} \tag{2.64}$$

Therefore, characterising the topological invariants of each AZ class is a matter of calculating the homotopy group $\pi_0(\mathcal{V})$, i.e. determining how many maps there are from the 0-sphere to the manifold $\mathcal{V}$. Recalling that the 0-sphere is simply a pair of points, calculation of the zeroth homotopy group is simply a question of *path connectedness*, that is a space X is path connected, $\pi_0(X) = 0$, if for every pair of points $x, y, \in X$ there is a path between them. As an example, consider the unitary group which corresponds to class A. Since every unitary matrix can be diagonalised by another unitary matrix, i.e. $A = V\Lambda V^\dagger$ for some unitary matrices A, V, Λ where $\Lambda = \mathrm{diag}(e^{i\theta_1}, e^{i\theta_2}, \cdots, e^{i\theta_n})$, and $\det \Lambda = 1 \implies \sum_i \theta_i = 0 \mod 2\pi$. There is therefore a map $f(t) = V\mathrm{diag}(e^{it\theta_1}, e^{it\theta_2}, \cdots, e^{it\theta_n})V^\dagger$ where $f(0) = \mathbb{1}_n$ and $f(1) = \Lambda$ connecting the identity to every unitary. Therefore, $U(n)$ is path connected and $\pi_0(\mathcal{C}_1) = \{1\}$, i.e. the homotopy group contains exactly one element and is trivial. On the other hand, the manifold $\bigcup_m U(n+m)/(U(n) \times U(m))$ is not path connected. While each component of $\mathcal{C}_0$ is path connected the full space is made up of disconnected components. Therefore, there are an integer number disconnected components of the space and $\pi_0(\mathcal{C}_0) = \mathbb{Z}$. Using Bott periodicty of complex spaces, we conclude that for large enough m

$$\pi_d(U) = \begin{cases} 0 & n \text{ is even} \\ \mathbb{Z} & n \text{ is odd.} \end{cases} \tag{2.65}$$

Similarly, the path connected components of the real classifying spaces can be calculated to give the full topological classification. The table below details the topological invariants of these classifying spaces for the dimensions $0 \leq d \leq 7$, after which the sequence repeats:

class	S	P	T	d=0	1	2	3	4	4	6	7
A				$\mathbb{Z}$	0	$\mathbb{Z}$	0	$\mathbb{Z}$	0	$\mathbb{Z}$	0
AIII	1			0	$\mathbb{Z}$	0	$\mathbb{Z}$	0	$\mathbb{Z}$	0	$\mathbb{Z}$
AI			1	$\mathbb{Z}$	0	0	0	$2\mathbb{Z}$	0	$\mathbb{Z}_2$	$\mathbb{Z}_2$
BDI	1	1	1	$\mathbb{Z}_2$	$\mathbb{Z}$	0	0	0	$2\mathbb{Z}$	0	$\mathbb{Z}_2$
D		1		$\mathbb{Z}_2$	$\mathbb{Z}_2$	$\mathbb{Z}$	0	0	0	$2\mathbb{Z}$	0
DIII	1	1	-1	0	$\mathbb{Z}_2$	$\mathbb{Z}_2$	$\mathbb{Z}$	0	0	0	$2\mathbb{Z}$
AII			-1	$2\mathbb{Z}$	0	$\mathbb{Z}_2$	$\mathbb{Z}_2$	$\mathbb{Z}$	0	0	0
CII	1	-1	-1	0	$2\mathbb{Z}$	0	$\mathbb{Z}_2$	$\mathbb{Z}_2$	$\mathbb{Z}$	0	0
C		-1		0	0	$2\mathbb{Z}$	0	$\mathbb{Z}_2$	$\mathbb{Z}_2$	$\mathbb{Z}$	0
CI	1	-1	1	0	0	0	$2\mathbb{Z}$	0	$\mathbb{Z}_2$	$\mathbb{Z}_2$	$\mathbb{Z}$

$2\mathbb{Z}$ represents the set of even integers. Note the patterns present in the homotopy groups of the complex and real spaces, namely $\pi_{n+1}(C_q) \simeq \pi_n(C_{q+1 \mod 2})$ and $\pi_{n+1}(\mathcal{R}_q) \simeq \pi_n(\mathcal{R}_{q+1 \mod 8})$.

2.2.4 Beyond the Tenfold Way

The classification given above describes a concise and formulaic approach to interrogating the topological properties of matter, and provides condensed matter physicists with a crucial set of tools that may aid in the understanding of exotic phases of matter. However, soon after the theoretical prediction and experimental discovery of TIs protected by a $\mathbb{Z}_2$ invariant, it was found that 3D lattices with Hamiltonians that respected no antiunitary symmetries (that is, class A systems) could still host topologically non-trivial states [163]. Furthermore, new research has delved beyond the stable regime of K-theory to consider low rank systems that can host fragile and delicate topology predicted by homotopy theory. We end this chapter with a brief discussion on extensions to the tenfold way.

Crystalline Symmetries

As yet, we have only discussed how the local symmetries of a Hamiltonian, namely the time-reversal, particle-hole and chiral symmetries, are used to characterise the topological properties of the system in terms of the tenfold way of Altland-Zirnbauer topological classes. However, in the following chapters we will heavily rely on spatial symmetries to extend this classification. In particular, the local symmetries previously discussed will not necessarily be respected by the introduction of a magnetic exchange term, however a composite symmetry $M = gA$, where A is one of the antiunitary symmetries discussed above and g is a space group symmetry, is respected. This section will briefly discuss the theoretical foundations of extending the tenfold way with crystalline symmetries.

First, we define the action of a space group symmetry on the Bloch Hamiltonian. An element of the space group of a system G is denoted $\{p|\boldsymbol{a}\} \in G$ which acts on position as $\boldsymbol{x} \rightarrow p\boldsymbol{x} + \boldsymbol{a}$. The element p is an element of the point group $p \in P$, the class of symmetry elements on the lattice that leave the origin fixed. For each $g_p = \{p|\boldsymbol{a}_p\} \in G$, one can define a unitary operator, U_p, that acts on the Bloch Hamiltonian, giving the symmetry relation in momentum space

$$U_p(\boldsymbol{k})H(\boldsymbol{k})U_p^{\dagger}(\boldsymbol{k}) = H(p\boldsymbol{k}). \tag{2.66}$$

The unitary transformation adheres to the symmetry of the lattice such that $U_p(\boldsymbol{k}) = U_p(\boldsymbol{k}+\boldsymbol{G})$ where $\boldsymbol{G}$ is a reciprocal lattice vector. Note that for crystalline symmetries which leave a point fixed, i.e. $\boldsymbol{k}_0 = p\boldsymbol{k}_0$, the Hamiltonian commutes with the unitary symmetry $[H(\boldsymbol{k}_0), U_p(\boldsymbol{k}_0)]$, meaning that if $\boldsymbol{k}_0$ is a TRIM then it is possible to define the topological invariants at that point in the eigenspace of $U_p(\boldsymbol{k}_0)$.

Systems in which TRS is broken, but remain protected by another emergent antiunitary symmetry have already been discussed in the previous chapter, namely antiferromagnetic TIs where the combination of half a lattice translation and TRS still provides topological protection according to a $\mathbb{Z}_2$ index. In general, however, one can consider spatial symmetries from the space group of the Hamiltonian acting in unison with TRS as well. Such an extension to the topological classification based on the local antiunitary symmetries described in this chapter is similar to the notion of a topological crystalline insulators (TCI) [46].

Following the theoretical description of a 3D TI, it was soon noticed that the presence of additional spatial symmetries could greatly simplify the task of computing the $\mathbb{Z}_2$ invariant, however spatial symmetries can also modify and extend the topological classification of materials beyond the tenfold way. Weak topological insulators rely on the presence of a translational symmetry on the lattice, however additional point group symmetries can lead to the existence topologically protected phases in cases where antiunitary symmetries alone may not prove sufficient. Such phases of matter are generically known as TCIs. As an example, consider a tetragonal lattice with fourfold rotational symmetry around the z-axis C_{4z} and a spinless TRS, T where $T^2 = 1$. Consulting the AZ-classification table, one finds this system is in class AI which hosts only topologically trivial phases in 2D and 3D. However, solving for the electronic dispersion of the system in a slab geometry (i.e. a translationally invariant 2D system) demonstrates the existence of a doubly degenerate quadratic band crossing forming surface states on the (001)-surface. Indeed, by considering the composite symmetry $U_{C_{4z}}T$

and noticing that $(U_{C_{4z}}T)^2 = -1$ one can demonstrate that these doublet bands admit a $\mathbb{Z}_2$ classification.

A more concrete demonstration of the role of space group symmetries in the physics of topological states can be found from a slight adjustment to the definition of the sewing matrix, introduced by Fu and Kane [47] and discussed in the previous chapter. Recall the definition of the sewing matrix in equation 1.74 as

$$w_{mn}(\boldsymbol{k}) = \langle u_m(-\boldsymbol{k})| T |u_n(\boldsymbol{k})\rangle . \tag{2.67}$$

which is calculated over the set of occupied bands. It is specifically the elements of the sewing matrix at the TRIM, Γ_i, that are the objects of importance in the context of calculating the $\mathbb{Z}_2$ invariants. In particular, the strong topological invariant ν_0 is given by

$$\begin{aligned} (-1)^{\nu_0} &= \prod_i \delta_i \quad \text{where} \\ \delta_i &= \frac{\sqrt{\det\{w_(\Gamma_i)\}}}{\mathrm{Pf}(w(\Gamma_i))}. \end{aligned} \tag{2.68}$$

However, the set of points Γ_i are fixed by the space group of the lattice, motivating us to determine how the space group transforms under a space group symmetry, U_p:

$$\begin{aligned} w_{mn}(\boldsymbol{k}) &= \langle u_m(-\boldsymbol{k})|Tu_n(\boldsymbol{k})\rangle \\ &= \langle u_m(-p\boldsymbol{k}| U_p^\dagger T U_p |u_n(p\boldsymbol{k})\rangle \\ &= w_{mn}(p\boldsymbol{k}), \end{aligned} \tag{2.69}$$

implying that where high symmetry points are related to one another by the lattice point group, the values of δ at these points must be equal. A concrete example provided by Slager [163] considers a square lattice with TRIM given at the points $\Gamma = (0,0), X = (\pi,0), Y = (0,\pi), M = (\pi,\pi)$. From the definition of the $\mathbb{Z}_2$ topological invariant given above, it is clear that a non-trivial phase can only exist when an odd number of δ_i are negative. Therefore, the tuple $(\delta_\Gamma, \delta_X, \delta_Y, \delta_M) = (1,-1,-1,1)$ should result in a trivial phase, according to the tenfold way. However, the presence of the C_4 symmetry in the square lattice leads to a non-trivial topological phase protected by crystal symmetry. In particular, because the X and Y points are related by C_4 symmetry (i.e. they are symmetry equivalent TRIM), the band inversions at these points are pinned in the topological phase, resulting in a TCI. It is clear from this example that it is not simply the product of the values of δ_i at the TRIM that control the topological properties of the phase, as those TRIM related by a spatial symmetry must necessarily have the sign of δ_i equal. It is therefore sufficient to consider a subset of inequivalent TRIM in the BZ that are *not* related by any spatial symmetry. Alternatively, one considers the set of TRIM that are equivalent in the sense that they are related by spatial symmetry. The values of δ for all TRIM within each set are, therefore, equal. Labelling each set of TRIM $a, b, c, \cdots$, distinct topological phases are produced by setting one of $\delta_a = -1$ (the signs can be reversed, leaving the resulting phase unaffected). This procedure is general enough to be abstracted to the topological classification of materials with any space group symmetry [163].

Using the above ideas, one is then in a position to build out an equivariant K-theory that incorporates spatial symmetries, as presented by Kruthoff *et. al.* [96]. First, one considers the high symmetry points in the band structure. At these points, the Bloch Hamiltonian commutes with elements of the little co-group $\tilde{G}_{\boldsymbol{k}} = G_{\boldsymbol{k}}/T$, where $G_{\boldsymbol{k}}$ is the little group consists of the set of space group symmetries that leave $\boldsymbol{k}$ invariant up to a reciprocal lattice vector and $T \subset G$ is the subgroup of lattice translations (the little co-group is therefore the point group of the little group). As mentioned above, eigenfunctions of $H(\boldsymbol{k})$ at these points are also eigenfunctions of the little co-group. Consequently, the valence band states at $\boldsymbol{k}$ form a representation of $\tilde{G}_{\boldsymbol{k}}$. Furthermore, one can consider how these representations along high symmetry lines connect to one another. Specifically considering the case of class A systems, the representations of these bands must connect continuously at their endpoints. Rephrased, given a symmetry operation and a Bloch state, the eigenvalue of this operation cannot suddenly change at the endpoint of a high symmetry line in the BZ. Using this simple observation, a straightforward combinatorial algorithm can be developed that amounts to connecting representations at high symmetry points in the BZ according to a set of gluing conditions. Such a procedure, although built from little more than elementary band representation theory, completely classifies the topological phases in class A where additional crystalline symmetries are considered for one and two dimensions, and agrees with the formal K-theoretic results. In the following chapter we will revisit the topic of extensions to the tenfold way utilising crystalline symmetries.

Small dimensional exceptions

To conclude this chapter, we will briefly discuss the situation where we do not consider the limit of very large Hamiltonians. We only briefly mentioned in a previous section that considering Hamiltonians with a small number of bands was not particularly useful for a stable classification, but we will flesh out these issues in more detail here.

Examining the table of topological invariants given in (2.2.3), we find that class A has no topologically non-trivial phase in three-dimensions, i.e. there is no QAHE phase in 3D. However, consider a two band Hamiltonian with one band filled in class A of the AZ classification. The classifying space of this system is given by the Grassmannian $G_1(\mathbb{C}^2) = U(2)/U(1)\times U(1)$ which is homotopy equivalent to the 2-sphere. The Hamiltonian of the system is then given by

$$H(\boldsymbol{k}) = \boldsymbol{n}(\boldsymbol{k}) \cdot \boldsymbol{\sigma} \tag{2.70}$$

Therefore, we can consider H to be a map from the 3-torus to the 2-sphere, that is the 3D-BZ to the surface of a sphere embedded in $\mathbb{R}^3$. Following the discussion of the previous section, we wish to determine the number of topologically distinct ground states that exist by calculating the homotopy group of such a map, $[\mathbb{T}^3, S^2]$. As before, we will restrict our discussion to strong invariants and take the torus as a sphere. This gives us a somewhat surprising result that we do indeed have the possibility of a topologically non-trivial phase:

$$\pi_3(S^2) = \mathbb{Z} \tag{2.71}$$

This is the well known *Hopf fibration* describing a non-trivial mapping of the 3-sphere to the 2-sphere $f : S^3 \longrightarrow S^2$. Referring to our above discussion on bundles, we identify the triplet (S^3, S^2, f) as a fibre bundle with $f^{-1}(\{x\}) = S^1 \quad \forall x \in S^2$ as the fibres. The Hopf index, which is the topological index characterising the system, therefore takes on integer values and is calculated as

$$\chi(n) = -\int_{BZ} \boldsymbol{\Omega} \cdot \boldsymbol{A} \mathrm{d}\boldsymbol{k} \tag{2.72}$$

where $\boldsymbol{\Omega} = \nabla \times \boldsymbol{A}$ is the Berry curvature and $\boldsymbol{A}$ is the Berry connection [32, 98]. The presence of a non-zero Hopf index guarantees the presence of topologically protected gapless surface states at the interface between the Hopf model and a normal insulator/vacuum. This phase, therefore, exists outside the tenfold classification of topological phases, but the restriction on the number of bands needs to be fixed means that this is known as a *delicate* topological phase. Indeed, augmenting the Hopf insulator by a single trivial band destroys the topology. K-theory and the notion of stable equivalence are, therefore, a more robust method of classifying topological spaces. It is experimentally challenging to realise a Hopf insulator because of the necessity of only two bands in a three dimensional model, ruling out many material systems. Nevertheless, it has been recently proposed that a Hopf insulator could be realised on a lattice of dipolar spins [154] and that Floquet engineering on an optical lattice can be utilised to supply the necessary third periodic dimension to a two-band model in two dimensions to realise this phase [214].

More generally, however, restricting to finite/small rank leads us away from K-theory and stable equivalence and towards homotopy classification. This, along with the consideration of multiple band gaps within the electronic band structures, has led to a new field of interest known as multi-gap topology where nodal points between bands can possess *non-Abelian* topological invariants, also referred to as homotopy charges in this context [23, 20, 22]. Such homotopy charges have observable effects in the form of non-Abelian braiding of phonons [137, 138], temperature driven topological phase transitions [30] and the manipulation of topological band nodes in metamaterials [73, 74]. In addition the out-of-equilibrium drynamics of such systems have proved to be a fruitful topic of study [213, 208, 161].

Chapter 3

Flat-bands in Antiferromagnetic Topological Insulators

3.1 Chapter Summary

This chapter introduces extensions to the tenfold-way of topological classification discussed in the previous chapter by considering magnetic textures and the presence of reflection symmetries. In particular, by considering the magnetic space group and composite magnetic symmetries we investigate extensions to class A and AIII materials in magnetic topological insulators. In particular, when considering an in-plane magnetisation one can engineer a set of dispersionless edge states at $E = 0$ protected by the underlying chiral symmetry of the lattice. Lattice simulations are performed on a toy model before considering more realistic materials by adopting parameters for the BSTS family of TIs.

3.2 Introduction

In section 1.3, intrinsically magnetic TIs were highlighted as a means to introduce long range magnetic order across the Dirac electrons in a TI, with the QAHE discussed as a potential application of these AFMTIs. In this chapter we will examine other spin configurations, with a particular focus on in-plane alignment, and demonstrate that both ferromagnetic and antiferromagnetic coupling of spins between layers can lead to interesting layer-dependent effects. As previously discussed, when only considering the surface Hamiltonian, such a configuration simply results in a shift of the Dirac cones in k-space by an amount proportional to the magnetisation, i.e.

$$\begin{aligned} H &= \hbar v_F(k_y\sigma_x - k_x\sigma_y) + \boldsymbol{M}_{\parallel}\cdot\boldsymbol{\sigma} \\ &= \hbar v_F\left((k_y + M_x)\sigma_x - (k_x - M_y)\sigma_y\right) \\ &= \hbar v_F(k'_y\sigma_x - k'_x\sigma_y) \end{aligned} \tag{3.1}$$

However, as we shall demonstrate in this chapter, when considering a multilayer heterostructure we can engineer non-trivial effects on the band structure with an in-plane magnetisation. In particular, we observe dispersionless regions in the electronic band structure with the states forming these flat-bands strongly localised along the edges of our material geometry, i.e. quasiparticles of infinite effective mass. We will show that, depending on the type of coupling between layers, the electronic dispersion relations in even and odd layer samples with in-plane magnetisation can be topologically distinct from one another, comparable to the case of the QAHE/Axion Insulator states in odd/even layer samples with out-of-plane magnetisation.

The vanishing kinetic energy in flat-bands makes them of particular interest in condensed matter physics, due to the possibility of enhanced electron-electron interactions leading to correlated many body physics. Topological flat-bands have recently been observed in twisted bilayer graphene [110], prompting a great deal of interest. Other material set-ups have been proposed as a means to generate flat-bands [169, 199], but the recent discovery of intrinsic magnetic topological insulators provides a new means of engineering them. In particular, we will take inspiration from the $\mathrm{MnBi_2Te_4}$ family of intrinsic magnetic TIs and examine the effect of ferromagnetic and antiferromagnetic coupling of magnetic moments between layers on the formation of flat-bands. As discussed in section 1.3.2, recent research has focused heavily on the compound MnBi2Te4, which orders along the z axis (that is, along the growth axis), and is viewed as the most promising candidate for observation of a high-temperature QAHE, however there is a wider family of AFMTIs supporting different spin configurations. For instance, $\mathrm{VBi_2Te_4}$ and $\mathrm{EuBi_2Te_4}$, see Figure 3.1, possess an easy in-plane magnetisation axis and could provide a promising route to engineer the flat-bands discussed in this chapter.

In order to model multilayer magnetic topological insulators akin to the $\mathrm{MnBi_2Te_4}$ family of AFMTIs discussed in 1.3, we adopt the model for $\mathrm{Bi_2Se_3}$ proposed by Liu *et. al.* [112], namely

$$H(\boldsymbol{k}) = C(\boldsymbol{k}) + M(\boldsymbol{k})\tau_z + v(k_x\sigma_x + k_y\sigma_y)\tau_x + v_z k_z\sigma_z\tau_x + w(k_x^3 - 3k_xk_y^2)\tau_y, \tag{3.2}$$

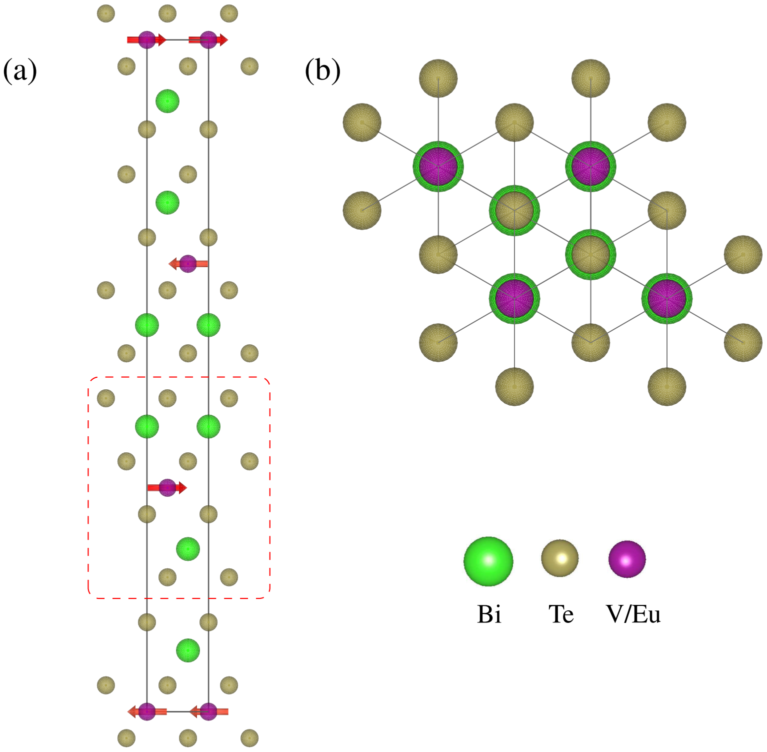

Fig. 3.1 Crystal structure of VBi_2Te_4/$EuBi_2Te_4$ along the (a) a-axis and (b) c-axis. The crystal structure is rhombohedral with the space group $R\bar{3}m$. The crystal is a layered structure formed of septuple layers (red box) separated by a van der Waals gap. The paramagnetic unit cell (black box) is shown in (a), however it should be noted that the A-type antiferromagnetism of this material leads to a magnetic unit cell twice the length of that shown. Figure produced with VESTA [120].

$C(\boldsymbol{k}) = C_0 + C_1 k_z^2 + C_2(k_x^2 + k_y^2)$ and $M(\boldsymbol{k}) = M_0 + M_1 k_z^2 + M_2(k_x^2 + k_y^2)$ and we have set $\hbar = 1$. Unless otherwise stated, we will set $C(\boldsymbol{k}) = 0$. The material dependent parameters $A, B, \ldots$ can be calculated *ab. initio* using $\mathbf{k} \cdot \mathbf{p}$ theory. A topological phase emerges from this model when $M_0 M_1 < 0$. As the parameter M_0 physically corresponds to the energy gap between the bulk conduction and valence bands, topologically protected edge modes will occur when $M_0 < 0$ if $M_1 > 0$. We will eventually discretise this model on a hexagonal lattice to perform electronic structure calculations, however we will first examine the symmetries of this system in a slab geometry by discretising along the z axis. The Hamiltonian of such a system is given by

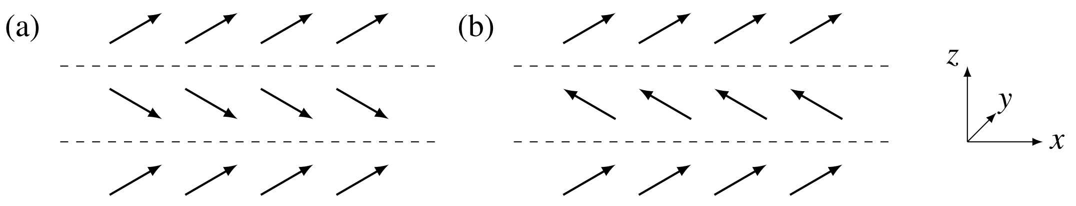

Fig. 3.2 The canted magnetisation configurations considered in this paper. Such configurations can be achieved by applying an external magnetic field perpendicular to the easy magnetic axis of an antiferromagnetic topological insulator.

$$H = \begin{pmatrix} H_1 & T_z & 0 & \cdots & 0 \\ T_z^\dagger & H_2 & T_z & \cdots & 0 \\ \vdots & & \ddots & & \vdots \\ 0 & & \cdots & T_z^\dagger & H_n \end{pmatrix} \tag{3.3}$$

where the onsite Hamiltonian and exchange terms are

$$\begin{gathered} H_j = H_0 + H_{\text{exc}} \quad \text{where} \\ H_0 = C(\boldsymbol{k}) + \tilde{M}(\boldsymbol{k})\tau_z + v(k_x\sigma_x + k_y\sigma_y)\tau_x + w(k_x^3 - 3k_xk_y^2)\tau_y \\ H_{\text{exc}} = \boldsymbol{M}_j \cdot \boldsymbol{\sigma}, \end{gathered} \tag{3.4}$$

and the interlayer hopping term is given by

$$T_z = -M_1\tau_z - \frac{iB}{2}\sigma_z\tau_x, \tag{3.5}$$

where $0 < j < n$ is the layer index, $\boldsymbol{M}_j$ is the exchange term within the j^{th} layer and $\tilde{M}(\boldsymbol{k}) = M_0 + 2M_1 + M_2(k_x^2 + k_y^2)$.

We will consider two different types of magnetisation configurations in this chapter - one where the z-component of the magnetisation is antiferromagnetically coupled between layers and there is an in-plane (IP) canting, see Figure 3.2(a), given by the magnetisation vector

$$\boldsymbol{M}_{\parallel}(\boldsymbol{r}) = M_0(\sin(\theta)\cos(\phi), \sin(\theta)\sin(\phi), (-1)^z\cos(\theta)) \tag{3.6}$$

and another where the in-plane component of the magnetisation is antiferromagnetically coupled between layers and there is an out-of-plane (OOP) canting, see Figure 3.2(b), given by the vector

$$\boldsymbol{M}_{\perp}(\boldsymbol{r}) = M_0((-1)^z\sin(\theta)\cos(\phi), (-1)^z\sin(\theta)\sin(\phi), \cos(\theta)) \tag{3.7}$$

As we shall see in subsequent sections, the antiferromagnetic coupling between magnetic moments in adjacent layers will result in even and odd layer systems exhibiting distinct behaviours.

3.3 Symmetry Classification

3.3.1 Topological Symmetries

We begin by classifying odd and even layer Hamiltonians with various magnetisation configurations, according to the ten Altland-Zirnbauer (AZ) symmetry classes, by considering the action of three non-spatial symmetry operations on the Bloch Hamiltonian as described in Chapter 2

$$\begin{aligned} SH(\boldsymbol{k})S^{-1} &= -H(\boldsymbol{k}), \\ TH(\boldsymbol{k})T^{-1} &= H(-\boldsymbol{k}), \\ PH(\boldsymbol{k})P^{-1} &= -H(-\boldsymbol{k}). \end{aligned} \tag{3.8}$$

where P and T are the particle-hole and time-reversal symmetry operators, respectively. Before accounting for the effect of the exchange term we note a relevant symmetry in the onsite and interlayer hopping terms, given in 3.4 and 3.5,

$$\sigma_z\tau_x H_0 \sigma_z\tau_x = -H_0, \quad \sigma_z\tau_x T_z \sigma_z\tau_x = -T_z^\dagger \tag{3.9}$$

implying the existence of a chiral symmetry given by

$$S = \begin{pmatrix} 0 & 0 & \cdots & 0 & \sigma_z\tau_x \\ 0 & 0 & \cdots & \sigma_z\tau_x & 0 \\ \vdots & & \ddots & & \vdots \\ \sigma_z\tau_x & 0 & \cdots & 0 & 0 \end{pmatrix}. \tag{3.10}$$

Examining the effect of the chiral symmetry operator $\mathcal{S}$ on our exchange term,

$$\sigma_z\tau_x H_{exc} \sigma_z\tau_x = -\boldsymbol{M}_{\parallel}\cdot\boldsymbol{\sigma} + M_z\sigma_z, \tag{3.11}$$

it is clear that odd-layer systems will possess chiral symmetry when $M_z = 0$, regardless of the canting direction. By contrast, even-layer systems will only possess a chiral symmetry for the IP canted configuration.

Turning our attention to the time-reversal (TR) and particle-hole (PH) symmetries, we note that the onsite and interlayer terms obey the relations

$$\begin{aligned} \sigma_y H_0^T(\boldsymbol{k})\sigma_y &= H_0(-\boldsymbol{k}), \quad & \sigma_y T_z \sigma_y &= T_z^\dagger \\ \sigma_x \tau_x H_0^T(\boldsymbol{k}) &= -H_0(-\boldsymbol{k}), \quad & \tau_x \sigma_x T_z \tau_x \sigma_x &= -T_z \end{aligned} \tag{3.12}$$

providing us with the relevant transformations

$$\begin{aligned} T = U_T K \quad \text{where} \quad U_T &= \begin{pmatrix} i\sigma_y & 0 & \cdots & 0 & 0 \\ 0 & i\sigma_y & \cdots & 0 & 0 \\ \vdots & & \ddots & & \vdots \\ 0 & 0 & \cdots & 0 & i\sigma_y \end{pmatrix}, \\ P = U_P K \quad \text{where} \quad U_P &= \begin{pmatrix} 0 & 0 & \cdots & 0 & \sigma_x\tau_x \\ 0 & 0 & \cdots & \sigma_x\tau_x & 0 \\ \vdots & & \ddots & & \vdots \\ \sigma_x\tau_x & 0 & \cdots & 0 & 0 \end{pmatrix}. \end{aligned} \tag{3.13}$$

However, examining the effect of these symmetries on the exchange term

$$\begin{aligned} \sigma_y H_{exc}^T \sigma_y &= -\, M_x\sigma_x - M_y\sigma_y - M_z\sigma_z \\ \sigma_x\tau_x H_{exc}^T \tau_x\sigma_x &= M_x\sigma_x + M_y\sigma_y - M_z\sigma_z \end{aligned} \tag{3.14}$$

we observe that TR symmetry is broken for any magnetisation configuration, while PH symmetry is only respected in the case of even layer samples with OOP canting. Since this is the only symmetry present in even layer systems with in-plane canting and $\mathcal{P}^2 = U_P U_P^* = 1$, we therefore conclude that even layer samples with OOP canting are in class D, which can be topologically non-trivial in zero, one and two dimensions.

It is tempting to conclude that the remaining magnetisation configurations all belong to class A. In this case, the only topologically non-trivial behaviour would be due to some non-zero component of the magnetisation in the z direction, i.e. the QAHE or Axion insulator state (depending on the canting direction). However, at this point we will introduce the notion of 1D *TRS-like* and *PHS-like* operators, namely

$$
\begin{aligned}
T_{k_i} H(\boldsymbol{k}) T_{k_i}^{-1} &= H(k_1, k_2, ..., -k_i, ...k_n) \\
P_{k_i} H(\boldsymbol{k}) P_{k_i}^{-1} &= - H(k_1, k_2, ..., -k_i, ...k_n).
\end{aligned}
\tag{3.15}
$$

These transformations are possible through the combination of the TRS and PHS transformations given in 3.13 and additional spatial symmetries.

3.3.2 Spatial Symmetries

We will now begin identifying the spatial symmetries that will enable us to construct the TRS-like and PHS-like symmetries that will enable us to classify even and odd layer systems with various magnetisation configurations. Once again, we note the relevant symmetries in the onsite and interlayer terms

$$
\begin{aligned}
\tau_z H_0(\boldsymbol{k}) \tau_z &= H_0(-\boldsymbol{k}), \quad \tau_z T_z \tau_z = T_z^\dagger, \\
\sigma_x \tau_z H_0(\boldsymbol{k}) \tau_z \sigma_x &= H_0(-k_x, k_y), \quad \sigma_x \tau_z T_z \tau_z \sigma_x = T_z, \\
\sigma_x H_0(\boldsymbol{k}) \sigma_x &= H_0(k_x, -k_y), \quad \sigma_x T_z \sigma_x = T_z^\dagger.
\end{aligned}
\tag{3.16}
$$

The first of these implies the presence of an inversion symmetry

$$
I H(\boldsymbol{k}) I^{-1} = H(-\boldsymbol{k})
$$

$$
I = \begin{pmatrix} 0 & 0 & \cdots & 0 & \tau_z \\ 0 & 0 & \cdots & \tau_z & 0 \\ \vdots & & \ddots & & \vdots \\ \tau_z & 0 & \cdots & 0 & 0 \end{pmatrix}.
\tag{3.17}
$$

We note that this operator does not act on the spin degree of freedom and, therefore, inversion symmetry is respected in all odd layer systems and in even layer systems with in-plane canting when $\boldsymbol{M} = (M_x, M_y, 0)$ and out-of-plane canting when $\boldsymbol{M} = (0, 0, M_z)$ (these configurations essentially correspond to ferromagnetic coupling between spins in adjacent layers when the spins are orientated in and out-of the plane, respectively). The other two symmetries given in 3.16 are mirror/reflection symmetries. In the first instance

$$R_x H(\boldsymbol{k}) R_x^{-1} = H(-k_x, k_y)$$

$$R_x = \begin{pmatrix} i\sigma_x\tau_z & 0 & \cdots & 0 & 0 \\ 0 & i\sigma_x\tau_z & \cdots & 0 & 0 \\ \vdots & & \ddots & & \vdots \\ 0 & 0 & \cdots & 0 & i\sigma_x\tau_z \end{pmatrix}, \tag{3.18}$$

demonstrates the presence of a mirror symmetry about the x axis. Examining its effect on the exchange term

$$\sigma_x\tau_z H_{exc}\tau_z\sigma_x = M_x\sigma_x - M_y\sigma_y - M_z\sigma_z \tag{3.19}$$

we observe that mirror symmetry about the x axis is only respected in systems where $\boldsymbol{M} = (M_x, 0, 0)$. The final spatial symmetry is a mirror symmetry about the y axis given by

$$R_y H(\boldsymbol{k}) R_y^{-1} = H(k_x, -k_y)$$

$$R_y = \begin{pmatrix} 0 & 0 & \cdots & 0 & i\sigma_x \\ 0 & 0 & \cdots & i\sigma_x & 0 \\ \vdots & & \ddots & & \vdots \\ i\sigma_x & 0 & \cdots & 0 & 0 \end{pmatrix}. \tag{3.20}$$

Observing that R_y acts identically to R_x on the exchange term, we conclude that mirror symmetry about the y axis is respected in odd layer systems with $\boldsymbol{M} = (M_x, 0, 0)$ and in even layer systems with in-plane canting when $\boldsymbol{M} = (M_x, 0, M_z)$ and out-of-plane canting when $\boldsymbol{M} = (0, M_y, 0)$.

Finally, we observe that $R_x^2 = R_y^2 = -1$ due to the additional factor of i - it is required that $R_i^2 = -1$ in spin-$\frac{1}{2}$ systems due to fermionic statistics.

3.3.3 Extending the Topological Classification

The previous chapter briefly touched on how space group (SG) symmetries can be used to characterise topological materials beyond the tenfold way. The methodology proposed centred around the gluing conditions that arise at high-symmetry points in the band structure when considering band representations. In this chapter, we will build on the foundations laid out by that discussion and discuss how the introduction of magnetic terms in the Hamiltonian naturally leads us to consider the *magnetic space group* (MSG).

Magnetic terms in the Hamiltonian naturally break TRS and, as shown in the previous section, some spatial symmetries depending on the exact magnetic configuration. However, composite symmetries $m = Tg_p$ where $g_p = \{p|\boldsymbol{a}_p\} \in G$ is an element of the crystallographic SG, G, and T the time-reversal operation, may still be respected even where the individual symmetry terms comprising it are broken. For example, the $\mathrm{Mn_2Bi_2Te_4}$ discussed in the introductory chapter breaks TRS due to the presence of an antiferromagnetic ground state, yet respects the combined symmetry $S = t_{1/2,z}T$, where $t_{1/2,z}$ is half a unit cell translation along the z-axis, such that $SH_{MBT}(\boldsymbol{k})S^{-1} = H_{MBT}(-\boldsymbol{k})$. In general, for each composite symmetry $m = Tg_p$ one can define a TRS-like operator T_m that acts on the Hamiltonian and satisfies the relation

$$\begin{aligned} &T_m H(\boldsymbol{k}) T_m^{\dagger} = H(m\boldsymbol{k}) \quad \text{where} \\ &m\boldsymbol{k} = -p\boldsymbol{k}. \end{aligned} \tag{3.21}$$

Indeed, considering these composite symmetry elements allows us to compute the 1651 MSGs directly from the original 230 crystallographic SGss. For each of the 230 SGs there are potentially four types of MSGs that can be constructed. Type I contains 230 MSGs where $G_M = G$, i.e. no antiunitary symmetry is considered and the MSG is identical to the SG. Type II groups have the form $G_M = G + TG$, i.e. all the symmetry operations in G plus a time-reversed copy of it. The final two groups are of the form $G_M = H + mH$ where H is a subgroup of G with index 2 (i.e. the number of right cosets of H in G). If $m = Tg$ where g is a non-trivial point group operation (i.e. translationally equivariant) this is referred to as type III, and if $m = Tt_{1/2}$ where $t_{1/2}$ is a fractional lattice translation then it is referred to as type IV. From the definitions given above, type II materials respect TRS and describe non-magnetic materials. Recent work has focused on extending the topological classification presented in the previous chapter to the 1421 MSGs in type-I, -III and -IV materials, that is *magnetic topological crystalline insulators*. Topological classification of magnetic materials is an active area of research [21, 38, 137]. The aim of this subfield is to extend the original topological classification of materials via the tenfold way and generalize the underlying K-theory underpinning the results. Such characterization methods include the Wilson loop spectrum [4], where the Wilson loop operator is defined as,

$$\mathcal{W} = \mathcal{P} \exp\left\{ i \oint \mathrm{d}\boldsymbol{k} \cdot \mathcal{A} \right\} \tag{3.22}$$

where $\mathcal{A}_{mn} = \langle u_m | \nabla_{\boldsymbol{k}} | u_n \rangle$ is the non-Abelian Berry connection between the Bloch bands indexed by m and n). The eigenvalues of this operator are given as $\lambda_\alpha = e^i \gamma_a$ where the γ_α are real valued numbers that can be used to define the Wilson spectrum, known as Wilson phases. The winding of this spectrum can then be used to infer topologically non-trivial behaviour. For example, on a square lattice if we define the k_y directed Wilson loop to be

$$\mathcal{W}(k_x) = \mathcal{P} \exp\left\{ i \int_{-pi}^{pi} \mathrm{d}k_y \cdot \mathcal{A}(k_x, k_y) \right\} \tag{3.23}$$

then if the Wilson loop phases $\gamma(k_x$ wind non-trivially as k_x is varied from $-pi$ to π, then we can conclude there is a non-trivial topology. In this context, non-trivial winding is indicated by the number of times the phases wrap around $[-\pi, pi)$ as k_x traverses the BZ. The Wilson loop will be used later in this chapter to indicate the non-trivial topology of the flat-band systems studied.

In this work, we will investigate the extension of class A and class AIII materials (i.e. those where the introduction of an exchange term break TRS and PHS) using magnetic configurations that respect order-2 symmetries, namely reflection. The benefit of this approach is that we can map directly to the tenfold way and use the results presented in the previous chapter [122, 31, 158]. However, we should note that Liu Hamiltonian is derived from the assumption of a rhombohedral crystal with space group $R\bar{3}m$, see Figure 3.1 for the lattice structure. As such, one could consider magnetic extensions that utilise other SG symmetry elements such as threefold rotation around the $\hat{z}$-axis, $C_{3,z}$, twofold symmetry around the $\hat{x}$-axis, $R_{3,x}$, or inversion symmetry P. In addition, only a single Dirac cone at the Γ-point in the BZ is considered. For band crossings at higher momenta, defects and perturbations, such as dislocations, would play a more important role in the electronic properties of the system as outlined in [163, 160].

Now that we have identified the spatial symmetries present in the various magnetisation configurations, we define the TRS-like transformations as

$$\begin{aligned} T_{k_x} &= R_y T \\ T_{k_y} &= R_x T \end{aligned} \tag{3.24}$$

and similarly for the PHS-like transformations. Explicitly, these are given by the matrices

$$\begin{aligned} T_{k_x} &= U_T K \quad \text{where} \quad U_T = \begin{pmatrix} 0 & 0 & \cdots & 0 & i\sigma_z \\ 0 & 0 & \cdots & i\sigma_z & 0 \\ \vdots & & \ddots & & \vdots \\ i\sigma_z & 0 & \cdots & 0 & 0 \end{pmatrix} \quad \text{and} \quad T_{k_x}^2 = 1, \\ P_{k_x} &= U_P K \quad \text{where} \quad U_P = \begin{pmatrix} \tau_x & 0 & \cdots & 0 & 0 \\ 0 & \tau_x & \cdots & 0 & 0 \\ \vdots & & \ddots & & \vdots \\ 0 & 0 & \cdots & 0 & \tau_x \end{pmatrix} \quad \text{and} \quad P_{k_x}^2 = 1, \end{aligned} \tag{3.25}$$

for k_x, while the analogous set acting on k_y

$$\begin{aligned} T_{k_y} &= U_T K \quad \text{where} \quad U_T = \begin{pmatrix} i\sigma_z\tau_z & 0 & \cdots & 0 & 0 \\ 0 & i\sigma_z\tau_z & \cdots & 0 & 0 \\ \vdots & & \ddots & & \vdots \\ 0 & 0 & \cdots & 0 & i\sigma_z\tau_z \end{pmatrix} \quad \text{and} \quad T_{k_y}^2 = 1, \\ P_{k_y} &= U_P K \quad \text{where} \quad U_P = \begin{pmatrix} 0 & 0 & \cdots & 0 & \tau_y \\ 0 & 0 & \cdots & \tau_y & 0 \\ \vdots & & \ddots & & \vdots \\ \tau_y & 0 & \cdots & 0 & 0 \end{pmatrix} \quad \text{and} \quad P_{k_y}^2 = -1. \end{aligned} \tag{3.26}$$

Considering the k_x operators first, we will extend our previous discussion regarding the effect of the spatial symmetry operators on the exchange term and examine the effect of the TRS-like and PHS-like operations. The relevant equations are

$$\begin{aligned} \sigma_z H_{exc}^T \sigma_z &= -M_x\sigma_x + M_y\sigma_y + M_z\sigma_z \quad \text{and} \\ \tau_x H_{exc}^T \tau_x &= M_x\sigma_x - M_y\sigma_y + M_z\sigma_z. \end{aligned} \tag{3.27}$$

TRS-like symmetry is respected in even-layer systems with out-of-plane canting where $\boldsymbol{M} = (M_x, 0, M_z)$ and in-plane canting where $\boldsymbol{M} = (0, M_y, 0)$, and odd-layer systems where $\boldsymbol{M} = (0, M_y, M_z)$. By contrast, in all systems PHS-like symmetry is only respected when $\boldsymbol{M} = (0, M_y, 0)$.

	Configuration			
	In-plane		Out-of-plane	
$\boldsymbol{M} = (M_x, M_y, M_z)$	Even	Odd	Even	Odd
(M_x, M_y, M_z)	A	A	D	A
$(0, 0, M_z)$	AIII	A	A	A
$(M_x, M_y, 0)$	AIII	AIII	A	AIII
$(M_x, 0, 0)$	AIII	AIII	AI/C	AIII
$(0, M_y, 0)$	BDI/CI	BDI/CI	A	BDI/CI

Table 3.1 Topological classification of even and odd layer system under various magnetisation configurations.

Now we consider the k_y symmetry operators, namely

$$\begin{aligned} \sigma_z \tau_z H_{exc}^T \sigma_z \tau_z &= -M_x \sigma_x + M_y \sigma_y + M_z \sigma_z \quad \text{and} \\ \tau_y H_{exc}^T \tau_y &= M_x \sigma_x - M_y \sigma_y + M_z \sigma_z. \end{aligned} \tag{3.28}$$

In this case, TRS-like symmetry is satisfied in all systems where $\boldsymbol{M} = (0, M_y, M_z)$. On the other hand, PHS-like symmetry is satisfied in even layer systems with out-of-plane canting where $\boldsymbol{M} = (M_x, 0, 0)$ and in-plane canting where $\boldsymbol{M} = (0, M_y, M_z)$, and in odd layer systems where $\boldsymbol{M} = (0, M_y, 0)$.

The above arguments are summarised in 3.1 where the topological classification of even and odd layer systems with various magnetisation configurations are detailed.

Note that the final row contains entries of the form BDI/CI due to the choice of the 1D anti-unitary operators acting on k_x/k_y, respectively. For example, in the case of even layer systems with in-plane canting and $\boldsymbol{M} = (0, M_y, 0)$ with translational invariance along the y direction (i.e. k_y is a good quantum number), it may be more appropriate to interpret its classification as BDI than CI, since the TRS-like and PHS-like symmetry operators act on k_x while k_y may be interpreted as a parameter of the Hamiltonian, i.e. $H(\boldsymbol{k}) = H_{k_y}(k_x)$. That said, since classes C and CI are topologically trivial in the dimensions relevant to our current system (dots and wires) we will not discuss them any further.

3.4 Lattice Simulations

3.4.1 Hexagonal tight-binding model

In order to perform electronic structure calculations incorporating the hexagonal warping term $k_x^3 - 3k_xk_y^2$ on a hexagonal lattice, we will rewrite the Hamiltonian 3.3 described in the previous section in terms of the crystal momenta

$$\begin{aligned} k_1 &= k_x, \quad k_2 = \frac{1}{2}(k_x + \sqrt{3}k_y), \quad k_3 = k_z \implies \\ k_x &= k_1, \quad k_y = \frac{1}{\sqrt{3}}(2k_2 - k_1), \quad k_z = k_3. \end{aligned} \tag{3.29}$$

Then, in terms of the hexagonal coordinate vectors k_1, k_2, k_3, the low-energy Hamiltonian is given by

$$\begin{aligned} H(\boldsymbol{k}) =& C_0 + C_1k_3^2 + \frac{2C_2}{3}(k_1^2 + (k_1 - k_2)^2 + k_2^2) \\ &+ \left(M_0 + M_1k_3^2 + \frac{2M_2}{3}(k_1^2 + (k_1 - k_2)^2 + k_2^2)\right)\tau_z \\ &+ \frac{v}{3}\left(2k_1 + (k_1 - k_2) + k_2\right)\sigma_x\tau_x + \frac{v}{\sqrt{3}}\left(k_2 - (k_1 - k_2)\right)\sigma_y\tau_x + v_zk_3\sigma_z\tau_x \\ &+ \frac{4w}{3}(k_1^3 - k_2^3 - (k_1 - k_2)^3)\tau_y. \end{aligned} \tag{3.30}$$

In order to eventually perform real-space calculations, we need to restore the idea of a lattice model. Our next step, therefore, is to perform a lattice regularisation, namely the transformations

$$\begin{aligned} k_i &\to \frac{1}{L_i}\sin k_i \\ k_i^2 &\to \frac{2}{L_i}(1 - \cos k_i). \end{aligned} \tag{3.31}$$

For notational clarity, we shall set $L_i = 1$ for $i = 1, 2, 3$. The resulting lattice regularised Hamiltonian is given as

$$
\begin{aligned}
H(\boldsymbol{k}) =& \tilde{C}_0 - 2C_1 \cos k_3 - \frac{4C_2}{3}(\cos k_1 + \cos(k_1 - k_2) + \cos k_2) \\
&+ \left(\tilde{M}_0 - 2M_1 \cos k_3 - \frac{4M_2}{3}(\cos k_1 + \cos(k_1 - k_2) + \cos k_2)\right)\tau_z \\
&+ \frac{v}{3}\left(2\sin k_1 + \sin(k_1 - k_2) + \sin k_2\right)\sigma_x \tau_x \\
&+ \frac{v}{\sqrt{3}}\left(\sin k_2 - \sin(k_1 - k_2)\right)\sigma_y \tau_x \\
&+ w(-\sin k_1 + \sin k_2 + \sin(k_1 - k_2))\tau_y + v_z \sin k_3 \sigma_z \tau_x .
\end{aligned}
\tag{3.32}
$$

where $\tilde{C}_0 = C_0 + 2C_1 + 4C_2$ and $\tilde{M}_0 = M_0 + 2M_1 + 4M_2$.

The final step is now to perform a Fourier transform to move from the momentum representation to the position representation. Specifically,

$$
c_{\boldsymbol{k}} = \sum_{\boldsymbol{r}_i} e^{-i\boldsymbol{k}\cdot\boldsymbol{r}_i} c_{\boldsymbol{r}_i}
\tag{3.33}
$$

where $\boldsymbol{r}_i$ is the position vector of a particular atomic site and the sum runs over the full dimensions of the sample. Finally, we arrive at the real space lattice Hamiltonian

$$
\begin{aligned}
H_{lat} = \sum_{\boldsymbol{r}_i} c^{\dagger}_{\boldsymbol{r}_i}\left(\tilde{C}_0 + \tilde{M}_0\tau_z\right)c_{\boldsymbol{r}_i} &+ c^{\dagger}_{\boldsymbol{r}_i}\left(-\frac{iv}{3}\sigma_x\tau_x - \frac{2M_2}{3}\tau_z - \frac{2C_2}{3} + \frac{iw}{2}\tau_y\right)c_{\boldsymbol{r}_i+\delta_1} \\
&+ c^{\dagger}_{\boldsymbol{r}_i}\left(-\frac{iv}{6}\sigma_x\tau_x - \frac{iv}{2\sqrt{3}}\sigma_y\tau_x - \frac{2M_2}{3}\tau_z - \frac{2C_2}{3} - \frac{iw}{2}\tau_y\right)c_{\boldsymbol{r}_i+\delta_2} \\
&+ c^{\dagger}_{\boldsymbol{r}_i}\left(-\frac{iv}{6}\sigma_x\tau_x + \frac{iv}{2\sqrt{3}}\sigma_y\tau_x - \frac{2M_2}{3}\tau_z - \frac{2C_2}{3} - \frac{iw}{2}\tau_y\right)c_{\boldsymbol{r}_i+\delta_3} \\
&+ c^{\dagger}_{\boldsymbol{r}_i}\left(\frac{-iv}{2}\sigma_z\tau_x - M_1\tau_z - C_1\right)c_{\boldsymbol{r}_i+\delta_4} + \text{h.c.}
\end{aligned}
\tag{3.34}
$$

where $\delta_1 = (1, 0, 0)$, $\delta_2 = (\frac{1}{2}, \frac{\sqrt{3}}{2}, 0)$, $\delta_3 = (\frac{1}{2}, -\frac{\sqrt{3}}{2}, 0)$ and $\delta_4 = (0, 0, 1)$ and h.c. denotes the Hermitian conjugate. The relevant exchange term can then be trivially added as an additional spin-dependent onsite potential.

Lattice simulations are performed using the open-source Python package Kwant. In the following section, unless otherwise stated, we have used $M_0 = -2, M_1 = 1, M_2 = 1, A = 1, v_z = 0.5, w = 1.5$ as our choice of parameters. In addition, we will set the lattice constant at 1 nm. In section 3.4.3 we will link theory back to reality by performing lattice simulations with more realistic set of material parameters.

3.4.2 Flat-bands in AIII and BDI

In this section we present the results of the electronic properties for even and odd layer systems in a nanowire geometry. In the following and unless stated otherwise, the magnitude of the exchange field will be fixed at $|\boldsymbol{M}| = 1.5$. This value has been chosen as it is above the critical value for flat band formation in all systems studied. In general, the critical field value for flat-band formation is a complex function of the material parameters, so an analytic solution is not presented. In general, we will avoid direct analytical calculations and will instead focus on symmetry considerations as a means to explain our results. To avoid finite-size effects as best as possible whilst also respecting computational resources and limiting simulation times, the number of lattice points in the direction of the finite dimension will be set to 81 i.e. 40 lattice points either side of the $(x, y) = (0, 0)$ plane (the odd choice of number reflects the choice of placing a lattice site at the origin). Finite-size effects will generally be more prevalent in nanoribbons with a larger number of layers. Due to the difficulty in deriving a closed form solution the localization length has not been calculated for the flat-band edge states, however the value of 81 was identified after a set of convergence tests that iteratively increased the system size by 10 lattice in either direction. The criteria for convergence was set as the point at which the energy of flat-bands around the Γ-point changed by less than $1e - 4$ using the parameters given above.

For comparison with later results, we first calculate the energy dispersion relationships of two and three layer systems with no exchange interaction. The bulk dispersions are shown in Figure 3.3 and the 1D dispersion for wires with translational invariance in the x direction are shown in Figure 3.4. An identical set of plots are obtained for the 1D dispersion relations in the k_y direction. While a Dirac point (DP) is visible in both 1D systems, corresponding to edge states propagating along the length of the nanoribbon, when comparing the dispersion relations of the bulk systems one finds that only the 3-layer system possesses a DP at the Γ point. One can understand the difference in the presence (or absence) of a DP at the Γ point by interpreting the Hamiltonian given in 3.3 as a stack of 2D TIs coupled to one another in the z-direction [48].

We will now analyse the results for finite exchange fields.

In-plane canting

We will first begin by examining two layer systems, as the simplest even layer system. In Figures 3.5 and 3.6 we show the results of a numerical calculation of the energy dispersion relations for a two layer system with in-plane canting, periodic in the x (left) and y (right). In Figure 3.5, we demonstrate the evolution of the dispersion relations for the

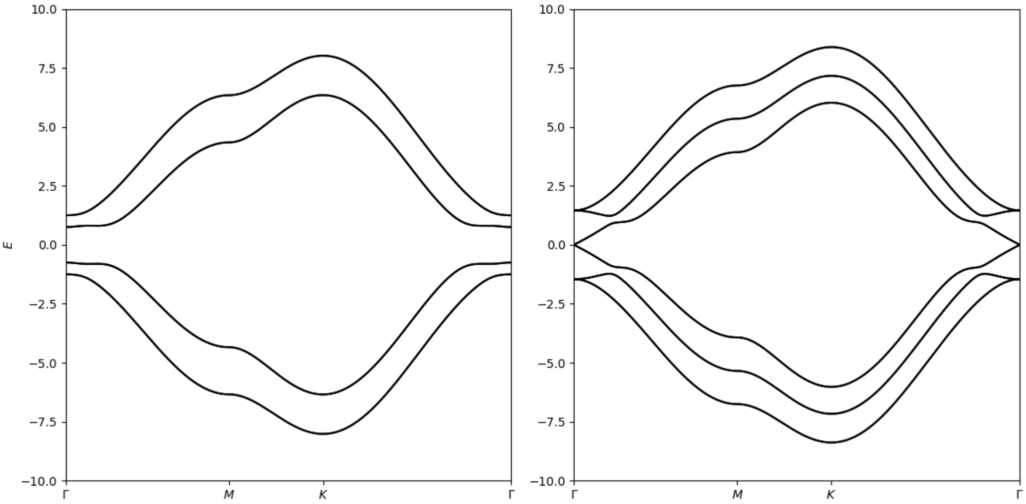

Fig. 3.3 Energy dispersion of a two (left) and three (right) layer system for with no exchange interaction present along the $\Gamma - M - K - \Gamma$ path in the hexagonal Brillouin Zone.

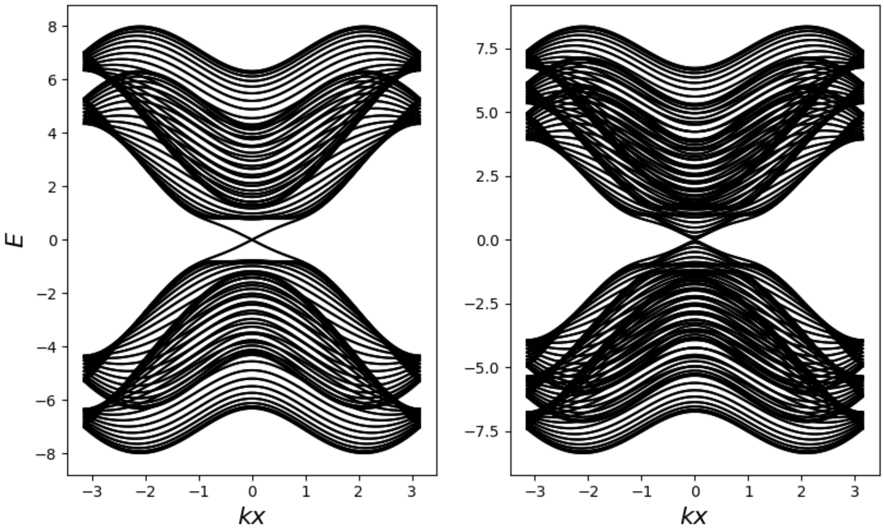

Fig. 3.4 2D bulk energy dispersion of a two (left) and three (right) layer system for with no exchange interaction present. Note that only the three layer system hosts Dirac points.

parameter sweep $\theta = (\pi/6, \pi/3, \pi/2)$ at $\phi = 0$, while in 3.6 we demonstrate the evolution for $\phi = (\pi/6, \pi/3, \pi/2)$ at $\theta = \pi/2$, where θ and ϕ are the polar and azimuthal angles defining the spherical polar coordinates as described in 3.6 and 3.7. Unless otherwise stated, angular parameter sweeps for both θ and ϕ will be presented for the values $(\pi/6, \pi/3, \pi/2)$ henceforth.

Note that at $\phi = 0$, the magnetisation breaks the mirror reflection symmetry R_x in the nanoribbon periodic in x, causing an energy dispersion which is asymmetric about $k_x = 0$ in the left-hand column of Figure 3.6. However, the most obvious features of both figures are the flat-bands that emerge for the magnetisation configurations $\boldsymbol{M} = (M, 0, 0)$ $(\theta = \pi/2, \phi = 0)$ and $\boldsymbol{M} = (0, M, 0)$ $(\theta = \pi/2, \phi = \pi/2)$, i.e. in plane magnetisation with ferromagnetic coupling between layers. We can examine the topological nature of these flat-bands by recalling that even layer systems with in-plane canting are in the AIII and BDI classifications for the magnetisation configurations $\boldsymbol{M} = (M, 0, 0)$ and $\boldsymbol{M} = (0, M, 0)$, respectively. As such, the flat-bands in both systems can be topologically characterised by a $\mathbb{Z}$ topological invariant known as the *winding number*.

Following the treatment laid out by [116], we note that Hamiltonians in the AIII and BDI classes both anticommute with the chiral symmetry operator, S, and can therefore be written in the homotopically equivalent, off-diagonal form

$$H_2(\boldsymbol{k}) = \begin{pmatrix} 0 & D(\boldsymbol{k}) \\ D^\dagger(\boldsymbol{k}) & 0 \end{pmatrix} \tag{3.35}$$

in the basis provided by the eigenvectors of S. While it is possible to solve for the spectrum of the two-layer system using the off-diagonal form of the matrix, it involves solving a depressed quartic equation and is not particularly illuminating. However, using the matrix $D(\boldsymbol{k})$ the winding number, ν can be calculated as

$$\begin{aligned} \nu(k_\parallel) &= -\frac{1}{2\pi}\mathrm{Im}\int \mathrm{d}k_\perp \mathrm{Tr}\left(\partial_{k_\perp} \ln D(\boldsymbol{k})\right) \\ &= -\frac{1}{2\pi}\mathrm{Im}\int \mathrm{d}k_\perp \partial_{k_\perp} \ln\det D(\boldsymbol{k}) \\ &= -\frac{1}{2\pi}\int \mathrm{d}k_\perp \partial_{k_\perp} \eta(\boldsymbol{k}) \end{aligned} \tag{3.36}$$

where $\eta(\boldsymbol{k}) = \mathrm{Im}\ln\det D(\boldsymbol{k})$ is the phase of the complex number $\det D(k)$ and $(k_\parallel, k_\perp)$ are momentum components parallel and perpendicular to the direction of the nanowire (e.g. $k_\parallel = k_x$ for a nanoribbon periodic in x). If the winding number $\nu(k_\parallel)$ is non-zero in areas of the BZ we can conclude that the system is topologically non-trivial. It is, therefore, instructive

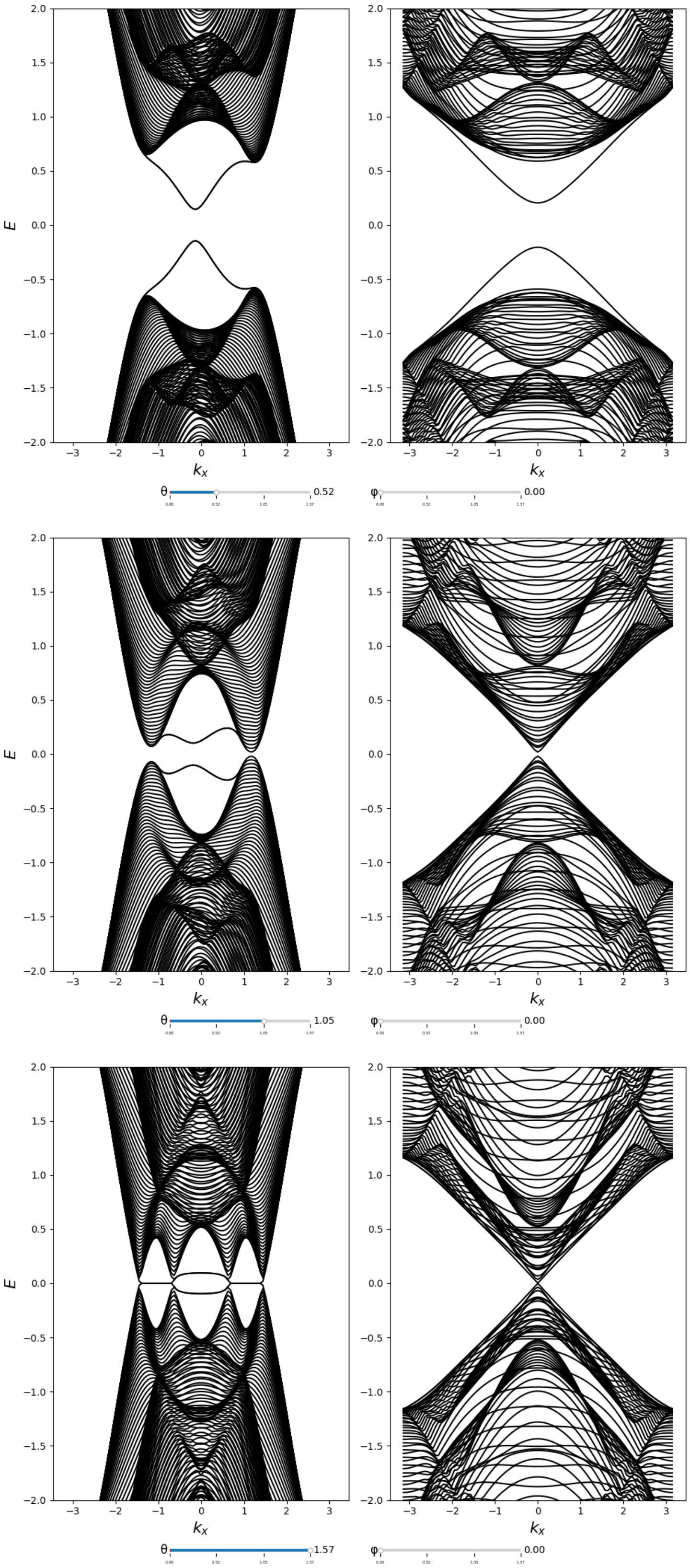

Fig. 3.5 Evolution of the electronic dispersion relations for a two layer system with in-plane canting for various values of θ at $\phi = 0$ for nanowire geometries infinite in the $\hat{x}$ (left) and $\hat{y}$ directions (right).

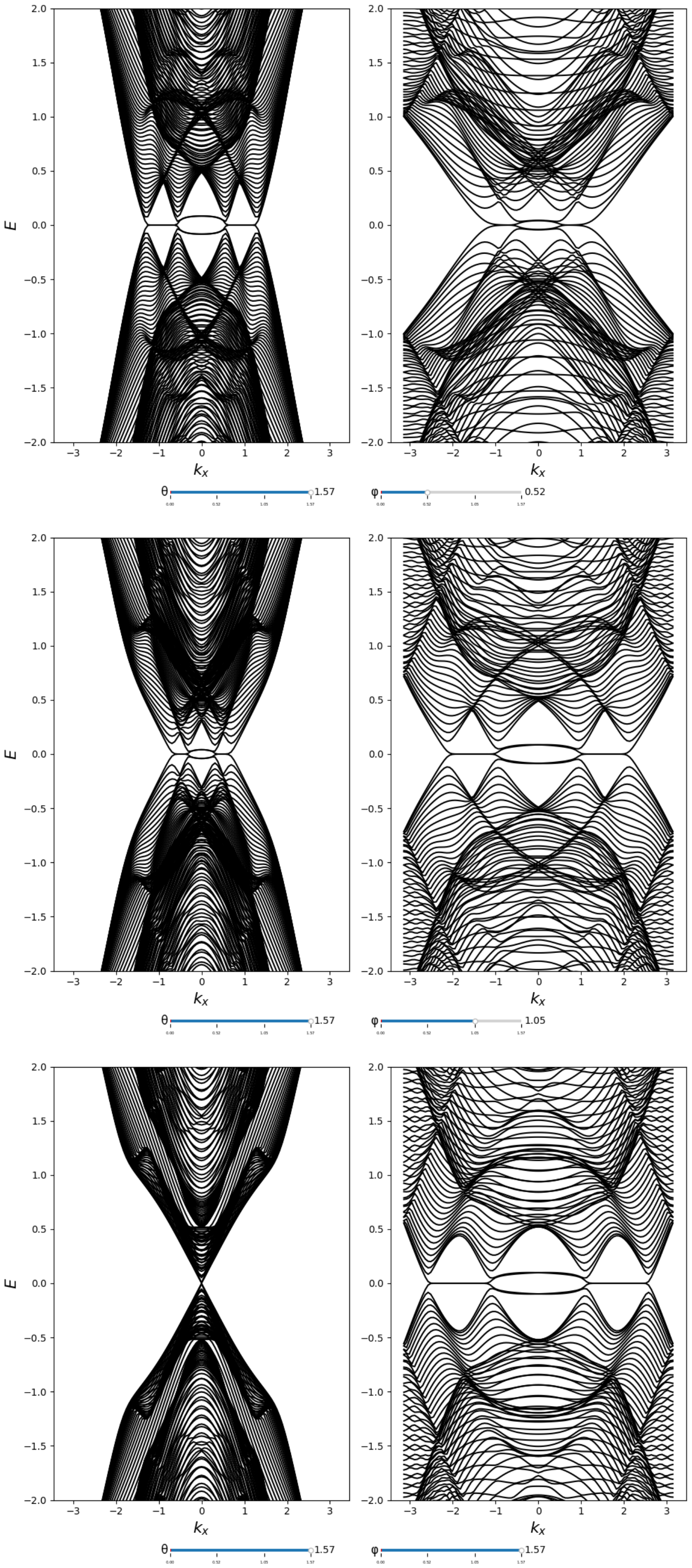

Fig. 3.6 Evolution of the electronic dispersion relations for a two layer system with in-plane canting for various values of ϕ at $\theta = \pi/2$ for nanowire geometries infinite in the $\hat{x}$ (left) and $\hat{y}$ directions (right).

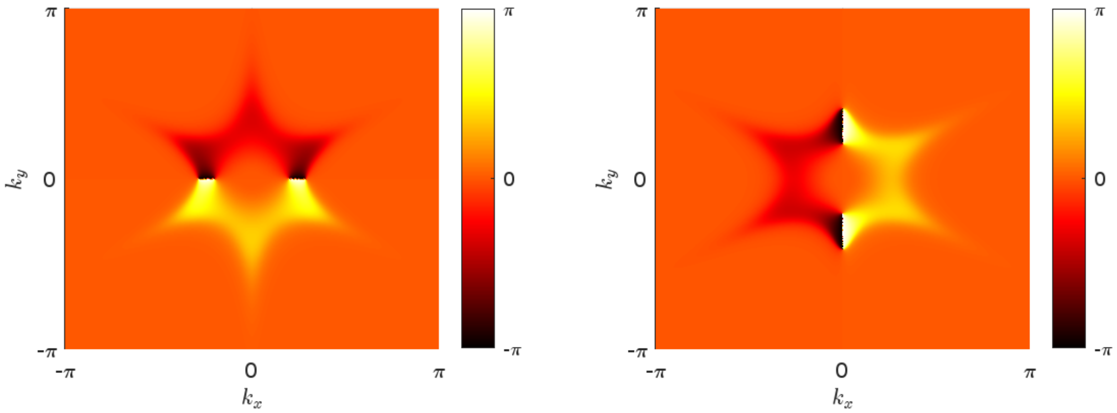

Fig. 3.7 Evolution of $\eta(\boldsymbol{k}) = \operatorname{Im}\ln\det D(\boldsymbol{k})$ across the Brillouin zone for the in-plane canted magnetisation configuration with $\boldsymbol{M} = (M, 0, 0)$ (left) and $\boldsymbol{M} = (0, M, 0)$ (right). Note that the BZ is hexagonal, however to more clearly see the effect of the hexagonal warping term, $\eta(\boldsymbol{k})$ is plotted against k_x and k_y.

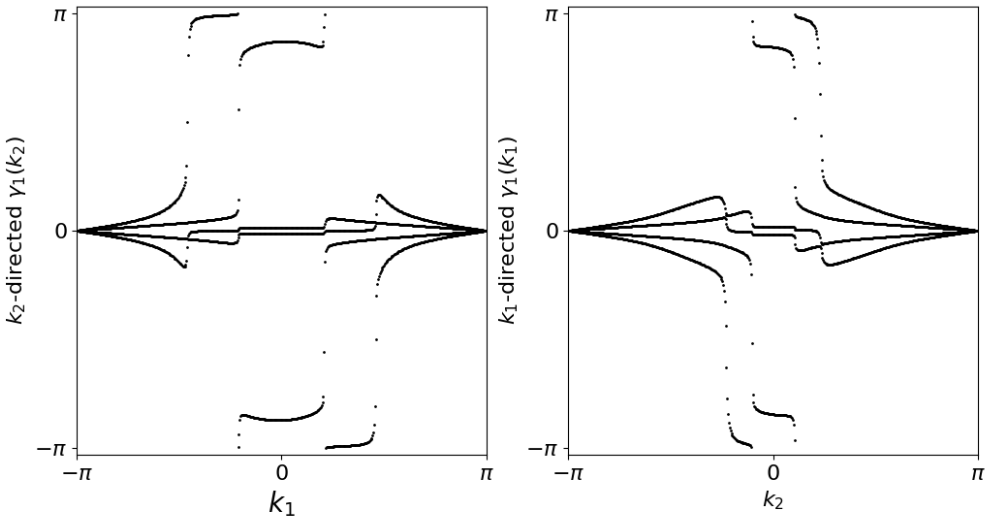

Fig. 3.8 Wilson loops of a two-layer nanoribbon periodic in the x-direction with in-plane magnetisation directed along the x axis and ferromagnetic coupling between layers, calculated over the valence bands at half-filling. A small canting in the z-direction has been added to make the winding of the Wilson loop more clearly visible. The left (right) panel shows the k_2 (k_1) directed Wilson loop against the k_1 (k_2) wavevector.

to examine the evolution of $\eta(\boldsymbol{k})$ across the full BZ when determining the topological nature of the flat-bands.

Figure 3.7 shows the evolution of η across the BZ for the magnetisation configurations $(M, 0, 0)$ (left) and $(0, M, 0)$ (right). In both configurations, singularities in the phase are present as $\eta(\boldsymbol{k})$ discontinuously changes from $-\pi$ to π. Comparing the bottom two rows of Figures 3.6 and 3.5 to 3.7 it is clear that these singularities correspond to the position of the flat-bands in the energy dispersion relationships of the two-layer nanoribbons and signal non-trivial topological behaviour. We conclude that the winding number $\nu(k_{\|}) = 1$ at the positions where the vortices appear in $\eta(\boldsymbol{k})$. In addition, the hexagonal warping due to the non-zero value of w in equation 3.34 and the underlying lattice structure is also apparent. While the underlying BZ of the Hamiltonian given in 3.34 is hexagonal, $\eta(\boldsymbol{k})$ is plotted against k_x, k_y in order to more clearly see the effect of the hexagonal warping term. The numerical calculation of η was performed with a bulk Hamiltonian, while dispersion relations were calculated on a discretised lattice Hamiltonian, finite in one direction. As such, the position of the singularities in η in the former calculation will not exactly match the position of the flat-bands in the latter.

Additional confirmation of the topologically non-trivial nature of the bands is confirmed by examining the Wilson loop flow of the system, as per [4, 19] and given by equation 3.22. The Wilson loop spectra shown in Figure 3.8 are calculated over the valence bands at half-filling using a slab geometry and integrating over the appropriate periodic directions provided by the wavevectors given in equation 3.29. The Wilson loop has only been calculated for a nanoribbon periodic in the x-direction with magnetisation configuration ($\theta = \pi/2, \phi = 0$. A small canting of the magnetisation in the z direction has been added in order to more clearly see the flow of the Wilson loop. The winding of the flat-band states is clearly visible. The reader should compare the positions of the flat-bands in the bottom left panel of 3.6 to the left hand image of 3.8, where the phases around $\pm pi$ match the dispersionless regions in the band structure.

Finally, examining the local density of states (LDOS) of a two-layer nanoribbon periodic in the x direction with $\boldsymbol{M} = (M, 0, 0)$ confirms that the states localised around $E = 0$ are edge state flat-bands, shown in Figure 3.9

Before moving on to a discussion of three layer systems, it is worth pausing and reflecting on why exactly flat-bands appear in this system. To do so, we will examine the bulk spectrum for a two layer system with in-plane canting and magnetisation configuration ($\theta = \pi/2, \phi = 0$), i.e. in-plane magnetisation along the x-axis with ferromagnetic coupling between layers. Figure 3.10 shows the bulk energy dispersion relation along the path $\Gamma - M - K - \Gamma$ in the hexagonal BZ. Two accidental band crossings are clearly visible along the $\Gamma - K$ line at some momenta $(k_x, k_y) = (k_1, 0)$ and $(k_x, k_y) = (k_2, 0)$, where $k_2 > k_1$ (we have an identical result when only the y component of the magnetisation is non-zero where we instead have nodal points at $(k_x, k_y) = (0, k_1)$ and $(k_x, k_y) = (0, k_2)$). We can conclude that beyond some

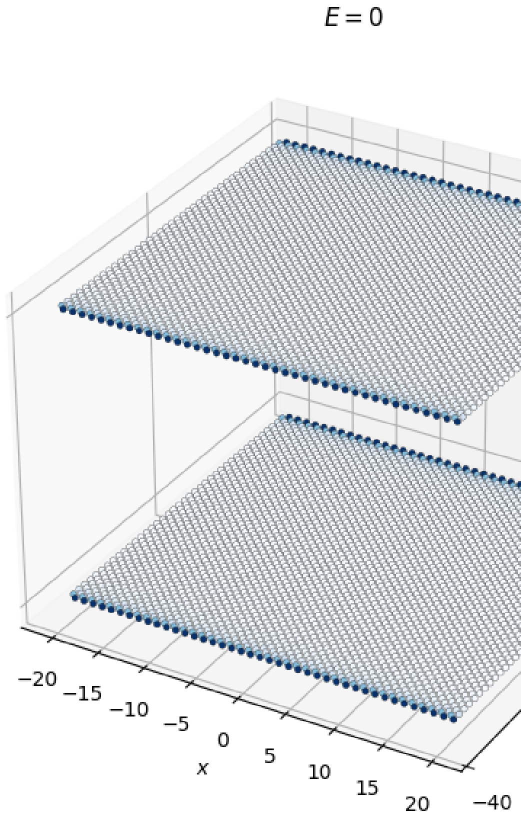

Fig. 3.9 Local density of states at $E = 0$ of a two-layer nanoribbon periodic in the x direction with magnetisation parameters $\theta = \pi/2, \phi = 0$ and in-plane canting (bottom left image of Figure 3.6).

critical magnetisation, which is generally a complex function of the system parameters and number of layers, an in-plane magnetisation can drive the system toward a semimetallic phase. Additionally the inversion symmetry, given in 3.17, enforces symmetry in the dispersion relation about $\boldsymbol{k} = 0$ for a nanoribbon periodic in x, resulting in another dipsersionless region between $(k_x, k_y) = (-k_1, 0)$ and $(k_x, k_y) = (-k_2, 0)$.

In general, however, we should not expect these topological surface states to exhibit zero dispersion. The robustness of these flat-bands is actually linked to the presence of chiral symmetry, given in equation 3.10 [146, 150]. In general, however, these flat-bands are not robust to chiral symmetry breaking terms. While we can still expect visible nodal lines for moderate values of $C(\boldsymbol{k} \neq 0)$, we should expect some bowing with the inclusion of chiral

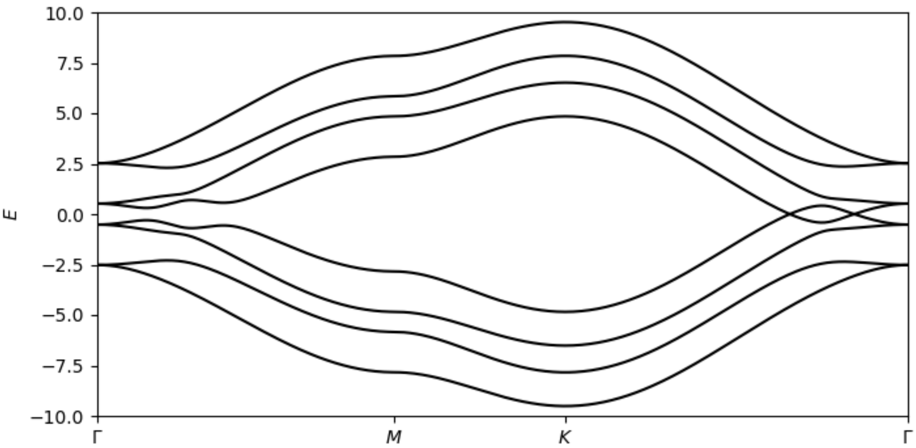

Fig. 3.10 2D bulk electronic dispersion along the path $\Gamma - M - K - \Gamma$ in the hexagonal Brillouin zone for a two layer system with in-plane magnetisation along the x axis and ferromagnetic coupling between layers.

symmetry breaking terms. This will discussed in greater detail in section 3.4.3.

Having completed our analysis of the edge state flat-bands in two-layer nanoribbons, we will move on to the examination of three layer systems. Figures 3.11 and 3.12 show the energy dispersion relations for a three-layer nanoribbon periodic in x (left) and y (right) across a sweep of the parameters θ and ϕ, respectively. Referring to table 3.1, we note that even and odd layer systems possess the same topological classification for in-plane canting magnetisation configurations. Given this, we might assume the dispersion relations of a three-layer system to be identical to those of a two-layer system and while there are indeed similarities, such as the evolution of zero-energy flat-band states away from $k = 0$ as $\theta \longrightarrow \pi/2$, there is additional complexity in the dispersion relation of three-layer nanoribbons in the form of the presence of a new dispersionless band centred around $k = 0$.

Once again examining the evolution of $\eta(\boldsymbol{k})$ across the BZ as an indicator of the topological nature of these bands, we do indeed observe the presence of singular behaviour centred around $k = 0$, shown in Figure 3.13. Interestingly, when comparing the behaviour of η for the $\boldsymbol{M} = (M, 0, 0)$ and $\boldsymbol{M} = (0, M, 0)$ configurations we observe slight differences in the singular regions away from $k = 0$. These lobes are far more pronounced in the $\boldsymbol{M} = (0, M, 0)$ configuration. Observe also similar behaviour in the electronic dispersion calculations, with the flat-bands away from $k = 0$ having a much broader extent in y periodic nanoribbons with $\boldsymbol{M} = (0, M, 0)$ than their x periodic counterparts. This anisotropy is due to the presence of the hexagonal warping term, $k_x^3 - 3k_xk_y^2$ in the Hamiltonian 3.2.

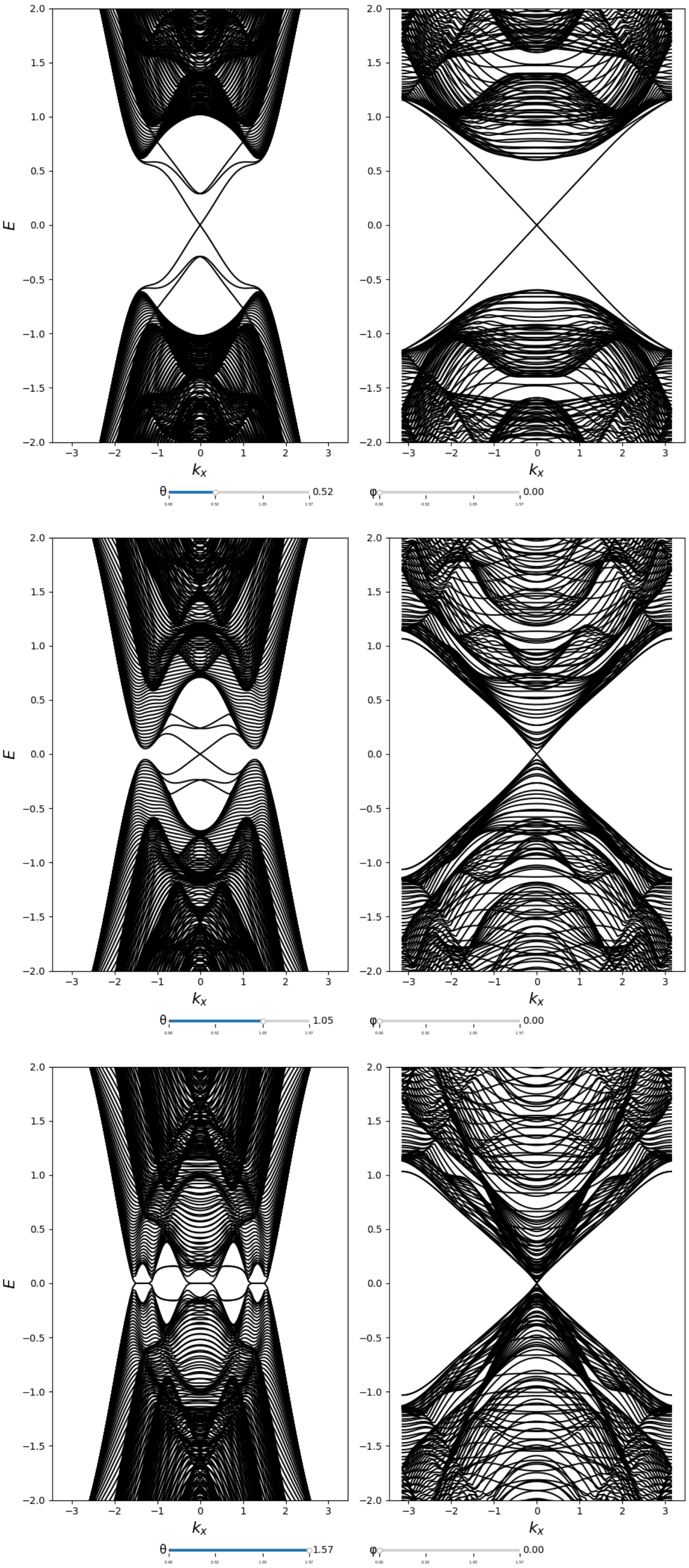

Fig. 3.11 Evolution of the electronic dispersion relations for a three layer system with in-plane canting for various values of θ at $\phi = 0$ for nanowire geometries infinite in the $\hat{x}$ (left) and $\hat{y}$ directions (right).

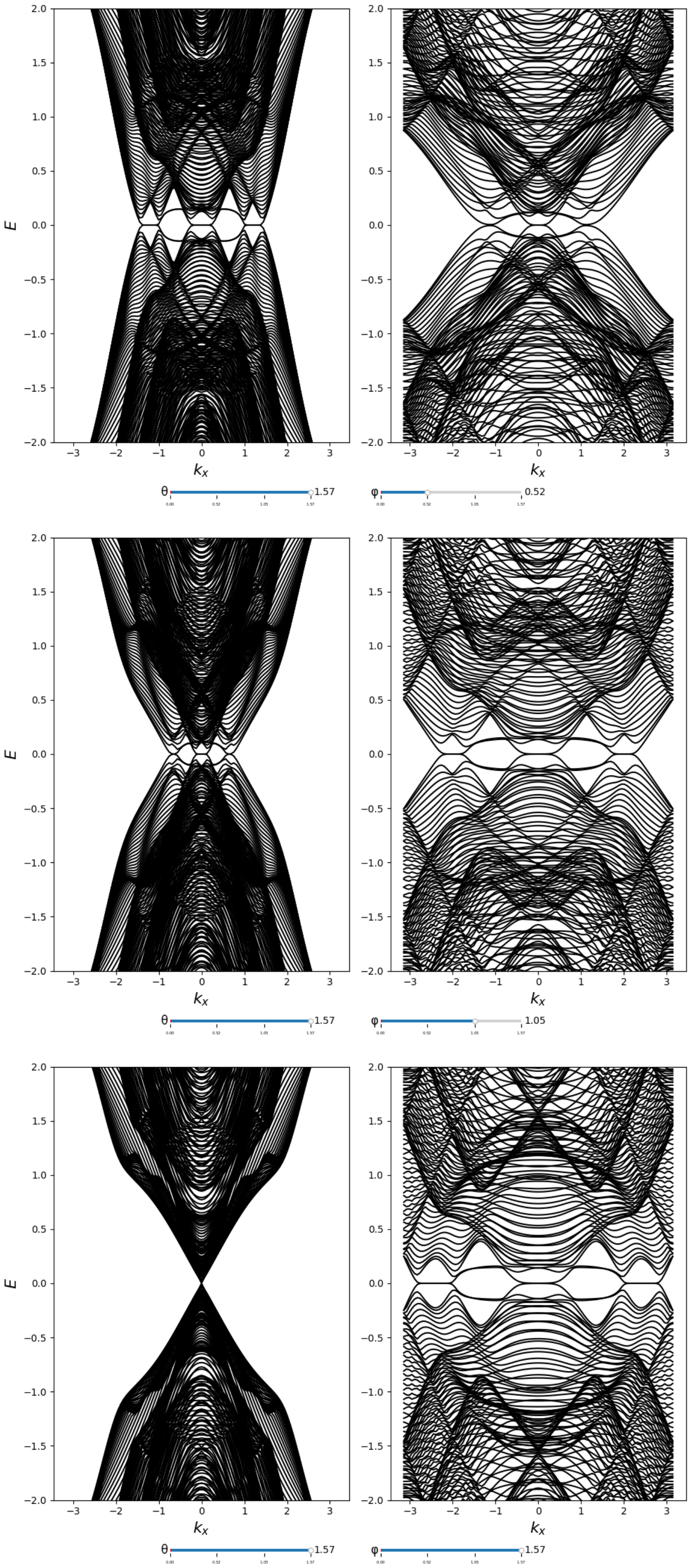

Fig. 3.12 Evolution of the electronic dispersion relations for a three layer system with in-plane canting for various values of ϕ at $\theta = \pi/2$ for nanowire geometries infinite in the $\hat{x}$ (left) and $\hat{y}$ directions (right).

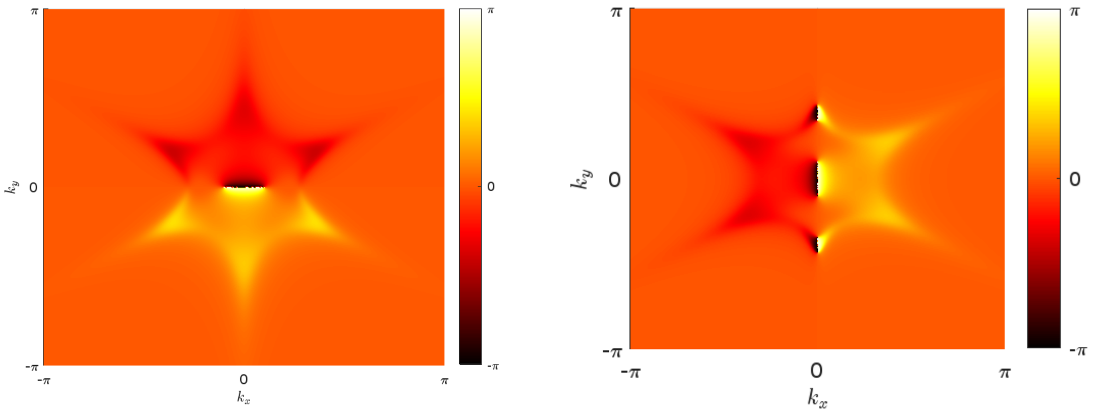

Fig. 3.13 Evolution of $\eta(\boldsymbol{k}) = \operatorname{Im} \ln \det D(\boldsymbol{k})$ across the Brillouin zone for the in-plane canted magnetisation configuration with $\boldsymbol{M} = (M, 0, 0)$ (left) and $\boldsymbol{M} = (0, M, 0)$ (right).

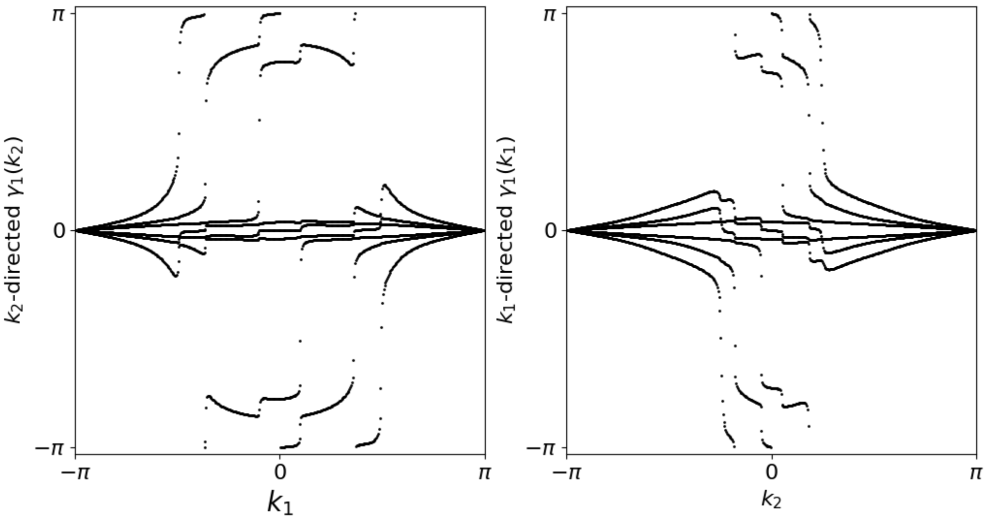

Fig. 3.14 Wilson loops of a three-layer nanoribbon periodic in the x-direction with in-plane magnetisation directed along the x axis and ferromagnetic coupling between layers, calculated over the valence bands at half-filling. A small canting in the z-direction has been added to make the winding of the Wilson loop more clearly visible. The left (right) panel shows the k_2 (k_1) directed Wilson loop against the k_1 (k_2) wavevector.

Again, the Wilson loops provide another means of probing the topological nature of the system, shown in Figure 3.14. An identical set-up was used to calcualte the Wilson loops as was used for the two-layer system shown in 3.8. The winding of the flat-bands states is clearly visible.

Similarly to the two-layer nanoribbon, the zero-energy flat-bands states localise along the edge of the nanoribbon, as shown in right-hand panel of Figure 3.16. Interestingly, the edge states penetrate much more deeply into the middle layer than the top or bottom layers.

Once again, it is instructive to examine the bulk dispersion of a three layer system to offer greater insight to the dispersion relation of the nanoribbon and the ultimate source of the flat-bands. The top row of Figure 3.15 shows the bulk energy dispersion relation along the path $\Gamma - M - K - \Gamma$ in the hexagonal BZ, while the bottom row shows a zoomed view of the dispersion along the $K - \Gamma$ path. As described above, the main difference between the dispersion relations of the two and three layer systems discussed above is that an additional flat-band appears in the three layer dispersion relation, centred around $k_i = 0$, where $i = x, y$ depending on the direction of the magnetisation and periodicity of the nanoribbon. Recall from Figure 3.3 that only three layer (in fact, all odd layer) systems possess a DP at the Γ point, while two layer (and all even layer) systems are gapped. A non-zero in-plane magnetisation will cause the DP to shift in k-space, as described in the chapter introduction. The presence of inversion symmetry, given in equation 3.17, ensures that he band structure is symmetric around $\boldsymbol{k} = 0$ and that there are DPs shifted by equal magnitude either side of Γ. This leads to the formation of nodal lines centred around Γ linking the two DPs in multilayer heterostructures with an odd number of layers. This effect is not present in even layer samples, where no DP exists at zero magnetisation. Additionally, just as was the case in two layer systems, the in-plane magnetisation can also lead to an accidental crossing of the bulk bands along the $\Gamma - K$ line in k-space in the three layer system, leading to the two additional nodal lines in 3.12. One can therefore use the odd layer systems with the magnetisation configurations discussed above to engineer a variety of TI-to-semimetal phase transitions. Such a phase transition could be detected through measurements of various quantum anomalies, such as the chiral anomaly, that can be observed through transport measurements [204]. Note that the central flat-band around $k_x = 0$ will appear for any non-zero magnetisation that lies entirely within the plane. The additional nodal lines will only form beyond the critical magnetisation that we can use to engineer a band crossing.

Finally, we conclude our investigation of in-plane canting orientations with a quick analysis of the dispersion relations of four and five layer systems. For brevity, only the dispersion relations for x periodic nanoribbons with the parameters $\theta = \pi/2, \phi = 0$ are presented. Figure 3.17 demonstrates that, once again, increasing the number of layers adds additional dispersionless bands around $E = 0$. As one asymptotically approaches the thermodynamic limit of a bulk sample, the expectation is that these separated flat-band regions would coalesce into a single flat-band localised around $E = 0$.

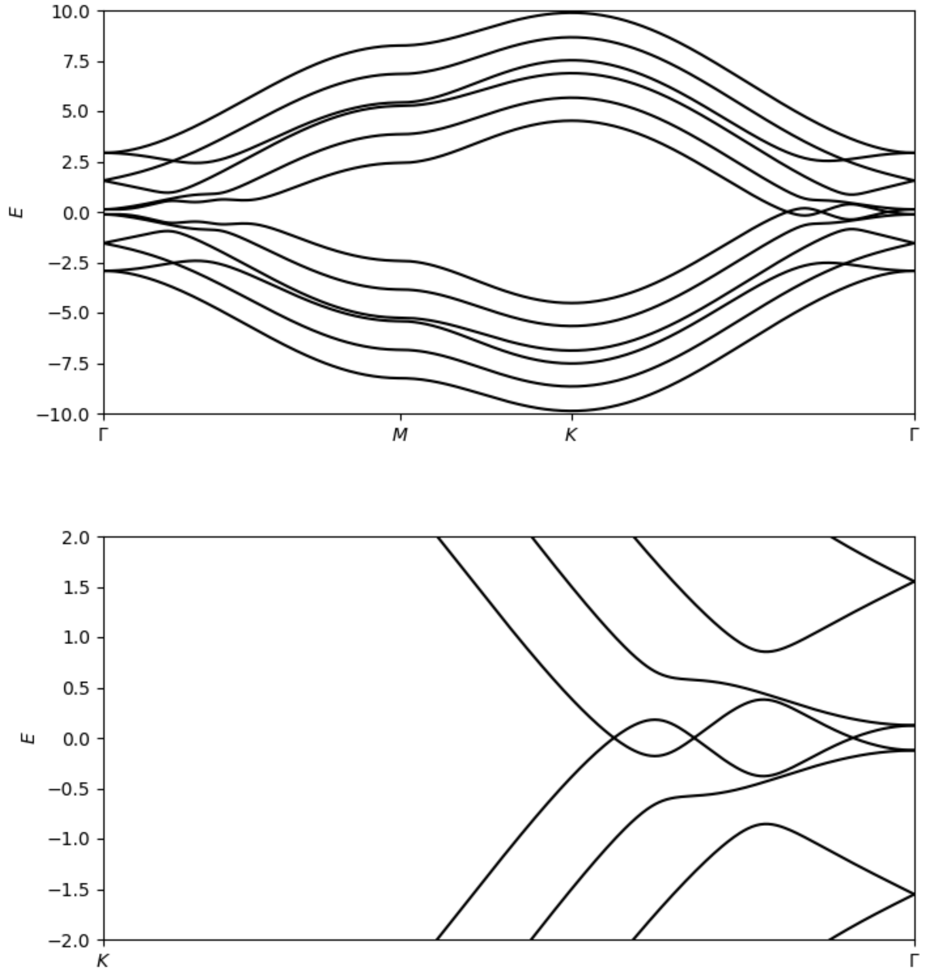

Fig. 3.15 2D bulk electronic dispersion along the path $\Gamma - M - K - \Gamma$ in the hexagonal Brillouin zone for a three layer system with in-plane magnetisation along the x axis and ferromagnetic coupling between layers. The bottom row of the figure shows a closer view of the band crossings along the $K - \Gamma$ path. Compared to the two layer system shown in Figure 3.10, an additional crossing exists. This is understood as the original DP, shifted in momentum space.

Out-of-plane canting

We begin our discussion of systems with out-of-plane canting with reference to table 3.1, noting that systems with an even number of layers are in Altland-Zirnbauer classes with no non-trivial topological invariants in our dimensions of interest. Analysing the electronic dispersion relations for a two-layer nanoribbon periodic in x and we do indeed find no evidence of flat-band behaviour when sweeping the magnetisation parameter $\theta \rightarrow \pi/2$,

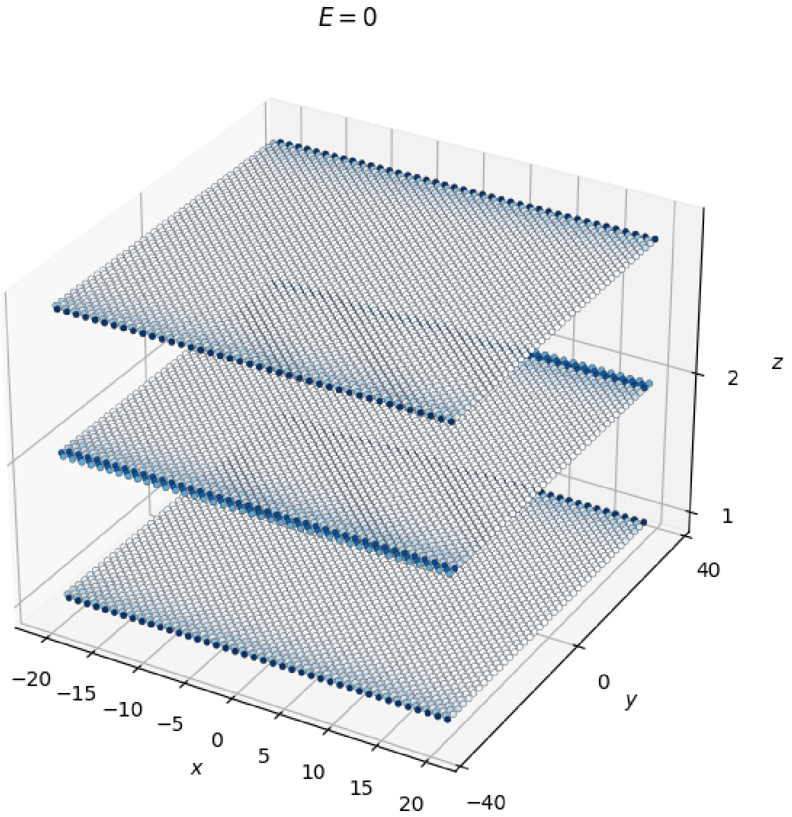

Fig. 3.16 Local density of states at $E = 0$ of a three-layer nanoribbon periodic in the x direction with magnetisation parameters $\theta = \pi/2, \phi = 0$ and in-plane canting.

as shown below in Figure 3.18. Indeed, this shouldn't be surprising given the previous discussion regarding the role of chiral symmetry in zero-energy flat-band formation. Since there is no magnetisation configuration in which we can respect chiral symmetry in even layer, out-of-plane canted system we can expect no zero-energy dispersionless regions in these systems. Therefore, rather than dwelling on even layer systems, this section will be devoted to the study of odd-layer nanoribbons.

Moving on to the analysis of three-layer nanoribbons as the simplest example of odd-layer systems, we present the results of electronic dispersion calculations for nanoribbon geometries periodic in the $\hat{x}$ and $\hat{y}$ directions for sweeps across the magnetisation parameters θ and ϕ in Figures 3.20 and 3.21. While even and odd layer systems with an in-plane canted

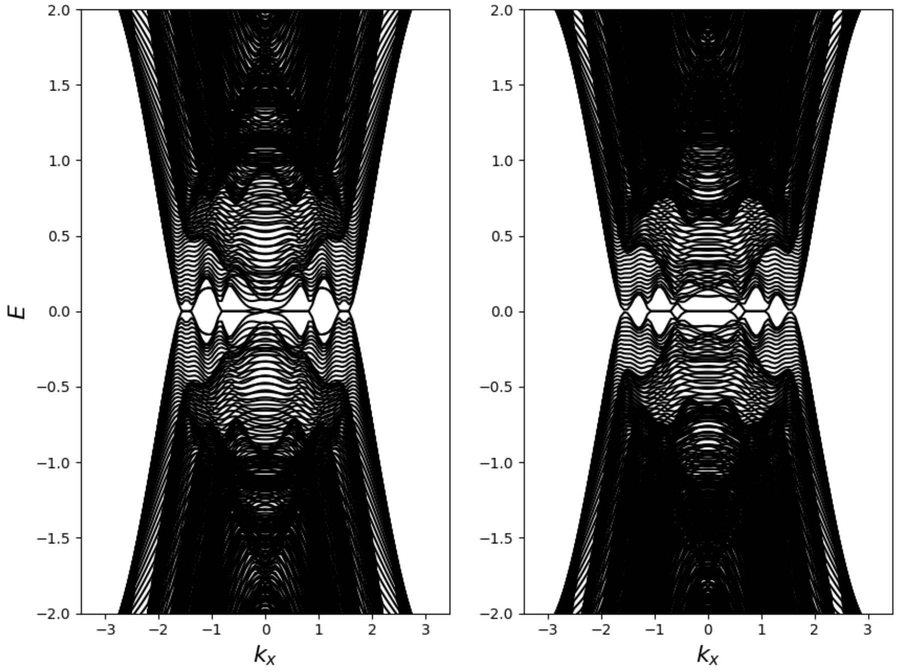

Fig. 3.17 Electronic dispersion relationships of four (left) and five (right) layer nanoribbons for the magnetisation configuration $\boldsymbol{M} = (M, 0, 0)$.

configuration displayed similar features in their dispersion relations, the distinct topological classifications between even and odd layer systems in out-of-plane configurations has resulted in a remarkably different set of band structures. Furthermore, the presence of out-of-plane rather than in-plane canting has resulted in an entirely new band structure in odd layer systems. Most notably, out-of-plane canting has led to the appearance of a single, wide flat-band centred around $k = 0$ in the configurations $\boldsymbol{M} = (M, 0, 0)$ $(\theta = \pi/2, \phi = 0)$ and $\boldsymbol{M} = (0, M, 0)$ $(\theta = \pi/2, \phi = \pi/2)$, i.e. in-plane magnetisation with antiferromagnetic coupling between layers. Furthermore, while in the case of in-plane canting increasing $\theta \longrightarrow \pi/2$ lead to the broadening of flat-bands in k-space, flat-bands only appear at exactly $\theta = \pi/2$ in the out-of-plane canted configuration when the bulk gap is closed. Rephrased, in the out-of-plane canted configuration the z-component of the magnetisation, M_z, can be used to continuously tune the group velocity of the low-energy topological states, as demonstrated in the bottom two rows of Figure 3.20. This is a result of an out-of-plane component of the magnetisation breaking the chiral symmetry 3.10. This offers the possibility of using a small perpendicular magnetic field $\boldsymbol{B} = B_z\hat{z}$ to control the transport behaviour of these topological nanoribbons. Alternatively, one can use an external perpendicular magnetic

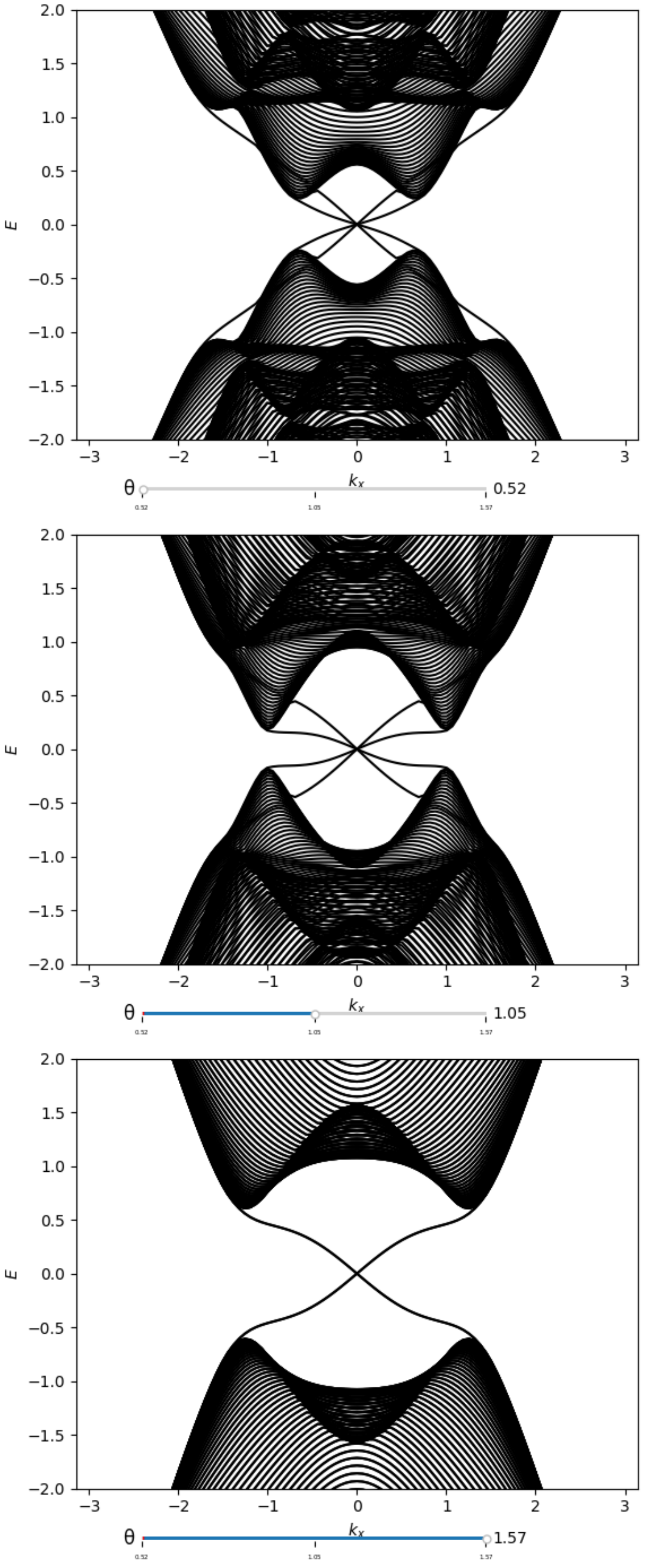

Fig. 3.18 Evolution of the electronic dispersion relations for a two-layer system with out-of-plane canting for various values of θ at $\phi = 0$ for a nanowire geometry infinite in the $\hat{x}$ direction. No dispersionless regions are observed at any point in the parameter sweep.

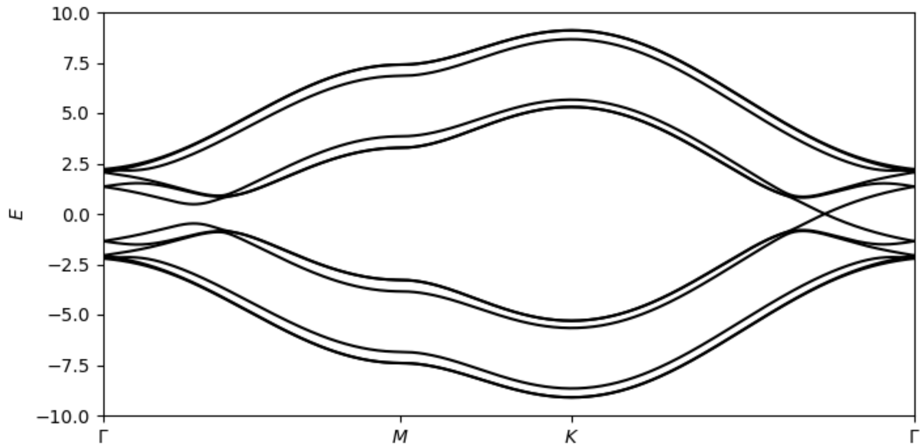

Fig. 3.19 2D bulk electronic dispersion along the path $\Gamma - M - K - \Gamma$ in the hexagonal Brillouin zone with magnetisation along the x axis and antiferromagnetic coupling between layers. The original DP at Γ has been shifted toward the K-point by an amount proportional to the magnetisation. Unlike the case of in-plane canting, as shown in Figures 3.10 and 3.10, there are no accidental band crossings caused by the bulk band gap closure.

field to engineer a Lifshitz transition observable through the use of a scanning tunnelling microscopy (STM) probe. Studies have shown that canted magnetic moments can arise in MTIs at interfaces, or even in bare AFMTIs [186, 82, 12]. It may, therefore, be expected that a non-zero out-of-plane external magnetic field would be required in order to realise a spin configuration with no net out-of-plane component. At a critical field, one would therefore observe a sudden change in the Fermi surface as a flat-band appeared through a large increase in the electron density which can be probed through the use of STM.

Once again, the presence of flat-bands can be understood from the perspective of the 2D bulk dispersion relation, shown in Figure 3.19. While in the case of in-plane canting at $(\theta = \pi/2, \phi = 0)$ (magnetisation along x with ferromagnetic coupling between layers) there was a critical magnetisation at which accidental band crossings occurred, this is not the case for systems with out-of-plane canting $(\theta = \pi/2, \phi = 0)$ (magnetisation along x with antiferromagnetic coupling between layers). Rather, we only see a shift of the original DP by an amount proportional to the magnetisation. In this case, there is no critical in-plane magnetisation, and a nodal line around the Γ point will always emerge where there is no z-component to the magnetisation (note that the dispersion relations have been calculated with magnetisation $m = 1.5$ for consistency with the previous section). Furthermore, the role of the out-of-plane canting is to gap out this original DP by acting as an effective mass term that breaks the chiral symmetry of the system.

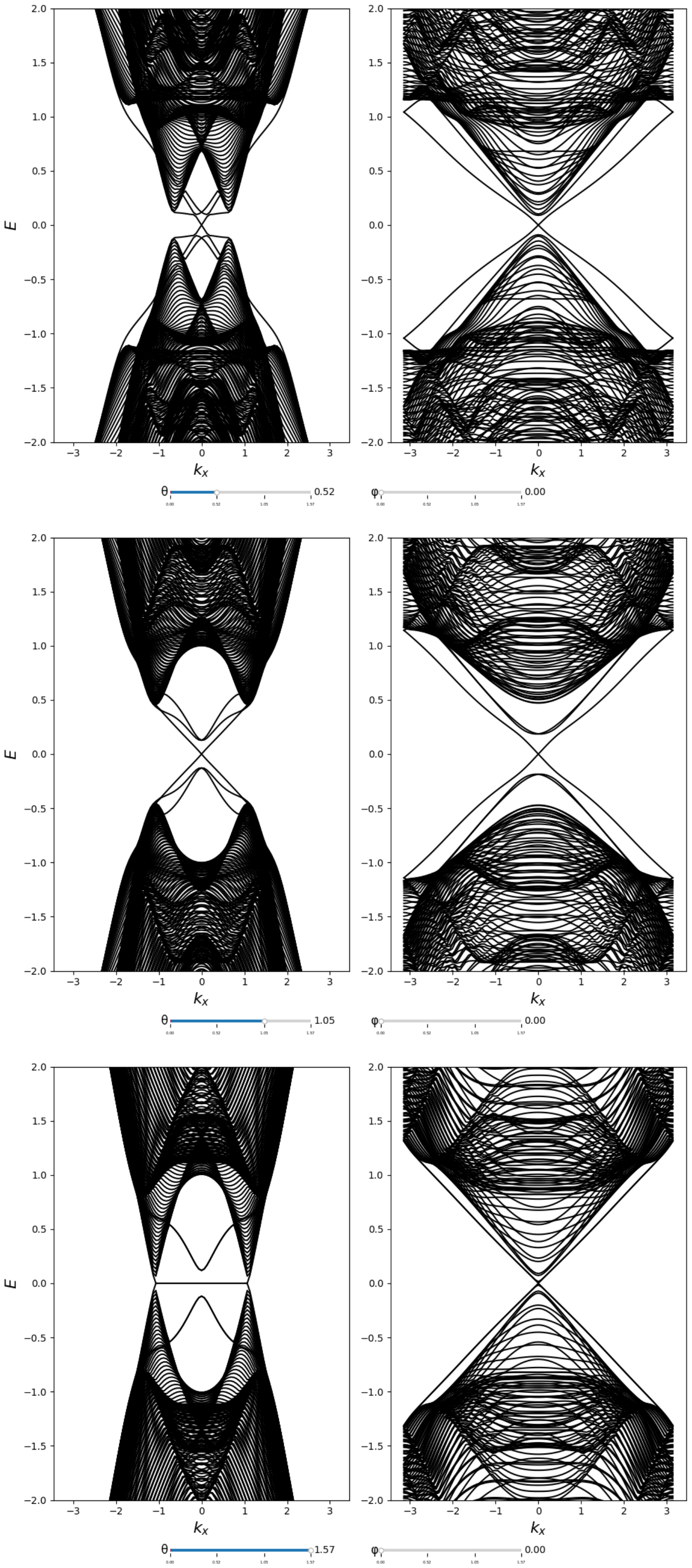

Fig. 3.20 Evolution of the electronic dispersion relations for a three-layer system with out-of-plane canting for various values of θ at $\phi = 0$ for nanowire geometries infinite in the $\hat{x}$ (left) and $\hat{y}$ (right) directions.

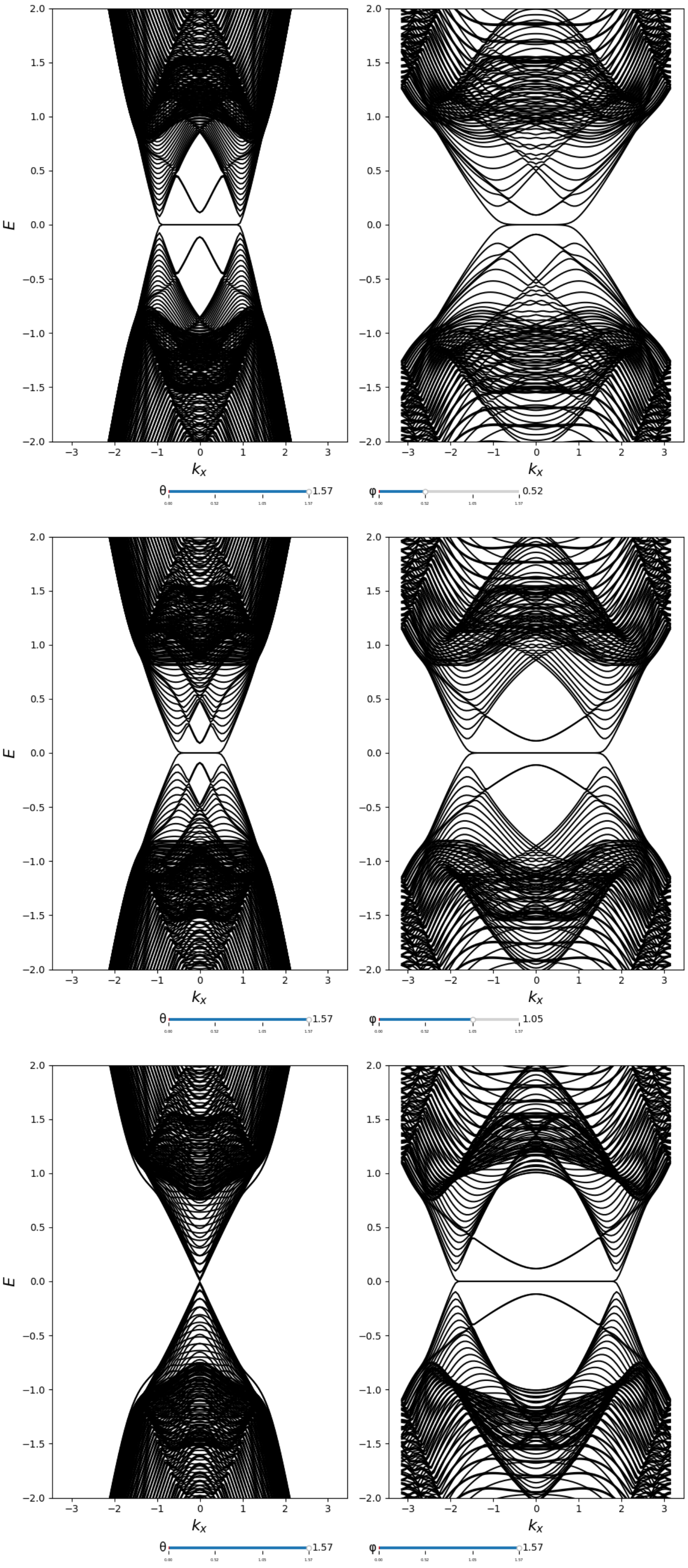

Fig. 3.21 Evolution of the electronic dispersion relations for a three-layer system with out-of-plane canting for various values of ϕ at $\theta = \pi/2$ for nanowire geometries infinite in the $\hat{x}$ (left) and $\hat{y}$ (right) directions.

Analysing the behaviour of $\eta(\boldsymbol{k})$ in Figure 3.22 as an indicator of the topological behaviour of these flat-bands, we once again observe singular behaviour in the areas where the flat-bands are located implying a non-zero value of the winding number in these regions. Furthermore, as the top row demonstrates of 3.22, the bands retain their topological character even with $M_z \neq 0$. This gives further credence to the idea of a perpendicular field controlling topological electronic transport.

The winding of the Wilson loop in this system can also, once again, establish the topologically non-trivial nature of the flat-band, shown in Figure 3.23. In contrast to the case of three-layer systems with in-plane canting, shown in Figure 3.14 one should note that only one of the fully branches winds. This difference can be explained by noting that the three dispersionless regions in the three-layer system with in-plane canting arise from three different band crossing points, where-as the single flat-band in this system arises from only a single band crossing.

We conclude our characterisation of the topological flat-bands in three-layer systems by analysing the LDOS of a nanoribbon periodic in the $\hat{x}$. Figure 3.24 shows the LDOS of three-layer nanoribbon for $\theta = \pi/3, \pi/2$ (top/bottom row) at $E = -0.05, 0.0$ (left/right columns).

First, examining the LDOS at $\theta = \pi/2, E = 0.0$ (bottom right) we find that the topological flat-bands are edge states (identically to the in-plane configuration) but are localised entirely on the top and bottom layers of the nanoribbon. Surprisingly, when the magnetisation vector is canted in the $\hat{z}$ direction (top right panel) the edge states (which now have a non-zero group velocity, see Figure 3.20) are now strongly localised within the middle layer with only a very faint contribution from the top or bottom layers). Roughly the same behaviour occurs for the LDOS calculated at $E = -0.05$ (left column), however in this case the states contributing to the LDOS at $\theta = \pi/2$ are more strongly localised across the centre of the top and bottom layers rather than the edges (recall that the bands at $E = -0.05$ are dispersive at both $\theta = \pi/3$ and $\theta = \pi/2$). We therefore conclude that not only can a perpendicular component of the magnetisation tune the group velocity of the topological bands, but these results suggest a non-zero M_z can also alter the spatial distribution of the topological states.

Analysing the dispersion relation of a five-layer nanoribbon with $\theta = \pi/2, \phi = 0$, shown in Figure 3.25, suggests that the central flat-band present in the three-layer system is actually a universal feature in all odd-layered systems.

However, the LDOS of a five-layer nanoribbon, shown in Figure 3.26, paints a much more complex picture. As before, we calculate the LDOS at $E = -0.05, 0.0$ and with the configuration $\theta = \pi/3, \pi/2$ and $\phi = 0$. In the five-layer geometry, we observe the surprising

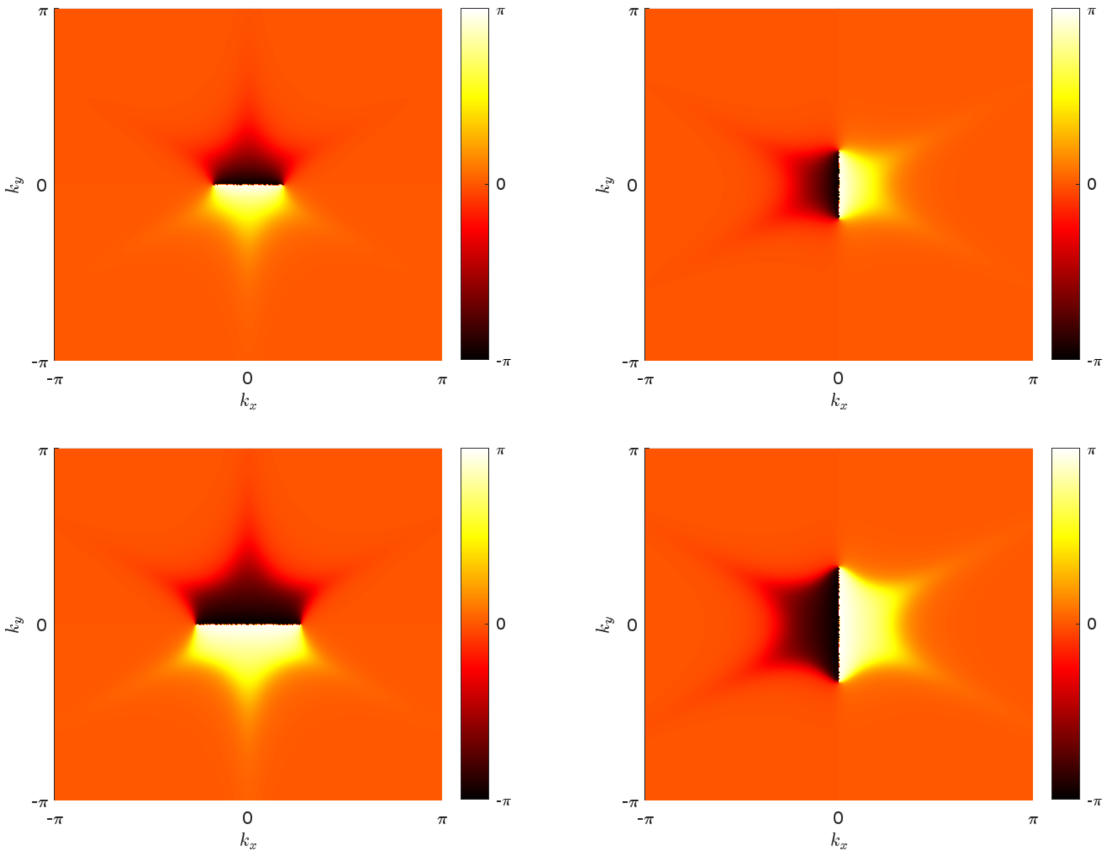

Fig. 3.22 Evolution of $\eta(\boldsymbol{k}) = \operatorname{Im}\ln\det D(\boldsymbol{k})$ across the Brillouin zone for the out-of-plane canted magnetisation configuration for various values of the parameters θ and ϕ. The top row shows $\theta = \pi/3$ while the bottom shows $\theta = \pi/2$. The left hand column shows $\phi = 0$ and the right $\phi = \pi/2$.

result that the LDOS is highly localised only on (odd) layers at $\theta = \pi/2$ for both energy values being investigated, as shown in the bottom row of 3.26. Furthermore, while in the three-layer nanoribbon the LDOS was localised within the middle layer at $\theta = \pi/3$ it is most highly localised on the top and bottom surface of the five-layer nanoribbon, as shown by the deeper shade of blue in the top row of Figure 3.26. While not presented here, the localization of the states on odd layers has been confirmed for 7 layer samples and is robust to changes in material parameters when $M_z = 0$. This is in fact a manifestation of the well-known result that bipartite lattices can host majority sublattice chiral flat-bands [141]. In our case, the even and odd layers of the magnetic TI heterostructure are the sublattices. Finally, note the presence of a diagonal symmetry plane evident in Figures 3.24 and 3.26 with $\theta = \pi/3$ and $E = -0.05$ (top left image in each figure). This can be understood as a consequence of the R_y symmetry present in $\hat{x}$-periodic systems given in equation 3.20, which has an anti-diagonal

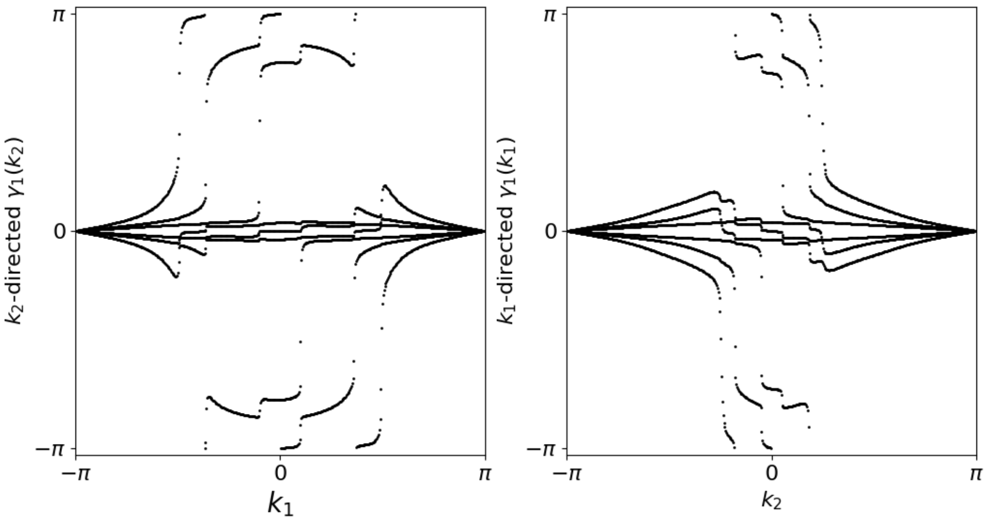

Fig. 3.23 Wilson loops of a three-layer nanoribbon periodic in the x-direction with in-plane magnetisation directed along the x axis and antiferromagnetic coupling between layers, calculated over the valence bands at half-filling. A small canting in the z-direction has been added to make the winding of the Wilson loop more clearly visible. The left (right) panel shows the k_2 (k_1) directed Wilson loop against the k_1 (k_2) wavevector.

form. Therefore, the presence of R_y symmetry in $\hat{x}$-periodic systems suggests the presence of mirror planes with normals parallel to the $\hat{y}$ and $\hat{z}$ axes, creating a resultant diagonal mirror plane.

To summarise, in this section we have shown that using in-plane magnetisation one can engineer flat-bands in a multilayer topological insulator heterostructure. In particular, we have shown that in-plane magnetisation with ferromagnetic coupling between moments in adjacent layers, shown in the left panel of Figure 3.27, leads to flat bands in even and odd layer samples while antiferromagnetic coupling between layers, shown on the right of Figure 3.27, gives flat bands in odd layered samples only. The viability of this approach in real materials is discussed in the following section.

3.4.3 Nodal lines in realistic materials

Having shown that in-plane magnetisation in TI multilayers can produce dispersionless electronic bands, it is worth reflecting on which material systems are required to observe such electronic structures. Before concluding this chapter, we will attempt to link theory back to reality by introducing more realistic material parameters than those used in the prior section.

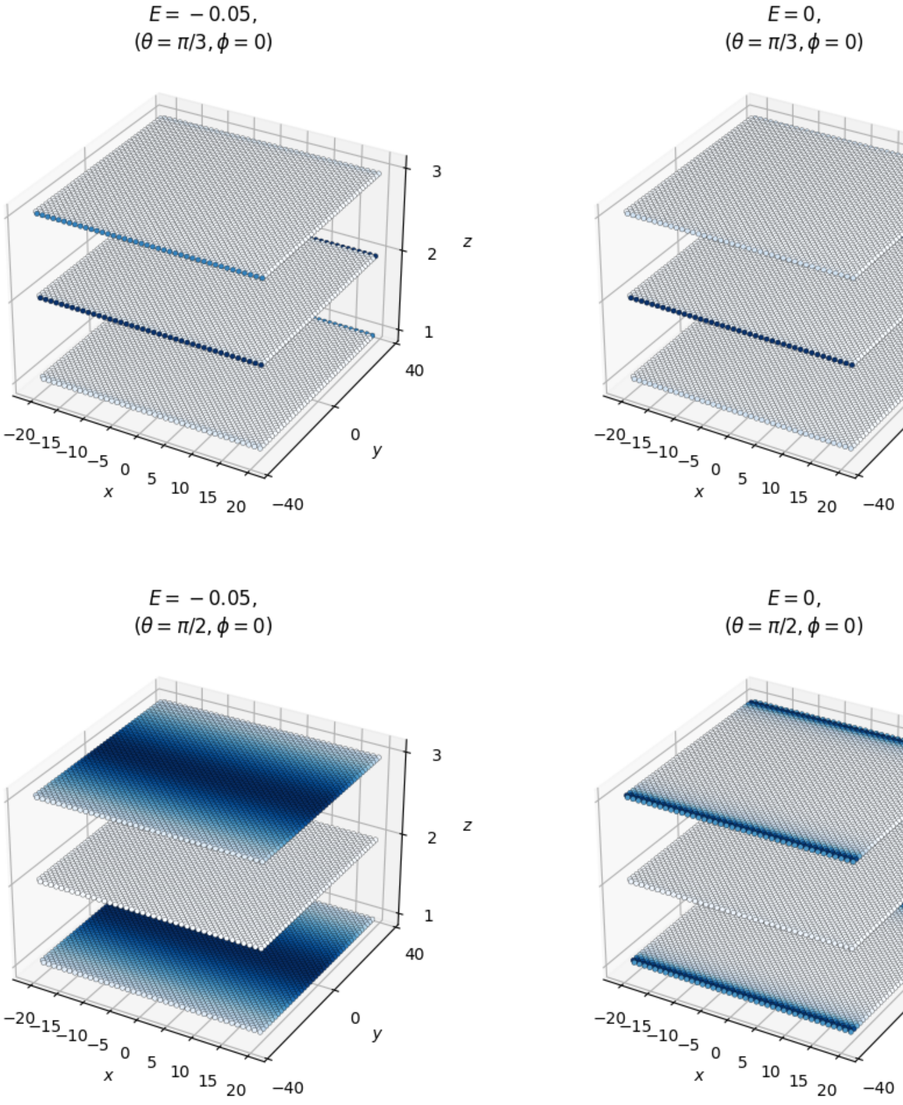
$E = -0.05$, $(\theta = \pi/3, \phi = 0)$

$E = 0$, $(\theta = \pi/3, \phi = 0)$

$E = -0.05$, $(\theta = \pi/2, \phi = 0)$

$E = 0$, $(\theta = \pi/2, \phi = 0)$

Fig. 3.24 Local density of states plots of a three-layer nanoribbon periodic in the $\hat{x}$ direction. The top row shows $\theta = \pi/3$ while the bottom shows $\theta = \pi/2$. The left hand column shows $E = -0.05$ and the right $E = 0$.

In the introduction, the $MnBi_2Te_4$ family of AFMTIs was briefly mentioned as a candidate system for multilayer magnetic TIs, with VBi_2Te_4 and $EuBi_2Te_4$ mentioned as particularly promising candidates due to their easy in-plane magnetisation axis. Studies on these materials remain limited and no set of material parameters fitting the Hamiltonian given in 3.2 have been derived using DFT. Therefore, in order to perform lattice simulations with a realistic set of parameters we will refer to those given for the BSTS family of TIs [112]. In particular, we

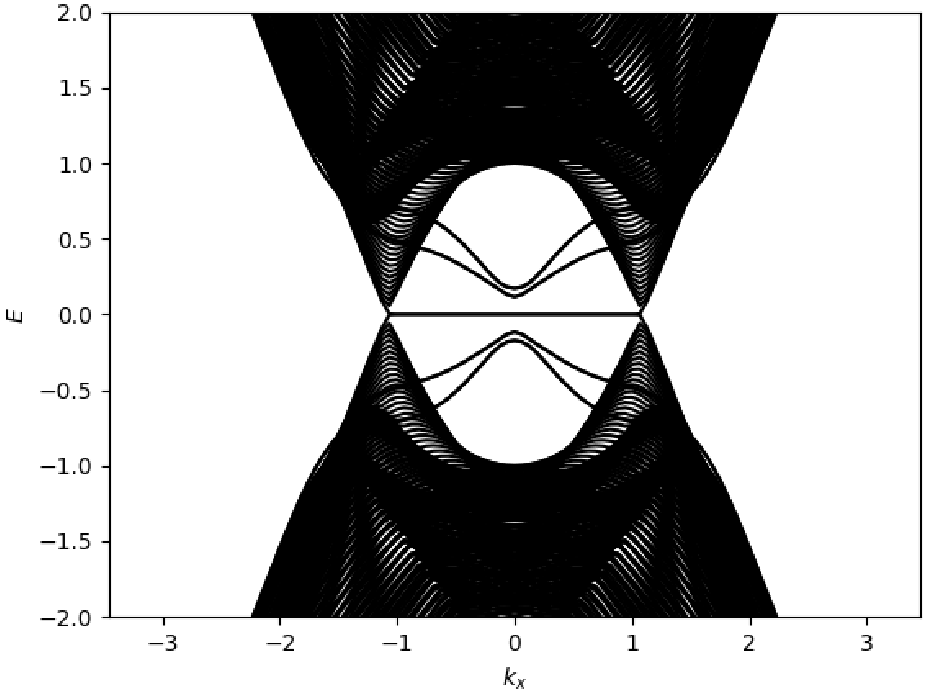

Fig. 3.25 Electronic dispersion relation of a five-layer nanoribbon periodic in the $\hat{x}$ direction with out-of-plane canting for $\theta = \pi/2, \phi = 0$.

will adopt the parameters given for Bi_2Te_3 and Bi_2Se_3, given in table 3.2. The in-plane and out-of-plane lattice constants are given as a = 4.33 Å and c = 40.33 Å, respectively [35].

So far, we have only studied instances where flat-bands arise in systems respecting chiral symmetry by enforcing $C(\boldsymbol{k}) = 0$. With our choice of realistic material parameters we have introduced a term that will cause this symmetry to be broken, meaning that topological invariants like the winding number can no longer be used to characterize a topological flat-band. Nevertheless, an in-plane component of the magnetisation can still be used to close the bulk band gap to create a number of nodal points in the dispersion relation. That said, given that chiral symmetry is integral to the formation of zero-energy flat bands, particle-hole/chiral symmetry breaking terms in the Hamiltonian should be expected to lead to some finite dispersion. In the following we will examine the electronic properties of the systems that were shown to demonstrate flat-band behaviour using realistic parameters.

The electronic dispersion relations of a two layer system periodic in x with and magnetisation configuration ($\theta = \pi/2, \phi = 0$) and ferromagnetic coupling between layers is shown in Figure 3.28. Parameters representative of Bi_2Te_3 and Bi_2Se_3 are shown on the left and the right of the image, respectively. An exchange field of m = 1.5 eV has been chosen. We

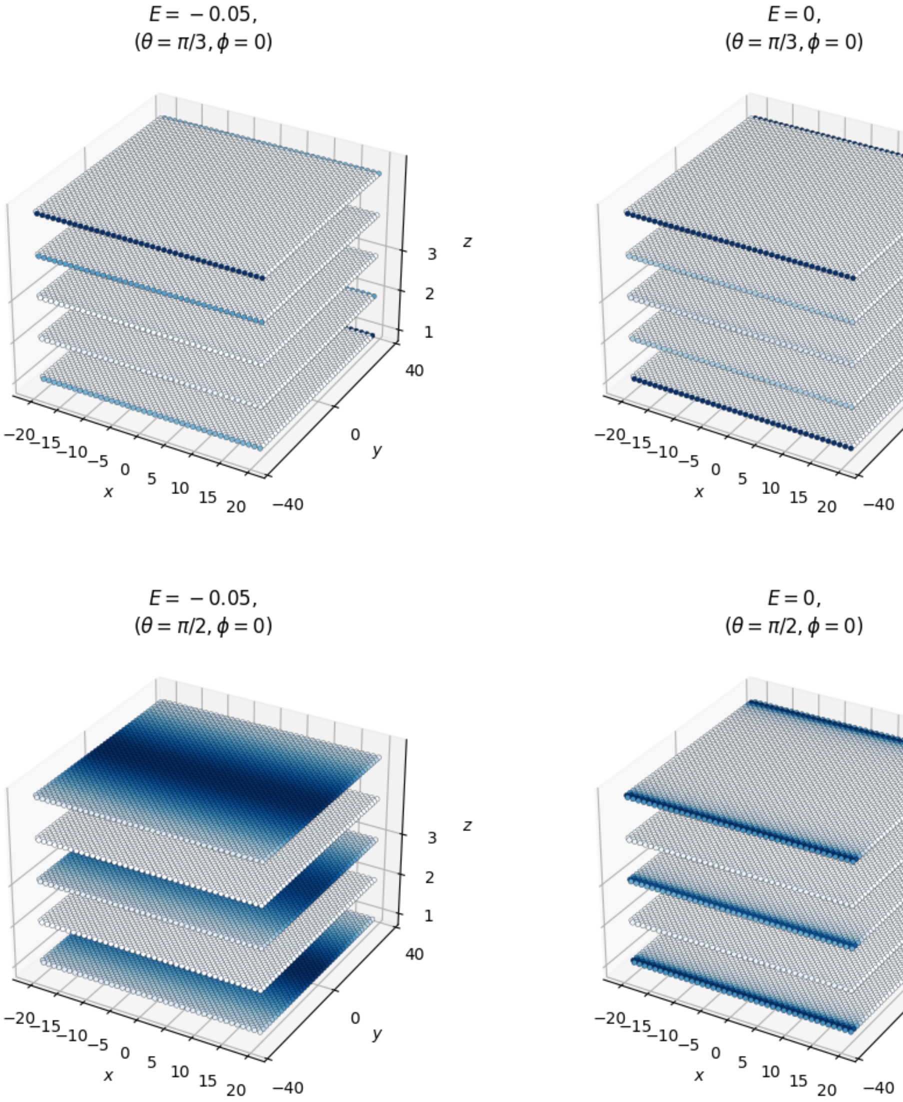

Fig. 3.26 Local density of states plots of a five-layer nanoribbon periodic in the $\hat{x}$ direction. The top row shows $\theta = \pi/3$ while the bottom shows $\theta = \pi/2$. The left hand column shows $E = -0.05$ and the right $E = 0$.

note that for both sets of parameters there are nodal lines with a small, but finite, dispersion centred around $k_x = 0$ rather than the two disjoint dispersionless regions that were previously observed in 3.6. However, there are some interesting differences between the two material systems. Firstly, we observe that the nearly flat-band overlaps with a dispersive set of bulk bands in Bi_2Te_3 due to slightly larger PHS breaking terms, $C(\boldsymbol{k})$. Secondly, the enhanced interlayer hopping present in Bi_2Se_3 (i.e. the parameter v_z), has led to nearly flat-bands appearing at two distinct energies, separated by a small band gap, in contrast to the situation

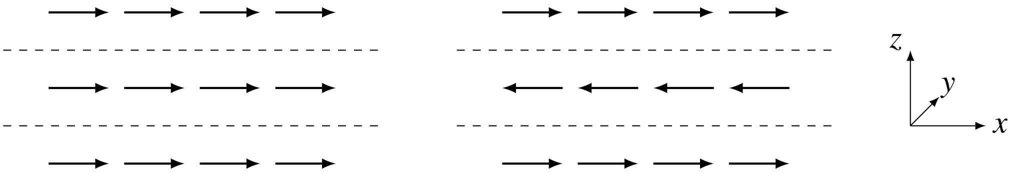

Fig. 3.27 The magnetisation leading to flat-band systems for the model given in 3.2 with $C(\boldsymbol{k}) = 0$. The left hand image shows an in-plane magnetisation with ferromagnetic coupling between layers, while the right shows antiferromagnetic coupling. Note that in the situation of antiferromagnetic coupling, flat=-bands only appear in odd-layered systems.

in Bi_2Te_3 where the bands have appeared coalesce more tightly. This can be understood as a result of the broken chiral symmetry no longer protecting the nodal points at $E = 0$ that were previously observed in the bulk dispersion 3.10.

The situation of three-layer nanoribbons is similar, as shown in Figure 3.29, but where there was a band gap in the two-layer case we have a visible third band in Bi_2Se_3 ensuring that the system is gapless once again. As in the case of the lattice simulations with the toy parameters, realistic three band systems have an additional DP at Γ at zero magnetisation which is shifted in k-space by the in-plane magnetisation. It is not possible to see the splitting of the three bands in Bi_2Te_3, once again due to the suppressed value of the interlayer coupling term v_z.

Finally, the results of lattice simulations for a three-layer system with in-plane magnetisation and antiferromagnetic coupling between layers is shown in Figure 3.30. We see no evidence of the splitting of nodal lines that was observed in three-layer systems with ferromagnetic coupling, Figure 3.29, consistent with the behaviour of the toy model only having a single band crossing due to the shift of the original DP in momentum space. While not shown here, the LDOS of the nodal lines is localized over all three layers of the system.

	Bi_2Te_3	Bi_2Se_3
C_0/eV	-0.18	-0.0083
$C_1/\text{eV}\text{Å}^2$	6.55	5.74
$C_2/\text{eV}\text{Å}^2$	49.68	30.4
M_0/eV	-0.3	-0.28
$M_1/\text{eV}\text{Å}^2$	2.79	6.86
$M_2/\text{eV}\text{Å}^2$	57.38	44.5
$v/\text{eV Å}$	2.78	3.33
$v_z/\text{eV Å}$	0.3	2.26
$w/\text{eV}\text{Å}^3$	45.02	50.6

Table 3.2 Material parameters for the model given in 3.2 for Bi_2Te_3 and Bi_2Se_3 [112].

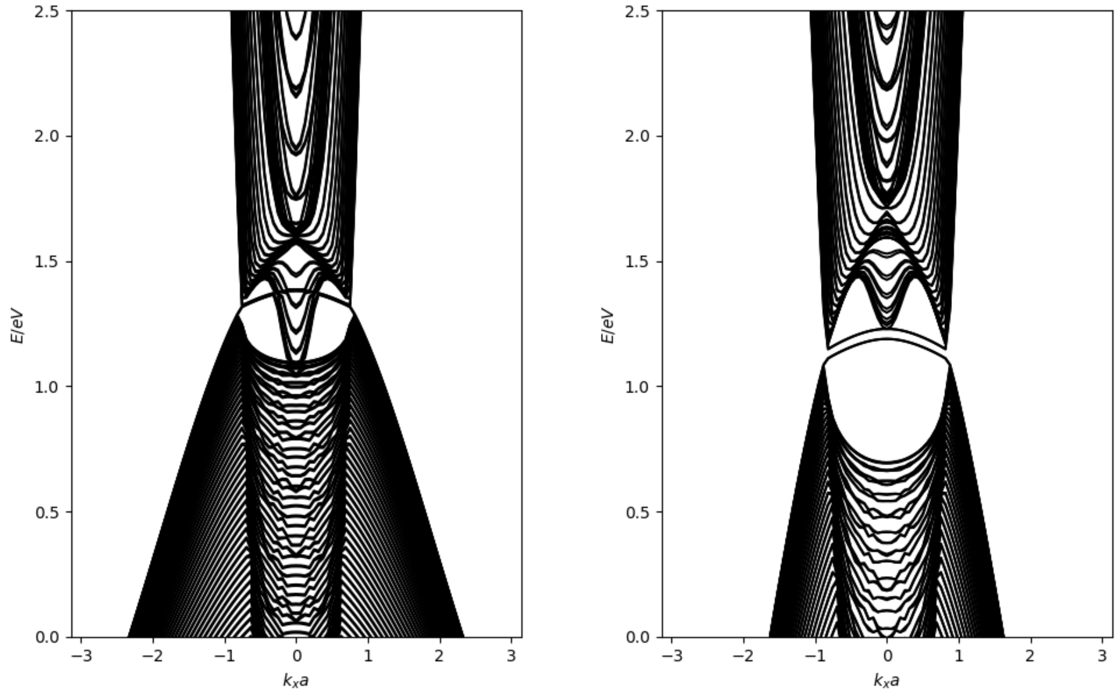

Fig. 3.28 Dispersion of a two-layer system periodic in x with and magnetisation configuration ($\theta = \pi/2, \phi = 0$) and ferromagnetic coupling between layers with parameters derived for Bi_2Te_3 (left) and Bi_2Se_3 (right). A magnetisation energy of 1.5 eV has been used.

Recall from Figures 3.24 and 3.26 that the LDOS around the flat-bands using the toy model parameters was confined to odd layers. This result should not come as a surprise, as the presence of majority sublattice flat-bands relied on the chiral symmetry of the model, which is now broken by the $C(\boldsymbol{k})$ term.

While it is encouraging that nearly flat-bands persist even in realistic materials through the use of in-plane magnetisation, it must be noted that the value of $m = 1.5\,\text{eV}$ is extremely high. While nodal points in the 1D band structure occur at a lower critical magnetisation for both sets of material parameters tested (around $m \approx 0.8\,\text{eV}$ for a two-layer system) this magnetisation energy is required to ensure the nodal lines reside in the band gap of the material and are isolated from the bulk bands. If we were to try and engineer these nodal lines in a bare TI with an external magnetic field, then assuming a g-factor of ≈ 4 for the BSTS family we would need a field strength on the order of tens of thousands of Tesla which is practically infeasible. In addition, exchange splittings in intrinsic magnetic TIs have been estimated to be on the order of 10s of millielectronvolts [105, 202, 68], meaning that it is

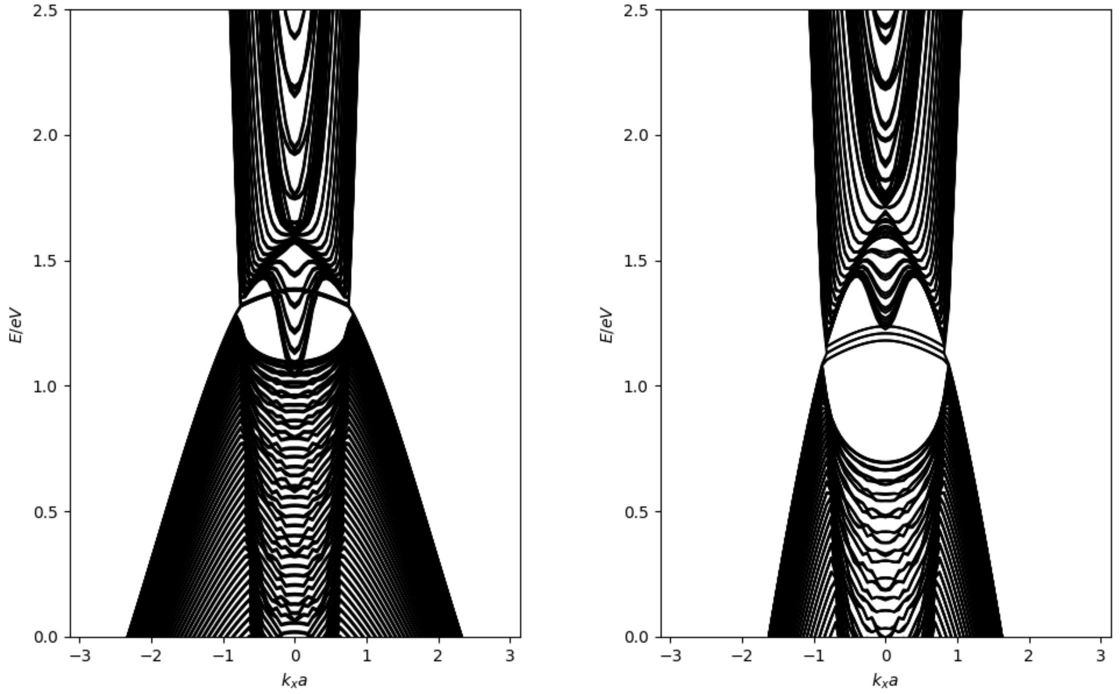

Fig. 3.29 Dispersion of a three-layer system periodic in x with and magnetisation configuration ($\theta = \pi/2, \phi = 0$) and ferromagnetic coupling between layers with parameters derived for Bi_2Te_3 (left) and Bi_2Se_3 (right). A magnetisation energy of 1.5 eV has been used. In contrast to the two-layer case, the dispersion is gapless due to a central nodal line arising from the original DP that has been shifted from Γ in momentum space.

unlikely that one could experimentally probe these nodal lines in the $MnBi_2Te_4$ family of materials, meaning that heterostructure engineering may be required to develop a system with effective material parameters that allow observation of the flat-band topological surface states discussed here. Alternatively, one could adopt a different approach to engineering topological nodal lines, such as strain [99] or, as shall be discussed in the next chapter, magnetic domain walls.

3.5 Conclusion

To conclude, in this chapter we have examined the effect of the sign of the coupling between the magnetisation between layers, i.e. the electronic properties of materials with ferromagnetic vs antiferromagnetic coupling. We have shown that beyond a critical in-plane magnetisation,

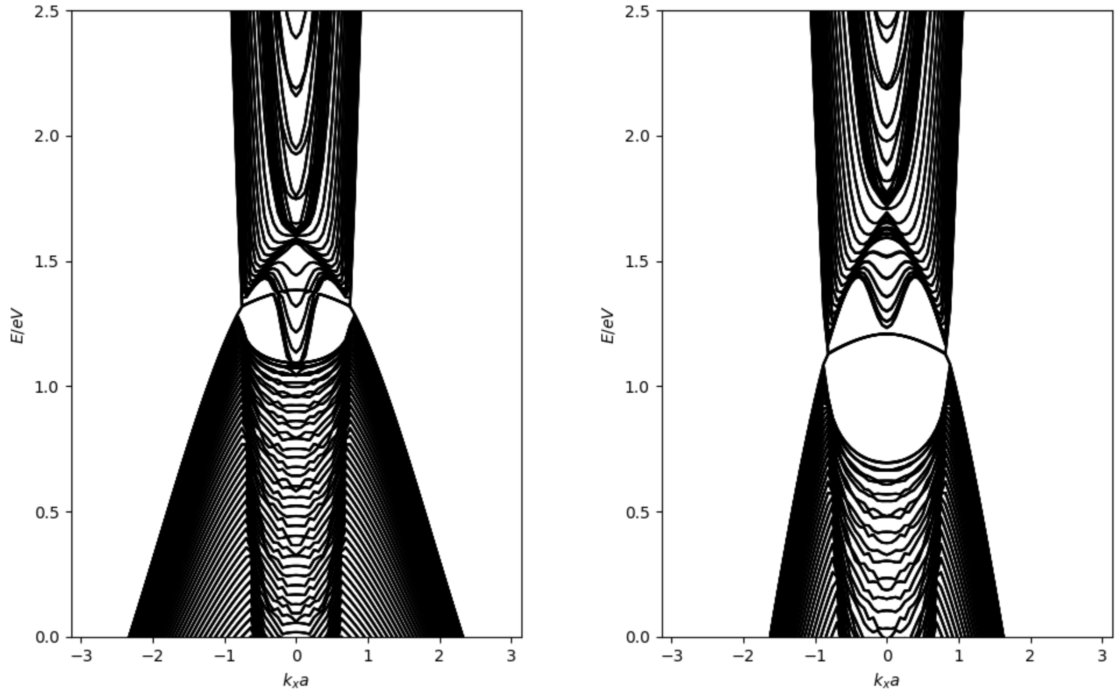

Fig. 3.30 Dispersion of a three-layer system periodic in x with and magnetisation configuration ($\theta = \pi/2, \phi = 0$) and ferromagnetic coupling between layers with parameters derived for Bi_2Te_3 (left) and Bi_2Se_3 (right). A magnetisation energy of 1.5 eV has been used. In contrast to the two-layer case, the dispersion is gapless due to a central nodal line arising from the original DP that has been shifted from Γ in momentum space.

one can drive the system towards an accidental band crossing in order to realise a pair of nodal points. In odd layer systems, these nodes can coexist with the original DP that has been shifted by an amount in k-space away from the Γ point and proportional to the magnetisation. Furthermore, in systems where here is an antiferromagnetic coupling between layers and an easy in-plane axis, an out-of-plane canting can tune the velocity of the boundary states. Such a situation could be engineered with an out-of-plane magnetic field. The feasibility of engineering a material system such as this one has been discussed, and the high exchange splittings required appear to preclude external magnetic fields or intrinsic magnetisation being a viable route forward due to the strength of the particle-hole symmetry breaking terms present in realistic materials.

In the next chapter we utilise the results given here, namely that a non-zero component of the in-plane magnetisation can be used to engineer flat-bands. In particular, we will show that the presence of domain walls and magnetic textures leads to the emergence of spin-polarized chiral flat-bands.

Chapter 4

Magnetic Domain Walls in Antiferromagnetic Topological Insulator Heterostructures

4.1 Chapter Summary

This chapter is primarily based on my paper *"Magnetic Domain Walls in Antiferromagnetic Topological Insulator Heterostructures"* published in *Physical Review B* in 2021, co-authored with Dr. Thierry Ferrus and Professor Crispin Barnes [34].

This chapter builds on the work of the previous, where the the presence of an in-plane magnetisation that respected the underlying chiral symmetry of the lattice was shown to lead to the appearance of flat-bands. In this chapter we explore the emergence of *spin-polarized flat bands* at head-to-head domain walls (DWs) in topological insulator heterostructures with in-plane magnetization and interlayer antiferromagnetic coupling. We show in the framework of quantum well physics that, by tuning the width of a DW, one can control the functional form of the bound states appearing across it. Furthermore, we demonstrate the effect that the number of layers in a multilayer sample has on the electronic dispersion. In particular, the alignment of the magnetization vectors on the top and bottom surfaces of odd-layer samples affords particle-hole symmetry, leading to the presence of linearly dispersing topologically nontrivial states around $E = 0$. By contrast, the lack of particle-hole symmetry in even-layer samples results in a gapped system, with spin-polarized flat bands appearing on either side of a band gap, with a characteristic energy well within terahertz energy scales. Such a system is a versatile platform for the development of spintronic devices and proposes one use in reconfigurable magnetic memory.

4.2 Introduction

In chapter 3 we investigated in-plane magnetism as a means to engineer topologically non-trivial flat-bands into the electronic dispersion relationship of a topological insulator. In this chapter, our investigations consider a multilayer heterostructure where the magnetisation vector is orientated in-plane with antiferromagnetic coupling between layers, as before, but now in the presence of magnetic textures, that is, magnetic domain walls (DWs). These DWs will be used as a means of modifying both the electronic dispersion relation and the spin-polarisation of the electronic states of the TI heterostructures. In particular, the presence of head-to-head DWs (tail-to-tail, equivalently) leads to the formation of quasiparticles with infinite effective mass, localised around the DW [140]. The existence of these quasiparticles may be inferred through a topological argument. For in-plane magnetisation, the Dirac cones will be shifted by equal and opposite amounts in momentum space either side of a DW. The continuity of the energy dispersion relation demands that there must be a band of bound states joining these two Dirac cones across the DW. Furthermore, in order to respect the spin-momentum locked nature of the Dirac fermions, such electronic bands must be spin-polarised.

Throughout this work, we focus on the case of transverse head-to-head (tail-to-tail) DWs. A schematic of a multilayer heterostructure with this spin texture is given in Figure 4.1. While such DWs are more experimentally challenging to realise and control than vortex DWs [177], they offer the advantage of a non-zero in-plane stray field which is a necessary requirement for DW detection in any device [135]. Furthermore, we shall see that there exists a bound charge across head-to-head DWs in magnetic TIs, facilitating both the detection and controlled displacement of the DWs across a macroscopic sample using a local electric field. Bound states have been studied extensively, for example through the use of dislocations, defects and magnetic fluxes. The interested reader is referred to [160, 76, 164, 173, 198, 118, 84, 85] for additional information on the matter.

4.3 Bound States at a Domain Wall

Before we examine the more complex situation of an AFMTI, we will examine the existence of bound states localised around DWs of varying width within a magnetic TI using a simple surface model. We adopt the massless Dirac-Rashba Hamiltonian, which describes the surface states of a TI, given as

$$h_0 = \hbar v_f (\boldsymbol{\sigma} \times \boldsymbol{k})_{\hat{z}} + h_{exc}, \tag{4.1}$$

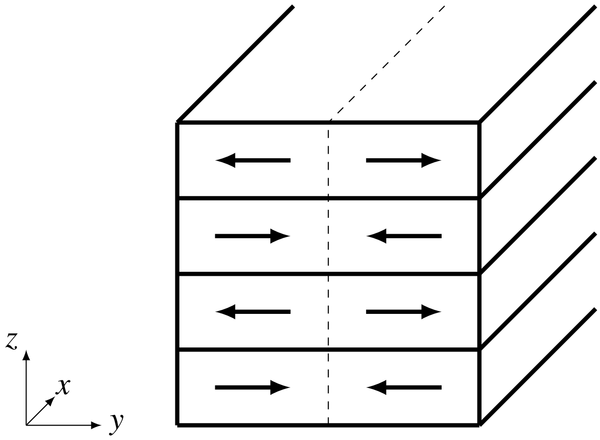

Fig. 4.1 Schematic of a multilayer TI heterostructure with in-plane magnetism and antiferromagnetic coupling between adjacent layers. In this article, we will consider samples of infinite length along the x axis. The magnetisation in each layer either side of the domain wall (dashed line) is shown by black arrows. A sharp head-to-head (tail-to-tail, equivalently) domain wall is shown, however it should be noted that competition between the magnetocrystalline and exchange energies will lead to a realistic domain wall having a finite width.

in the $\hat{\sigma}_z$ basis, where v_f is the Fermi velocity and $\hat{\sigma}_{x,y,z}$ are the Pauli matrices acting on the spin states of the Hamiltonian [58]. Neglecting the exchange term h_{exc} for the moment, this minimal model captures the low-energy physics of single-particle TI edge states near the Dirac point effectively, namely their localisation at the surface and exponential decay into the bulk, and spin-momentum locking. At higher energies, one should also consider the presence of higher order momenta terms (e.g. cubic terms that give rise to hexagonal warping) or disorder terms.

From here, we will adopt units where $\hbar = v_f = 1$. The proximity interaction between local spins and Dirac electrons is accounted for via the introduction of an exchange term

$$h_{exc} = \boldsymbol{M} \cdot \boldsymbol{\sigma}, \tag{4.2}$$

where the vector field $\boldsymbol{M}$ is interpreted as the local magnetisation with magnitude constant M. In order to model domain walls, the in-plane component of the magnetisation is allowed to rotate around the $\hat{z}$ axis, i.e. Bloch domain walls. We may also generally incorporate a canting of the magnetisation in the $\hat{z}$ direction such that there is a non-zero magnetic moment. This phenomenon, known as spin-canting, is observable in some antiferromagnetic materials as they are cooled towards absolute zero and is therefore an important consideration in our investigation of AFMTIs. As a result, the magnetisation vector is

$$\boldsymbol{M} = (M_x(y), M_y(y), M_z) \tag{4.3}$$

It should be noted here that the minimal model described above omits a number of terms that would affect the spin dynamics of our system, leading to a deviation from the simple set-up described. In order to comprehensively model the spin dynamics one would of course have to run a set of micromagnetic simulations, however on the level of the single-particle Hamiltonian one can consider additional terms due to anisotropy an the antisymmetric exchange interaction, also known as the Dzyaloshinski-Moriya interaction (DMI), given by the term

$$H_{DMI} = \sum_{i,j} J_{DMI} \boldsymbol{S}_i \times \boldsymbol{S}_j. \tag{4.4}$$

where J_{DMI} is the DMI coupling constant and $\boldsymbol{S}_i$ is the local spin at site i. The DMI arises in crystals with strong spin-orbit and broken inversion symmetry. Specifically in the multilayer heterostructures that we will later discuss, the DMI is mediated by topological surface states and will generally lead to the formation of nontrivial magnetic textures in MTIs, such as skyrmions which can be detected through the topological Hall effect [143], or topological magnons which in hexagonal materials generally exhibit a Dirac like magnon dispersion relation [104, 36]. Generally the DMI occurs at interfaces between ferromagnetic/non-magnetic materials, for instance due to charge fluctuations at the interface coupling to magnetic moments, meaning that we should also expect it in the multilayer heterostructures discussed here [128, 152]. As we shall discuss later, one possible means to engineer the magnetic textures proposed is through the use of a proximate (anti-)ferromagnet. In this system, in particular, one should expect a non-negligible DMI at the interface. We will not consider these terms in the treatment outlined here and will adopt a simpler picture of localized magnetism, however the interested reader is referred to Hayakawa *et. al.* [59] for a more detailed discussion on the microscopic theory of the DMI in topological and Rashba materials.

In the remainder of this section we shall now show that flat bands constituting bound states, localised across the DW, occur regardless of DW width, i.e. bound states exist across arbitrarily smooth or abrupt DWs of the form given in (4.3).

Owing to the spatially varying exchange field, k_y is no longer a good quantum number. We make the substitution $k_y \to -i\partial_y$ to account for this spatial variation and to solve for the confined surface states of this model. In doing so, we obtain two differential equations for each spin state

$$\begin{aligned}\xi\psi_\sigma(y) =&[(-i\partial_y + M_x) + i\sigma(k_x - M_y)]\\&[(-i\partial_y + M_x) - i\sigma(k_x - M_y)]\psi_\sigma(y)\end{aligned} \tag{4.5}$$

where $\sigma = \pm 1$ corresponds to the two $\hat{\sigma}_z$ basis states at energy E and $\xi = E^2 - M_z^2$. In the case of an infinite strip, one can use the Jackiw-Rebbi argument [72, 26] to show that there must be a bound state at $E = \pm M_z$ satisfying the 1D Dirac equation

$$[(-i\partial_y + M_x) - i\sigma(k_x - M_y)]\psi_\sigma(y) = 0 \tag{4.6}$$

which admits solutions of the form

$$\psi_\sigma(y) \propto \exp\left(-i\int_{\mathbb{R}} M_x \mathrm{d}y - \sigma\int_{\mathbb{R}}(k_x - M_y)\mathrm{d}y\right) \tag{4.7}$$

Depending on the exact form of M_y only one of $\psi_{\uparrow/\downarrow}$ will satisfy the boundary condition $\lim_{y\to\infty}\psi_\sigma(y) = 0$. However, as previously mentioned, our main interest is in solutions for systems of finite width. In the following we will demonstrate the existence of low energy flat-bands by considering the squared Hamiltonian of (4.1), in agreement with the topological arguments for their existence made in the introduction. In the first instance, we will consider a sharp domain wall of the form $M_y = M(2\theta(y) - 1)$, where $\theta(y)$ is the Heaviside step function and M is a constant. We choose $M > 0$ and note that the $M > 0$ and $M < 0$ cases are related by a unitary transformation satisfying $h_0(k_x, -i\partial_y, M) = \sigma_y R_y h_0(k_x, -i\partial_y, -M)R_y^\dagger\sigma_y$, where R_y is a reflection operator that takes $y \to -y$ such that $\partial_y \to -\partial_y$ and $M_y \to -M_y$. We expand equation (4.5)

$$\begin{aligned}\xi\psi_\sigma(y) &= [-\partial_y^2 + (k_x - M_y)^2 + \sigma\partial_y M_y]\psi_\sigma\\&= [-\partial_y^2 + V(y)]\psi_\sigma(y),\end{aligned} \tag{4.8}$$

to obtain the 1D time-independent Schrödinger equation with the spin-dependent effective potential $V(y) = (k_x - \mathrm{sgn}(y)M)^2 + 2\sigma M\delta(y)$ where $\mathrm{sgn}(y)$ gives the sign of y. In the case of an infinite strip, solving this equation recovers the solution given in (4.7). A finite strip of length L can be modelled by adding an infinite potential in the region $|y| > L/2$. In this case, we must satisfy the boundary conditions $\psi_\sigma(y = \pm L/2) = 0$ and continuity of the wavefunction at $y = 0$. The lowest energy bound states are found at $E = \pm M_z$ and are given by,

$$\psi_\sigma(y) = \begin{cases} \frac{\psi(0)\sinh\left(\lambda_+(y+\frac{L}{2})\right)}{\sinh\left(\lambda_+\frac{L}{2}\right)} & y < 0 \\ \frac{\psi(0)\sinh\left(\lambda_-(y-\frac{L}{2})\right)}{-\sinh\left(\lambda_-\frac{L}{2}\right)} & y \geq 0 \end{cases} \tag{4.9}$$

where $\lambda_\pm = |k_x \pm M|$. In the case of the infinite strip only one of the two spin states satisfies the boundary conditions, however the finite strip now hosts spin polarised flat-bands at $E = \pm M_z$ for $|k_x| < M$, which evolve into a pair of dispersive bands for $|k_x| > M$. Furthermore, the wavefunctions for both spin states are localised around the domain wall at $y = 0$.

Of course, while a sharp DW can prove instructive, it is unlikely to be energetically stable and, in a more realistic setting, the magnetisation vector will switch over a larger length scale. With this in mind, we will now consider the situation where the DW varies smoothly over a longer distance. In the case of the finite strip we can model a smooth DW, to first approximation, as

$$(M_x, M_y) = \begin{cases} (0, -M), & y < -l, \\ M\left((1-(\frac{y}{l})^2)^{\frac{1}{2}}, \frac{y}{l}\right), & -l \leq y \leq l, \\ (0, M), & y > l. \end{cases} \tag{4.10}$$

Although linear variation of the in-plane exchange field may appear crude, it can be seen as the lowest order term in a more realistic DW such as $M_y = M \tanh y/l$ and therefore valid in the limit of wide DWs. Furthermore, while it is possible to analytically solve for a smooth DW of the form $\boldsymbol{M} = M(\operatorname{sech} y/l, \tanh y/l)$ by recasting the whole system in terms of Euler's hypergeometric equation, it offers little physical insight and is algebraically dense. As such, we adopt a linearised potential as a model for a smooth DW.

To calculate the energy spectrum of this system, we define the operators $\hat{a} = (-i\partial_y + M_x) + i(k_x - M_y)$. The commutation relation of these operators satisfies

$$[\hat{a}, \hat{a}^\dagger] = \partial_y M_y \tag{4.11}$$

using the canonical commutation relation and the commutator identity $[f(X), Y] = [X, Y]\frac{\partial f}{\partial X}$. Far from the edges of the system within the region $|y| < l$, the Hamiltonian is given by

$$\hat{h} = \begin{pmatrix} M_z & \sqrt{\frac{2M}{l}}\hat{c} \\ \sqrt{\frac{2M}{l}}\hat{c}^\dagger & -M_z \end{pmatrix}, \tag{4.12}$$

where we have defined the creation and annihilation operators for the harmonic oscillator $\hat{c} = \sqrt{\frac{l}{2M}}\hat{a}$ satisfying $[\hat{c}, \hat{c}^\dagger] = 1$, $\hat{c}\,|n\rangle = n\,|n-1\rangle$ and $\hat{c}^\dagger\,|n\rangle = n\,|n+1\rangle$ where $\langle x|n\rangle = H_n(x)$ are the usual Hermite polynomials of the quantum harmonic oscillator. Representing $\hat{h}$ in the restricted basis $\{|n-1\rangle, |n\rangle\}$ we find h_n equal to

$$h_n = \begin{pmatrix} M_z & \frac{1}{l_n} \\ \frac{1}{l_n} & -M_z \end{pmatrix} \tag{4.13}$$

where $l_n = \frac{l_s}{\sqrt{2n}}$ and the characteristic length scale is $l_s = \sqrt{\frac{l}{M}}$. Solving the secular equation, far from the edges a Landau level (LL) spectrum appears due to the linear variation of the in-plane exchange field with spectrum

$$E_n = \pm\sqrt{M_z^2 + \frac{1}{l_n^2}}, \tag{4.14}$$

and associated solutions

$$\psi_{n,\sigma}(y) \propto H_n(y/l_s)\exp\left(-y^2/4l_s^2\right) \quad \text{for} \quad |y| < l. \tag{4.15}$$

Before concluding this section, it is worth presenting an alternative treatment of (4.1) that will allow us to apply some well known results to calculate the electron accumulation (i.e. bound charge) due to the DW. We begin by rewriting (4.1) as

$$h_0 = (\boldsymbol{\sigma} \times (\boldsymbol{k} - e\boldsymbol{a}(\boldsymbol{r}))_{\hat{z}} + M_z\sigma_z, \tag{4.16}$$

where we interpret $\boldsymbol{a}$ as an "axial vector potential" due to the magnetisation, $\boldsymbol{a} = \frac{1}{e}\boldsymbol{M} \times \hat{z}$. Equation (4.16) implies that an electron will "feel" an effective axial magnetic field given by $\boldsymbol{b} = \nabla \times \boldsymbol{a}$ which, in terms of the magnetisation vector, $\boldsymbol{M}$, is

$$\boldsymbol{b}(\boldsymbol{r}) = \frac{1}{e}\left(\hat{z} \cdot \nabla\boldsymbol{M}(\boldsymbol{r}) - \nabla \cdot \boldsymbol{M}(\boldsymbol{r})\hat{z}\right). \tag{4.17}$$

Furthermore, it is a well known result within quantum mechanics that a vector potential coupled to an electron's momentum will induce a quantum Hall response

$$J_i = \sigma_H \epsilon_{ij} e_j \tag{4.18}$$

where J_i and e_i are the i^{th} components of the current density and axial electric field vectors, respectively, $\sigma_H = \frac{e^2}{2\pi}$ is the quantised Hall conductance and ϵ_{ij} is the two-dimensional Levi-Civita tensor. See 1.1.1 for a paedagogical review on the QHE. Note that we are considering the *axial* electric field, defined as $\boldsymbol{e} = -\partial_t \boldsymbol{a}$ (where ∂_t is the time derivative). Substituting the quantum Hall response into the charge conservation equation we have

$$\begin{aligned} \frac{\partial \rho}{\partial t} &= -\nabla \cdot \boldsymbol{J} \\ &= -\sigma_H (\nabla \times \boldsymbol{e})_{\hat{z}}, \end{aligned} \tag{4.19}$$

where ρ is the electron density. Finally, we use the Maxwell-Faraday equation to express the axial electric field in terms of axial magnetic field

$$\begin{aligned} \frac{\partial \rho}{\partial t} &= -\,\sigma_H \left(\frac{\partial \boldsymbol{b}}{\partial t} \right)_{\hat{z}} \implies \\ \Delta\rho &= -\sigma_H b_z, \end{aligned} \tag{4.20}$$

where $\Delta\rho = \rho(b_z) - \rho(0)$ is the change in electron density across the domain wall between the ground state and a non-zero z-component axial magnetic field, b_z. Therefore, In the case of our head-to-head domain walls $\Delta\rho$ is generally given as

$$\Delta\rho = -\frac{e}{2\pi} \partial_y M_y. \tag{4.21}$$

In the case of a sharp domain wall centred around $y = 0$, $M_y = M(2\theta(y) - 1)$ and the accumulated bound charge due to the DW is given by

$$\Delta\rho = -\frac{e}{\pi} M \delta(y) \tag{4.22}$$

i.e. the bound charge is localised around the DW and proportional to the absolute value of the magnetisation vector. This result is in agreement with those obtained in equations 4.9 and 4.15 for the wavefunctions of Hamiltonians with sharp and wide DWs, respectively. It is straightforward to extend this formalism to a multilayer sample, such as that shown in Figure 4.1.

4.4 $\boldsymbol{k} \cdot \boldsymbol{p}$ model for an AFMTI

Having discussed the formation of bound states in the limits of both sharp and wide DWs, we are now equipped to develop a model AFMTI Hamiltonian with transverse head-to-head DWs. We adopt a Burkov-Balents approach [25] in which we consider thin film TI layers separated by wide band gap normal insulator (NI) layers representing the van der Waals gap between TI layers. We may consider the NI to be the vacuum, in which case any states existing within the NI are due to tunnelling between the topological layers either side. Within each TI layer, the non-magnetic part of the Hamiltonian is given as

$$H_{tf} = h_0 \tau_z + t_s \tau_x, \tag{4.23}$$

in the basis $(|t, \uparrow\rangle, |t, \downarrow\rangle, |b, \uparrow\rangle, |b, \downarrow\rangle)^T$, where t/b represent the top and bottom surfaces in each TI layer, $\uparrow / \downarrow$ represent the up/down spin states in the $\hat{\sigma}_z$ basis, and $\hat{\sigma}_{x,y,z}$ and $\hat{\tau}_{x,y,z}$ are Pauli matrices mixing the spins and the surfaces respectively [114]. The first term, h_0, is the surface Hamiltonian of a TI with its surface normal parallel to the $\hat{z}$ direction, as given in (4.1). The second term, $t_s = (m + Bk^2)$, gives the intralayer coupling between surfaces in the same TI layer. The exchange interaction between localised magnetic moments and the Dirac electrons in the j$^{\text{th}}$ TI layer is given as $H_{j,exc} = \boldsymbol{M}_j \cdot \boldsymbol{\sigma}$, where the interlayer antiferromagnetic coupling gives the in-plane component of the exchange field as $\boldsymbol{M}_{j,\parallel} = (-1)^j (M_x, M_y)^T = (-1)^j \boldsymbol{M}_\parallel$. Therefore, depending on the parity of the number of layers, the magnetisation on the top and bottom surfaces of a multilayer sample will be aligned (odd layers) or anti-aligned (even layers), similar to the situation discussed in Chapter 3. We once again consider the formation of head-to-head (tail-to-tail) DWs as described in equation (4.3). As was the case in chapter 3, the model we shall consider here will host only a single DP at the Γ point. The DWs described here will therefore result in an effective mass term, however if we had DPs at different points in the BZ then we would expect a different coupling. In addition, we note that the model given here is not representative of bulk intrinsic magnetic TIs and instead only describes the edge states. In the MnBi$_2$Te$_4$ family of compounds, changing the number of layers changes the magnetic coupling between layers from AFM to FM (and vice versa) [130]. In general, therefore, we should include these terms as they will have observable effects on the electronic properties of the system. They are omitted here due to the small number of layers considered.

Including the magnetic contribution and the coupling between layers, the full Hamiltonian of the multilayer AFMTI is given by

$$H(k_x, -i\partial_y) = \begin{pmatrix} H_+ & T_z & 0 & 0 & \\ T_z^\dagger & H_- & T_z & 0 & \\ 0 & T_z^\dagger & H_+ & T_z & \cdots \\ \vdots & & & \ddots & \\ & & 0 & T_z^\dagger & H_\eta \end{pmatrix} \tag{4.24}$$

where $H_\eta = H_{tf} + \eta \boldsymbol{M}_\parallel \cdot \boldsymbol{\sigma} + M_z \sigma_z$ is the intralayer Hamiltonian, including a canting of the exchange field towards the z axis, and $T_z = t_d \tau_-$ gives the interlayer hopping between nearest neighbour TI layers. We have again made the substitution $k_y \longrightarrow -i\partial_y$ to account for the spatial variation of $\boldsymbol{M}_{\|}$. The index $\eta = \pm 1$ is used to determine the orientation of the magnetisation depending on the parity of the layer in question.

We are now in the position to consider the effect of the parity of the number of layers on the electronic dispersion of an AFMTI. In order to do so we will consider the simplest, non-trivial examples of even and odd layer parity samples, that is, two and three layer AFMTIs. This is simply for clarity, as the results we obtain for these systems are also applicable for larger even and odd layer systems.

In order to solve for a multilayer sample, one can adopt a perturbation theory approach or a numerical scheme. Here we present a numerical solution, calculated by discretising Hamiltonian (4.24) on a square lattice through the use of the finite-difference approximation. All results are for samples of length 50 nm in the $\hat{y}$ dimension. Accordingly, parameters in the Hamiltonian are chosen as $\hbar v_f = 300\,\text{meV nm}$, $m = 25\,\text{meV}$, $B = -100\,\text{meVnm}^2$, $t_d = 50\,\text{meV}$ [114, 207]. For completeness, the results of a perturbative calculation for two and three layer systems are presented in Appendix A.

4.4.1 Two Layer System

Using the notation of (4.24), the Hamiltonian of a two layer system is given as

$$H_2 = \begin{pmatrix} H_+ & T_z \\ T_z & H_- \end{pmatrix}. \tag{4.25}$$

In systems with an even number of layers the magnetisation vectors will be anti-aligned on opposite surfaces of the sample, breaking inversion symmetry. However, this Hamiltonian possesses a C_2 rotation symmetry, $[H_2, P] = 0$, where P is given by

$$P = \begin{pmatrix} 0 & \sigma_z\tau_x \\ \sigma_z\tau_x & 0 \end{pmatrix}. \tag{4.26}$$

Exploiting this symmetry, H_2 (4.25) can be block diagonalised, using the shared eigenbasis of H_2 and P

$$U_P H_2 U_P^\dagger = H_2' = \begin{pmatrix} H^+ & 0 \\ 0 & H^- \end{pmatrix}, \tag{4.27}$$

where U_P is the unitary matrix formed of the eigenvectors of P and the two sub-blocks $H^\pm$ are given by

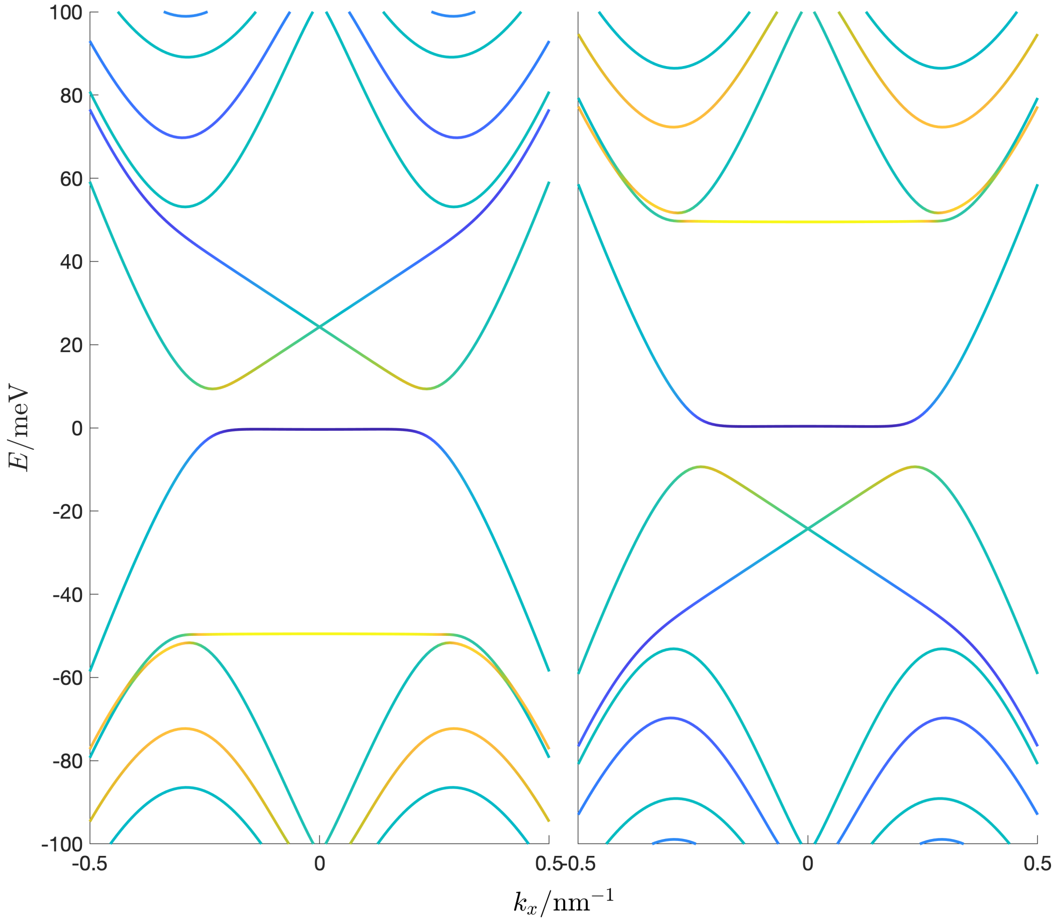

Fig. 4.2 Electronic dispersion relations from the sub-block Hamilonians H^+ (left) and H^- (right). States are coloured according to their spin-z expectation value, $S_z = \langle\Psi|\,\sigma_z\,|\Psi\rangle$, with spin up and down given by yellow and blue, respectively.

$$H^{\pm} = \begin{pmatrix} h_0 + \boldsymbol{M}_{\parallel} \cdot \boldsymbol{\sigma} + M_z\sigma_z & t_s \\ t_s & -h_0 + \boldsymbol{M}_{\parallel} \cdot \boldsymbol{\sigma} + (M_z \pm t_d)\sigma_z \end{pmatrix}, \tag{4.28}$$

where the sub-blocks are labelled according to the corresponding eigenvalues of P, $\alpha_p = \pm 1$ (see Appendix A for further details). Written in this form, it is slightly easier to see that the two layer system possess a chiral symmetry when $M_z = 0$:

$$\begin{gathered} CH_2'(\boldsymbol{k})C^{\dagger} = -H_2'(\boldsymbol{k}) \quad \text{where} \\ C = \begin{pmatrix} 0 & \sigma_z\tau_z \\ \sigma_z\tau_z & 0 \end{pmatrix}. \end{gathered} \tag{4.29}$$

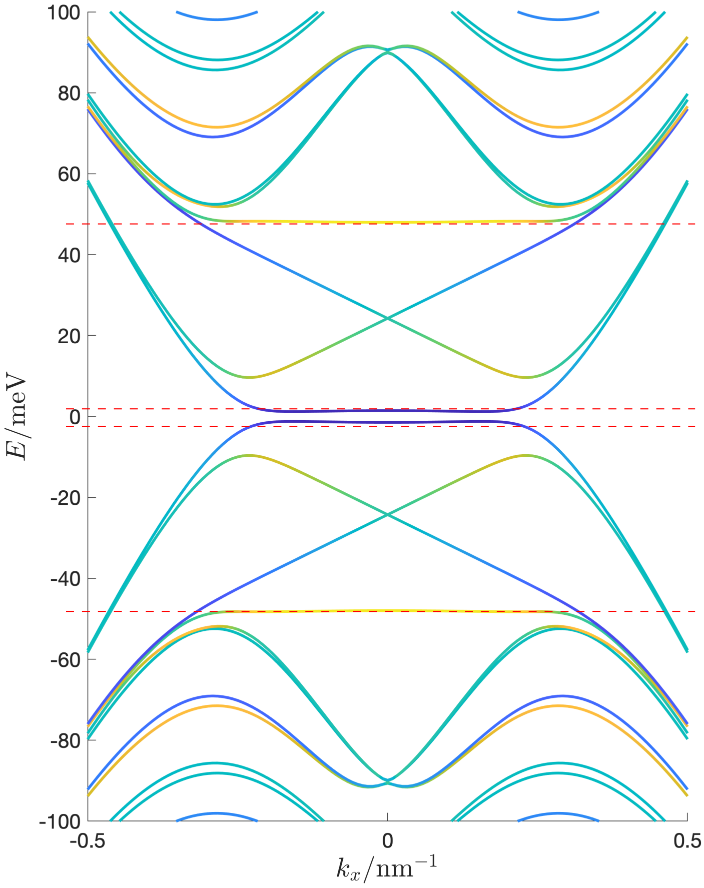

Fig. 4.3 The electronic dispersion of a 50 nm wide, two layer system with $M_z = 0$. The dashed red lines correspond to the energies that the thermally broadened LDOS images given in Figure 4.4 are calculated at, where the lowest energy cut corresponds to the leftmost image.

The result of this is that the bandstructures of the two sub-block Hamiltonians, (4.28), should be the inverse of one another, i.e. an eigenstate $\left|\psi_{n,\sigma,\boldsymbol{k}}\right\rangle$ at energy $E_{n,\boldsymbol{k}}$ of one sub-block should also be an eigenstate of the other at energy $-E_{n,\boldsymbol{k}}$, where $\sigma =\uparrow/\downarrow$ is the spin of the electron. Furthermore, it is interesting to note that (4.28) is identical to the thin film Hamiltonian given in (4.23) with an additional spin-dependent surface inversion asymmetry equal to $\pm t_d$. Comparison of (4.28) to the surfac Hamiltonian (4.1) implies that we should expect the appearance of flat-bands at $E \approx M_z$ and $E \approx (M_z \pm t_d)$ with states localised across the DW at $y = L/2$, along with edge-states localised around $y = 0, L$ due to the intralayer coupling term, t_s.

These hypotheses are confirmed through numerical diagonalisation of the discretised lattice Hamiltonian, as shown in Figure 4.2 which plots the energy dispersions of the separate sub-blocks, $H^{\pm}$, with a sharp domain wall, $M_y = 2M(\theta(y) - 1)$, and $M_z = 0$. We focus on the case $M > 0$ as it is related to the $M < 0$ case by a unitary transformation, the effect of

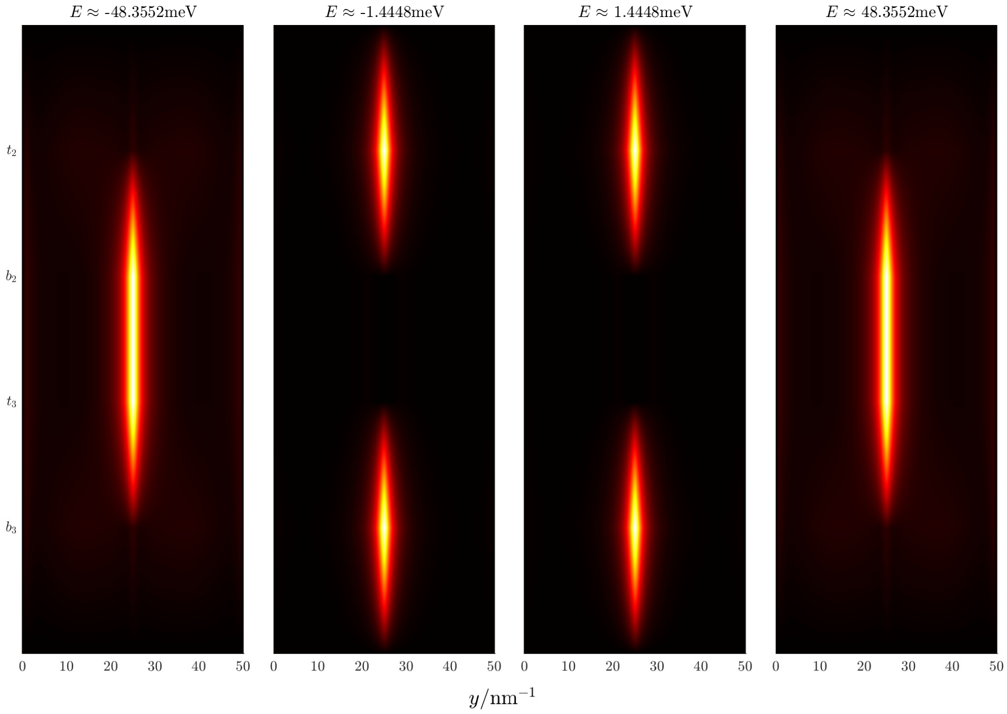

Fig. 4.4 The thermally broadened LDOS given at energies corresponding to the flat bands. From left to right, $E \approx -t_d, 0, 0, t_d$. The vertical position in the multilayer structure is shown along the z axis where, for example, t_1 denotes the top surface of the 1st layer. The LDOS was calculated using equation (4.30) with $k_B T = 1$ meV. The cuts in the dispersion relation at which the LDOS has been calculated are shown in the dispersion relation in Figure 4.3.

which is simply to flip the spin-polarisation of the flat-bands as discussed in section 4.3. Spin-polarised flat-bands appear in both band structures at $E \approx 0$ and $E \approx \pm t_d$, along with edge-bands with Dirac points at $E \approx \pm t_d/2$. These bands are formed from the remnants of flat-bands that would have otherwise formed at $E = 0$ and $E = \pm t_d$, had it not been for the intralayer coupling term, t_s. The strength of the coupling between these edge-states and the proximate flat-bands can be controlled by tuning the energy difference between them, using M_z, or using the intralayer coupling term, t_s.

The full band structure of the two layer system is shown in Figure 4.3. As the complete spectrum of H_2 is composed of the H^+ and H^- spectra, there is only a small direct band gap between the two low energy flat-bands of each block. By varying the coupling between the top and bottom surfaces of each TI layer using the parameter m, which appears as the wavevector independent term in the intralayer coupling t_s, the band gap can be enhanced by controlling the interaction between the flat-bands and the edge-states.

Shown in Figure 4.4 are the thermally broadened local density of states (LDOS) at energies around the flat bands. The thermally broadened LDOS is calculated as

$$\rho(y, z, E) \propto \int_{BZ} dk_x \sum_n \omega(E - E_n) |\psi_n(k_x, y, z)|^2, \tag{4.30}$$

where E_n and $\psi_n(k_x, y, z)$ are the energy and eigenstate of the n^{th} band, respectively, and $\omega(E) = -\frac{\partial}{\partial E} f(E)$ is a thermal broadening function, where $f(E)$ is the Fermi-Dirac distribution. The thermally broadened LDOS, rather than the standard definition of the LDOS, is chosen for this calculation as it is directly related to the electronic properties of the system at experimentally relevant temperatures, T. For example, the differential conductance measured by a scanning tunnelling microscopy (STM) probe is dependent on the thermally broadened LDOS. Furthermore, taking the limit $T \longrightarrow 0$ recovers the definition of the standard LDOS, i.e.

$$\lim_{T \to 0} \rho(y, z, E) = LDOS(y, z, E) = \int_{BZ} dk_x \sum_n \delta(E - E_n) |\psi_n(k_x, y, z)|^2. \tag{4.31}$$

As demonstrated using the surface model (4.1) the flat-band states are strongly localised around the domain wall. Interestingly, we find that the low energy flat-band states are localised across the top and bottom surfaces of the sample, while those at $E \approx \pm t_d$ are located within the bulk (i.e. split across b_1/t_2). The C_2 rotation symmetry of the two layer system demands that the top and bottom surfaces are equivalent, hence that the low energy states are split equally across them. However, a small electric field applied along the growth ($\hat{z}$) direction can break this symmetry, biasing one side of the sample with respect to the other. One would expect this to have an experimentally measurable consequence in terms of the anomalous Hall effect along the domain wall. Electrons transmitted through the DW will be subjected to out-of-plane spin polarization (in the case of $M_z > 0$, the flat-bands consist entirely of spin-down electrons). The strong SOC in TI heterostructures will lead to a transverse current, i.e. an observable Hall effect. Where one side the the heterostructure is biased with respect to the other, as described above, this could in theory lead to a Hall effect confined to a single layer. This would almost certainly not be observable in a bare AFMTI, however may be possible in a multilayer heterostructure where MTI layers are separated from one another by a wide band-gap normal insulator with a high dielectric constant.

We conclude our investigation of the two layer system by examining the effect of a canted magnetisation, i.e. $M_z \neq 0$. Figure 4.5 shows the effect that M_z has on the dispersion relation of the two layer system. The cases $M_z > 0$ and $M_z < 0$ are related via a unitary

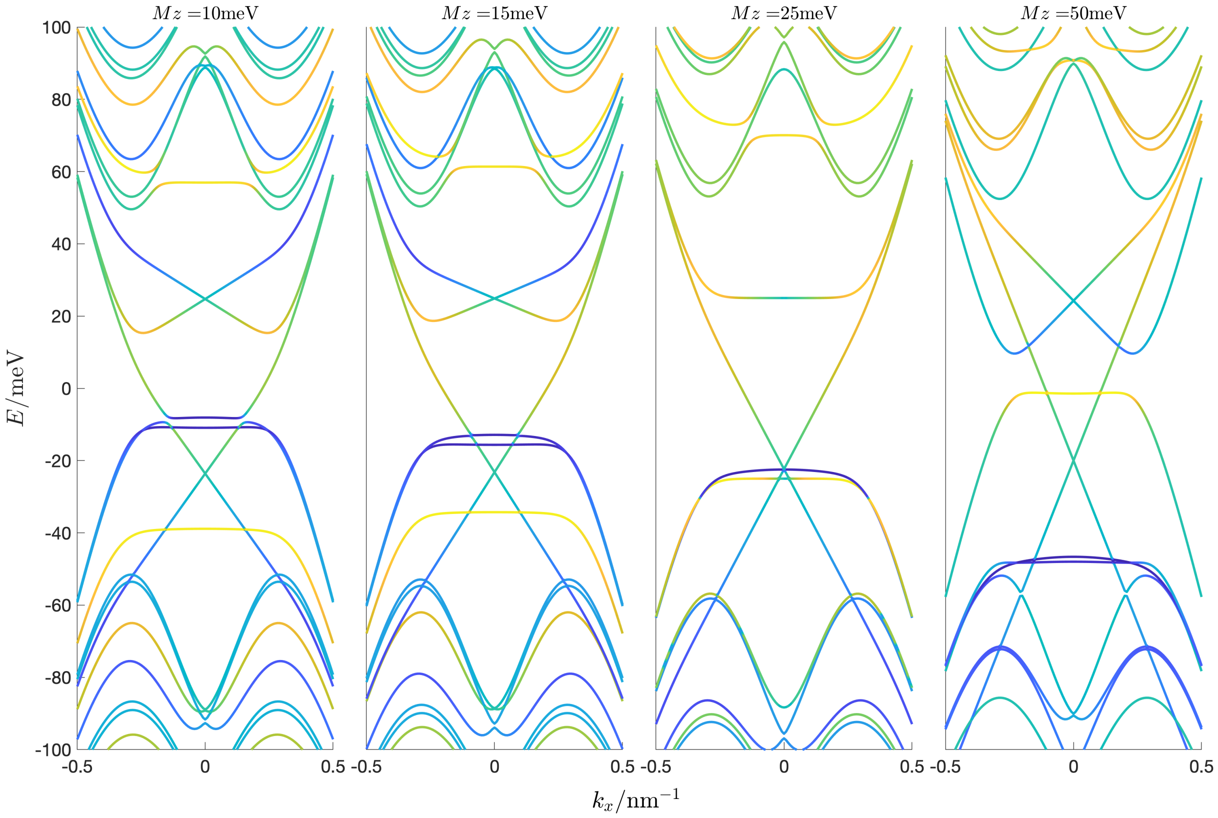

Fig. 4.5 The effect of $M_z \neq 0$ on a two layer system. From left to right, $M_z = 10, 15, 25, 50$meV.

transformation and so we present results only on the former. Most obviously, the presence of a non-zero canting breaks the chiral symmetry of the system, given by equation (4.29), ensuring that the bandstructure is no-longer symmetric around $E = 0$. Moderate values of M_z shifts the position of the spin down (up) flat-bands downwards (upwards), i.e. the Zeeman effect, reducing the gap in the H^+ block between the low energy flat-band and the edge-states. Increasing $M_z > t_d/2$ removes the anti-crossing between the flat-band and the edge state at $E \approx -t_d/2$ in the H^+ sub-block, leading to a pair of linear dispersing edge-states. However, the behaviour of the edge-states in the H^- block is strikingly different. The remnants of the flat-bands comprising these bands shift in energy, leading to a reduction in the group velocity until the edge-states are themselves a set of flat-bands at $M_z = t_d/2 = 25$ meV. A further increase in M_z leads to a complete inversion of the H^- edge state bands, as shown in the right most panel of Figure 4.5. These results demonstrate the control an experimentalist may wield upon this system through the use of an external magnetic field. Before concluding, it is worth briefly commenting on the magnetisation energies required to tune the energy of the flat bands. If we adopt g-factors of $g_z \approx 10$ for perpendicular magnetic fields, as motivated by the order of magnitude of the g-factors for the BSTS family of TIs [112], then the average external perpendicular magnetic field required to generate a magnetisation energy of $m \approx 25\,\mathrm{meV}$ is around 40T which, while certainly experimentally possible, is certainly not within the reach of most day-to-day lab equipment. Alternative means to realise the flat-bands discussed above are given in section 4.6.

4.4.2 Three Layer System

Again, in the notation of (4.24), the Hamiltonian of a three layer system is

$$H_3 = \begin{pmatrix} H_+ & T_z & 0 \\ T_z^\dagger & H_- & T_z \\ 0 & T_z^\dagger & H_+ \end{pmatrix} \tag{4.32}$$

Here, as in all odd layer systems, the magnetisation vector aligns on the top and bottom surfaces of the multilayer sample, affording the system inversion symmetry

$$\begin{gathered} IH_3(\boldsymbol{k})I^\dagger = H_3(-\boldsymbol{k}) \quad \text{where} \\ I = \begin{pmatrix} 0 & 0 & \tau_x \\ 0 & \tau_x & 0 \\ \tau_x & 0 & 0 \end{pmatrix}. \end{gathered} \tag{4.33}$$

We will exploit this inversion symmetry in demonstrating the particle-hole symmetry of the system, which satisfies

$$\begin{gathered} \Gamma H_3(\boldsymbol{k})\Gamma^\dagger = -H_3(-\boldsymbol{k}) \quad \text{where} \\ \Gamma = \begin{pmatrix} 0 & 0 & i\sigma_y\tau_y \\ 0 & i\sigma_y\tau_y & 0 \\ i\sigma_y\tau_y & 0 & 0 \end{pmatrix} K, \end{gathered} \tag{4.34}$$

where K is the complex conjugation operator. In this case, $\Gamma^2 = -1$, i.e. an anti-unitary operator. The presence of particle-hole symmetry within this model implies we should expect that edge states will exist around $E = 0$, that is, low-energy, topologically non-trivial states. Both inversion and particle-hole symmetry are respected even in the case of $M_z \neq 0$, for all odd layer systems.

The electronic dispersion of a three layer system is shown in Figure 4.6 with $M_z = 5\,\mathrm{meV}$ to clearly show the formation of gapless low energy edge-states between the spin-polarised

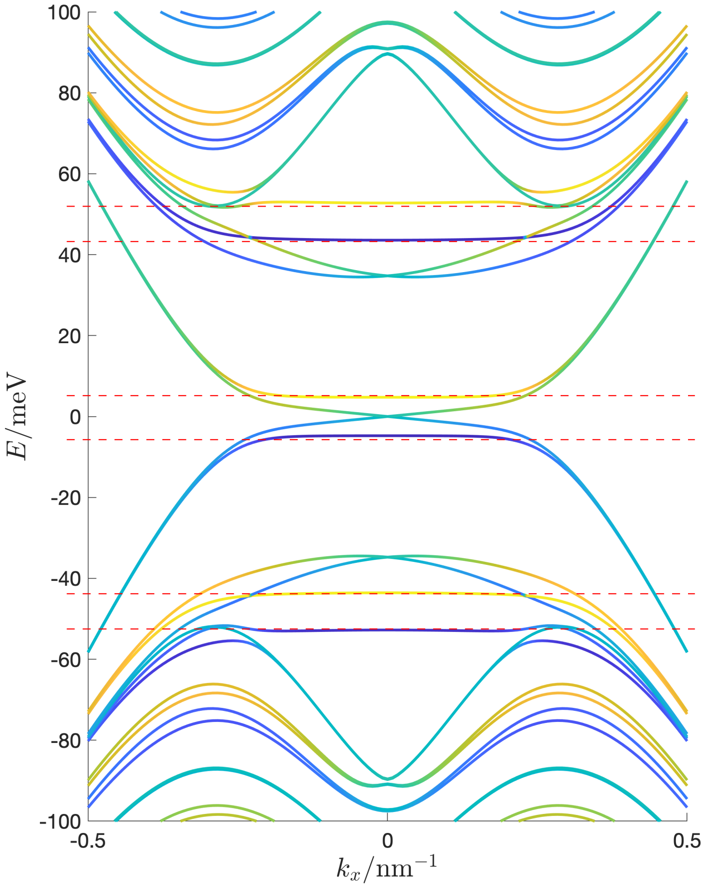

Fig. 4.6 The electronic dispersion of a 50 nm wide three layer sample with $M_z = 5$ meV. The dashed red lines correspond to the energies that the thermally broadened LDOS images given in Figure 4.7 are calculated at, where the lowest energy cut corresponds to the leftmost image.

flat-bands at $E \approx \pm M_z$. Due to the particle-hole symmetry of the system, we observe that if there exists a state $\left|\psi_{n,\sigma,\boldsymbol{k}}\right\rangle$ at energy $E_{n,\boldsymbol{k}}$ then there is a state $\left|\psi_{n,-\sigma,-\boldsymbol{k}}\right\rangle$ at energy $-E_{n,-\boldsymbol{k}}$ related by the particle-hole operator given in equation (4.34). It is also notable that in addition to the low-energy topological edge-states, there are two more pairs of edge-states with crossings at $E \approx \pm t_d/\sqrt{2}$.

Also shown are the LDOS of flat-bands in Figures 4.7. In contrast to the flat-band states in the two layer model, the low-energy flat-band states at $E \approx \pm M_z$ in the three layer system are strongly localised around the DW on either the top or bottom surface due to the presence of reflection symmetry. Thermal broadening effects show a small intensity on the opposite surface of the sample, however as the temperature is decreased the LDOS will become more highly localised on one surface only. As is the case in two-layer samples, higher energy flat-bands correspond to DW states localised within the bulk layers (i.e. across b_1/t_2 and b_2/t_3). Hereafter, these states will be referred to as bulk flat-bands.

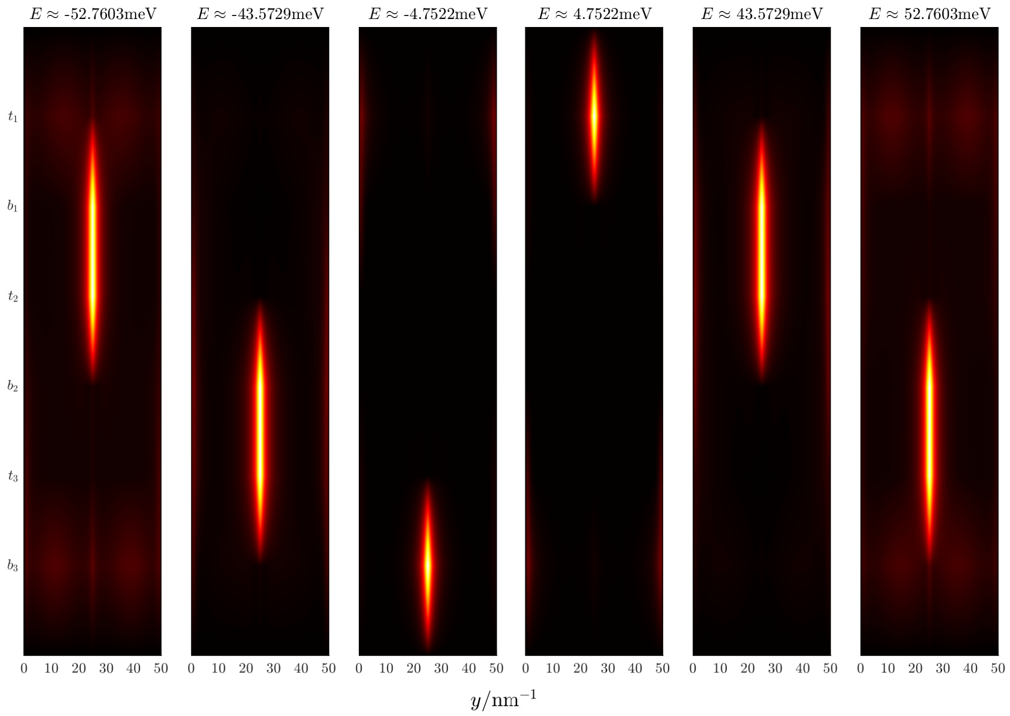

Fig. 4.7 The thermally broadened LDOS in a three layer system given at energies corresponding to the flat bands. From left to right $E \approx -t_d - M_z, -t_d + M_z, -M_z, M_z, t_d - M_z, t_d + M_z$. The LDOS was calculated using equation (4.30) with $k_B T = 1$ meV. The cuts in the dispersion relation at which the LDOS has been calculated are shown in the dispersion relation in Figure 4.6.

Analogously to the behaviour of the two layer model, we can tune the coupling between these bulk edge-states and the corresponding flat-bands by varying the parameter M_z. Again, we only consider the case $M_z > 0$ and present our results in Figure 4.8. Similarly to the two layer system, the effect of moderate values of M_z is a Zeeman effect. As the low energy flat-bands are shifted away from $E = 0$, the group velocity of the low energy edge-states increases. At larger values of M_z the bulk flat-bands are migrate towards $E = 0$ and beyond, eventually removing the anti-crossing between these flat-bands and the edge-states at $E \approx \pm t_d/\sqrt{2}$. Therefore, at large values of M_z, the resultant band structure is three uncoupled Dirac cones bounded by a series of flat-bands.

While it is possible in the two layer model to induce a band gap on the order of meV by tuning the parameters in the Hamiltonian, this is not the case for a three layer sample due to the low energy topological states. However, we may exploit the finite size effect [211] in order to gap these topological states.

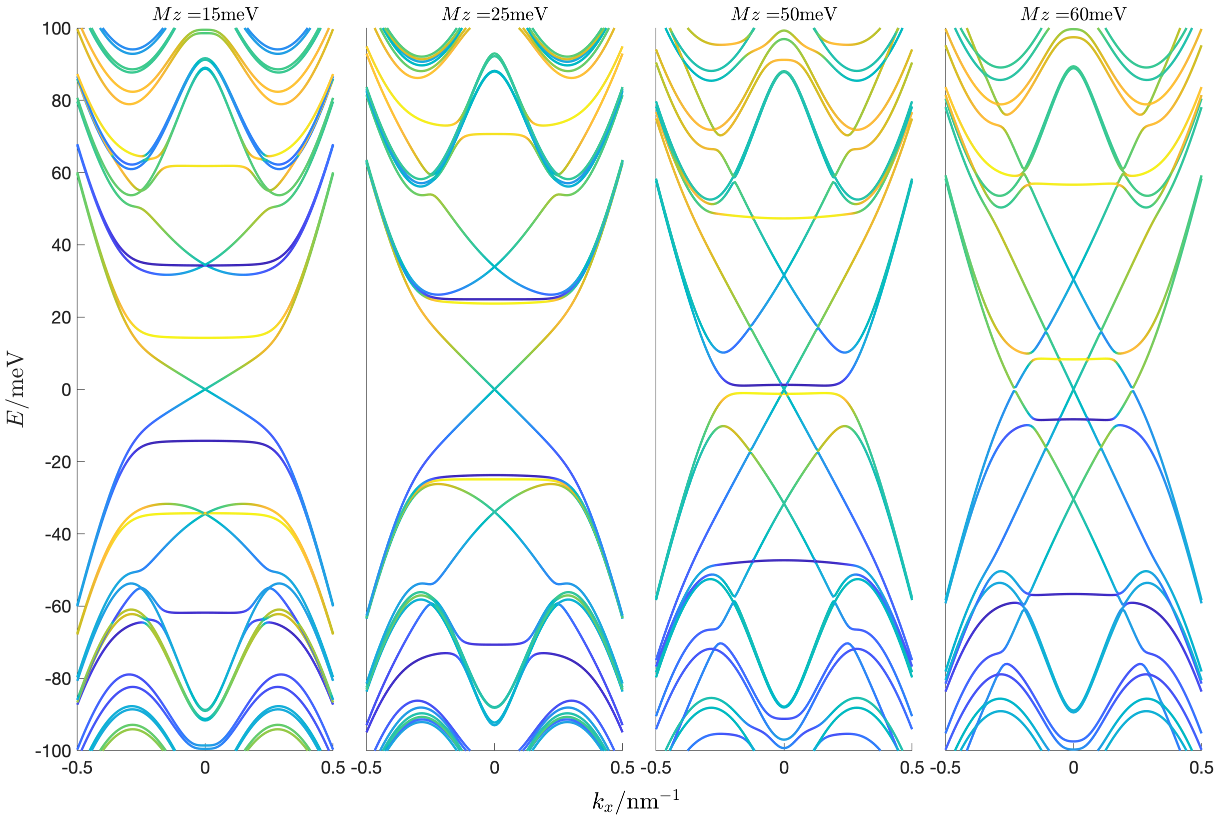

Fig. 4.8 The effect of $M_z \neq 0$ on a three layer system. From left to right, $M_z = 15, 25, 50, 60$meV.

4.5 Other Domain Wall Configurations

Having shown that head-to-head DWs in TIs can provide a suitable playground to engineer spin-polarised flat-bands, it is worth investigating whether we obtain the same or similar results through considering more general DW configurations.

In the first instance, are the presence of flat-bands in multilayer AFMTIs robust to the presence of DWs of finite width? Given the results of section 4.3, we should expect that they are when the local spins are confined to the xy plane - i.e. a transverse head-to-head DW - as demonstrated in Figure 4.9(a). Figure 4.10 confirms that this is indeed the case for two and three layer systems where the magnetisation is allowed to vary smoothly as $\boldsymbol{M}_t(\boldsymbol{r}) = (-1)^z M(\operatorname{sech}(y/l), \tanh(y/l), 0)$, where $2l = 50\,\mathrm{nm}$ is the total width of the DW. Apart from the exact energies the flat-bands are located at, the low-energy dispersion relations of both systems are practically identical to those for the case of the sharp domain wall. For brevity, the thermally broadened LDOS around the flat-bands is not shown for either system,

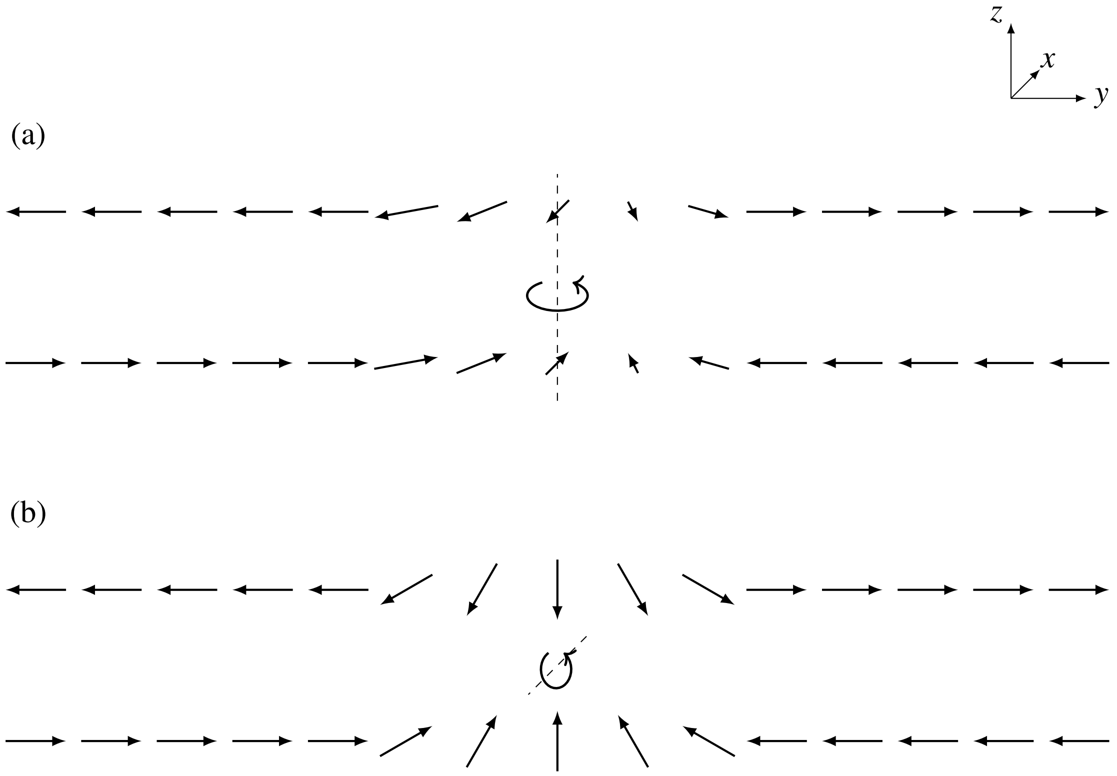

Fig. 4.9 Possible head-to-head (tail-to-tail) DW configurations in an A-type antiferromagnet. (a) shows a transverse DW where the spins are restricted to lie in the xy plane, rotating around the z axis, where-as (b) shows the out-of-plane DW configuration where spins rotate along the x axis and are restricted to the yz plane.

however they are identical to those presented in the previous section except for the fact that they are now broadened across the entire width of the finite sized DW.

Figure 4.9(b) demonstrates an alternative, out-of-plane (OOP) configuration where the local spins are restricted to the yz plane, $\boldsymbol{M}_{oop}(\boldsymbol{r}) = (-1)^z M(0, \tanh(y/l), \operatorname{sech}(y/l))$. Given the results of the previous section, namely that a global canting of the magnetisation in the z direction resulted in a shift of the flat-bands in energy according to the Zeeman effect, we should naively expect a similar effect from an OOP DW. However, we find that flat-bands in two-layer systems are not robust to this spin configuration. As shown in Fig 4.11, the bands characterising states localised around the DW retain their spin polarisation, but take on a more parabolic character. While in the transverse configuration a globally uniform canting of the magnetisation resulted in a shift of the energy bands, the spatial variation of the z component in the OOP configuration results in the states localised around the DW gaining a finite effective mass. Furthermore, the presence of an antiferromagnetic coupling along the z axis also demonstrates the breaking of C_2 rotation symmetry that was present for transverse

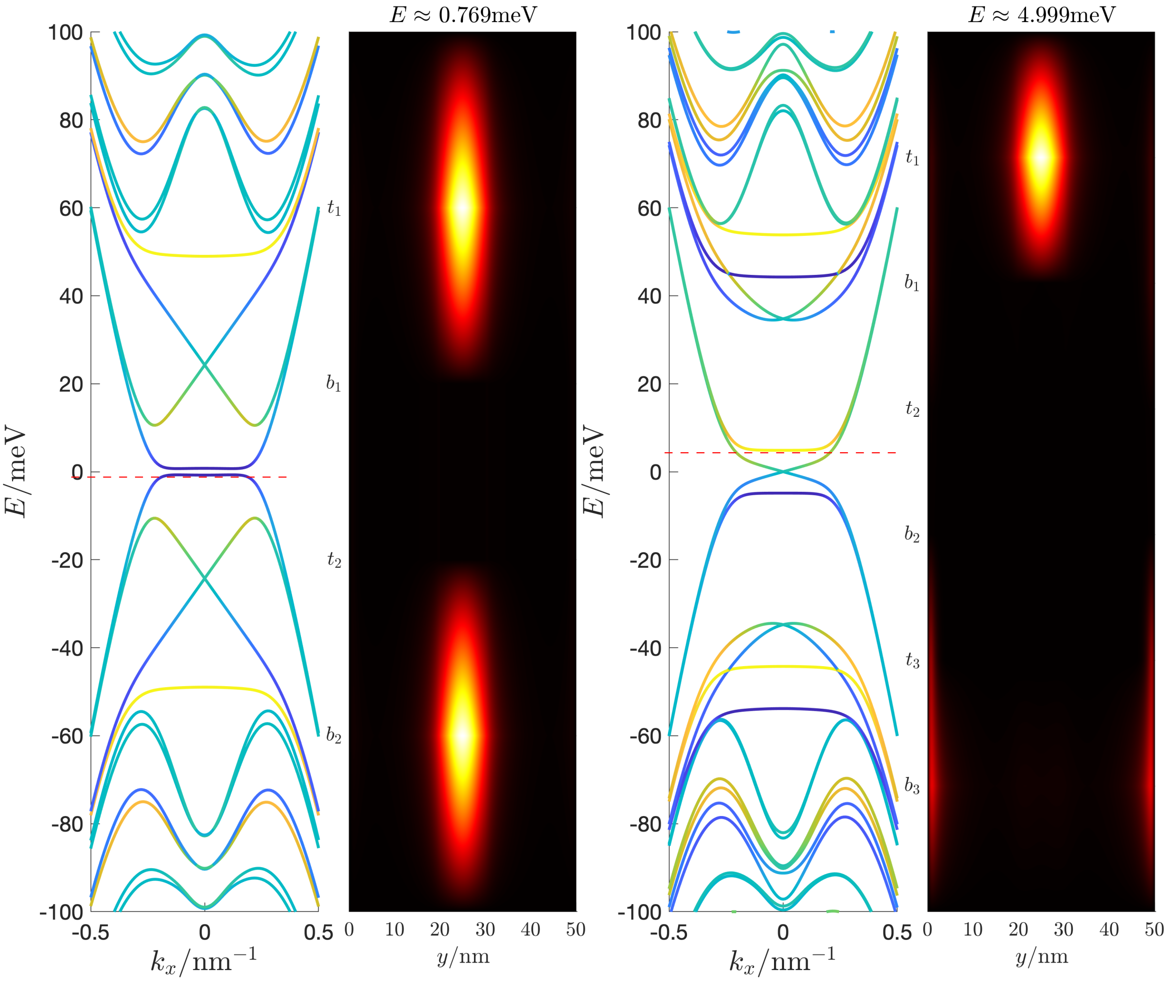

Fig. 4.10 The dispersion relations of a two and three layer system as well as the thermally broadened LDOS of selected domain wall states. The dispersion relations are near identical to those for a sharp DW configuration, however the LDOS is now broadened across the entire width of the domain wall. The dashed red lines correspond to the energies that the associated thermally broadened LDOS images to the right of each dispersion are calculated at.

spin configurations. As a result the states localised along the width of the DW now reside in a single layer, as shown in Fig 4.11, rather than across both layers of the system, as in Fig 4.4.

Turning our attention to a three-layer system with an OOP spin configuration we find that the low-energy flat-bands survive despite the introduction of a spatially varying magnetisation along the z axis, in contrast to the behaviour of an OOP two-layer system, as shown in Fig 4.12. Examining the LDOS around these flat-bands, we find that they only contain states localised along the edges of the system - states localised around the DW have been ’gapped out’ and, similarly to the two-layer system, comprise electronic bands with a finite effective mass. The three-layer system does, however, retain its inversion symmetry even in the OOP

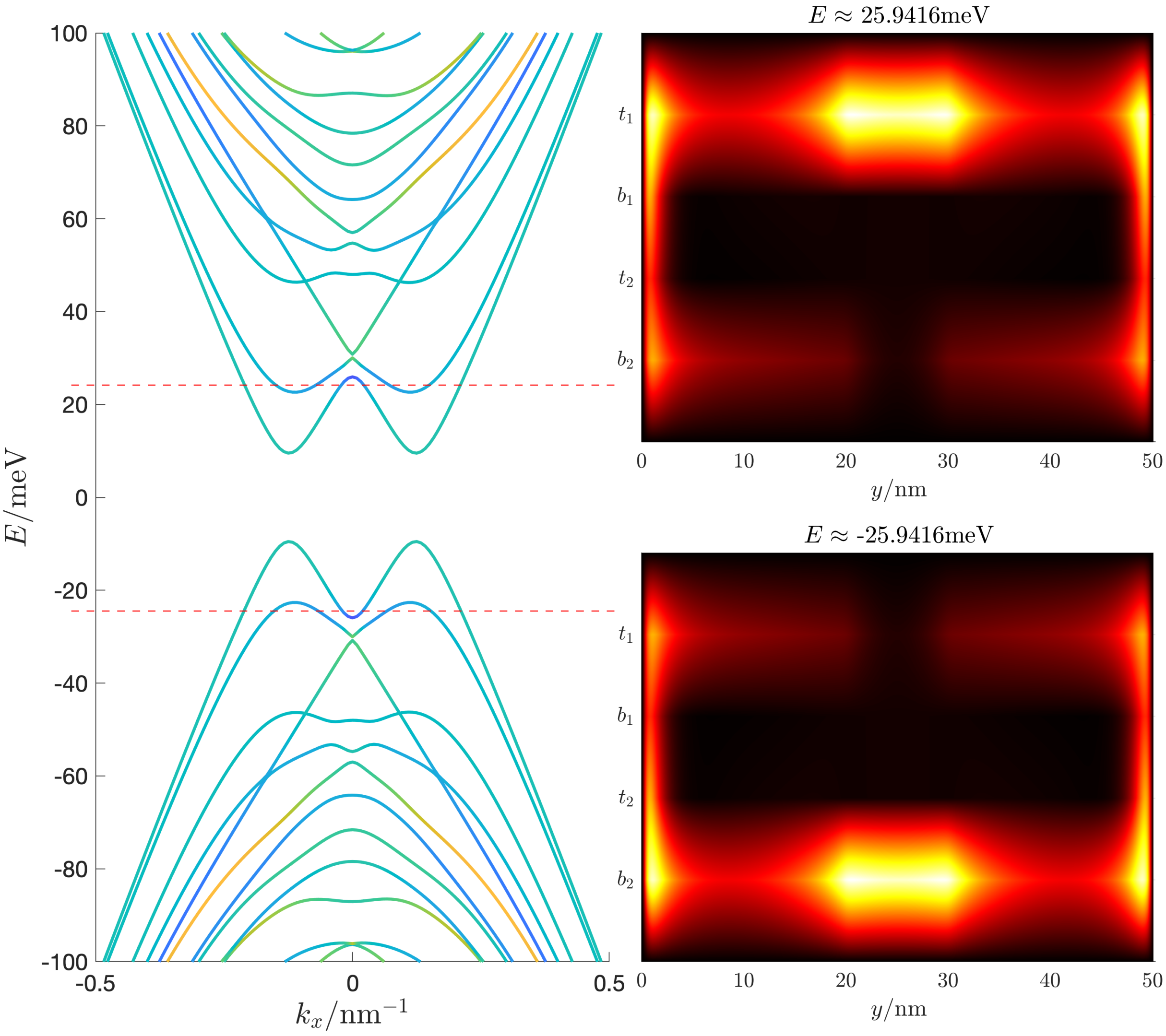

Fig. 4.11 (a) The dispersion relations of a two layer system with a DW with spin configuration restricted to the yz plane and of total width $2l = 10\,\mathrm{nm}$ and (b) the thermally broadened LDOS's around the lowest energy parabolic bands. The dashed red lines across the dispersion relation correspond to the energies that the associated thermally broadened LDOS images to the right of each dispersion are calculated at. In order to more easily distinguish the parabolic DW bands from adjacent electronic bands we have used the parameters $\hbar v_f = 300\,\mathrm{meV\,nm}$, $m = 25\,\mathrm{meV}$, $B = -100\,\mathrm{meV\,nm}^2$, $t_d = 75\,\mathrm{meV}$ and $M = 50\,\mathrm{meV}$.

spin configuration. As a result, the location of the DW states in the OOP configuration is similar to that in the transverse one.

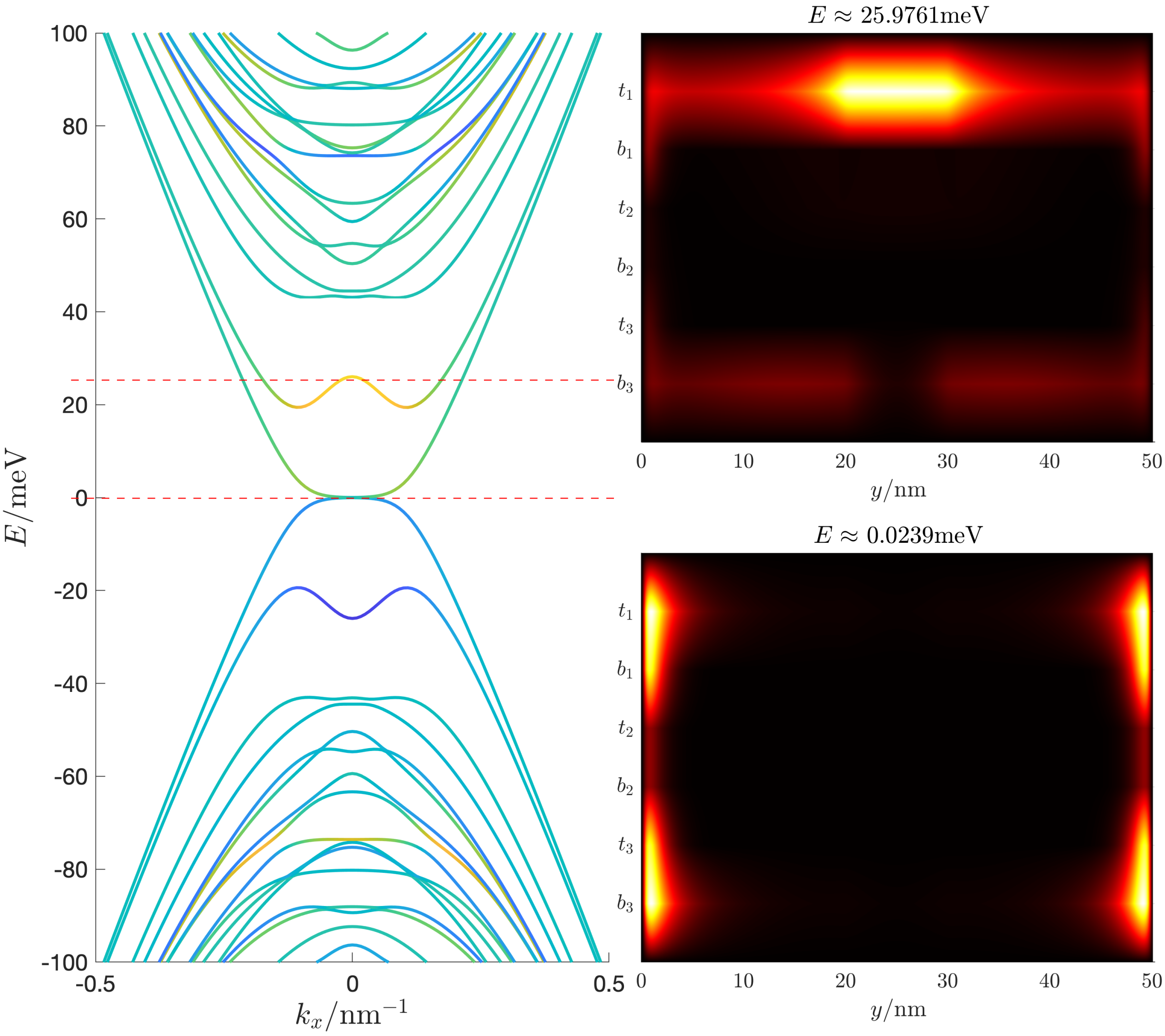

Fig. 4.12 The dispersion relation, of a two layer system with a DW with spin configuration restricted to the yz plane and of total width $2l = 10\,$nm, left panel, and the thermally broadened LDOS's around the lowest energy parabolic bands, right panel. The dashed red lines across the dispersion relation correspond to the energies that the associated thermally broadened LDOS images to the right of each dispersion are calculated at. In order to more easily distinguish the parabolic DW bands from adjacent electronic bands we have used the parameters $\hbar v_f = 300\,$meV nm, $m = 25\,$meV, $B = -100\,$meV nm^2, $t_d = 75\,$meV and $M = 50\,$meV.

4.6 Discussion and Conclusion

As discussed in Chapters 1 and 3, the V/EuBi$_2$Te$_4$ material system possesses an in-plane magnetisation as the lowest energy configuration and, as such, may also prove to be a suitable system in which to engineer the spin configurations proposed and discussed in this chapter.

However, while this material system possesses the required in-plane easy magnetisation axis it should be noted that we have not considered the energetics of these spin configurations and that, in general, determining the DW structure in a material is a complex problem involving the consideration of shape anisotropy, magnetocrystalline anisotropy and stray fields amongst other effects. However, adopting the formalism set out by Araki *et. al.* [8], we may perform a brief 'back-of-the-envelope' calculation to estimate the energy of the DW configurations considered in this chapter. For simplicity, we only consider the surface Hamiltonian (4.1). For such a Hamiltonian, the free energy per unit area due to the magnetic texture is given as

$$f[\boldsymbol{M}] = \int_{\mathbb{R}} dy \left(J_1 [\nabla \boldsymbol{M}]^2 + J_2 [\nabla \times \boldsymbol{M}]^2 \right), \tag{4.35}$$

where $[\nabla \boldsymbol{M}]^2 = \sum_{i,j} (\partial_i M_j)^2$, $[\nabla \times \boldsymbol{M}]^2 = \sum_i (\nabla \times \boldsymbol{M})_i^2$ and

$$\begin{aligned} J_1 &= \frac{1}{10} \frac{1}{48\pi^2 v_f^3} \\ J_2 &= \frac{1}{48\pi^2 v_f^3} \left(\ln \frac{k_c}{k_f} - \frac{11}{15} \right), \end{aligned} \tag{4.36}$$

where k_c is the momentum cut-off describing the limits of the Brillouin zone and k_f is the Fermi wavevector. In order to analyse the energetics of the transverse and OOP configurations, we will introduce the exchange couplings $J_{\|}, J_{\perp} > 0$ which give the strength of the exchange coupling between the Dirac fermions and the local spins in-plane and out-of-plane, respectively. As such, the magnetisation vectors for the transverse and OOP configurations in the simple surface model (4.1) are $\boldsymbol{M}_t(\boldsymbol{r}) = J_{\|} M_0 (\operatorname{sech} y/l, \tanh y/l, 0)$ and $\boldsymbol{M}_{oop}(\boldsymbol{r}) = M_0 (0, J_{\|} \tanh y/l, J_{\perp} \operatorname{sech} y/l)$. Substituting these magnetisation vectors into (4.35), we find that the excitation energies of each configuration are

$$\begin{aligned} f_t &= \frac{2 M_0^2 J_{\|}^2}{l} \left(J_1 + \frac{2}{3} J_2 \right) \\ f_{oop} &= \frac{2 M_0^2 (2 J_{\|}^2 + J_{\perp}^2)}{3l} (J_1 + J_2), \end{aligned} \tag{4.37}$$

with the energy difference between the two configurations $\Delta f = f_{oop} - f_t$ given by

$$\Delta f = \frac{2 M_0^2}{3l} \left((J_1 + J_2) J_{\perp}^2 - J_1 J_{\|}^2 \right). \tag{4.38}$$

As expected, the transverse configuration has a lower excitation energy than the OOP for $J_{\parallel} < J_{\perp}$, i.e. an easy in-plane axis. It is important to note that this calculation has only considered the energy of the magnetic texture and the magnetocrystalline anisotropy, but effects such as shape anisotropy will play an equally important part in determining the DW configuration. These effects can be incorporated through micromagnetic simulations and numerical solutions of the Landau-Lifshitz-Gilbert equation. Furthermore, while we have only considered transverse and OOP head-to-head DWs, there are numerous other possible configurations, such as Bloch, spiral, vortex, etc. The aim of this chapter is not to provide an exhaustive discussion regarding the energetics of all DW configurations, but merely an introduction to the analysis of magnetic textures and their utility as a playground to engineer novel Dirac quasiparticles, and the interested reader should refer to the extensive literature on the subject of DW energetics.

Of course, it may be the case that engineering a head-to-head (tail-to-tail) DW configuration in an intrinsically magnetic TI such as, $EuBi_2Te_4$ or VBi_2Te_4, may prove too experimentally challenging in a realistic device architecture. In addition, as noted in the text, the external magnetic fields required to realise the out-of-plane component of the magnetisation in order to tune the energy of the flat bands is on the order of 10s of Tesla, which is out of reach for most laboratories and certainly not feasible in commercial applications. It should, however, be possible to find a magnetic insulator that can be placed proximate to the surfaces of a thin film TI in order to couple Dirac electrons to local spins via the magnetic proximity effect, given that the in-plane component of the magnetisation is within the range of exchange splittings in ferromagnetic materials and intrinsic magnetic TIs [187, 105]. This set-up would provide the additional benefit that the proximate insulators could be used as a dielectric should a front and/or back gated device architecture be developed in order to tune the chemical potential. However, as discussed above, additional terms such as the asymmetric exchange interaction become more important at interfaces, meaning that it may be quite challenging to realise a head-to-head DW as required here. Indeed, more complex spin textures would be expected. The stray field caused by an adjacent ferromagnet may also distort the band structure, however one could rectify this by using a proximate antiferromagnetic insulator. In addition, one would have to potentially limit the size of the multilayer heterostructures to one or two layers, as it is impractical to create a heterostructure with magnetisation configuration as complex as shown in 4.1.

In recent years strain has also been identified as a means to generate gauge fields in Dirac materials through elastic distortions [156, 70]. Practically, it is essentially impossible to generate a strain field that realises a layer dependent gauge field as we have here, however a proposal to realise flat-bands on the surface of topological crystalline insulator (TCI) using a periodic array of dislocations has been made [169]. This set-up is closely related to the simple surface models that were studied in section 4.3. Finally, as mentioned in the introduction to this chapter, bound states have been observed in a number of systems utilising defects and lattice dislocations. While the analysis above showed that spin-polarization of edge states can be achieved through the use of in-plane magnetic texture and external fields, it is interesting to note that one can influence spin edge transport through the use of defects such as grain boundaries [162, 80].

To conclude, motivated by the recent discovery of intrinsic magnetic TIs with an easy in-plane axis, in this chapter we have investigated the appearance of bound states at head-to-head DWs in AFMTIs with ground-state planar magnetism, as motivated by the findings in chapter 3 where it was found in-plane magnetism can lead to chiral flat-band states around $E = 0$. However, while the flat-bands in Chapter 3 were a result of chiral symmetry and accidental band crossings, here they arise from the presence of bound states across a DW. We began our discussion by investigating the cases of sharp and slowly varying DWs and showed that spin-polarised flat-bands (i.e. quasiparticles with an infinite effective mass) exist in systems with transverse spin configurations. We extended this treatment to an $\boldsymbol{k} \cdot \boldsymbol{p}$ model of a multilayer AFMTI and investigated two and three layer multilayer heterostructures, showing that the parity of the number of layers, rather than the absolute number, strongly affects the electronic dispersion. We have also shown that the presence of flat-bands is sensitive to the DW configuration, by considering the case of OOP DWs and demonstrating the evolution of spin-polarised flat-bands into those with a finite effective mass. Finally, we have concluded this chapter by briefly considering the material systems that could be used to observe these quasiparticles, as well as their uses in device technologies an the study of fundamental phenomena.

Chapter 5

Conclusion

The work carried out over the course of this thesis has provided an outline into how magnetism can play an important role in tuning the topological character and the low energy electronic structure of condensed matter systems. This has important applications in the development of future technologies and devices that may offer a future for topological matter in industry, beyond the now outdated promise of TIs as a replacement for silicon. In this chapter we will briefly summarise the results of this thesis before offering ideas for future work and research.

5.1 Summary

In Chapter 1 the theory of topology in condensed matter was introduced before a literature review covering the state of the art in topological condensed matter, in large part devoted to the description of magnetic TIs. These were discussed mainly with regards to an alternative application of TIs, beyond just as a possible replacement for silicon. Indeed, as we discussed, it appears extremely unlikely that bare TIs will become a viable material platform for low energy electronics due to sustained difficulties in processing them into devices and low mobilities due to thin film imperfections causing parasitic bulk conduction.

However, it appears that magnetic TIs may provide an ideal platform to release the quantum anomalous Hall effect which could provide the basis for low-power electronic and spintronic devices as well as a viable material platform for the emergence of Majorana fermions, the building blocks of topological quantum computation. At the time of writing, there has been no conclusive evidence with regards to the synthesis and braiding of Majorana fermions and they remain a controversial topic in the field of topological condensed matter physics. Nevertheless, the interplay of magnetism and topology is one of the most intensely researched topics across the field of condensed matter physics and the last six years of research has seen the $MnBi_2Te_4$ (MBT) family of intrinsically magnetic TIs emerge as promising candidates for room temperature quantum anomalous Hall insulators and possible material platforms for other spintronic device applications.

Chapter 2 contained a detailed study of topological invariants, beginning with an introduction of the symmetry classification of condensed matter systems and the resulting 'tenfold way', also known as the Altland-Zirnbauer classification, resulting from the consideration of time-reversal, particle-hole and chiral symmetry as anti-unitary symmetries that can be used to classify irreducible Hamiltonians. Clifford algebras were then introduced as a mechanism to keep track of the symmetries present in condensed matter systems, due to the existence of a mapping between the generators of the Clifford algebra and the anti-unitary symmetries mentioned above. This led to the study of the modern theory of topological classification in condensed matter and a description of Kitaev's *Clifford extension problem* as a means to construct a periodic table of topological phases for gapped single-particle Hamiltonians. Finally, the notion of a topological invariant was introduced for each class of the Altland-Zirnbauer classification and Bott periodicity was used to develop the theory of topological invariants in different dimensions.

In Chapter 3, we investigated a magnetic TI system discretised on a hexagonal lattice with the introduction of a magnetic exchange term, similar to the model for the intrinsic magnetic TIs with antiferromagnetic coupling between spins in adjacent layers introduced in Chapter 1. We considered two ground-state configurations - one where the spins aligned along the $\hat{z}$ axis and the other where they aligned in the plane. We then extended this study by considering the possibility of *canted* magnetisation configurations, i.e. spins canted in-plane for a ground state easy axis along the $\hat{z}$ direction and spins canted along the $\hat{z}$ direction for an in-plane easy axis. The discussions regarding topological classification outlined in Chapter 2 where utilised in order to determine how the topological character of the system could be altered by the magnetisation configuration and the parity of the number of layers in the system (i.e. even or odd numbers of layers).

Through the calculation of electronic dispersion relations and the local density of states at various energies in nanoribbon geometries, we were able to demonstrate the presence of low-energy flat-bands formed of edge states. Furthermore, the magnetisation configuration and the number of layers present in the material was determined to be crucial to both the presence and the nature of these flat-bands. When considering systems with in-plane canting, we found that low-energy flat-bands with states localised along the edge of the nanoribbon formed when the spins aligned in the plane of the nanoribbon, irrespective of the number of layers. However, in systems with out-of-plane canting, flat-bands appeared only in *odd* layer systems when the spins were aligned in the plane as a result of the topologically trivial nature of even layer systems with out-of-plane canting. Furthermore, it was shown that the local density of states at the energy around the dispersionless regions of these flat-bands was highly localised at the top and bottom surfaces and *every other layer*. We concluded this chapter by suggesting VBi_2Te_4 and $EuBi_2Te_4$ as possible candidates for the observation of these flat bands.

Chapter 4 saw an extension of the work in Chapter 3 to consider domain walls in antiferromagnetic TIs with in-plane magnetisation. It was shown that such a system also contains flat-bands, but this time of a spin-polarised nature in the presence of a head-to-head (tail-to-tail, equivalently) domain walls. While in Chapter 3 in-plane magnetisation was shown to result in low-energy flat-bands only in multilayer samples, we presented a topological argument for the presence of flat-bands in single layer systems and provided a simple analytic calculation to demonstrate the presence of spin-polarised flat-bands even in a surface Hamiltonian with head-to-head domain walls. We also presented an alternative interpretation of the in-plane magnetisation on the surface of a topological insulator as an axial magnetic field, demonstrating that the states forming the flat band were highly localised around the domain wall.

A $\boldsymbol{k} \cdot \boldsymbol{p}$ model was discretised on a square lattice in order to extend this study to multilayer samples. A numerical approach was adopted to perform electronic dispersion and local density of states calculations in two and three layer nanoribbons. Similarly to Chapter 3 we demonstrated that the electronic structure was highly dependent on the number of layers present in the sample, a consequence of various spatial symmetries present. We introduced additional complexity by considering domain walls of a finite width, showing that the conclusions for drawn in the case of sharp head-to-head domain walls remained valid. We concluded this chapter by offering a discussion on the feasibility of engineering such domain walls in magnetic TIs by calculating the energy of formation for head-to-head versus Neel domain walls and offered the possibility of using strain fields to introduce terms into topological insulator Hamiltonians similar to those introduced by a spatially varying exchange field.

5.2 Further Work

Given more time, there are numerous avenues of interest that the author would have desired to investigate based on the results presented in Chapters 3 and 4. However, the unfortunate truth is that time waits for no one and a PhD must must end somewhere. Below I give three examples of future work that could extend the original research presented in this thesis and conducted throughout this PhD.

In Chapters 3 and 4, the presence of flat-bands were presented as the main results of each chapter. In the former, a key claim was that the velocity of the flat-bands present in a system with in-plane magnetism and antiferromagnetic coupling between layers could be tuned with an out-of-plane canting, and that this could be verified in electronic transport simulations. It would be a reasonably straightforward matter to complete such simulations, using the code the was developed for Chapter 3 and 4. Furthermore, rather than simply just including an out-of-plane canting in the magnetisation vector, it would be enlightening to simulate the application of a perpendicular magnetic field, B_z, which would have the additional effect of modifying the hopping terms, according to the Peierls substitution.

In the introduction, higher order topology was briefly discussed as a generalisation of the topological effects present in topological insulators. For instance, will a first-order 3D topological insulator will possess conductive surface states, a second-order 3D topological insulator will possess 1D hinge states. In general, in an N-dimensional higher order topological insulator (HOTI) there will be $N - d$ dimensional states, where $d > 1$ is the order. Some of the earliest work into HOTI's focussed on the presence of an in-plane magnetisation to drive a TI into a HOTI state - specifically, in finite samples when the in-plane magnetisation is orientated towards the corners of the sample zero-energy corner states emerge, a hallmark of higher-order topology. Interestingly, there has been very little research conducted into how an antiferromagnetic coupling between adjacent layers in a multilayer TI heterostructure influence the presence of higher order topology. Some exploratory analysis of the effect of such a coupling was conducted in finite, hexagonal samples with the Hamiltonian described in Chapter 3, however time constraints ensured that no conclusive results were generated which could be presented in this thesis. Investigating the effect of such magnetic configurations would, once again, be a reasonably doable exercise with the code developed during this PhD.

Finally, there are obvious limitations with the approaches adopted in both chapters, namely the adherence to a single particle Hamiltonian throughout the electronic structure calculations. The small value of the kinetic energy of the electron in a flat or nearly flat-band means that effects such as electron-electron interactions can no longer be ignored due to the highly localised nature of the electrons in a confined region of space. The inclusion of such terms in the Hamiltonian can promote correlated electronic states and the emergence of exotic many-body phenomena, such as fractional quantum Hall states and unconventional superconductivity. We note here that the models considered in Chapters 3 and 4 do not consider the effect of particle-hole symmetry breaking terms, and these will generally break the symmetries discussed in these chapters, however when these terms are small we would expect the previously flat-bands to acquire only a small velocity meaning that a large density of states and enhanced electron correlations should still be present in realistic materials with the magnetic textures described. A more involved extension of this work would be to theoretically analyse and simulate Dirac Hamiltonians, with and without the particle-hole symmetry breaking terms, with magnetic textures in real space in a two-body setting.

Bibliography

[1] Abanin, D. A. and Pesin, D. A. (2011). Ordering of Magnetic Impurities and Tunable Electronic Properties of Topological Insulators. *Physical Review Letters*, 106(13):136802.

[2] Abramovici, G. and Kalugin, P. (2012). Clifford modules and symmetries of topological insulators. *International Journal of Geometric Methods in Modern Physics*, 09(03):1250023.

[3] Aitani, M., Sakamoto, Y., Hirahara, T., Yamada, M., Miyazaki, H., Matsunami, M., Kimura, S.-i., and Hasegawa, S. (2013). Fermi-level tuning of topological insulator thin films. *Japanese Journal of Applied Physics*, 52(11R):110112.

[4] Alexandradinata, A., Dai, X., and Bernevig, B. A. (2014). Wilson-loop characterization of inversion-symmetric topological insulators. *Physical Review B*, 89(15):155114.

[5] Altland, A. and Zirnbauer, M. R. (1997). Nonstandard symmetry classes in mesoscopic normal-superconducting hybrid structures. *Physical Review B*, 55(2):1142–1161.

[6] Ando, Y. (2013). Topological insulator materials. *Journal of the Physical Society of Japan*, 82(10):102001.

[7] Anirban, A. (2019). *Topological Insulators Interfaced with Trivial and Ferromagnetic Insulators*. PhD thesis, University of Cambridge, Cambridge.

[8] Araki, Y. and Nomura, K. (2016). Spin textures and spin-wave excitations in doped dirac-weyl semimetals. *Phys. Rev. B*, 93(9):094438.

[9] Atiyah, M. F., Bott, R., and Shapiro, A. (1964). Clifford modules. *Topology*, 3:3–38.

[10] Atiyah, M. F. and Singer, I. M. (1969). Index theory for skew-adjoint fredholm operators. *Publications Mathématiques de l'Institut des Hautes Études Scientifiques*, 37(1):5–26.

[11] Avron, J. E., Seiler, R., and Simon, B. (1983). Homotopy and Quantization in Condensed Matter Physics. *Physical Review Letters*, 51(1):51–53.

[12] Bac, S.-K., Koller, K., Lux, F., Wang, J., Riney, L., Borisiak, K., Powers, W., Zhukovskyi, M., Orlova, T., Dobrowolska, M., Furdyna, J. K., Dilley, N. R., Rokhinson, L. P., Mokrousov, Y., McQueeney, R. J., Heinonen, O., Liu, X., and Assaf, B. A. (2022). Topological response of the anomalous hall effect in $MnBi_2Te_4$ due to magnetic canting. *npj Quantum Materials*, 7(1):1–7.

[13] Bansal, N., Kim, Y. S., Brahlek, M., Edrey, E., and Oh, S. (2012). Thickness-Independent Transport Channels in Topological Insulator Bi2Se3 Thin Films. *Physical Review Letters*, 109(11):116804.

[14] Bansal, N., Kim, Y. S., Edrey, E., Brahlek, M., Horibe, Y., Iida, K., Tanimura, M., Li, G.-H., Feng, T., Lee, H.-D., Gustafsson, T., Andrei, E., and Oh, S. (2011). Epitaxial growth of topological insulator Bi_2Se_3 film on si(111) with atomically sharp interface. *Thin Solid Films*, 520(1):224–229.

[15] Bardarson, J. H. (2008). A proof of the Kramers degeneracy of transmission eigenvalues from antisymmetry of the scattering matrix. *Journal of Physics A: Mathematical and Theoretical*, 41(40):405203.

[16] Bernevig, B. A., Hughes, T. L., and Zhang, S.-C. (2006). Quantum Spin Hall Effect and Topological Phase Transition in HgTe Quantum Wells. *Science*, 314(5806):1757–1761.

[17] Berry, M. (1984). Quantal phase factors accompanying adiabatic changes. *Proceedings of the Royal Society of London. A. Mathematical and Physical Sciences*, 392(1802):45–57.

[18] Borisova, S., Krumrain, J., Luysberg, M., Mussler, G., and Grützmacher, D. (2012). Mode of Growth of Ultrathin Topological Insulator Bi2Te3 Films on Si (111) Substrates. *Crystal Growth & Design*, 12(12):6098–6103.

[19] Bouhon, A., Black-Schaffer, A. M., and Slager, R.-J. (2019). Wilson loop approach to fragile topology of split elementary band representations and topological crystalline insulators with time-reversal symmetry. *Physical Review B*, 100(19):195135.

[20] Bouhon, A., Bzdušek, T., and Slager, R.-J. (2020a). Geometric approach to fragile topology beyond symmetry indicators. *Physical Review B*, 102(11):115135. Publisher: American Physical Society.

[21] Bouhon, A., Lange, G. F., and Slager, R.-J. (2021). Topological correspondence between magnetic space group representations and subdimensions. *Physical Review B*, 103(24):245127.

[22] Bouhon, A., Timmel, A., and Slager, R.-J. (2023). Quantum geometry beyond projective single bands. arXiv:2303.02180 [cond-mat, physics:hep-th, physics:quant-ph].

[23] Bouhon, A., Wu, Q., Slager, R.-J., Weng, H., Yazyev, O. V., and Bzdušek, T. (2020b). Non-abelian reciprocal braiding of weyl points and its manifestation in zrte. *Nature Physics*, 16(11):1137–1143.

[24] Breunig, O. and Ando, Y. (2022). Opportunities in topological insulator devices. *Nature Reviews Physics*, 4(3):184–193.

[25] Burkov, A. A. and Balents, L. (2011). Weyl semimetal in a topological insulator multilayer. *Phys. Rev. Lett.*, 107(12):127205.

[26] Callan, C. G. and Harvey, J. A. (1985). Anomalies and fermion zero modes on strings and domain walls. *Nuclear Physics B*, 250(1):427–436.

[27] Cartan, E. (1926). Sur une classe remarquable d'espaces de riemann. *Bulletin de la Société Mathématique de France*, 54:214–264.

[28] Chang, C.-Z., Zhang, J., Feng, X., Shen, J., Zhang, Z., Guo, M., Li, K., Ou, Y., Wei, P., Wang, L.-L., Ji, Z.-Q., Feng, Y., Ji, S., Chen, X., Jia, J., Dai, X., Fang, Z., Zhang, S.-C., He, K., Wang, Y., Lu, L., Ma, X.-C., and Xue, Q.-K. (2013). Experimental Observation of the Quantum Anomalous Hall Effect in a Magnetic Topological Insulator. *Science*, 340(6129):167–170.

[29] Chen, B., Fei, F., Zhang, D., Zhang, B., Liu, W., Zhang, S., Wang, P., Wei, B., Zhang, Y., Zuo, Z., Guo, J., Liu, Q., Wang, Z., Wu, X., Zong, J., Xie, X., Chen, W., Sun, Z., Wang, S., Zhang, Y., Zhang, M., Wang, X., Song, F., Zhang, H., Shen, D., and Wang, B. (2019). Intrinsic magnetic topological insulator phases in the Sb doped MnBi2Te4 bulks and thin flakes. *Nature Communications*, 10(1):4469.

[30] Chen, S., Bouhon, A., Slager, R.-J., and Monserrat, B. (2022). Non-abelian braiding of weyl nodes via symmetry-constrained phase transitions. *Physical Review B*, 105(8):L081117. Publisher: American Physical Society.

[31] Chiu, C.-K., Teo, J. C. Y., Schnyder, A. P., and Ryu, S. (2016). Classification of topological quantum matter with symmetries. *Reviews of Modern Physics*, 88(3):035005.

[32] Deng, D.-L., Wang, S.-T., Shen, C., and Duan, L.-M. (2013). Hopf insulators and their topologically protected surface states. *Physical Review B*, 88(20):201105.

[33] Deng, Y., Yu, Y., Shi, M. Z., Guo, Z., Xu, Z., Wang, J., Chen, X. H., and Zhang, Y. (2020). Quantum anomalous Hall effect in intrinsic magnetic topological insulator MnBi2Te4. *Science*, 367(6480):895–900.

[34] Devlin, N. B., Ferrus, T., and Barnes, C. H. W. (2021). Magnetic domain walls in antiferromagnetic topological insulator heterostructures. *Phys. Rev. B*, 104(9):054433.

[35] Ding, L., Hu, C., Ye, F., Feng, E., Ni, N., and Cao, H. (2020). Crystal and magnetic structures of magnetic topological insulators $MnBi_2Te_4$ and $MnBi_4Te_7$. *Physical Review B*, 101(2):020412.

[36] dos Santos Dias, M., Biniskos, N., dos Santos, F. J., Schmalzl, K., Persson, J., Bourdarot, F., Marzari, N., Blügel, S., Brückel, T., and Lounis, S. (2023). Topological magnons driven by the dzyaloshinskii-moriya interaction in the centrosymmetric ferromagnet Mn_5Ge_3. *Nature Communications*, 14(1):7321. Publisher: Nature Publishing Group.

[37] Dyson, F. J. (1962). The Threefold Way. Algebraic Structure of Symmetry Groups and Ensembles in Quantum Mechanics. *Journal of Mathematical Physics*, 3(6):1199–1215.

[38] Elcoro, L., Wieder, B. J., Song, Z., Xu, Y., Bradlyn, B., and Bernevig, B. A. (2021). Magnetic topological quantum chemistry. *Nature Communications*, 12(1):5965.

[39] Eremeev, S. V., Men'shov, V. N., Tugushev, V. V., and Chulkov, E. V. (2015). Interface induced states at the boundary between a 3D topological insulator Bi2Se3 and a ferromagnetic insulator EuS. *Journal of Magnetism and Magnetic Materials*, 383:30–33.

[40] Eremeev, S. V., Otrokov, M. M., and Chulkov, E. V. (2018). New Universal Type of Interface in the Magnetic Insulator/Topological Insulator Heterostructures. *Nano Letters*, 18(10):6521–6529.

[41] Eremeev, S. V., Rusinov, I. P., Koroteev, Y. M., Vyazovskaya, A. Y., Hoffmann, M., Echenique, P. M., Ernst, A., Otrokov, M. M., and Chulkov, E. V. (2021). Topological Magnetic Materials of the (MnSb2Te4)·(Sb2Te3)n van der Waals Compounds Family. *The Journal of Physical Chemistry Letters*, 12(17):4268–4277.

[42] Ertem, Ü. (2017). Index of Dirac operators and classification of topological insulators. *Journal of Physics Communications*, 1(3):035001.

[43] Essin, A. M., Moore, J. E., and Vanderbilt, D. (2009). Magnetoelectric Polarizability and Axion Electrodynamics in Crystalline Insulators. *Physical Review Letters*, 102(14):146805.

[44] Ezawa, M. (2018). Magnetic second-order topological insulators and semimetals. *Physical Review B*, 97(15):155305.

[45] Figueroa, A. I., Bonell, F., Cuxart, M. G., Valvidares, M., Gargiani, P., van der Laan, G., Mugarza, A., and Valenzuela, S. O. (2020). Absence of magnetic proximity effect at the interface of Bi_2Se_3 and $(Bi, Sb)_2Se_3$ with eus. *Physical Review Letters*, 125(22):226801.

[46] Fu, L. (2011). Topological Crystalline Insulators. *Physical Review Letters*, 106(10):106802. Publisher: American Physical Society.

[47] Fu, L. and Kane, C. L. (2006). Time reversal polarization and a Z_2 adiabatic spin pump. *Physical Review B*, 74(19):195312.

[48] Fu, L. and Kane, C. L. (2007). Topological insulators with inversion symmetry. *Physical Review B*, 76(4):045302.

[49] Fu, L. and Kane, C. L. (2008). Superconducting Proximity Effect and Majorana Fermions at the Surface of a Topological Insulator. *Physical Review Letters*, 100(9):096407.

[50] Fu, L., Kane, C. L., and Mele, E. J. (2007). Topological Insulators in Three Dimensions. *Physical Review Letters*, 98(10):106803.

[51] Ge, J., Liu, Y., Li, J., Li, H., Luo, T., Wu, Y., Xu, Y., and Wang, J. (2020). High-Chern-number and high-temperature quantum Hall effect without Landau levels. *National Science Review*, 7(8):1280–1287.

[52] Ginley, T. P., Wang, Y., and Law, S. (2016). Topological Insulator Film Growth by Molecular Beam Epitaxy: A Review. *Crystals*, 6(11):154.

[53] Grutter, A. J. and He, Q. L. (2021). Magnetic proximity effects in topological insulator heterostructures: Implementation and characterization. *Physical Review Materials*, 5(9):090301.

[54] Gu, M., Li, J., Sun, H., Zhao, Y., Liu, C., Liu, J., Lu, H., and Liu, Q. (2021). Spectral signatures of the surface anomalous Hall effect in magnetic axion insulators. *Nature Communications*, 12(1):3524.

[55] Haldane, F. D. M. (1988). Model for a Quantum Hall Effect without Landau Levels: Condensed-Matter Realization of the "Parity Anomaly". *Physical Review Letters*, 61(18):2015–2018.

[56] Hall, E. H. (1879). On a new action of the magnet on electric currents. *American Journal of Mathematics*, 2(3):287–292.

[57] Halperin, B. I. (1982). Quantized Hall conductance, current-carrying edge states, and the existence of extended states in a two-dimensional disordered potential. *Physical Review B*, 25(4):2185–2190.

[58] Hasan, M. Z. and Kane, C. L. (2010). Colloquium: Topological insulators. *Rev. Mod. Phys.*, 82(4):3045–3067.

[59] Hayakawa, Y., Imai, Y., and Kohno, H. (2023). Dzyaloshinskii-moriya interaction in strongly spin-orbit coupled systems: General formula and application to topological and rashba materials. *Physical Review B*, 108(6):064409. Publisher: American Physical Society.

[60] He, Q. L., Hughes, T. L., Armitage, N. P., Tokura, Y., and Wang, K. L. (2022). Topological spintronics and magnetoelectronics. *Nature Materials*, 21(1):15–23.

[61] He, Q. L., Kou, X., Grutter, A. J., Yin, G., Pan, L., Che, X., Liu, Y., Nie, T., Zhang, B., Disseler, S. M., Kirby, B. J., Ratcliff II, W., Shao, Q., Murata, K., Zhu, X., Yu, G., Fan, Y., Montazeri, M., Han, X., Borchers, J. A., and Wang, K. L. (2017). Tailoring exchange couplings in magnetic topological-insulator/antiferromagnet heterostructures. *Nature Materials*, 16(1):94–100.

[62] He, Q. L., Yin, G., Yu, L., Grutter, A. J., Pan, L., Chen, C.-Z., Che, X., Yu, G., Zhang, B., Shao, Q., Stern, A. L., Casas, B., Xia, J., Han, X., Kirby, B. J., Lake, R. K., Law, K. T., and Wang, K. L. (2018). Topological Transitions Induced by Antiferromagnetism in a Thin-Film Topological Insulator. *Physical Review Letters*, 121(9):096802.

[63] Hikami, S., Larkin, A. I., and Nagaoka, Y. (1980). Spin-Orbit Interaction and Magnetoresistance in the Two Dimensional Random System. *Progress of Theoretical Physics*, 63(2):707–710.

[64] Hoefer, K., Becker, C., Wirth, S., and Hao Tjeng, L. (2015). Protective capping of topological surface states of intrinsically insulating Bi_2Te_3. *AIP Advances*, 5(9):097139.

[65] Hor, Y. S., Richardella, A., Roushan, P., Xia, Y., Checkelsky, J. G., Yazdani, A., Hasan, M. Z., Ong, N. P., and Cava, R. J. (2009). p-type Bi_2Se_3 for topological insulator and low-temperature thermoelectric applications. *Physical Review B*, 79(19):195208.

[66] Hou, Y. S. and Wu, R. Q. (2021). Alloying vanadium in $MnBi_2Te_4$ for robust ferromagnetic coupling and quantum anomalous hall effect. *Physical Review B*, 103(6):064412.

[67] Hsieh, D., Qian, D., Wray, L., Xia, Y., Hor, Y. S., Cava, R. J., and Hasan, M. Z. (2008). A topological Dirac insulator in a quantum spin Hall phase. *Nature*, 452(7190):970–974.

[68] Hu, C., Qian, T., and Ni, N. (2024). Recent progress in MnBi2nTe3n+1 intrinsic magnetic topological insulators: crystal growth, magnetism and chemical disorder. *National Science Review*, 11(2):nwad282.

[69] Huan, S., Zhang, S., Jiang, Z., Su, H., Wang, H., Zhang, X., Yang, Y., Liu, Z., Wang, X., Yu, N., Zou, Z., Shen, D., Liu, J., and Guo, Y. (2021). Multiple magnetic topological phases in bulk van der waals crystal $\mathrm{MnSb_4Te_7}$. *Physical Review Letters*, 126(24):246601.

[70] Ilan, R., Grushin, A., and Pikulin, D. (2020). Pseudo-electromagnetic fields in 3d topological semimetals. *Nature Review Physics*, 2(1):29–41.

[71] Inhofer, A., Tchoumakov, S., Assaf, B. A., Fève, G., Berroir, J. M., Jouffrey, V., Carpentier, D., Goerbig, M. O., Plaçais, B., Bendias, K., Mahler, D. M., Bocquillon, E., Schlereth, R., Brüne, C., Buhmann, H., and Molenkamp, L. W. (2017). Observation of volkov-pankratov states in topological hgte heterojunctions using high-frequency compressibility. *Physical Review B*, 96(19):195104.

[72] Jackiw, R. and Rebbi, C. (1976). Solitons with fermion number $\frac{1}{2}$. *Phys. Rev. D*, 13(12):3398–3409.

[73] Jiang, B., Bouhon, A., Lin, Z.-K., Zhou, X., Hou, B., Li, F., Slager, R.-J., and Jiang, J.-H. (2021). Experimental observation of non-Abelian topological acoustic semimetals and their phase transitions. *Nature Physics*, 17(11):1239–1246.

[74] Jiang, B., Bouhon, A., Wu, S.-Q., Kong, Z.-L., Lin, Z.-K., Slager, R.-J., and Jiang, J.-H. (2024). Observation of an acoustic topological euler insulator with meronic waves. *Science Bulletin*, 69(11):1653–1659.

[75] Jo, N. H., Wang, L.-L., Slager, R.-J., Yan, J., Wu, Y., Lee, K., Schrunk, B., Vishwanath, A., and Kaminski, A. (2020). Intrinsic axion insulating behavior in antiferromagnetic $\mathrm{MnBi_6Te_{10}}$. *Physical Review B*, 102(4):045130.

[76] Juričić, V., Mesaros, A., Slager, R.-J., and Zaanen, J. (2012). Universal probes of two-dimensional topological insulators: Dislocation and π flux. *Physical Review Letters*, 108(10):106403. Publisher: American Physical Society.

[77] Just, S., Lüpke, F., Cherepanov, V., Tautz, F. S., and Voigtländer, B. (2020). Parasitic conduction channels in topological insulator thin films. *Physical Review B*, 101(24):245413.

[78] Kane, C. L. and Mele, E. J. (2005a). Quantum Spin Hall Effect in Graphene. *Physical Review Letters*, 95(22):226801.

[79] Kane, C. L. and Mele, E. J. (2005b). Z_2 Topological Order and the Quantum Spin Hall Effect. *Physical Review Letters*, 95(14):146802.

[80] Kariyado, T. and Slager, R.-J. (2019). *pi*-fluxes, semimetals, and flat bands in artificial materials. *Physical Review Research*, 1(3):032027.

[81] Karoubi, M. (1978). *K-Theory: An Introduction*. Springer-Verlag.

[82] Katmis, F., Lauter, V., Nogueira, F. S., Assaf, B. A., Jamer, M. E., Wei, P., Satpati, B., Freeland, J. W., Eremin, I., Heiman, D., Jarillo-Herrero, P., and Moodera, J. S. (2016). A high-temperature ferromagnetic topological insulating phase by proximity coupling. *Nature*, 533(7604):513–516.

[83] Kaufmann, R. M., Li, D., and Wehefritz–Kaufmann, B. (2024). Topological insulators and K-theory. *Journal of Mathematical Physics*, 65(4):043502.

[84] Kawamura, K. (1978a). A new theory on scattering of electrons due to spiral dislocations. *Zeitschrift für Physik B Condensed Matter*, 29(2):101–106.

[85] Kawamura, K. (1978b). Scattering of electrons due to screw dislocations. *Zeitschrift für Physik B Condensed Matter*, 30(1):1–11.

[86] Kennedy, R. and Guggenheim, C. (2015). Homotopy theory of strong and weak topological insulators. *Physical Review B*, 91(24):245148.

[87] Kim, Y. S., Brahlek, M., Bansal, N., Edrey, E., Kapilevich, G. A., Iida, K., Tanimura, M., Horibe, Y., Cheong, S.-W., and Oh, S. (2011). Thickness-dependent bulk properties and weak antilocalization effect in topological insulator $\mathrm{Bi_2Se_3}$. *Physical Review B*, 84(7):073109.

[88] King-Smith, R. D. and Vanderbilt, D. (1993). Theory of polarization of crystalline solids. *Physical Review B*, 47(3):1651–1654.

[89] Kitaev, A. (2009). Periodic table for topological insulators and superconductors. *AIP Conference Proceedings*, 1134(1):22–30.

[90] Klimovskikh, I. I. t. (2020). Tunable 3D/2D magnetism in the $(\mathrm{MnBi_2Te_4})(\mathrm{Bi_2Te_3})_m$ topological insulators family. *npj Quantum Materials*, 5(1):1–9.

[91] Ko, W., Jeon, I., Kim, H. W., Kwon, H., Kahng, S.-J., Park, J., Kim, J. S., Hwang, S. W., and Suh, H. (2013). Atomic and electronic structure of an alloyed topological insulator, $\mathrm{Bi_{1.5}Sb_{0.5}Te_{1.7}Se_{1.3}}$. *Scientific Reports*, 3(1):2656.

[92] Kohmoto, M. (1985). Topological invariant and the quantization of the Hall conductance. *Annals of Physics*, 160(2):343–354.

[93] Koirala, N., Brahlek, M., Salehi, M., Wu, L., Dai, J., Waugh, J., Nummy, T., Han, M.-G., Moon, J., Zhu, Y., Dessau, D., Wu, W., Armitage, N. P., and Oh, S. (2015). Record Surface State Mobility and Quantum Hall Effect in Topological Insulator Thin Films via Interface Engineering. *Nano Letters*, 15(12):8245–8249.

[94] Konig, M., Wiedmann, S., Brüne, C., Roth, A., Buhmann, H., Molenkamp, L. W., Qi, X.-L., and Zhang, S.-C. (2007). Quantum spin hall insulator state in hgte quantum wells. *Science*, 318(5851):766–770.

[95] Kremer, G., Zhu, K., Pierron, T., Fournee, V., Ledieu, J., Andrieu, S., Kierren, B., Moreau, L., Malterre, D., He, K., Xue, Q.-K., Fagot-Revurat, Y., and Lu, Y. (2019). Recovery of surface state bands after desorption of Te capping layer on $(\mathrm{Bi}_{1-x}\mathrm{Sb}_x)_2\mathrm{Te}_3$ ternary topological insulators. *Journal of Physics D: Applied Physics*, 52(49):494002.

[96] Kruthoff, J., de Boer, J., van Wezel, J., Kane, C. L., and Slager, R.-J. (2017). Topological classification of crystalline insulators through band structure combinatorics. *Physical Review X*, 7(4):041069.

[97] Lai, Y., Ke, L., Yan, J., McDonald, R. D., and McQueeney, R. J. (2021). Defect-driven ferrimagnetism and hidden magnetization in $\mathrm{MnBi_2Te_4}$. *Physical Review B*, 103(18):184429. Comment: 9 pages, 6 figures.

[98] Lapierre, B., Neupert, T., and Trifunovic, L. (2021). n-band Hopf insulator. *Physical Review Research*, 3(3):033045.

[99] Lau, A., Hyart, T., Autieri, C., Chen, A., and Pikulin, D. I. (2021). Designing Three-Dimensional Flat Bands in Nodal-Line Semimetals. *Physical Review X*, 11(3):031017.

[100] Laughlin, R. B. (1981). Quantized Hall conductivity in two dimensions. *Physical Review B*, 23(10):5632–5633.

[101] Lawson, H. B. and Michelsohn, M.-L. (2016). *Spin Geometry (PMS-38), Volume 38*. Princeton University Press.

[102] Leggett, A. J. (1975). A theoretical description of the new phases of liquid He^3. *Reviews of Modern Physics*, 47(2):331–414.

[103] Lei, C. and MacDonald, A. H. (2021). Gate-tunable quantum anomalous Hall effects in $\mathrm{MnBi_2Te_4}$ thin films. *Physical Review Materials*, 5(5):L051201.

[104] Li, C.-K., Yao, X.-P., and Chen, G. (2021). Twisted magnetic topological insulators. *Physical Review Research*, 3(3):033156. Publisher: American Physical Society.

[105] Li, J., Li, Y., Du, S., Wang, Z., Gu, B.-L., Zhang, S.-C., He, K., Duan, W., and Xu, Y. (2019). Intrinsic magnetic topological insulators in van der Waals layered $\mathrm{MnBi_2Te_4}$-family materials. *Science Advances*, 5(6):eaaw5685.

[106] Li, M., Chang, C.-Z., Wu, L., Tao, J., Zhao, W., Chan, M. H., Moodera, J. S., Li, J., and Zhu, Y. (2015). Experimental verification of the van vleck nature of long-range ferromagnetic order in the vanadium-doped three-dimensional topological insulator $\mathrm{Sb_2Te_3}$. *Physical Review Letters*, 114(14):146802.

[107] Li, Z., Li, J., He, K., Wan, X., Duan, W., and Xu, Y. (2020). Tunable interlayer magnetism and band topology in van der Waals heterostructures of $\mathrm{MnBi_2Te_4}$-family materials. *Physical Review B*, 102(8):081107.

[108] Lian, B., Sun, X.-Q., Vaezi, A., Qi, X.-L., and Zhang, S.-C. (2018). Topological quantum computation based on chiral Majorana fermions. *Proceedings of the National Academy of Sciences*, 115(43):10938–10942.

[109] Liang, L.-U., Yen, Y.-H., Chou, C.-W., Chen, K.-H. M., Lin, H.-Y., Huang, S.-W., Hong, M., Kwo, J., and Hoffmann, G. (2021). Protected long-time storage of a topological insulator. *AIP Advances*, 11(2):025245.

[110] Lisi, S., Lu, X., Benschop, T., de Jong, T. A., Stepanov, P., Duran, J. R., Margot, F., Cucchi, I., Cappelli, E., Hunter, A., Tamai, A., Kandyba, V., Giampietri, A., Barinov, A., Jobst, J., Stalman, V., Leeuwenhoek, M., Watanabe, K., Taniguchi, T., Rademaker, L., van der Molen, S. J., Allan, M. P., Efetov, D. K., and Baumberger, F. (2021). Observation of flat bands in twisted bilayer graphene. *Nature Physics*, 17(2):189–193.

[111] Liu, C., Wang, Y., Li, H., Wu, Y., Li, Y., Li, J., He, K., Xu, Y., Zhang, J., and Wang, Y. (2020). Robust axion insulator and Chern insulator phases in a two-dimensional antiferromagnetic topological insulator. *Nature Materials*, 19(5):522–527.

[112] Liu, C.-X., Qi, X.-L., Zhang, H., Dai, X., Fang, Z., and Zhang, S.-C. (2010). Model Hamiltonian for topological insulators. *Physical Review B*, 82(4):045122.

[113] Liu, J. and Hesjedal, T. (2021). Magnetic Topological Insulator Heterostructures: A Review. *Advanced Materials*, page 2102427.

[114] Lu, H.-Z., Shan, W.-Y., Yao, W., Niu, Q., and Shen, S.-Q. (2010). Massive dirac fermions and spin physics in an ultrathin film of topological insulator. *Phys. Rev. B*, 81(11):115407.

[115] Lu, H.-Z. and Shen, S.-Q. (2014). Weak localization and weak anti-localization in topological insulators. In *Spintronics VII*, volume 9167, pages 263–273. SPIE.

[116] Matsuura, S., Chang, P.-Y., Schnyder, A. P., and Ryu, S. (2013). Protected boundary states in gapless topological phases. *New Journal of Physics*, 15(6):065001.

[117] Men'shov, V. N., Shvets, I. A., and Chulkov, E. V. (2019). Interface effects on the magnetic-proximity-induced quantized Hall response in heterostructures based on three-dimensional topological insulators. *Physical Review B*, 99(11):115301.

[118] Mesaros, A., Slager, R.-J., Zaanen, J., and Juričić, V. (2013). Zero-energy states bound to a magnetic π-flux vortex in a two-dimensional topological insulator. *Nuclear Physics B*, 867(3):977–991.

[119] Mikitik, G. P. and Sharlai, Y. V. (2012). Berry phase and the phase of the Shubnikov–de Haas oscillations in three-dimensional topological insulators. *Physical Review B*, 85(3):033301.

[120] Momma, K. and Izumi, F. (2011). Vesta 3 for three-dimensional visualization of crystal, volumetric and morphology data. *Journal of Applied Crystallography*, 44(6):1272–1276.

[121] Mong, R. S. K., Essin, A. M., and Moore, J. E. (2010). Antiferromagnetic topological insulators. *Physical Review B*, 81(24):245209.

[122] Morimoto, T. and Furusaki, A. (2013). Topological classification with additional symmetries from Clifford algebras. *Physical Review B*, 88(12):125129.

[123] Morimoto, T., Furusaki, A., and Mudry, C. (2015). Anderson localization and the topology of classifying spaces. *Physical Review B*, 91(23):235111.

[124] Mussler, G. (2021). Molecular-Beam Epitaxy of 3D Topological Insulator Thin Films and Devices on Si Substrates. *physica status solidi (b)*, 258(1):2000007.

[125] Nevola, D., Li, H. X., Yan, J.-Q., Moore, R. G., Lee, H.-N., Miao, H., and Johnson, P. D. (2020). Coexistence of Surface Ferromagnetism and a Gapless Topological State in $MnBi_2Te_4$. *Physical Review Letters*, 125(11):117205.

[126] Newton, P. J., Mansell, R., Holmes, S. N., Myronov, M., and Barnes, C. H. W. (2017). Weak localization and weak antilocalization in doped germanium epilayers. *Applied Physics Letters*, 110(6):062101.

[127] Ngabonziza, P., Stehno, M. P., Myoren, H., Neumann, V. A., Koster, G., and Brinkman, A. (2016). Gate-Tunable Transport Properties of In Situ Capped Bi_2Te_3 Topological Insulator Thin Films. *Advanced Electronic Materials*, 2(8):1600157.

[128] Nogueira, F. S., Eremin, I., Katmis, F., Moodera, J. S., van den Brink, J., and Kravchuk, V. P. (2018). Fluctuation-induced neel and bloch skyrmions at topological insulator surfaces. *Physical Review B*, 98(6):060401. Publisher: American Physical Society.

[129] Otrokov, M. M., Menshchikova, T. V., Vergniory, M. G., Rusinov, I. P., Vyazovskaya, A. Y., Koroteev, Y. M., Bihlmayer, G., Ernst, A., Echenique, P. M., Arnau, A., and Chulkov, E. V. (2017). Highly-ordered wide bandgap materials for quantized anomalous Hall and magnetoelectric effects. *2D Materials*, 4(2):025082.

[130] Otrokov, M. M., Rusinov, I. P., Blanco-Rey, M., Hoffmann, M., Vyazovskaya, A. Y., Eremeev, S. V., Ernst, A., Echenique, P. M., Arnau, A., and Chulkov, E. V. (2019). Unique thickness-dependent properties of the van der waals interlayer antiferromagnet $MnBi_2Te_4$ films. *Physical Review Letters*, 122(10):107202.

[131] Otrokov, M. M. t. (2019). Prediction and observation of an antiferromagnetic topological insulator. *Nature*, 576(7787):416–422.

[132] Ou, Y., Liu, C., Jiang, G., Feng, Y., Zhao, D., Wu, W., Wang, X.-X., Li, W., Song, C., Wang, L.-L., Wang, W., Wu, W., Wang, Y., He, K., Ma, X.-C., and Xue, Q.-K. (2018). Enhancing the Quantum Anomalous Hall Effect by Magnetic Codoping in a Topological Insulator. *Advanced Materials*, 30(1):1703062.

[133] Pai, C.-F. (2018). Switching by topological insulators. *Nature Materials*, 17(9):755–757.

[134] Pankratov, O. A., Pakhomov, S. V., and Volkov, B. A. (1987). Supersymmetry in heterojunctions: Band-inverting contact on the basis of $Pb_{1-x}Sn_xTe$ and $Hg_{1-x}Cd_xTe$. *Solid State Communications*, 61(2):93–96.

[135] Parkin, S. S. P., Hayashi, M., and Thomas, L. (2008). Magnetic domain-wall racetrack memory. *Science*, 320(5873):190–194.

[136] Paul, N. and Fu, L. (2021). Topological magnetic textures in magnetic topological insulators. *Physical Review Research*, 3(3):033173.

[137] Peng, B., Bouhon, A., Monserrat, B., and Slager, R.-J. (2022a). Phonons as a platform for non-Abelian braiding and its manifestation in layered silicates. *Nature Communications*, 13(1):423. Publisher: Nature Publishing Group.

[138] Peng, B., Bouhon, A., Slager, R.-J., and Monserrat, B. (2022b). Multigap topology and non-Abelian braiding of phonons from first principles. *Physical Review B*, 105(8):085115.

[139] Pereira, V. M., Wu, C.-N., Höfer, K., Choa, A., Knight, C.-A., Swanson, J., Becker, C., Komarek, A. C., Rata, A. D., Rößler, S., Wirth, S., Guo, M., Hong, M., Kwo, J., Tjeng, L. H., and Altendorf, S. G. (2021). Challenges of topological insulator research: Bi_2Te_3 thin films and magnetic heterostructures. *physica status solidi (b)*, 258(1):2000346.

[140] Petrov, E. K., Men'shov, V. N., Rusinov, I. P., Hoffmann, M., Ernst, A., Otrokov, M. M., Dugaev, V. K., Menshchikova, T. V., and Chulkov, E. V. (2021). Domain wall induced spin-polarized flat bands in antiferromagnetic topological insulators. *Phys. Rev. B*, 103(9):235142.

[141] Ramachandran, A., Andreanov, A., and Flach, S. (2017). Chiral flat bands: Existence, engineering, and stability. *Physical Review B*, 96(16):161104.

[142] Rao, W., Zhou, Y.-L., Wu, Y.-j., Duan, H.-J., Deng, M.-X., and Wang, R.-Q. (2021). Theory for linear and nonlinear planar Hall effect in topological insulator thin films. *Physical Review B*, 103(15):155415.

[143] Rastogi, S., Shahi, N., Kumar, V., Shukla, G. K., Bhattacharjee, S., and Singh, S. (2023). Revealing the origin of the topological hall effect in the centrosymmetric shape memory heusler alloy Mn_2NiGa: A combined experimental and theoretical investigation. *Physical Review B*, 108(22):224108. Publisher: American Physical Society.

[144] Ren, Z., Taskin, A. A., Sasaki, S., Segawa, K., and Ando, Y. (2011). Optimizing $Bi_{2-x}Sb_xTe_{3-y}Se_y$ solid solutions to approach the intrinsic topological insulator regime. *Physical Review B*, 84(16):165311.

[145] Resta, R. and Vanderbilt, D. (2007). *Theory of Polarization: A Modern Approach*. Springer.

[146] Ryu, S. and Hatsugai, Y. (2002). Topological origin of zero-energy edge states in particle-hole symmetric systems. *Physical Review Letters*, 89(7):077002.

[147] Ryu, S., Schnyder, A. P., Furusaki, A., and Ludwig, A. W. W. (2010). Topological insulators and superconductors: Tenfold way and dimensional hierarchy. *New Journal of Physics*, 12(6):065010.

[148] Salehi, M., Brahlek, M., Koirala, N., Moon, J., Wu, L., Armitage, N. P., and Oh, S. (2015). Stability of low-carrier-density topological-insulator Bi_2Se_3 thin films and effect of capping layers. *APL Materials*, 3(9):091101.

[149] Schindler, F., Cook, A. M., Vergniory, M. G., Wang, Z., Parkin, S. S. P., Bernevig, B. A., and Neupert, T. (2018). Higher-order topological insulators. *Science Advances*, 4(6):eaat0346.

[150] Schnyder, A. P. and Ryu, S. (2011). Topological phases and surface flat bands in superconductors without inversion symmetry. *Physical Review B*, 84(6):060504.

[151] Schnyder, A. P., Ryu, S., Furusaki, A., and Ludwig, A. W. W. (2009). Classification of Topological Insulators and Superconductors. *AIP Conference Proceedings*, 1134(1):10–21.

[152] Scholten, M., Facio, J. I., Ray, R., Eremin, I. M., van den Brink, J., and Nogueira, F. S. (2021). Finite temperature fluctuation-induced order and responses in magnetic topological insulators. *Physical Review Research*, 3(3):L032014. Publisher: American Physical Society.

[153] Schrunk, B., Kushnirenko, Y., Kuthanazhi, B., Ahn, J., Wang, L.-L., O'Leary, E., Lee, K., Eaton, A., Fedorov, A., Lou, R., Voroshnin, V., Clark, O. J., Sánchez-Barriga, J., Bud'ko, S. L., Slager, R.-J., Canfield, P. C., and Kaminski, A. (2022). Emergence of fermi arcs due to magnetic splitting in an antiferromagnet. *Nature*, 603(7902):610–615.

[154] Schuster, T., Flicker, F., Li, M., Kotochigova, S., Moore, J. E., Ye, J., and Yao, N. Y. (2021). Realizing Hopf Insulators in Dipolar Spin Systems. *Physical Review Letters*, 127(1):015301.

[155] Shan, W.-Y., Lu, H.-Z., and Shen, S.-Q. (2010). Effective continuous model for surface states and thin films of three-dimensional topological insulators. *New Journal of Physics*, 12(4):043048.

[156] Shapourian, H., Hughes, T. L., and Ryu, S. (2015). Viscoelastic response of topological tight-binding models in two and three dimensions. *Phys. Rev. B*, 92:165131.

[157] Shikin, A. M., Estyunin, D. A., Zaitsev, N. L., Glazkova, D., Klimovskikh, I. I., Filnov, S. O., Rybkin, A. G., Schwier, E. F., Kumar, S., Kimura, A., Mamedov, N., Aliev, Z., Babanly, M. B., Kokh, K., Tereshchenko, O. E., Otrokov, M. M., Chulkov, E. V., Zvezdin, K. A., and Zvezdin, A. K. (2021). Sample-dependent dirac-point gap in $\mathrm{MnBi_2Te_4}$ and its response to applied surface charge: A combined photoemission and ab initio study. *Physical Review B*, 104(11):115168.

[158] Shiozaki, K., Sato, M., and Gomi, K. (2017). Topological crystalline materials: General formulation, module structure, and wallpaper groups. *Physical Review B*, 95(23):235425.

[159] Shoenberg, D. (1984). *Magnetic Oscillations in Metals*. Cambridge Monographs on Physics. Cambridge University Press, Cambridge.

[160] Slager, R.-J. (2019). The translational side of topological band insulators. *Journal of Physics and Chemistry of Solids*, 128:24–38.

[161] Slager, R.-J., Bouhon, A., and Ünal, F. N. (2024). Non-abelian floquet braiding and anomalous dirac string phase in periodically driven systems. *Nature Communications*, 15(1):1144.

[162] Slager, R.-J., Juričić, V., Lahtinen, V., and Zaanen, J. (2016). Self-organized pseudo-graphene on grain boundaries in topological band insulators. *Physical Review B*, 93(24):245406.

[163] Slager, R.-J., Mesaros, A., Juričić, V., and Zaanen, J. (2013). The space group classification of topological band-insulators. *Nature Physics*, 9(2):98–102.

[164] Slager, R.-J., Mesaros, A., Juričić, V., and Zaanen, J. (2014). Interplay between electronic topology and crystal symmetry: Dislocation-line modes in topological band insulators. *Physical Review B*, 90(24):241403. Publisher: American Physical Society.

[165] Slager, R.-J., Rademaker, L., Zaanen, J., and Balents, L. (2015). Impurity-bound states and green's function zeros as local signatures of topology. *Physical Review B*, 92(8):085126.

[166] Šmejkal, L., Mokrousov, Y., Yan, B., and MacDonald, A. H. (2018). Topological antiferromagnetic spintronics. *Nature Physics*, 14(3):242–251.

[167] Stone, M., Chiu, C.-K., and Roy, A. (2010). Symmetries, dimensions and topological insulators: The mechanism behind the face of the Bott clock. *Journal of Physics A: Mathematical and Theoretical*, 44(4):045001.

[168] Swatek, P., Wu, Y., Wang, L.-L., Lee, K., Schrunk, B., Yan, J., and Kaminski, A. (2020). Gapless Dirac surface states in the antiferromagnetic topological insulator $MnBi_2Te_4$. *Physical Review B*, 101(16):161109.

[169] Tang, E. and Fu, L. (2014). Strain-induced partially flat band, helical snake states and interface superconductivity in topological crystalline insulators. *Nature Physics*, 10(12):964–969.

[170] Taskin, A. A., Legg, H. F., Yang, F., Sasaki, S., Kanai, Y., Matsumoto, K., Rosch, A., and Ando, Y. (2017). Planar Hall effect from the surface of topological insulators. *Nature Communications*, 8(1):1340.

[171] Taskin, A. A., Ren, Z., Sasaki, S., Segawa, K., and Ando, Y. (2011). Observation of Dirac Holes and Electrons in a Topological Insulator. *Physical Review Letters*, 107(1):016801.

[172] Tchoumakov, S., Jouffrey, V., Inhofer, A., Bocquillon, E., Plaçais, B., Carpentier, D., and Goerbig, M. O. (2017). Volkov-Pankratov states in topological heterojunctions. *Physical Review B*, 96(20):201302.

[173] Teo, J. C. Y. and Kane, C. L. (2010). Topological defects and gapless modes in insulators and superconductors. *Physical Review B*, 82(11):115120. Publisher: American Physical Society.

[174] Thouless, D. J., Kohmoto, M., Nightingale, M. P., and den Nijs, M. (1982). Quantized Hall Conductance in a Two-Dimensional Periodic Potential. *Physical Review Letters*, 49(6):405–408.

[175] v. Klitzing, K., Dorda, G., and Pepper, M. (1980). New Method for High-Accuracy Determination of the Fine-Structure Constant Based on Quantized Hall Resistance. *Physical Review Letters*, 45(6):494–497.

[176] Vandenberghe, W. G. and Fischetti, M. V. (2017). Imperfect two-dimensional topological insulator field-effect transistors. *Nature Communications*, 8(1):1–8.

[177] Vanhaverbeke, A., Bischof, A., and Allenspach, R. (2008). Control of domain wall polarity by current pulses. *Phys. Rev. Lett.*, 101(10):107202.

[178] Walsh, L. A., Green, A. J., Addou, R., Nolting, W., Cormier, C. R., Barton, A. T., Mowll, T. R., Yue, R., Lu, N., Kim, J., Kim, M. J., LaBella, V. P., Ventrice, C. A., McDonnell, S., Vandenberghe, W. G., Wallace, R. M., Diebold, A., and Hinkle, C. L. (2018). Fermi Level Manipulation through Native Doping in the Topological Insulator Bi2Se3. *ACS Nano*, 12(6):6310–6318.

[179] Walsh, L. A. and Hinkle, C. L. (2017). Van der Waals epitaxy: 2D materials and topological insulators. *Applied Materials Today*, 9:504–515.

[180] Wang, J., Lian, B., Qi, X.-L., and Zhang, S.-C. (2015). Quantized topological magnetoelectric effect of the zero-plateau quantum anomalous Hall state. *Physical Review B*, 92(8):081107.

[181] Wang, W., Ou, Y., Liu, C., Wang, Y., He, K., Xue, Q.-K., and Wu, W. (2018a). Direct evidence of ferromagnetism in a quantum anomalous Hall system. *Nature Physics*, 14(8):791–795.

[182] Wang, Y., Ginley, T. P., and Law, S. (2018b). Growth of high-quality Bi_2Se_3 topological insulators using $(Bi_{1-x}In_x)_2Se_3$ buffer layers. *Journal of Vacuum Science & Technology B, Nanotechnology and Microelectronics: Materials, Processing, Measurement, and Phenomena*, 36(2):02D101.

[183] Wang, Y., Zhu, D., Wu, Y., Yang, Y., Yu, J., Ramaswamy, R., Mishra, R., Shi, S., Elyasi, M., Teo, K.-L., Wu, Y., and Yang, H. (2017). Room temperature magnetization switching in topological insulator-ferromagnet heterostructures by spin-orbit torques. *Nature Communications*, 8(1):1–6.

[184] Watanabe, R., Yoshimi, R., Kawamura, M., Kaneko, Y., Takahashi, K. S., Tsukazaki, A., Kawasaki, M., and Tokura, Y. (2022). Enhancement of anomalous hall effect in epitaxial thin films of intrinsic magnetic topological insulator $MnBi_2Te_4$ with Fermi-level tuning. *Applied Physics Letters*, 120(3):031901.

[185] Watanabe, R., Yoshimi, R., Kawamura, M., Mogi, M., Tsukazaki, A., Yu, X. Z., Nakajima, K., Takahashi, K. S., Kawasaki, M., and Tokura, Y. (2019). Quantum anomalous Hall effect driven by magnetic proximity coupling in all-telluride based heterostructure. *Applied Physics Letters*, 115(10):102403.

[186] Wei, P., Katmis, F., Assaf, B. A., Steinberg, H., Jarillo-Herrero, P., Heiman, D., and Moodera, J. S. (2013). Exchange-coupling-induced symmetry breaking in topological insulators. *Physical Review Letters*, 110(18):186807.

[187] Wei, P., Lee, S., Lemaitre, F., Pinel, L., Cutaia, D., Cha, W., Katmis, F., Zhu, Y., Heiman, D., Hone, J., Moodera, J. S., and Chen, C.-T. (2016). Strong interfacial exchange field in the graphene/EuS heterostructure. *Nature Materials*, 15(7):711–716.

[188] Wu, G., Chen, H., Sun, Y., Li, X., Cui, P., Franchini, C., Wang, J., Chen, X.-Q., and Zhang, Z. (2013). Tuning the vertical location of helical surface states in topological insulator heterostructures via dual-proximity effects. *Scientific Reports*, 3(1):1233.

[189] Wu, H., Chen, A., Zhang, P., He, H., Nance, J., Guo, C., Sasaki, J., Shirokura, T., Hai, P. N., Fang, B., Razavi, S. A., Wong, K., Wen, Y., Ma, Y., Yu, G., Carman, G. P., Han, X., Zhang, X., and Wang, K. L. (2021). Magnetic memory driven by topological insulators. *Nature Communications*, 12(1):6251.

[190] Wu, H., Zhang, P., Deng, P., Lan, Q., Pan, Q., Razavi, S. A., Che, X., Huang, L., Dai, B., Wong, K., Han, X., and Wang, K. L. (2019a). Room-Temperature Spin-Orbit Torque from Topological Surface States. *Physical Review Letters*, 123(20):207205.

[191] Wu, Y., Guo, Q., Zheng, Q., Xu, X., Liu, T., Liu, Y., Yan, Y., Wang, D., Long, S., Wang, L., Yang, S., Teng, J., Du, S., and Yu, G. (2019b). Stabilizing the Fermi Level of Cr-Doped Magnetic Topological Insulators by Al Passivation. *The Journal of Physical Chemistry C*, 123(6):3823–3828.

[192] Xu, Y., Miotkowski, I., Liu, C., Tian, J., Nam, H., Alidoust, N., Hu, J., Shih, C.-K., Hasan, M. Z., and Chen, Y. P. (2014). Observation of topological surface state quantum Hall effect in an intrinsic three-dimensional topological insulator. *Nature Physics*, 10(12):956–963.

[193] Yan, B., Zhang, D., and Felser, C. (2013). Topological surface states of Bi_2Se_3 coexisting with se vacancies. *physica status solidi (RRL) – Rapid Research Letters*, 7(1-2):148–150.

[194] Yan, J. (2021). The elusive quantum anomalous Hall effect in $MnBi_2Te_4$: A materials perspective.

[195] Yan, J.-Q., Zhang, Q., Heitmann, T., Huang, Z., Chen, K. Y., Cheng, J.-G., Wu, W., Vaknin, D., Sales, B. C., and McQueeney, R. J. (2019). Crystal growth and magnetic structure of $MnBi_2Te_4$. *Physical Review Materials*, 3(6):064202.

[196] Yang, Q. I., Dolev, M., Zhang, L., Zhao, J., Fried, A. D., Schemm, E., Liu, M., Palevski, A., Marshall, A. F., Risbud, S. H., and Kapitulnik, A. (2013). Emerging weak localization effects on a topological insulator–insulating ferromagnet (Bi_2Se_4-eus) interface. *Physical Review B*, 88(8):081407.

[197] Yasuda, K., Mogi, M., Yoshimi, R., Tsukazaki, A., Takahashi, K. S., Kawasaki, M., Kagawa, F., and Tokura, Y. (2017). Quantized chiral edge conduction on domain walls of a magnetic topological insulator. *Science*, 358(6368):1311–1314.

[198] Ye, L., Qiu, C., Xiao, M., Li, T., Du, J., Ke, M., and Liu, Z. (2022). Topological dislocation modes in three-dimensional acoustic topological insulators. *Nature Communications*, 13(1):508.

[199] Yin, J.-X., Zhang, S. S., Chang, G., Wang, Q., Tsirkin, S. S., Guguchia, Z., Lian, B., Zhou, H., Jiang, K., Belopolski, I., Shumiya, N., Multer, D., Litskevich, M., Cochran, T. A., Lin, H., Wang, Z., Neupert, T., Jia, S., Lei, H., and Hasan, M. Z. (2019). Negative flat band magnetism in a spin–orbit-coupled correlated kagome magnet. *Nature Physics*, 15(5):443–448.

[200] Ying, Z., Zhang, S., Chen, B., Jia, B., Fei, F., Zhang, M., Zhang, H., Wang, X., and Song, F. (2022). Experimental evidence for dissipationless transport of the chiral edge state of the high-field Chern insulator in $MnBi_2Te_4$ nanodevices. *Physical Review B*, 105(8):085412.

[201] Yu, R., Zhang, W., Zhang, H.-J., Zhang, S.-C., Dai, X., and Fang, Z. (2010). Quantized Anomalous Hall Effect in Magnetic Topological Insulators. *Science*, 329(5987):61–64.

[202] Zaitsev, N. L., Rusinov, I. P., Menshchikova, T. V., and Chulkov, E. V. (2023). Interplay between exchange-split dirac and rashba-type surface states at the $MnBi_2Te_4$/bitei interface. *Physical Review B*, 107(4):045402.

[203] Zhang, H., Liu, C.-X., Qi, X.-L., Dai, X., Fang, Z., and Zhang, S.-C. (2009). Topological insulators in Bi_2Se_3, Bi_2Te_3 and Sb_2Te_3 with a single Dirac cone on the surface. *Nature Physics*, 5(6):438–442.

[204] Zhang, Q. R., Zeng, B., Chiu, Y. C., Schönemann, R., Memaran, S., Zheng, W., Rhodes, D., Chen, K.-W., Besara, T., Sankar, R., Chou, F., McCandless, G. T., Chan, J. Y., Alidoust, N., Xu, S.-Y., Belopolski, I., Hasan, M. Z., Balakirev, F. F., and Balicas, L. (2019). Possible manifestations of the chiral anomaly and evidence for a magnetic field induced topological phase transition in the type-I Weyl semimetal TaAs. *Physical Review B*, 100(11):115138.

[205] Zhang, R.-X., Wu, F., and Das Sarma, S. (2020). Möbius Insulator and Higher-Order Topology in $MnBi_{2n}Te_{3n+1}$. *Physical Review Letters*, 124(13):136407.

[206] Zhang, S., Kronast, F., van der Laan, G., and Hesjedal, T. (2018). Real-Space Observation of Skyrmionium in a Ferromagnet-Magnetic Topological Insulator Heterostructure. *Nano Letters*, 18(2):1057–1063.

[207] Zhang, Y., He, K., Chang, C.-Z., Song, C.-L., Wang, L.-L., Chen, X., Jia, J.-F., Fang, Z., Dai, X., Shan, W.-Y., et al. (2010). Crossover of the three-dimensional topological insulator Bi_2Se_3 to the two-dimensional limit. *Nature Physics*, 6(8):584–588.

[208] Zhao, W., Yang, Y.-B., Jiang, Y., Mao, Z., Guo, W., Qiu, L., Wang, G., Yao, L., He, L., Zhou, Z., Xu, Y., and Duan, L. (2022). Quantum simulation for topological euler insulators. *Communications Physics*, 5(1):1–8.

[209] Zhao, Y. and Liu, Q. (2021). Routes to realize the axion-insulator phase in $MnBi_2Te_4(Bi_2Te_3)_n$ family. *Applied Physics Letters*, 119(6):060502.

[210] Zheng, S.-H., Duan, H.-J., Wang, J.-K., Li, J.-Y., Deng, M.-X., and Wang, R.-Q. (2020). Origin of planar Hall effect on the surface of topological insulators: Tilt of Dirac cone by an in-plane magnetic field. *Physical Review B*, 101(4):041408.

[211] Zhou, B., Lu, H.-Z., Chu, R.-L., Shen, S.-Q., and Niu, Q. (2008). Finite size effects on helical edge states in a quantum spin-hall system. *Phys. Rev. Lett.*, 101(24):246807.

[212] Zhu, W., Song, C., Liao, L., Zhou, Z., Bai, H., Zhou, Y., and Pan, F. (2020). Quantum anomalous Hall insulator state in ferromagnetically ordered $MnBi_2Te_4/VBi_2Te_4$ heterostructures. *Physical Review B*, 102(8):085111.

[213] Ünal, F. N., Bouhon, A., and Slager, R.-J. (2020). Topological euler class as a dynamical observable in optical lattices. *Physical Review Letters*, 125(5):053601.

[214] Ünal, F. N., Eckardt, A., and Slager, R.-J. (2019). Hopf characterization of two-dimensional Floquet topological insulators. *Physical Review Research*, 1(2):022003.

Appendix A

Perturbative Calculations of AFMTIs with Domain Walls

In Chapter 4 numerical simulations, utilising the finite-difference approximation, for layered AFMTI models were presented. In this appendix we present perturbative calculations of the bandstructure and bound states of two and three layer heterostructures, for completeness.

A.1 Two Layers

As discussed in the text, we note that the Hamiltonian, H_2 given in equation (4.25) is symmetric under a C_2 rotation symmetry, $[H, P] = 0$ where

$$P = \begin{pmatrix} 0 & \sigma_z \tau_x \\ \sigma_z \tau_x & 0. \end{pmatrix} \tag{A.1}$$

We therefore block diagonalise H_2 according to the unitary matrix formed of the eigenvectors of P

$$U_P = \frac{1}{\sqrt{2}} \begin{pmatrix} 1 & 0 & 0 & 0 & 0 & 0 & 1 & 0 \\ 0 & 1 & 0 & 0 & 0 & 0 & 0 & -1 \\ 0 & 0 & 1 & 0 & 1 & 0 & 0 & 0 \\ 0 & 0 & 0 & 1 & 0 & -1 & 0 & 0 \\ 1 & 0 & 0 & 0 & 0 & 0 & -1 & 0 \\ 0 & 1 & 0 & 0 & 0 & 0 & 0 & 1 \\ 0 & 0 & -1 & 0 & 1 & 0 & 0 & 0 \\ 0 & 0 & 0 & -1 & 0 & -1 & 0 & 0 \end{pmatrix}, \tag{A.2}$$

to give

$$U_P H_2 U^\dagger U_P = \begin{pmatrix} H^+ & 0 \\ 0 & H^- \end{pmatrix} \tag{A.3}$$

where $H^\pm$ is given by (4.28) and written in the basis $\frac{1}{\sqrt{2}}(|t_1,\uparrow\rangle \pm |b_2,\uparrow\rangle, |t_1,\downarrow\rangle \mp |b_2,\downarrow\rangle, |t_2,\uparrow\rangle \pm |b_1,\uparrow\rangle, -|t_2,\downarrow\rangle \pm |b_1,\downarrow\rangle)^T$.

To demonstrate the formation of bound states in a two layer model we set $k_x = 0$ and consider a sharp head-to-head domain wall, $M_y = M(2\theta(y) - 1)$, in the Hamiltonian given by (4.28). Following this, we act upon $H^\pm$ with the unitary transformation given by

$$U = \begin{pmatrix} \mathbb{1} & 0 \\ 0 & i\sigma_z \end{pmatrix} e^{i\tau_y \frac{\pi}{4}} \begin{pmatrix} \mathbb{1} & 0 \\ 0 & \sigma_y \end{pmatrix}, \tag{A.4}$$

to give

$$U H^\pm U^\dagger = H_0^\pm + H_1^\pm, \tag{A.5}$$

where $H_0^\pm$ is treated as the zeroth order Hamiltonian and $H_1^\pm$ is the perturbation, given by

$$\begin{aligned} H_0^\pm &= k_y \mu_x \eta_z + M_y \mu_y \eta_z + t_s \mu_y \mp \frac{t_d}{2}\mu_z \\ H_1^\pm &= -(M_z \pm \frac{t_d}{2})\eta_y, \end{aligned} \tag{A.6}$$

where $\mu_{x,y,z}$ and $\eta_{x,y,z}$ are Pauli pseudospin operators. First, solving for the unperturbed Hamiltonian, the eigenstates, $\psi_{\mu,\eta}$ must satisfy

$$\begin{aligned} \left(E^2 - \frac{t_d^2}{4}\right)\psi_{\mu,\eta} = {} & [\eta k_y - i\mu\eta M_y - i\mu t_s] \\ & [\eta k_y + i\eta\mu M_y + i\mu t_s]\psi_{\mu,\eta}, \end{aligned} \tag{A.7}$$

where $\mu, \eta = \pm 1$. Using the trial wavefunction $\psi_{\mu,\eta} = e^{\lambda y}$, we find the roots $\pm\lambda_{\mu,\eta,\pm}$ at $E = \mp\mu t_d/2$ given by

$$\lambda_{\mu,\eta,\pm} = \frac{1}{2B}\left(-\mu\eta \pm \sqrt{1 + 4B(m + \eta M_y)}\right). \tag{A.8}$$

Note that we must make the substitution $M_y = -M$ for $y < 0$ and $M_y = M$ for $y > 0$ resulting in the piecewise quantum state,

$$\psi_{\mu,\eta} = \begin{cases} \alpha_< e^{\lambda^<_{\mu,\eta,+}} + \beta_< e^{\lambda^<_{\mu,\eta,-}} & \text{for } y < 0, \\ \alpha_> e^{\lambda^>_{\mu,\eta,+}} + \beta_> e^{\lambda^>_{\mu,\eta,-}} & \text{for } y > 0, \end{cases} \tag{A.9}$$

where $\lambda^<_{\mu,\eta,\pm}$ and $\lambda^<_{\mu,\eta,\pm}$ are roots in the half spaces $y < 0$ and $y > 0$, respectively. The coefficients $\alpha_{<,>}$ and $\beta_{<,>}$ may be fixed by considering continuity of the wavefunction at $y = 0$ and satisfying the boundary conditions $\psi_{\mu,\eta}(y = \pm L/2) = 0$ giving

$$\begin{aligned} \alpha_< &= \frac{1 - \exp\left((\lambda^>_{\mu,\eta,+} - \lambda^>_{\mu,\eta,-})L/2\right)}{1 - \exp\left(-(\lambda^<_{\mu,\eta,+} - \lambda^<_{\mu,\eta,-})L/2\right)}\alpha_>, \\ \beta_< &= \frac{1 - \exp\left((\lambda^>_{\mu,\eta,+} - \lambda^>_{\mu,\eta,-})L/2\right)}{1 - \exp\left((\lambda^<_{\mu,\eta,+} - \lambda^<_{\mu,\eta,-})L/2\right)}\alpha_>, \\ \beta_> &= -\left(1 - \exp\left((\lambda^>_{\mu,\eta,+} - \lambda^>_{\mu,\eta,-})L/2\right)\right)\alpha_>, \end{aligned} \tag{A.10}$$

where the final coefficient, $\alpha_>$ is fixed by normalisation of the wavefunction, $\int_{-L/2}^{L/2} dy \left|\psi_{\mu,\eta}\right|^2 = 1$. This results in two states localised at either edge ($\mu = 1, \eta = \pm 1$), at energy $E = \mp t_d/2$, and at the domain wall ($\mu = -1, \eta = \pm 1$), at energy $E = \pm t_d/2$.

Introducing the perturbing Hamiltonian, $H_1^\pm$, states are shifted by an amount given by

$$\Delta E^\pm_{\mu,\eta} = \eta(M_z \pm \frac{t_d}{2}) \int_{-L/2}^{L/2} i\psi^*_{\mu,\eta}\psi_{\mu,-\eta} dy. \tag{A.11}$$

States localised around the domain wall are shifted in energy by an amount $\sim \eta(M_z \pm t_d/2)$ owing to their strong overlap, resulting in DW states at $E \approx M_z \pm t_d$ and $E \approx -M_z$. By contrast, the overlap between edge-states is extremely small in wide samples since states are localised on opposite edges. As a result, edge-states remain located around $E \approx \mp t_d/2$.

A.2 Three Layers

Again, we set $k_x = 0$ and adopt a sharp head-to-head domain wall. Noting that the Hamiltonian, H_3, given in equation (4.32) is symmetric under reflection, $RH_3(k_y, M_y, M_z)R^{-1} = H_3(k_y, M_y, -M_z)$, where

$$R = \begin{pmatrix} 0 & 0 & \tau_x\sigma_y \\ 0 & \tau_x\sigma_y & 0 \\ \tau_x\sigma_y & 0 & 0 \end{pmatrix}, \tag{A.12}$$

We block diagonalise H_3 using the unitary matrix formed of the eigenvectors of R, given by

$$U_R = \begin{pmatrix} \omega & \Sigma_x \\ \omega & -\Sigma_x \end{pmatrix} \tag{A.13}$$

where

$$\begin{gathered} \omega = \frac{1}{\sqrt{2}} \begin{pmatrix} e^{i\pi/4} & 0 & 0 & 0 & 0 & 0 \\ 0 & e^{i\pi/4} & 0 & 0 & 0 & 0 \\ 0 & 0 & e^{i\pi/4} & 0 & 0 & 0 \\ 0 & 0 & 0 & e^{i\pi/4} & 0 & 0 \\ 0 & 0 & 0 & 0 & e^{i\pi/4} & 0 \\ 0 & 0 & 0 & 0 & 0 & e^{i\pi/4} \end{pmatrix} \\ \Sigma_x = \frac{1}{\sqrt{2}} \begin{pmatrix} 0 & 0 & 0 & 0 & 0 & e^{3i\pi/4} \\ 0 & 0 & 0 & 0 & e^{-i\pi/4} & 0 \\ 0 & 0 & 0 & e^{3i\pi/4} & 0 & 0 \\ 0 & 0 & e^{-i\pi/4} & 0 & 0 & 0 \\ 0 & e^{3i\pi/4} & 0 & 0 & 0 & 0 \\ e^{-i\pi/4} & 0 & 0 & 0 & 0 & 0 \end{pmatrix} \end{gathered} \tag{A.14}$$

resulting in the block diagonal Hamiltonian

$$H_3^{'} = \begin{pmatrix} H_{3,+} & M \\ M^{\dagger} & H_{3,-} \end{pmatrix} \tag{A.15}$$

where $H_{3,\pm}$ and M are 6×6 matrices given by

$$H_{3,\pm} = \begin{pmatrix} k_y\sigma_x + M_y\sigma_y & t_s & 0 \\ t_s & -k_y\sigma_x + M_y\sigma_y & t_d \\ 0 & t_d & k_y\sigma_x - (M_y \pm t_s)\sigma_y) \end{pmatrix} \tag{A.16}$$

$$M = \begin{pmatrix} M_z\sigma_z & 0 & 0 \\ 0 & M_z\sigma_z & 0 \\ 0 & 0 & M_z\sigma_z \end{pmatrix}$$

In order to write this in the form of an unperturbed Hamiltonian and a perturbation, we first act on the subblocks $H_{3,\pm}$ with the unitary matrix

$$U_1 = \begin{pmatrix} \frac{1}{\sqrt{2}}\mathbb{1}_2 & \frac{1}{\sqrt{2}}\sigma_y & 0 \\ -\frac{1}{\sqrt{2}}\mathbb{1}_2 & \frac{1}{\sqrt{2}}\sigma_y & 0 \\ 0 & 0 & \sigma_x \end{pmatrix} \tag{A.17}$$

to give

$$U_1 H_{3,\pm} U_1^\dagger = \begin{pmatrix} k_y\sigma_x + (M_y + t_s)\sigma_y & 0 & -\frac{i}{\sqrt{2}}t_d \\ 0 & k_y\sigma_x + (M_y - t_s)\sigma_y & -\frac{i}{\sqrt{2}}t_d \\ \frac{i}{\sqrt{2}}t_d & \frac{i}{\sqrt{2}}t_d & k_y\sigma_x + (M_y \pm t_s)\sigma_y \end{pmatrix} \tag{A.18}$$

Then, depending on the subblock, we transform according to the unitary matrix

$$U_+ = \begin{pmatrix} 0 & \mathbb{1}_2 & 0 \\ -\frac{1}{\sqrt{2}}\mathbb{1}_2 & 0 & -\frac{i}{\sqrt{2}}\mathbb{1}_2 \\ -\frac{1}{\sqrt{2}}\mathbb{1}_2 & 0 & \frac{i}{\sqrt{2}}\mathbb{1}_2 \end{pmatrix} \quad \text{or} \quad U_- = \begin{pmatrix} -\mathbb{1}_2 & 0 & 0 \\ 0 & \frac{1}{\sqrt{2}}\mathbb{1}_2 & \frac{i}{\sqrt{2}}\mathbb{1}_2 \\ 0 & \frac{1}{\sqrt{2}}\mathbb{1}_2 & -\frac{i}{\sqrt{2}}\mathbb{1}_2 \end{pmatrix} \tag{A.19}$$

to give $\mathrm{diag}(U_+U_1, U_-U_1)H_3'\mathrm{diag}(U_1^\dagger U_+^\dagger, U_1^\dagger U_-^\dagger) = H_0 + H_1$, where $H_0 = \mathrm{diag}(H_0^+, H_0^-)$ is interpreted as the unperturbed Hamiltonian where

$$H_0^\pm = \begin{pmatrix} k_y\sigma_x + (M_y \mp t_s)\sigma_y & 0 & 0 \\ 0 & k_y\sigma_x + (M_y \pm t_s)\sigma_y - \frac{t_d}{\sqrt{2}}\sigma_z & 0 \\ 0 & 0 & k_y\sigma_x + (M_y \pm t_s)\sigma_y + \frac{t_d}{\sqrt{2}}\sigma_z \end{pmatrix} \tag{A.20}$$

and a perturbation, H_1, given by

$$H_1 = \begin{pmatrix} 0 & \frac{t_d}{2}\sigma_z & -\frac{t_d}{2}\sigma_z & M_z\sigma_z & 0 & 0 \\ \frac{t_d}{2}\sigma_z & 0 & 0 & 0 & M_z\sigma_z & 0 \\ -\frac{t_d}{2}\sigma_z & 0 & 0 & 0 & 0 & M_z\sigma_z \\ M_z\sigma_z & 0 & 0 & 0 & \frac{t_d}{2}\sigma_z & -\frac{t_d}{2}\sigma_z \\ 0 & M_z\sigma_z & 0 & \frac{t_d}{2}\sigma_z & 0 & 0 \\ 0 & 0 & M_z\sigma_z & -\frac{t_d}{2}\sigma_z & 0 & 0 \end{pmatrix} \tag{A.21}$$

Hereafter, we may adopt the derivation is very similar to the two-layer model and is not presented here, for brevity.